HETEROATOM-DOPED PHOTOREDUCED GRAPHENE OXIDE PHOTOCATALYSTS FOR REMOVAL OF VOLATILE ORGANIC COMPOUNDS

TAI XIN HONG

INSTITUTE FOR ADVANCED STUDIES
UNIVERSITI MALAYA
KUALA LUMPUR

2022

HETEROATOM-DOPED PHOTOREDUCED GRAPHENE OXIDE PHOTOCATALYSTS FOR REMOVAL OF VOLATILE ORGANIC COMPOUNDS

TAI XIN HONG

THESIS SUBMITTED IN FULFILMENT OF THE REQUIREMENTS FOR THE DEGREE OF DOCTOR OF PHILOSOPHY

INSTITUTE FOR ADVANCED STUDIES
UNIVERSITI MALAYA
KUALA LUMPUR

2022

UNIVERSITI MALAYA
ORIGINAL LITERARY WORK DECLARATION

Name of Candidate: Tai Xin Hong
Matric No: HVA 190009 (17058733/2)
Name of Degree: Doctor of Philosophy
Title of Dissertation: Heteroatom-doped Photoreduced Graphene Oxide Photocatalysts for Removal of Volatile Organic Compounds

Field of Study: Engineering and Engineering Trades (Chemical and Process)

I do solemnly and sincerely declare that:

(1) I am the sole author/writer of this Work;
(2) This Work is original;
(3) Any use of any work in which copyright exists was done by way of fair dealing and for permitted purposes and any excerpt or extract from, or reference to or reproduction of any copyright work has been disclosed expressly and sufficiently and the title of the Work and its authorship have been acknowledged in this Work;
(4) I do not have any actual knowledge nor do I ought reasonably to know that the making of this work constitutes an infringement of any copyright work;
(5) I hereby assign all and every rights in the copyright to this Work to the University of Malaya ("UM"), who henceforth shall be owner of the copyright in this Work and that any reproduction or use in any form or by any means whatsoever is prohibited without the written consent of UM having been first had and obtained;
(6) I am fully aware that if in the course of making this Work I have infringed any copyright whether intentionally or otherwise, I may be subject to legal action or any other action as may be determined by UM.

Candidate's Signature Date: 22.9.2022

Subscribed and solemnly declared before,

Witness's Signature Date: 24.9.2022

Name:
Designation:

Heteroatom-doped Photoreduced Graphene Oxide Photocatalysts for Removal of Volatile Organic Compounds

ABSTRACT

Indoor air quality (IAQ) has become a great concern as people today spend most of their time indoors, particularly during the Covid-19 pandemic era. Indoor air pollutants such as volatile organic compounds (VOCs) significantly deteriorate air quality and endanger human health. Photocatalytic oxidation (PCO) is a promising method for air remediation because of its ability to operate under ambient conditions to degrade and mineralise VOCs into harmless compounds such as carbon dioxide (CO_2). Recently, the use of metal-free photocatalyst has emerged as a cost-effective, sustainable, lightweight, and earth abundance approach for various photocatalytic applications. Graphene oxide (GO) is a promising metal-free carbon-based photocatalyst that showed photocatalytic activities for dye degradation, water splitting, and CO_2 reduction. Nevertheless, the application of GO and heteroatom (e.g, boron (B), nitrogen (N), and fluorine (F)) doped GO in the PCO of air pollutants have not been explored yet. There are two common strategies to enhance the photoactivity and properties of GO, namely reduction and heteroatom-doping. Therefore, an effective, green, and scalable method to simultaneously reduce and dope GO was developed. In this study, GO was transformed into photoreduced graphene oxide (PRGO) and doped with heteroatom via a facile photoirradiation technique. The photoactivity of the PRGO was 2.4 times better than GO due to the narrower band gap and slower charge carrier recombination rate. Besides that, GO was simultaneously reduced and doped via photoirradiation with B, N, and F heteroatoms as BPRGO, NPRGO, and FPRGO, respectively. The VOCs photodegradation efficiencies of the photocatalysts followed the pseudo-first-order kinetic (k) as according to this

sequence: NPRGO (100%, k = 0.38 h^{-1}) > FPRGO (80.4%, k = 0.26 h^{-1}) > BPRGO (67.7%, k = 0.19 h^{-1}) > PRGO (27.0%, k = 0.06 h^{-1}) > GO (13.7%, k = 0.03 h^{-1}). Additionally, VOCs were successfully mineralised into CO_2 by the heteroatom-doped PRGO photocatalysts with mineralisation efficiency up to 100% for NPRGO-0.5. The improved photocatalytic activities of the heteroatoms-doped PRGO were attributed to their increment of charge carrier densities after doping, which resulted in slower charge carrier recombination rates. Among the heteroatom-doped PRGO, the NPRGO had the slowest charge carrier recombination rate because of its n-type conductivity. As an n-type semiconductor, the N dopants formed a shallow donor level near the conduction band of NPRGO. During photocatalysis, if a photoexcited electron falls from the conduction band of NPRGO, the shallow dopant level could trap the electron and reemit it back to the conduction band easily, therefore preventing the electron from recombining with a hole at the valence band. Moreover, the NPRGO could be reused for five PCO cycles without any significant loss in photoactivity. Through mechanism studies, it was determined that the photogenerated hole was the most significant reactive species in the PCO processes. This study provides new insights into a scalable photoirradiation method for producing effective metal-free PRGO-based photocatalysts for air purification.

Keywords: Photocatalysis, Air remediation, n-type, p-type, semiconductor, photoreduction

Penyingkiran Sebatian Organik Meruap Oleh Fotomangkin Berasaskan Heteroatom-dop Grafin Oksida Tersinar

ABSTRAK

Kualiti udara dalaman (IAQ) amat penting kerana orang ramai hari ini menghabiskan sebahagian besar masa mereka di dalam rumah, terutamanya pada era pandemik Covid-19 ini. Bahan pencemar udara dalaman seperti sebatian organik meruap (VOCs) mencemar kualiti udara dan membahayakan kesihatan manusia. Pengoksidaan fotokatalitik (PCO) adalah satu kaedah pembersihan udara dalam keadaan persekitaran untuk merendahkan dan menguraikan VOCs kepada sebatian tidak berbahaya seperti karbon dioksida (CO_2). Baru-baru ini, fotomangkin bebas logam telah digunakan untuk pelbagai aplikasi fotokatalitik. Grafin Oksida (GO) ialah fotomangkin berasaskan karbon dan bebas logam yang boleh menjalankan aktiviti fotokatalitik seperti penguraian pewarna, pemisahan air, dan reduksi CO_2. Namun begitu, penggunaan GO dan heteroatom (contohnya boron (B), nitrogen (N) dan fluorin (F)) -dop GO dalam pembersihan udara masih belum diterokai. Terdapat dua strategi umum untuk meningkatkan aktiviti fotomangkin dan sifat GO, iaitu reduksi GO dan pendopan heteroatom. Oleh itu, satu kaedah hijau untuk mengurangkan GO dan dop GO secara serentak telah dihasilkan. Dalam kajian ini, GO telah diubah menjadi grafin oksida tersinar (PRGO) dan didopkan dengan heteroatom melalui satu teknik penyinaran foto yang mudah. Aktiviti fotomangkin PRGO adalah 2.4 kali lebih baik daripada GO tulen kerana pengoptimuman jurang jalur dan kadar penggabungan semula pembawa cas yang lebih perlahan. Selain itu, GO telah berjaya direduksi dan didop secara serentak melalui penyinaran foto dengan heteroatom B, N, dan F sebagai BPRGO, NPRGO, dan FPRGO. Kadar fotodegradasi VOCs bagi fotomangkin mengikuti kinetik pseudo-kadar pertama (k)

seperti urutan ini: NPRGO (100%, k = 0.38 h^{-1}) > FPRGO (80.4%, k = 0.26 h^{-1}) > BPRGO (67.7%, k = 0.19 h^{-1}) > PRGO (27.0%, k = 0.06 h^{-1}) > GO (13.7%, k = 0.03 h^{-1}). Selain itu, VOCs berjaya diuraikan menjadi CO_2 dengan kadar penguraian sehingga 100% bagi NPRGO-0.5. Aktiviti fotopemangkin yang lebih baik oleh heteroatom-dop PRGO telah dikaitkan dengan peningkatan ketumpatan pembawa cas selepas pendopan, yang mengakibatkan kadar penggabungan semula pembawa cas yang lebih perlahan. Antara PRGO yang didopkan dengan heteroatom, NPRGO mempunyai kadar penggabungan semula pembawa cas yang paling perlahan kerana jenis kekonduksiannya. Sebagai semikonduktor jenis-n, N membentuk paras penderma cetek berhampiran dengan jalur pengaliran NPRGO. Semasa fotocatalisis, jika elektron fototeruja jatuh daripada jalur pengaliran NPRGO, paras dopan cetek tersebut boleh memerangkap elektron dan memancarkannya semula ke jalur pengaliran dengan mudah, oleh itu menghalang elektron daripada bergabung semula dengan lohong pada jalur valensi. Selain itu, NPRGO boleh digunakan semula untuk lima kitaran PCO tanpa sebarang kehilangan ketara dalam aktiviti fotomangkinan. Melalui kajian mekanisme, telah ditentukan bahawa lohong yang dijana foto adalah spesies reaktif yang paling ketara dalam proses PCO. Kajian ini memberikan pandangan baharu tentang kaedah penyinaran foto untuk menghasilkan fotomangkin berasaskan PRGO bebas logam yang berkesan untuk pembersihan udara.

Kata kunci: Pemangkinan foto, pemulihan udara, jenis-n, jenis-p, semikonduktor, pengurangan foto

ACKNOWLEDGEMENTS

Firstly, I want to thank my family for their love and support. They have supported me unconditionally in all the ups and downs.

I would like to express my deepest gratitude to my supervisors Assoc. Prof. Dr. Juan Joon Ching and Assoc. Prof. Dr. Lai Chin Wei for the opportunity given to me to embark on this eye-opening research career. Thank you for the continuous support, patience, advice (on research and personal), knowledge, and guidance throughout the last 4 years. I am contented and proud of the achievements that we have accomplished together despite the hardships.

My sincere thanks also go to Prof. Thomas Yang Chung Kuang and Dr. Pan Guan Ting for the invaluable research experience at the National Taipei University of Technology. The experience equipped me with important hands-on skills in handling various research instruments. Besides that, I also want to thank Dr. Lee Kian Mun for the advice and input that improved my research and thesis.

I would also like to thank the staffs, officers, and professors in the Institute for Advanced Studies (IAS) and Nanotechnology and Catalysis Research Centre (NANOCAT) for the assistance in streamlining my PhD study. My sincere thanks go to my fellow laboratory colleagues for the discussions, supports, and kindness that we had together.

Thank you to the research grants from the Ministry of Education (FRGS/1/2021/STG05/UM/02/3) and Universiti Malaya (PPSI-2020-CLUSTER-IDIG03 and ST080-2021) for the financial support of this research.

Last but not least, thank you to Ms. Valerie Siong for the companion throughout this difficult journey.

TABLE OF CONTENTS

LIST OF FIGURES

LIST OF TABLES

LIST OF SYMBOLS AND ABBREVIATIONS

$\bullet O_2^-$	:	Superoxide radicals
•OH	:	Hydroxyl radicals
2D	:	Two-dimensional
AC	:	Alternating current
AFM	:	Atomic force microscopy
Ag	:	Silver
Ag_2NO_3	:	Silver nitrate
AgCl	:	Silver chloride
Al	:	Aluminium
AO	:	Acridine Orange
Ar	:	Argon
at%	:	Atomic%
B	:	Boron
B_2O_3	:	Boron oxide
Be	:	Beryllium
BE	:	Binding energy
BGNR	:	Boron-doped graphene nanoribbon
BGO	:	Boron-doped graphene oxide
Bi_2O_3	:	Bismuth oxide
Bi_2WO_6	:	Bismuth tungstate
BP	:	Black phosphorus
BPRGO	:	Boron-doped photoreduced graphene oxide
BQ	:	1,4-benzoquinone
Br	:	Bromine
BrGO	:	Boron-doped reduced graphene oxide
BTEX	:	benzene, toluene, ethylbenzene and xylene
BVO	:	Bismuth vanadate
C	:	Carbon
CB	:	Conduction band
CBM	:	Minimum of conduction band
Cl	:	Chlorine
CO	:	Carbon monoxide
CO_2	:	Carbon dioxide
CoO	:	Cobalt oxide
Cu	:	Copper
Cu_2O	:	Copper oxide
CVD	:	Chemical vapour deposition
DI	:	Deionised
DMPO	:	dimethyl-1-pyrroline
e^-	:	Electron
EA	:	Electron affinity
E_a	:	Acceptor level
E_d	:	Donor level
EDTA-2Na	:	edentate disodium
EDX	:	Energy-dispersive X-ray spectroscopy

E_F	:	Fermi level
E_G	:	Bandgap
EI	:	Ionisation energy
EIS	:	Electrochemical impedance spectroscopy
EPD	:	Electrophoretic deposition
E_{photon}	:	Photon energy
ESR	:	Electron spin resonance
E_{vac}	:	Vacuum energy
F	:	Fluorine
F_2	:	Fluorine gas
Fe	:	Iron
Fe_2O_3	:	Iron oxide
FGO	:	Fluorine-doped graphene oxide
FID	:	Flamed-ionization detector
FPRGO	:	Fluorine-doped photoreduced graphene oxide
FrGO	:	Fluorine-doped reduced graphene oxide
FTIR	:	Fourier-transform infrared
FTO	:	Fluorine-doped tin oxide
Ga	:	Gallium
GaN	:	Galium nitride
GC	:	Gas chromatography
gCN	:	Graphitic carbon nitride
GO	:	Graphene oxide
H^+	:	Hydrogen ion
H_2	:	Hydrogen gas
H_2O	:	Water
H_2O_2	:	Hydrogen peroxide
H_2SO_4	:	Sulphuric acid
H_3BO_3	:	Boric acid
H_3PO_4	:	Phosphoric acid
HCl	:	Hydrochloric acid
HF	:	Hydrofluoric acid
Hg	:	Mercury
HOMO	:	Highest occupied molecular orbital
h_{VB}^+	:	Photogenerated hole carrier at the valence band
I	:	Iodine
IAQ	:	Indoor air quality
In	:	Indium
In_2O_3	:	Indium oxide
IPA	:	Isopropanol
IR	:	Infrared
K	:	Potassium
KBr	:	Potassium bromide
KE	:	Kinetic energy
$KMnO_4$	:	Potassium permanganate
Li	:	Lithium
LUMO	:	Lowest unoccupied molecular orbital
MB	:	Methylene blue

MEK	:	Methyl ethyl ketone
$Mg(NO_3)_2$	:	Magnesium nitrate
Mo	:	Molybdenum
MO	:	Methyl orange
M-S	:	Mott-Schottky
MW	:	Molecular weight
N	:	Nitrogen
N_2	:	Nitrogen gas
N_A	:	Number of ionized acceptor atoms
Na	:	Sodium
Na_2SO_4	:	Sodium sulphate
Nb	:	Niobium
N_D	:	Number of ionized donor atoms
NGO	:	Nitrogen-doped graphene oxide
NGQD	:	Nitrogen-doped graphene quantum dot
NH_3	:	Ammonia
NHE	:	Normal hydrogen electrode
NO_2	:	Nitrogen dioxide
NPRGO	:	Nitrogen-doped photoreduced graphene oxide
NrGO	:	Nitrogen-doped reduced graphene oxide
O	:	Oxygen
O_2	:	Oxygen gas
O_3	:	Ozone
OBGs	:	Oxygenated boron groups
OCGs	:	Oxygenated carbon groups
PAH	:	Polycyclic aromatic hydrocarbons
PCO	:	Photocatalytic oxidation
PEC	:	photoelectrochemical
PID	:	Photo-ionization detector
PL	:	Photoluminescence
PM	:	Particulate matter
ppb	:	Part per billion
ppm	:	Part per million
PRGO	:	Photoreduced graphene oxide
Pt	:	Platinum
rGO	:	Reduced-graphene oxide
RH%	:	Relative humidity%
RhB	:	Rhodamine B
ROS	:	Reactive oxygen species
SBS	:	Sick building syndrome
SEM	:	Scanning electron microscopy
Si	:	Silicon
SiC	:	Silicon carbide
Sn	:	Tin
SnO_2	:	Tin oxide
SnS_2	:	Tin sulphide
Ta	:	Tantalum
t-BuOH	:	tert-butanol

TCE	:	Trichloroethylene
TEOA	:	triethanolamine
TFA	:	Trifluoroacetic acid
TiO_2	:	Titanium dioxide
TVOC	:	Total volatile organic compounds
USD	:	United States Dollar
UV	:	Ultraviolet
VB	:	Valence band
VBM	:	Maximum of valence band
Vis	:	Visible
VOC	:	Volatile organic compound
VOCs	:	Volatile organic compounds
WF	:	Work function
WHO	:	World Health Organization
WO_3	:	Tungsten trioxide
wt%	:	Weight%
Xe	:	Xenon
XPS	:	X-ray photoelectron spectroscopy
XRD	:	X-ray diffraction
Y	:	Yttrium
Zn	:	Zinc
ZnO	:	Zinc oxide
$ZnSnN_2$	:	Zinc tin nitride

LIST OF APPENDICES

CHAPTER 1: INTRODUCTION

1.1 Research Background

1.1.1 Indoor Air Quality (IAQ)

Nowadays, people are spending an average of 80 – 90% of their lives indoors (Jantunen et al., 1997). Since the outbreak of the COVID-19 pandemic in December 2019, the lockdown policies enforced by governments around the world meant that people recently spend almost all their time in indoor environments (Adam et al., 2021; Nicola et al., 2020). As a result, emission of particulate matter (PM), carbon monoxide (CO), nitrogen dioxide (NO_2), ozone (O_3), and volatile organic compounds (VOCs) from daily household activities such as cleaning, socialising, cooking, etc. can potentially expose indoor occupants to hazardous levels of air pollutants (Nadzir et al., 2020; Saha & Chouhan, 2020). Figure 1.1 simulates the sources and health risks of air pollutants in a typical household (Withgott et al., 2007). Shockingly, each year between 1 to 4 million people die from illnesses related to indoor air pollution (Ritchie & Roser, 2013; World Health Organization, 2021). Therefore, indoor air quality (IAQ) is one of the most essential determinants of human health and quality of life (Wolkoff, 2018).

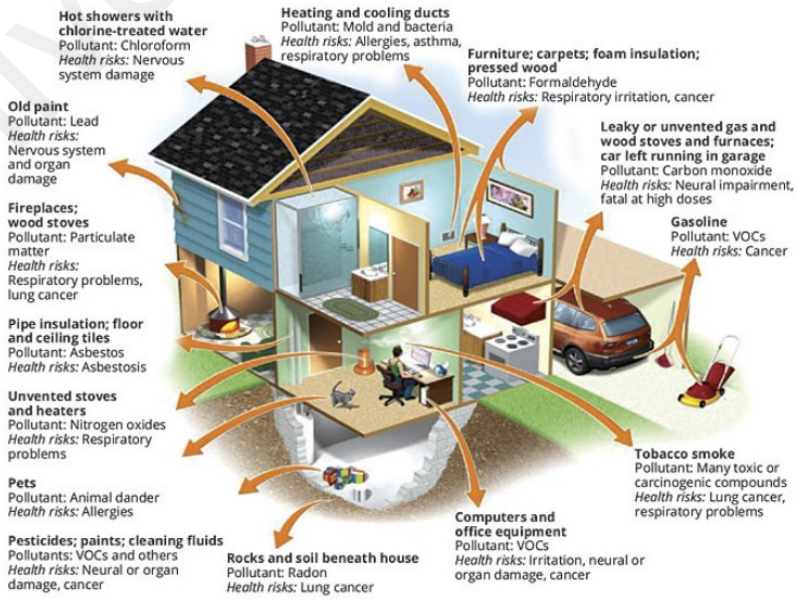

Figure 1.1: Sources of air pollutant emissions in a typical household. (Withgott et al., 2007)

1.1.2 Indoor volatile organic compounds (VOCs)

In modern residences, many organic chemicals are used as ingredients in household items. The organic chemicals that vaporize into gas under room conditions are collectively known as the VOCs (Control & Prevention; Salthammer, 2016). The Environmental Protection Agency (EPA) of USA further categorized VOCs by their volatility, which are very VOCs (VVOCs), VOCs, and semi-VOCs (SVOCs) (United States Environmental Protection Agency, 2022). VVOCs such as alkanes have a low boiling point between <0 to 100 °C. VOCs have a boiling point between 50 to 260 °C, such as alcohol, aldehyde, ketone, aromatic compound. SVOCs are less volatile and have a boiling point between 240 to 400 °C, such as pesticides and fire retardants. These VOCs are released from many indoor products or activities, such as cosmetic products, cleaning products, human breath, wood products, paint, medicine cooking, etc. (Kamal et al., 2016; Salthammer, 2016). Most indoor environments typically contain up to 50 types of VOCs ranging from 1 to 100 mg/m^3 (Jantunen et al., 1997). Since the composition of VOCs differs from one environment to another, the concentration of total VOCs (TVOC) is often used as an indicator for indoor VOCs contamination. According to the Department of Occupational Safety and Health (DOSH) of Malaysia, the acceptable limit of indoor TVOC is regulated at 3 ppm based on an 8 h time-weighted average (TWA) (Department of Occupational Safety and Health, 2022).

Concerns have been raised over the sick-building syndrome (SBS) of indoor occupants from exposure to VOCs (Jaakkola et al., 1994; Yu & Crump, 1998). The SBS caused by VOCs (Figure 1.2) is a combination of several symptoms such as eye, nose, throat, and skin irritation, dry mucous, headache, nausea, fatigue, and shortness of breath (Sanalife, 2021; World Health Organization, 1990). Notably, one of the most common indoor VOCs is methanol (boiling point 64.7 °C), in which the exposure to methanol could induce severe SBS and even death (Md Noor et al., 2020; Medina et al., 2017). It was reported

by the Occupational Safety and Health Administration (OSHA) of USA that the 8 h TWA exposure limit to methanol is at a higher concentration of 200 ppm (The National Institute for Occupational Safety and Health (NIOSH), 2011).

Figure 1.2: Symptoms of Sick Building Syndrome (SBS).
(Sanalife, 2021).

1.1.3 Removal of indoor VOCs with photocatalytic oxidation (PCO)

Generally, there are two ways to remove VOCs, namely the non-destructive and destructive methods. Non-destructive methods are preferred in some industries, where VOCs can be captured and reused to save costs (Z. Zhang et al., 2016). Meanwhile, the destructive method is suitable for the indoor environment to limit the exposure of occupants to toxic VOCs. Some of the methods for removing VOCs are adsorption, UV-ozone, ionisation, plasma degradation, thermal catalytic degradation, and photocatalytic oxidation (PCO) (He, Jeon, et al., 2021; Zhang et al., 2017). The adsorption method by

using porous absorbent is currently the most common non-destructive strategy. However, the adsorbent needs to be replaced periodically and the adsorption efficacy is heavily depressed under high humidity (Zhang et al., 2017). Other VOCs removal methods such as UV-ozone, ionisation, and plasma degradation may produce ozone as a hazardous by-product, while thermal catalytic degradation is very energy-intensive (He, Jeon, et al., 2021). Given the limitations of the aforementioned methods, PCO has emerged as an ideal destructive method for indoor air purification because it can operate under ambient conditions to degrade and mineralise VOCs by using photocatalysts. Besides that, the PCO method does not require chemicals or external energy input except light (He, Weon, et al., 2021).

Based on Figure 1.3a, the global photocatalyst market has been gradually expanding and reaching a market size of 1.6 billion USD in the year 2016 (Grand View Research, 2017). In the future, the market size of photocatalyst is expected to reach 4.58 billion USD by the year 2025. This is attributed to the increasing demand of photocatalysts for environmental remediation. Some of the developed countries like Germany, Japan, China, and the USA are investing heavily to commercialize more photocatalyst products. Among the applications of photocatalyst, air purification consisted about 23% of the photocatalyst market revenue in the year 2016 (Grand View Research, 2017). Figure 1.3 (b, c, and d) display the utilisation of PCO technology in commercial scales to purify air pollutants, such as in the air filter of Samsung AX7000 air cleaner (Weon et al., 2018), in the bathroom of Noi Bai International Airport, Hanoi, Vietnam (Miyauchi et al., 2016), and as an air-purifying curtain (IKEA, 2019).

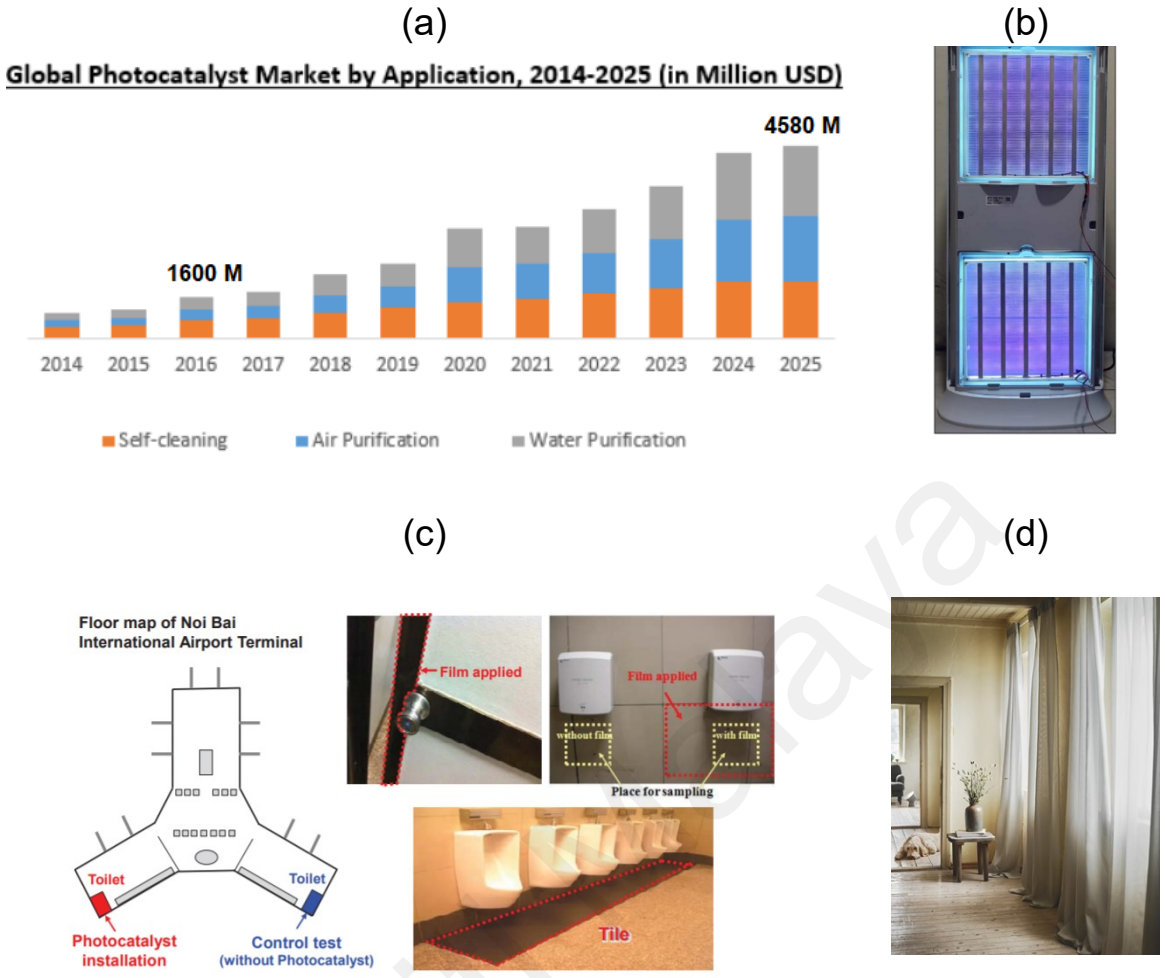

Figure 1.3: (a) Photocatalyst market revenue by application for the year 2016-2025, (b) Inside view of a Samsung AX7000 air cleaner with photocatalyst and UV-LEDs, (c) Photocatalyst coating in washrooms at Noi Bai International Airport, Vietnam, and (d) IKEA air-purifying curtain.
(Grand View Research, 2017; IKEA, 2019; Miyauchi et al., 2016; Weon et al., 2018).

1.1.4 Graphene oxide as metal-free photocatalyst

Up to date, titanium dioxide (TiO_2)-based materials is the most frequently studied photocatalysts for VOCs removal (Weon et al., 2019). In recent years, metal-free photocatalysts have emerged as a new class of photocatalyst, including carbon- (Hsu et al., 2013), silicon- (Gao et al., 2007), boron- (G. Liu et al., 2013), sulphur- (Liu et al., 2012), and phosphorus- (Wang et al., 2012) based photocatalysts. Metal-free photocatalysts are attractive because of their low cost and sustainability as compared to that of metal-based photocatalysts (Rosso et al., 2021). Among the carbon-based

photocatalysts, graphene oxide (GO) has attracted a lot of attention. GO is a 2D nanosheet with a high density of active sites for catalysis and a short distance for charge carrier diffusion (Yao et al., 2019). Additionally, GO as a metal-free photocatalyst is earth-abundant, lightweight, stable, and highly tuneable (C. Li et al., 2017; Rahman et al., 2020). In recent years, various GO-based photocatalysts have shown promising results in many photocatalytic applications. For instance, GO in the photoreduction of CO_2 into methanol (Hsu et al., 2013), reduced graphene oxide (rGO) in the photodegradation of aqueous dye (Wong et al., 2015), nitrogen (N)-/boron (B)- doped rGO in photocatalytic water splitting (Putri et al., 2017), and photoreduced graphene oxide (PRGO) in the photoreduction of heavy-metal ions (Yu et al., 2021).

1.2 Problem statement

The demand for photocatalysts is currently dominated by TiO_2 owing to the presence of few alternatives (Grand View Research, 2017). Considering the high demand of photocatalysts for air purification, the development of alternatives to TiO_2 is vital, such as by using GO as a metal-free photocatalyst. Nevertheless, despite the potential of GO-based photocatalyst, it has not been tested to degrade VOCs yet.

The photocatalytic activity of pristine GO is limited due to its wide bandgap and poor separation of photogenerated charge carriers (Albero et al., 2019; Pedrosa et al., 2020). As a result, many strategies were carried out to enhance the photocatalytic performance of GO. One of the strategies is to reduce and tune the oxygenated level of GO, which can narrow the bandgap and partially restore the sp^2 domains for better charge carrier transportation (Wang et al., 2018; Yu et al., 2021). However, the traditional methods to reduce GO are often harmful to the environment. For example, thermal, electrochemical, and microwave reduction methods are energy-extensive, while chemical reduction

methods require toxic chemicals (Gengler et al., 2013). Therefore, it is important to develop a green and environmentally friendly method to reduce GO for photocatalytic application.

Another effective method to improve the photoactivity of GO is via heteroatom-doping. For example, doping of GO with B, N, and S atoms improved the photocatalytic activity for dye degradation and water splitting (Huang et al., 2018; Singh et al., 2018; Yeh et al., 2013). Heteroatom-doping can increase the charge carrier density of the host semiconductor (Chen, 2004; Lin et al., 2011), therefore retarding the recombination of photogenerated charge carriers (Huang et al., 2020). Many techniques have been developed to fabricate heteroatom-doped GO photocatalysts, such as calcination (Putri et al., 2017), hydrothermal (Yang et al., 2017), and pyrolysis (Das et al., 2019). However, these techniques are often tedious, costly, and non-scalable. Therefore, a facile, scalable, and inexpensive method to mass-produce heteroatom-doped GO photocatalysts with high photocatalytic activity is needed. Moreover, there is a lack of study on the effects of heteroatom-doping configuration on the photocatalytic activity of heteroatom-doped GO photocatalysts.

1.3 Research Objectives

The main aim of this work is to develop efficient PRGO-based photocatalysts for the photodegradation of VOCs. The objectives are as follows:

1. To synthesize PRGO and heteroatom-doped PRGO (i.e., boron (B), nitrogen (N), and fluorine (F) dopants) from GO via a novel and green photoirradiation method.
2. To characterize the physicochemical and electrochemical properties of the PRGO and heteroatom-doped PRGO photocatalysts for the degradation of VOCs.

3. To study the photodegradation activity and mechanism of the PRGO and heteroatom-doped PRGO photocatalysts.

1.4 Scope of work

In this work, GO is synthesized with a modified Hummers' method. Then, the ability of GO to photodegrade VOCs is evaluated. To enhance the properties and photocatalytic activity of GO, a green photoirradiation technique was used to synthesize PRGO from GO. Next, to further enhance the efficiency of VOCs removal, GO was doped with heteroatoms (i.e., boron (B), fluorine (F), and nitrogen (N)) by photoirradiation methods. The properties and performances of the GO, PRGO, B-doped PRGO (BPRGO), F-doped PRGO (FPRGO), and N-doped PRGO (NPRGO) photocatalysts were compared. For example, the physicochemical properties of the photocatalysts were characterized by X-ray diffraction (XRD), Raman, X-ray Photoelectron Spectroscopy (XPS), Fourier-transform infrared (FTIR), Scanning Electron Microscope (SEM), Energy-dispersive X-ray Spectroscopy (EDX), and UV-Vis techniques. Meanwhile, the electrochemical properties of the photocatalysts were characterized by photoluminescence (PL), transient photocurrent, Mott-Schottky (M-S), and Electrochemical Impedance Spectroscopy (EIS). To evaluate the PCO performances, the photocatalysts were tested to photodegrade a model VOC, namely methanol under UV-A irradiation. Subsequently, the rate of mineralisation of methanol into CO_2 was studied. The best performing photocatalyst was further tested to degrade other VOCs, such as acetone and formaldehyde. Lastly, the band structures and PCO mechanism of the photocatalysts were discussed.

1.5 Thesis outline

This thesis is organized into five chapters. Chapter 1 (Introduction) introduces the background, problem statements, objectives, and outline of this work. Chapter 2 (Literature review) summarizes the types of indoor VOCs, factors affecting the PCO process, previous studies on GO-based photocatalyst, and previous applications of PRGO. Besides that, Chapter 2 also identifies research gaps from the past works. Chapter 3 (Methodology) describes the research methodology and material characterization techniques used. Chapter 4 - 7 present the results and discussions of the properties and photocatalytic performances of the photocatalysts. In Chapter 4, the effects of photoreduction duration on the PCO performance of PRGO was investigated. Chapter 5 shows the effects of photoinduced-doping duration on the PCO performance of BPRGO. Chapter 6 demonstrates the effects of photoinduced-doping duration on the PCO performance of FPRGO. Chapter 7 displays the effects of photoinduced-doping duration on the PCO efficiency of NPRGO. Besides that, Chapter 7 also compares the photocatalytic performances between the PRGO, BPRGO, FPRGO, and NPRGO photocatalysts. Lastly, Chapter 8 (Conclusion) concludes the findings of this work and provides suggestions for future work.

CHAPTER 2: LITERATURE REVIEW

In this chapter, the overview of volatile organic compounds (VOCs) as air pollutants is described in Section 2.1. Then the working principle of the photocatalyst is discussed (Section 2.2). Next, Section 2.3 reviews the mechanism, process parameters, experimental designs, and past studies on the removal of VOCs by PCO. Section 2.4 summarizes the past reports of graphene oxide-based and heteroatom-doped graphene oxide-based photocatalysts. Lastly, Section 2.5 discusses the past studies of PRGO and heteroatom-doped PRGO.

2.1 Volatile organic compounds (VOCs)

2.1.1 Introduction to volatile organic compounds (VOCs)

According to the World Health Organization (WHO), air pollution is one of the world's largest single environmental health risks (World Health Organization, 2010). Air pollution is defined as the contamination of indoor/outdoor air by several substances, which includes organic chemical contaminants, inorganic contaminants, pathogens, and particulate matters (Ott, 1982). A summary of the types of air pollutants is shown in Figure 2.1.

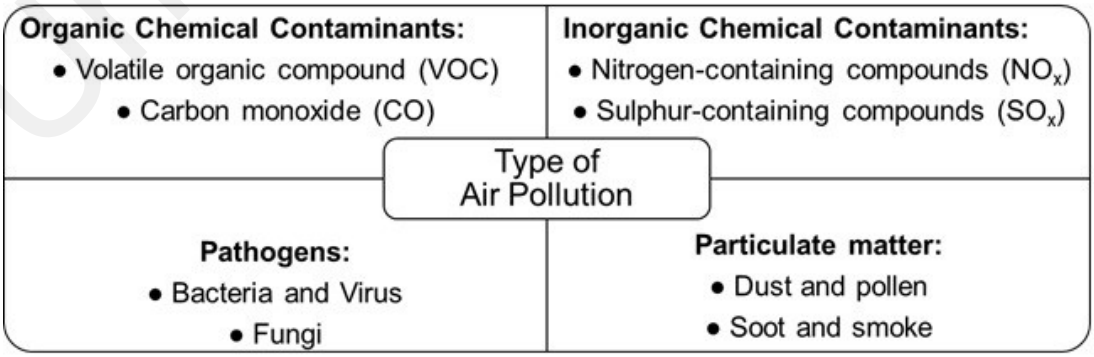

Figure 2.1: Summary of air pollutants.

Among the air pollutants, VOCs are commonly found in our daily lives. The WHO defines VOCs as any organic compounds with a boiling point between 50 to 260 °C (Wang et al., 2007). In a report by the Committee on the Effect of Climate Change (USA), VOCs are defined as any organic compounds with a vapour pressure >10 Pa (United States Environmental Protection Agency, 2017). In other words, VOCs are organic chemicals that can evaporate under normal indoor conditions. Most VOCs are toxic, carcinogenic, and mutagenic at higher concentrations (Zhang et al., 2017). Alarmingly, VOCs can be found in almost all indoor compounds such as industrial areas, offices, and homes (Khan & Ghoshal, 2000; Zou et al., 2019). Based on WHO, indoor air typically contains up to 50 types of VOCs each in concentration of 1 to 100 mg/m^3 (Jantunen et al., 1997). In some countries (i.e., United Kingdom), the concentration of indoor TVOC is 84 - 100% higher than that of outdoor environment. This is mainly due to the usage of VOCs-containing domestic products such as aerosol, cosmetics, and toiletries (Heeley-Hill et al., 2021). One of the major problems of indoor VOCs exposure is the "sick-building syndrome (SBS)" (Jaakkola et al., 1994; Mølhave, 1991; Yu & Crump, 1998). The SBS is a situation in which the occupants experience adverse health effects that appear to be related to the time spent in a particular indoor environment, but no specific illness can be identified. Generally, the SBS is a combination of several symptoms, such as eye, nose, and throat irritation, dry mucous, headache, nausea, difficulty in respiration, etc. (World Health Organization, 1990)

Some common types of VOCs are alcohols, aldehydes, aromatic compounds, halogenated VOCs, ketones, and polycyclic aromatic hydrocarbons (PAH). Exposure to alcohols (primarily methanol, ethanol, and isopropyl alcohol) causes serious central nervous system depression (Zhu & Wu, 2015). Exposure to aldehydes causes severe toxicity effects (Main & Hogan, 1983). Moreover, exposure to ketones induces ear, nose, and throat irritation (Kamal et al., 2016). Exposure to aromatic compound and PAH cause

confusion, dizziness, and even death (Kim, 2002; Kim et al., 2007). Furthermore, exposure to halogenated VOCs causes long term toxicity (Aranzabal et al., 2014). Table 2.1 summarizes some examples of the aforementioned VOCs.

Table 2.1: Sources and health impacts of major VOCs

Type of VOCs and examples	Indoor emission sources	Health impact	References
Alcohol Example: methanol, ethanol, propanol	Cosmetic product, cleaning product, wood and paper product, human breath, medicine	Central nervous system depression	(Ashurst & Nappe, 2018; Mirzaei et al., 2016; Salthammer, 2016)
Aldehyde Example: Formaldehyde, acetaldehyde	Wood and paper product, decorative materials, human breath	Throat and eye irritation, shortness of breath	(Malaka & Kodama, 1990; Salthammer, 2016)
Ketone Example: acetone, ethyl butyl ketone	Aerosol, paint, adhesive, cosmetic product	Irritation of ear, nose, and throat	(Kamal et al., 2016)
Aromatic compounds Example: benzene, toluene	Incomplete combustion of fuels, cooking	Toxic and carcinogenic	(Kamal et al., 2016; Kim, 2002)
Polycyclic aromatic hydrocarbons (PAH) Example: naphthalene, phenanthrene	Combustion of organic matters	Carcinogenic	(Kim, 2002; Kim et al., 2007)
Halogenated VOCs Example: Chloroform, Chlorobenzene	Wastewater	Bioaccumulation and toxicity in organism.	(Aranzabal et al., 2014)

2.1.2 Standards for Indoor Air Quality (IAQ)

2.1.2.1 Standards for TVOC

The measurement of TVOC is often used as an indication for indoor VOCs contamination. This is because the VOCs composition varies significantly from one environment to another. Most people would start to feel discomfort after being exposed to TVOC as low as 3 mg/m^3 (Mølhave, 1991). Hence, it is useful to use the TVOC concentration as a statistical reference to determine the IAQ. Several IAQ standards for TVOC were defined by various international agencies and bodies. These IAQ standards were implemented to limit the exposure of humans to VOCs and thus reducing the probability of SBS. Some countries set the IAQ standards as regulations (e.g., Malaysia), while some countries suggested the standards as guidelines (e.g., Hong Kong and Australia). Table 2.2 shows some of the IAQ standards around the world for TVOC

exposure. These standards reflect the upper limit of TVOC exposure before irritation or discomfort can occur to the occupants (Ayoko & Wang, 2014). Moreover, these IAQ standards often have some discrepancy between them. This is because some standards were based on the results of statistical studies whereas some were derived from practical experience (Abdul-Wahab et al., 2015). Nonetheless, there is a general consensus to keep the TVOC concentration at minimum.

Table 2.2: IAQ standards and guidelines for upper limit exposure to TVOC

Country	Organization	IAQ standard for TVOC	Ref.
Malaysia	Department of Occupational Safety and Health (DOSH)	3 ppm (8 h TWA)	(Department of Occupational Safety and Health, 2022)
Singapore	Institute of Environmental Epidemiology	3 ppm	(Institute of Environmental Epidemiology, 1996)
China	General Administration of Quality Supervision, Inspection, and Quarantine	0.6 mg/m^3 (8 h TWA)	(GB/T 18883-, 2002)
Hong Kong, China	Environmental Protection Department	Excellent: 0.2 mg/m^3 (8 h TWA) Good: 0.6 mg/m^3 (8 h TWA)	(MG HKIAQ, 2003)
Taiwan	Environmental Protection Administration	0.56 ppm	(Tsai, 2017)
Japan	Ministry of Health, Labour, and Welfare	0.4 mg/m^3	(Labour & Welfare, 2001)
Australia	National Health and Medical Research Council	0.5 mg/m^3 (1 h TWA)	(Brown, 1997)
Belgium	Federal Public Service Health, Food Chain Safety and Environment	0.2 mg/m^3	(Superior Health Council, 2017)

Besides the upper limit exposure to TVOC, there are some internationally accepted IAQ rating systems that classified the concentration of TVOC into several hazard levels. For example, the German Federal Environment Agency categorises TVOC concentration into 5 IAQ ratings (Umweltbundesamt, 2007). Level 1 (<0.3 mg/m^3) is the healthy level, Level 2 (0.3 – 1.0 mg/m^3) requires minimum ventilation, Level 3 (1.0 – 3.0 mg/m^3) needs intensified ventilation, Level 4 (3.0 – 10.0 mg/m^3) could affect well-being, and Level 5 (10 – 25 mg/m^3) is unhealthy.

Meanwhile, the WHO classified TVOC concentrations into 4 IAQ levels for the European countries (World Health Organization, 2010). TVOC concentration <0.2 mg/m^3 is a healthy target, 0.2 – 3.0 mg/m^3 is a multifactorial exposure range, 3.0 – 25 mg/m^3 is a discomfort range, while >25 mg/m^3 is a toxic range. Table 2.3 summarizes the IAQ classifications for TVOC by the concentrations.

Table 2.3: IAQ classification levels of TVOC concentrations

IAQ Level	German Federal Environment Agency		World Health Organisation	
	TVOC (mg/m^3)	Descriptions	TVOC (mg/m^3)	Descriptions
1	< 0.3	No hygienic consequences.	< 0.2	Comfortable and no effect
2	0.3 – 1.0	No relevant consequences, increased ventilation is recommended.	0.2- 3.0	Irritation and discomfort possible
3	1.0 – 3.0	Concerning hygienic aspects. Search for contamination sources and increase ventilation.	3.0 – 25.0	Irritation, discomfort, and headache
4	3.0 – 10.0	Major health consequences. Such rooms should not be used. Intensified ventilation and toxicological risk assessment are needed	> 25.0	Neurotoxic effects
5	10.0 – 25.0	Unacceptable concentration and required intensified ventilation. Rooms with TVOC> 25 mg/m³ should never be used.	-	-

2.1.2.2 Standards for methanol

Indoor occupants are constantly exposed to methanol through air, water, and food. For example, methanol is commonly found in fresh fruits, vegetables, fruit juices, alcoholic beverages, and food additives (Boobis et al., 2010). Besides food, the source of methanol vapour could be emitted from domestic products such as paints, washer fluids, antifreeze, adhesive, electronic equipment fuel cells, etc (World Health Organization, 1997). Recently, methanol has emerged as an alternative fuel for vehicles (Tian et al., 2018). The substitution of methanol for petroleum fuels might result in a greater release of methanol vapour into the environment. Meanwhile, occupational exposure to methanol vapour typically happens through inhalation during production or processing. This is because methanol is often used as a raw material/solvent for the production of many organic

chemicals and products. Additionally, methanol is also commonly found in refrigeration systems and wastewater treatment (Medina et al., 2017). All things considered, the use of methanol in households and workplaces are expected to become more common in the future. Based on the Occupational Safety and Health Administration (OHSA) of the USA, the permissible exposure limit to methanol is 200 ppm (or 260 mg/m^3) for an 8 h TWA (The National Institute for Occupational Safety and Health (NIOSH), 2011). Table 2.3 summarizes some of the regulations and guidelines for methanol vapour exposure limit in several countries (World Health Organization, 1997).

Methanol can enter a body by various means, which include inhalation, absorption through skin, eye contact, and ingestion. Alarmingly, humans rapidly absorb 60 – 85% of the inhaled methanol (Medina et al., 2017). The absorbed methanol is metabolised by the liver into formaldehyde, then into formate/formic acid, and finally into CO_2 (Boobis et al., 2010). The rate of methanol metabolism by the human body is approximately 25 mg/kg.h, which is seven times slower than the metabolism of ethanol (Medina et al., 2017). Due to the slow metabolism process of methanol, the human body could accumulate the toxic by-product formate, which causes methanol toxicity (Boobis et al., 2010).

Methanol has a faint alcohol odour that is only detectable to humans at a concentration above 2000 ppm (Sittig, 1981), which is ten times higher than its permissible exposure limit at 200 ppm. It is important to note that exposure to methanol can cause severe and fatal effects. In addition, the symptoms of methanol exposure do not happen immediately and thus can cause misdiagnosis, particularly to occupants who are unaware of the exposure. The adverse effects of methanol exposure may have a delay between 12 to 24 h (Purssell, 2018; World Health Organization, 1997). Methanol exposure is irritating to the eyes, skin, and respiratory tract. Besides that, methanol exposure can also cause headache, dizziness, nausea, and muscle pain. At prolonged exposure, it can even cause permanent damage to the optic nerve, reproductive system, and central nervous system,

which could result in blindness and organ failures (Boobis et al., 2010). Since the odour of toxic methanol vapour is such a poor indicator of its presence, it is vital to monitor and control the concentration of indoor methanol. This is to ensure compliance with the IAQ standards and prevent adverse health effects to the occupants.

Table 2.4: Regulations, guidelines, and standards for methanol exposure limit (World Health Organization, 1997)

Country	TWA Exposure limit Value (mg/m^3)
Australia, Denmark, Finland, France, Germany, Japan, Netherlands, Switzerland, United Kingdom, USA (OSHA)	260
Belgium, Ireland, Italy, Luxembourg, Portugal, Spain	262
Sweden	250
Czech Republic, Poland	100
Hungary	50
Former USSR	5

2.1.3 Indoor VOCs removal techniques

There are many strategies to remove VOC such as ventilation, adsorption, thermal incineration, thermal catalytic oxidation, biofiltration, and photocatalytic oxidation (PCO) (He, Jeon, et al., 2021; Zhang et al., 2017; Z. Zhang et al., 2016). Among these techniques, thermal incineration and catalytic oxidation are not suitable for indoor usage because they are costly, energy-intensive, and may produce dangerous by-products. Consequently, there are only a handful of techniques suitable to remove indoor VOCs, which are ventilation, adsorption, biofiltration, and PCO (Kabir & Kim, 2012).

2.1.3.1 Ventilation

Ventilation by introducing outdoor air into an indoor environment is an easy method to reduce the concentration of VOCs (Hernandez et al., 2020). However, there are a few drawbacks of using ventilation to remove indoor VOCs. For instance, the efficiency of ventilation is drastically affected by the surrounding air flowrate, air direction, temperature, and outdoor air quality, which are all uncontrollable natural factors (Chen,

2009). Moreover, ventilation might worsen the IAQ by allowing external air pollutants such as burning fuel, car exhaust, and dust particles to enter the indoor compound (Taylor et al., 2015). In addition, ventilation would increase the energy cost to maintain the indoor temperature due to heat loss from convection, particularly in countries with colder climates (Suszanowicz, 2018). Figure 2.2 illustrates a process of a room ventilation.

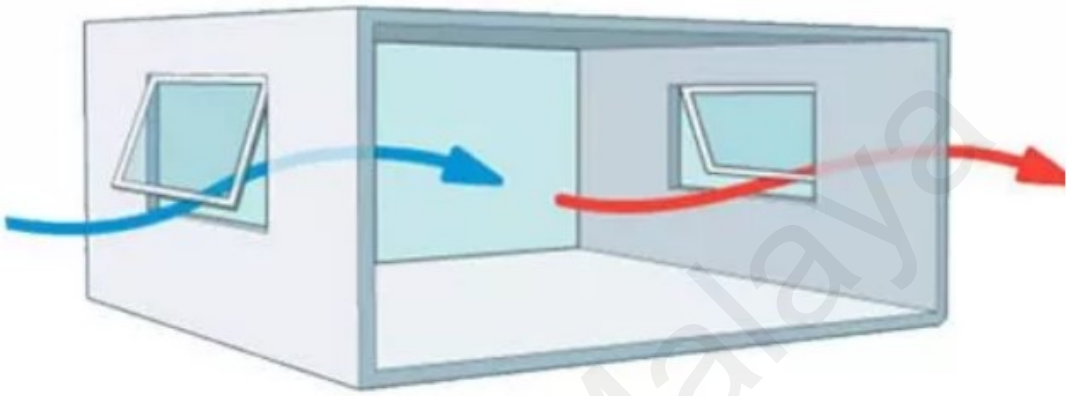

Figure 2.2: Ventilation for removal of indoor VOCs.
(Linquip Team, 2020)

2.1.3.2 Adsorption

Adsorption is a commonly used technique that adsorbs indoor VOCs by using an adsorbent (Zhang et al., 2017). Finding a suitable adsorbent is vital for the application of this technique. Carbon-based adsorbents such as activated carbon, biochar, carbon nanotube, graphene-based material, and mesoporous carbon are widely studied for VOCs adsorption (Zhang et al., 2017). This is due to the favourable properties of the carbon-based adsorbents, which include large specific surface area, high porous structure, good stability, and tuneable surface functional groups (X. Li et al., 2020). Nevertheless, the adsorption technology has a few drawbacks for practical usage. For instance, the adsorbents are required to be replaced frequently to maintain the adsorption efficiency (He, Jeon, et al., 2021). In addition, extra cost is needed to either desorb or dispose the used adsorbent (X. Li et al., 2020). Moreover, the rate of adsorption is heavily affected

by the surrounding humidity, in which most adsorbents perform poorly at higher indoor humidity (X. Li et al., 2020). Furthermore, most carbon-based adsorbent has an intrinsically nonpolar surface that limits the adsorption of polar indoor VOCs (Zhang et al., 2017). For example, it was reported that the adsorption capacity of activated carbon adsorbent for nonpolar toluene was 59.2 mg/g, but the adsorption capacity for polar methanol was only 10.6 mg/g (Oh et al., 2010). Figure 2.3 demonstrates a process of VOCs adsorption.

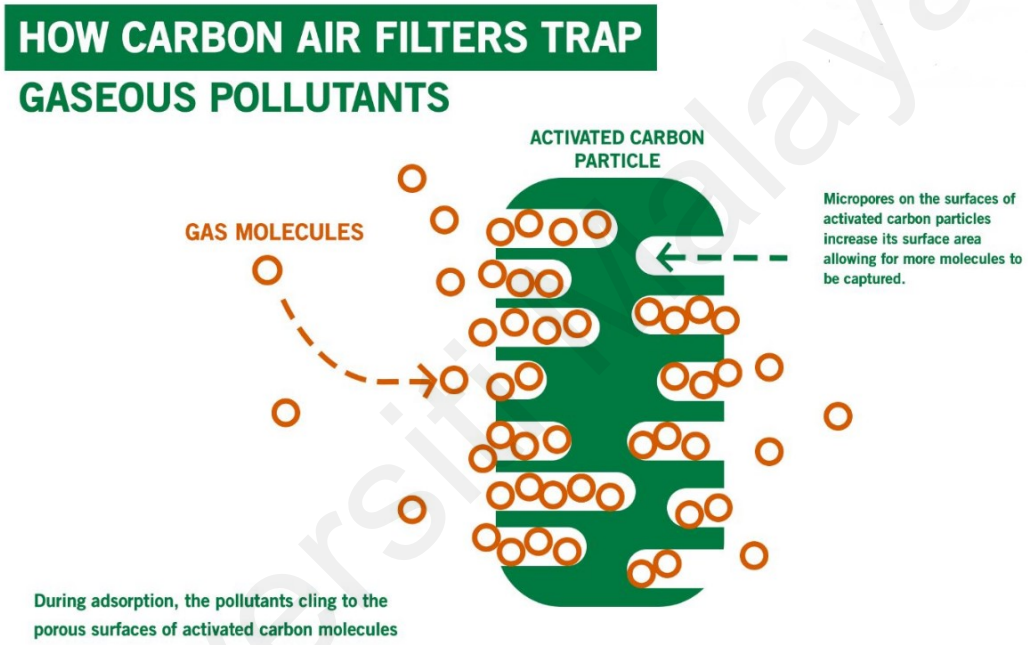

Figure 2.3: Adsorption with adsorbent for removal of VOCs.
(AO Smith, 2020)

2.1.3.3 Biofiltration

Biofiltration is an emerging method of utilizing microbes at plant roots to remove VOCs from indoor air. The VOCs are consumed by the root microbes to synthesise biomass, energy, and carbon dioxide (Russell et al., 2014). Several laboratory-scale studies have found that biofiltration can remove VOCs (e.g. formaldehyde, toluene, ethylbenzene, xylene) present at indoor concentrations, albeit with fluctuating efficiencies (Darlington et al., 2000; Darlington et al., 2001). Notably, plants grown in

hydroculture are more effective in removing VOCs than soil-grown plants because of the increased air flow to the root microbes (Kabir & Kim, 2012). Nevertheless, the information to date on the efficiency and mechanism of biofiltration in realistic indoor environments is still limited (Mannan & Al-Ghamdi, 2021). Moreover, biofiltration might increase the risk of fungal growth and spread in indoor spaces (Fleck et al., 2020; Irga et al., 2017). Besides that, it is difficult to estimate the sustainability and economic viability of a biofiltration system. This is due to the unforeseeable cost of construction, operation, maintenance, and disposal of the biofiltration system (Mannan & Al-Ghamdi, 2021). Figure 2.4 shows a setup of indoor biofiltration for VOCs.

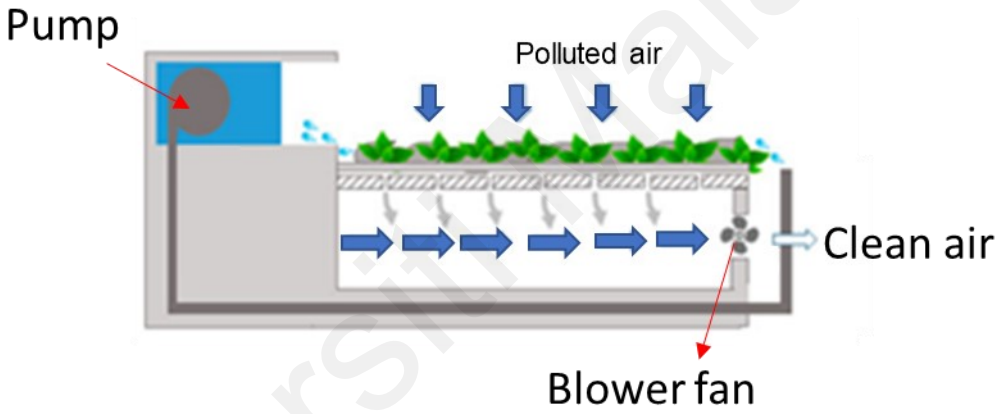

Figure 2.4: Green wall system as biofilter for indoor VOCs.
Adapted from (Mannan & Al-Ghamdi, 2021).

2.1.3.4 Photocatalytic oxidation (PCO)

Considering the limitations of the aforementioned VOCs removal strategies, PCO is a suitable technique for indoor air purification. The PCO process does not require any chemicals or energy input except light. Light energy is low in cost because it can be obtained from sunlight or ambient indoor lightning (Huang et al., 2016; Pichat, 2019). In addition, PCO can fully mineralise VOCs into harmless compounds such as water and CO_2, which is vital for treating indoor VOCs with high toxicity (H. Huang et al., 2015). Nevertheless, the PCO process still suffers from a few drawbacks, such as poor light

utilization of photocatalyst, slow photodegradation rate, difficulty to scale up, and deactivation of the photocatalyst. Therefore, more studies on the types of photocatalyst and PCO parameters are needed to improve the efficiency of removing indoor VOCs. The characteristics of photocatalyst and PCO process are further discussed in the following Section 2.2 and 2.3.

2.2 Photocatalyst

2.2.1 Introduction to the photocatalyst

In 1972, Honda and Fujishima pioneered the work of photocatalysis (Fujishima & Honda, 1972), since then many semiconductors have been invented for various photocatalytic applications (Hoffmann et al., 1995). Unfortunately, the practical application of photocatalysis at a commercial scale is still limited due to low photoactivity and poor efficiency (Djurišić et al., 2020).

The energy levels of a semiconductor/photocatalyst can be explained by the band theory. In the band structure of a photocatalyst, the maximum of the valence band (VBM) is equivalent to the highest occupied molecular orbitals (HOMO), which is the outermost electron orbital of the atom of the photocatalyst. Meanwhile, the minimum of the conduction band (CBM) is equivalent to the lowest unoccupied molecular orbitals (LUMO), which is the band of electron orbital that can be filled by photoexcited electrons. The distance between the VBM and CBM is known as the bandgap, which is also the minimum energy required to excite an electron from the energy level of the VBM to that of CBM (Kahn, 2016). A photocatalyst can absorb light energy exceeding its bandgap to form a pair of photoexcited electron and hole charge carriers at the conduction bands and valence bands, respectively. The charge carriers then either migrate to the surface of the photocatalyst to carry out chemical reactions or recombine with each other. This recombination phenomenon plays a negative role in the photocatalytic process. Hence for

the past decades, many strategies have been employed to reduce the recombination rate to improve the photocatalytic activity (Hoffmann et al., 1995). Some of the common strategies to reduce charge carrier recombination are doping with foreign atoms, surface modification, and formation of heterojunctions (Afroz et al., 2018).

A photocatalyst made of a single type of semiconductor can be known as a single photocatalyst or a sole photocatalyst. Typically, a single photocatalyst has a bandgap between 1.0 to 5.0 eV. Most photocatalysts are metal-based such as TiO_2, iron oxide (Fe_2O_3), copper oxide (Cu_2O), bismuth tungstate (Bi_2WO_6), etc. Besides that, there are also metal-free photocatalysts, such as silicon (Si), silicon carbide (SiC), graphitic carbon nitride (gCN), GO, rGO, PRGO, black phosphorus (BP), etc. From the band theory, the conduction band, valence band, and bandgap are the main factors governing the photoactivity of the photocatalyst. To photodegrade VOCs, ideally, the conduction band of the photocatalyst should be more negative than the potential of oxygen (O_2)/superoxide ($\bullet O_2^-$) radicals at -0.33V (vs. Normal hydrogen electrode (NHE) pH 7) to donate an electron and reduce O_2 to $\bullet O_2^-$ radicals. Meanwhile, the valence band should be more positive than the potential of H_2O/H^+ + hydroxyl (•OH) radicals (+2.38V vs. NHE pH 7) to accept an electron and oxidise water to •OH radicals (Saison et al., 2013). Hence, for an effective PCO process, a minimum bandgap of 2.71 eV is usually required as determined by the redox potential difference between $O_2/\bullet O_2^-$ and H_2O/•OH. Some photocatalysts like TiO_2 can be used as a single photocatalyst to produce both $\bullet O_2^-$ and •OH radicals. Conversely, some photocatalysts like tin oxide (SnO_2) and Bi_2WO_6 can only produce either one of the radicals due to the positions of their band edges. The bandgap and band structures of some common photocatalysts are summarized in Figure 2.5 (Hsu et al., 2013; Lee et al., 2016; C. Li et al., 2017; Reddy et al., 2015; Saison et al., 2013; Schreck & Niederberger, 2019).

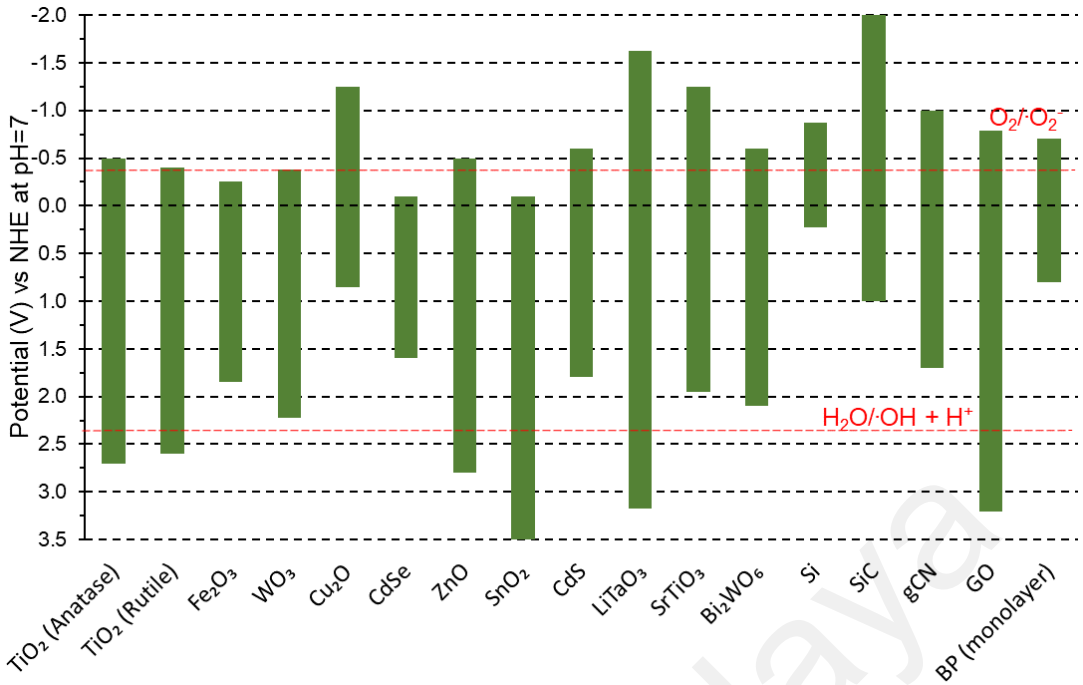

Figure 2.5: The conduction band, valence band, and bandgap of some common photocatalysts.

2.2.2 Direct and indirect bandgap of the photocatalyst

Intrinsically, a photocatalyst can have a direct bandgap, an indirect bandgap, or both. The difference between the direct and indirect bandgap is the crystal momentums (k-vector) between their VBM and CBM. If the momentum from the VBM to CBM is the same, the electrons at the valence bands need an increase of potential energy only to be photoexcited to the conduction band, and this is called a direct bandgap. Conversely, if the momentum from the VBM to CBM is different, the electrons at the valence band need the increase of potential energy and a change of momentum (through photon interaction with phonon; the phonon can be originated from atomic lattice vibration, thermal, or sound) to be photoexcited to the conduction band, this is known as an indirect bandgap. Therefore, upon photoexcitation, photocatalyst with a direct bandgap can produce the free-electron-hole pairs easier than photocatalyst with an indirect bandgap. However, photocatalyst with an indirect bandgap often has a slower charge carrier recombination rate than photocatalyst with a direct bandgap (University of Cambridge, 2020). The

concept of direct and indirect bandgaps is schematically shown in Figure 2.6. An example of a photocatalyst with an indirect bandgap is TiO_2, which has a bandgap between 3.25 to 3.36 eV (Tan et al., 2014; Zhang et al., 2010). Besides that, zinc oxide (ZnO) has a direct bandgap around 3.2 to 3.37 eV (Hoffmann et al., 1995; Kamarulzaman et al., 2015).

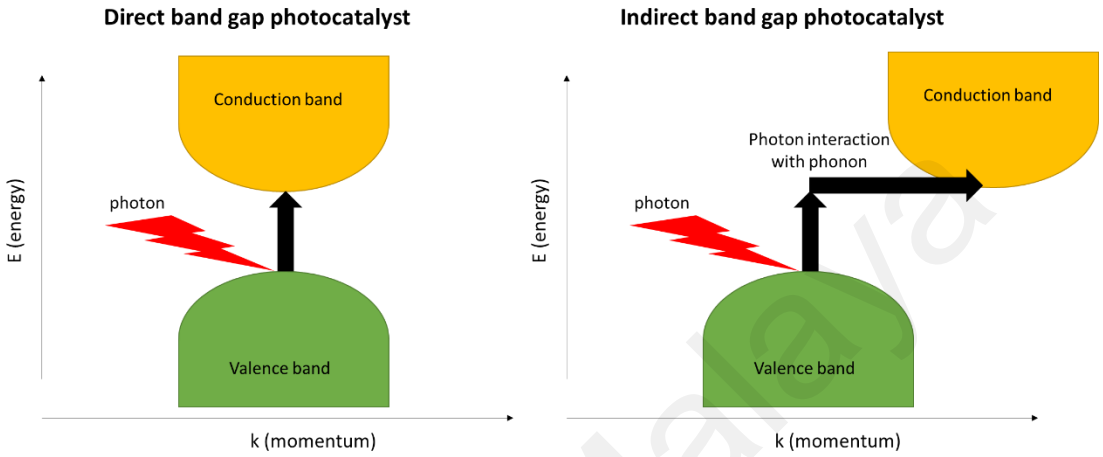

Figure 2.6: Direct bandgap and indirect bandgap photocatalyst.

2.2.3 p-type and n-type photocatalyst

Besides the valence band, conduction band, and bandgap, the other important energy levels in a semiconductor/photocatalyst are the vacuum energy (E_{vac}), fermi level (E_F), ionization energy (EI), work function (WF), and electron affinity (EA). The E_{vac} is the energy barrier that prevents the electron from escaping from the surface of the semiconductor to vacuum. In another word, E_{vac} is the energy level of an electron within a "few nm" outside of the semiconductor. The E_F is a hypothetical energy level that lies between the valence band and conduction band, which determines the probability of electron occupancy in the semiconductor. At thermodynamic equilibrium, the E_F has a 50% probability of being occupied with electrons at any given time. Besides that, E_F is also the highest energy level that an electron can occupy at absolute zero temperature in a semiconductor. The energy difference between the E_{VAC} and VBM is defined as the ionization energy (EI), which is the minimum energy required to ionize or remove an

electron from the semiconductor. WF is the energy difference between the E_F and E_{vac}, which represents the energy barrier that prevents an electron at the E_F to escape from the semiconductor. Lastly. EA is the energy required to add an electron from the E_{vac} to the CBM (Kahn, 2016).

A single photocatalyst usually has either a p-type or n-type conductivity. In a p-type photocatalyst, there are acceptor atoms that form acceptor levels near the valence band. These acceptor atoms can accept electrons from the valence band, which then create additional hole carriers in the valence band. Therefore, the majority charge carrier species of a p-type photocatalyst is the hole carrier, in which the hole carrier density is much greater than the free-electron carrier density. In another word, in a p-type photocatalyst, the probability of finding an electron at the conduction band is smaller than the probability of finding a hole at the valence band. Therefore, the E_F of a p-type photocatalyst is near to its valence band. The number of acceptor atoms ionized in the bulk of a p-type photocatalyst is called the acceptor density, N_A (cm^{-3}), where N_A is approximately equal to the hole carrier density (Bobrow, 1996). A higher N_A is beneficial for photoactivity, this is because a higher number of hole carriers can boost the oxidation reactions at the valence band (Luo et al., 2017).

In an n-type photocatalyst, there are donor atoms that form donor levels near the conduction band. The donor levels can donate electrons to the conduction band. Thus, the majority charge carrier of an n-type photocatalyst is the free-electron, in which the free-electron carrier density is much greater than the hole carrier density. For an n-type photocatalyst, the probability of finding an electron in the conduction band is bigger than the probability of finding a hole at the valence band. Therefore, the E_F of an n-type photocatalyst is near to its conduction band. The number of donor atoms ionized in the bulk of an n-type photocatalyst is called the donor density, N_D (cm^{-3}) (Aroutiounian et al., 2007), where N_D is roughly equal to the free-electron density (Bobrow, 1996). A higher

N_D is beneficial for photoactivity, this is because a higher number of free-electron can boost the reduction reactions at the conduction band (She et al., 2017). The band structures of a p-type and an n-type single photocatalyst are shown in Figure 2.7.

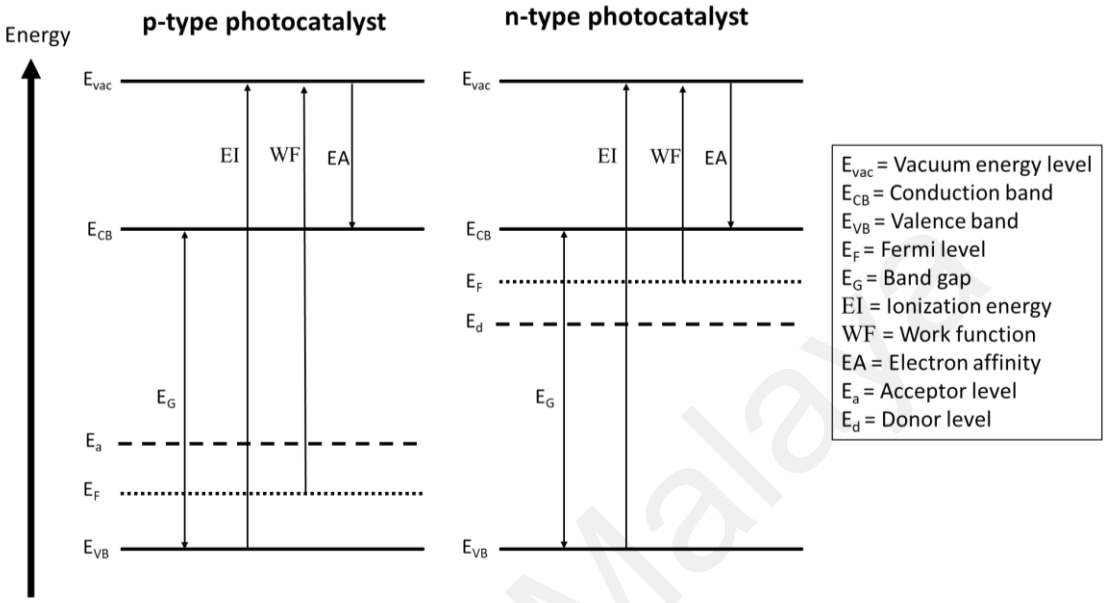

Figure 2.7: Electronic band structure of p-type and n-type single photocatalyst.

2.2.4 Doping of photocatalyst

The photoactivity of a single photocatalyst is usually hampered by limited light absorption range, fast recombination, or inadequate band edges. One of the techniques to improve the photocatalytic activity of a single photocatalyst is via doping. For example, there has been increasing interest to improve the electrical, optical, and structural properties of TiO_2 photocatalyst via doping (Khlyustova et al., 2020). Doping of TiO_2 often results in the formation of new energy levels between the conduction and valence bands, which can effectively narrow the bandgap, improve light absorption, and prevent fast charge carrier recombination (Nah et al., 2010; Nishikawa et al., 2017). Furthermore, doping of TiO_2 might lead to the appearance of oxygen vacancies and active sites, which can potentially boost photocatalytic activity (Nah et al., 2010).

There are two main types of dopant atoms, which are the acceptor (p-type) and the donor (n-type) dopant atoms. Generally, an acceptor dopant atom has lesser valence electrons than the host atoms of the pristine photocatalyst, while a donor dopant atom has more valence electrons than the host atoms of the pristine photocatalyst. For example, indium (In) and gallium (Ga) (valence electron = $3e^-$) are acceptor dopant atoms to TiO_2 (valence electron of Ti^{4+} = $4e^-$), while tantalum (Ta) and niobium (Nb) (valence electron = $5e^-$) are donor dopant atoms to TiO_2 (Amano et al., 2018).

In addition, it is possible to change the magnitude and type of conductivity of a photocatalyst via doping. For instance, Ghahramanifard et al. found that doping ZnO with copper (Cu) atoms changed the conductivity of ZnO from n-type to p-type. This is because the Cu atoms introduced an acceptor level within the bandgap of ZnO (Ghahramanifard et al., 2018). Besides that, Luo et al. also found that doping gCN with chlorine (Cl) acceptor atoms changed the conductivity of gCN from n-type to p-type (Luo et al., 2017). Since doping would change the concentration of acceptor atom density (N_A) and donor atom density (N_D), therefore the hole carrier and free-electron densities of the photocatalysts are also changed after doping.

2.2.4.1 Shallow and deep dopants

Acceptor/donor doping levels formed between the CBM and VBM of a semiconductor can be either shallow or deep. A shallow acceptor level is an acceptor level close to the valence band, while a shallow donor level is a donor level close to the conduction band. A shallow acceptor dopant can accept electrons from the valence band at room temperature without any external energy input because its ionization energy is smaller than kT, where k is the Boltzmann constant (8.62×10^{-5}), and T is the temperature (K). Likewise, a shallow donor dopant can donate electrons to the conduction band at room

temperature because of its small ionization energy (Brochen et al., 2012). Therefore, doping a photocatalyst with a shallow acceptor or donor dopant will increase the respective hole carrier or free-electron carrier density at room conditions. Conversely, a deep acceptor or donor dopant lay deep in the bandgap, therefore the deep levels cannot be ionized at room temperature. Moreover, deep dopant levels often act as traps/recombination sites during photocatalysis, which trap and recombine charge carriers. For example, an electron that falls from a conduction band to a shallow donor level can be easily reemitted back to the conduction band by the ambient temperature or light energy. However, an electron that falls from a conduction band to a deep donor level is more likely to recombine with a hole in the valence band. In another word, a shallow dopant level reduces charge carrier recombination, while a deep dopant level enhances charge carrier recombination (Murzin et al., 2020; Wang et al., 2020). For instance, Commandeur et al. found that yttrium (Y) as a donor dopant on ZnO nanorod, improved the photocatalytic water splitting process. This is because the Y atoms acted as shallow donors that increased the N_D and n-type conductivity, which resulted in lower charge carrier transport resistance and slower charge carrier recombination. The authors confirmed that Y was a shallow donor because (i) Y doping increased the N_D and (ii) there was no new distinct photoluminescence (PL) peak observed after Y doping (Commandeur et al., 2019). The increment of N_D meant a higher free-electron carrier density, a better n-type conductivity, and a longer charge carrier lifetime (Ma et al., 2020). Figure 2.8 illustrates the differences between an undoped pristine p-type photocatalyst, a shallow acceptor-doped p-type photocatalyst, and a deep acceptor-doped p-type photocatalyst.

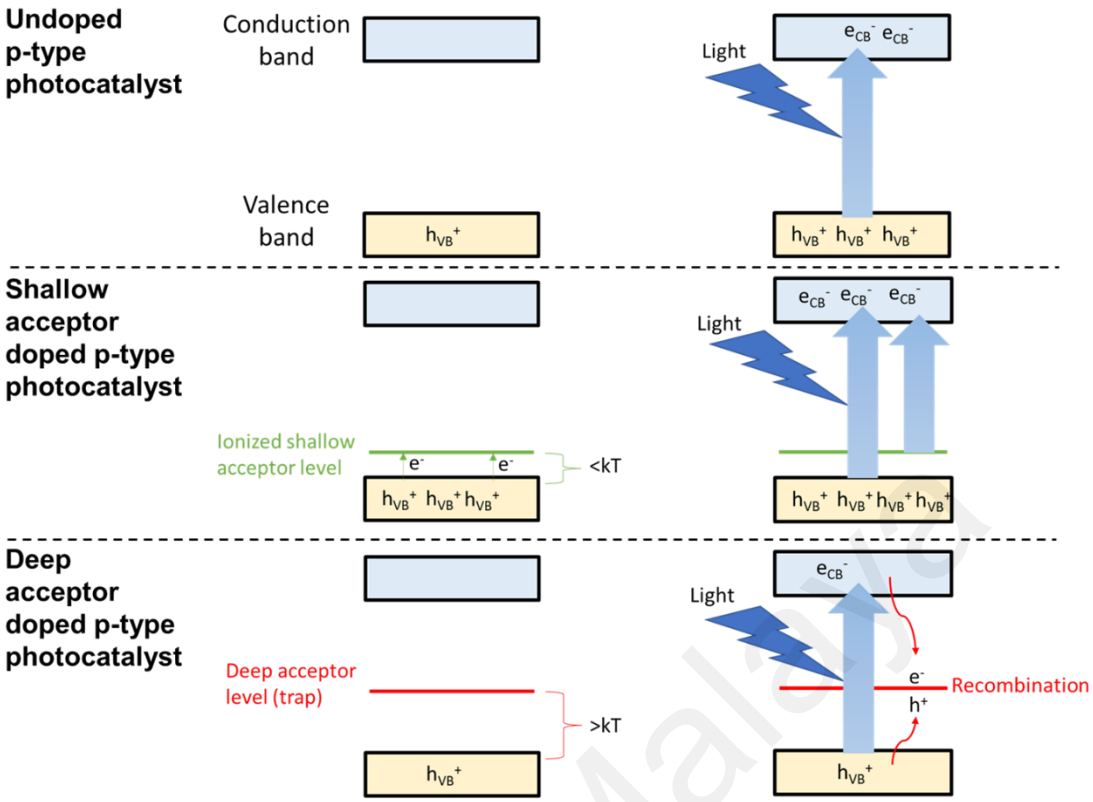

Figure 2.8: Example of shallow and deep acceptor dopants in p-type photocatalyst.

2.2.4.2 Dopant and bond type

It is possible for a dopant atom to form more than one type of bonding with the host atom. For instance, nitrogen (N) dopant can predominantly form three types of N-C bonds on graphene, which are the graphitic, pyrrolic, and pyridinic N-C bonds (Schiros et al., 2012). Although they are all N-C bonds, they induce different properties and doping effects. The graphitic-N dopant is connected to three sp^2 hybridized C neighbours and induces n-type doping. Meanwhile, the pyridinic (five-membered ring configuration) and pyrrolic (six-membered ring configuration) N-C bonds can be either p-type doping (if the N dopant has an electron lone pair) or n-type doping (if the N dopant is hydrogenated) (Lu et al., 2013). Besides that, different type of bonding can induce different effects on the fermi level and charge carrier density of the semiconductor. For example, in comparison to the pyridinic-N and pyrrolic-N dopants, the graphitic-N dopant can donate more electron to the CB and also shifts the fermi level closer to the CB (J. Zhang et al.,

2016). This indicates that the graphitic N-C bond can induce a stronger n-type doping effect than its counterparts. Therefore, it is important to control the type of bonding of a dopant on a semiconductor to achieve the desired properties.

2.2.4.3 Relative atomic size of dopant and host of a semiconductor

To select a suitable dopant for a semiconductor/photocatalyst, the relative size of the host atom and the dopant atom is vital. For instance, Zhang et al. discovered that an acceptor dopant with a similar atomic size to the host atoms in the semiconductor can be easily doped in high concentration (Zhang et al., 2008). Conversely, an acceptor dopant with a much smaller atomic size than the host atoms would result in a deep acceptor level. Besides that, it was found that beryllium (Be) dopant is a deep acceptor for gallium nitride (GaN) because of the atomic size mismatch between Be (112 pm) and Ga (187 pm) atoms, which resulted in local lattice distortion and hole localization (S. Jin et al., 2020; Lyons et al., 2013).

Wang et al. computed the usage of lithium (Li), sodium (Na), and potassium (K) as acceptor dopants in an n-type semiconductor zinc tin nitride ($ZnSnN_2$). Among the potential dopants, Li displayed a shallow acceptor behaviour. This was because Li and zinc (Zn) atoms have similar sizes, hence Li dopant could be doped into the lattice of $ZnSnN_2$ without causing significant lattice changes. Conversely, Na and K were deep acceptor dopants to $ZnSnN_2$ due to the atomic size mismatch between Na and K with the host Zn atoms. The Na and K dopants also disrupted the lattice of $ZnSnN_2$ and caused large displacement to the nearby N atoms (T. Wang et al., 2017).

Xie et al. computed the doping of halogen atoms, such as fluorine (F), chlorine (Cl), bromine (Br), and iodine (I) as acceptor dopants on the 2D nanosheet tin sulphide (SnS_2). It was found that there was an increasing trend of formation energy with the increasing

atomic size of the acceptor dopant. Among the halogen dopants, F acceptor dopant had the lowest formation energy, and thus F was the shallowest acceptor dopant. This was because F has the closest atomic size to tin (Sn), as compared to the other halogen dopants (Xia et al., 2014). In short, the greater the atomic size mismatch of dopant and host atoms, the deeper the doping level, which can lead to the formation of more compensating defects. The compensation defects would act as recombination centres/traps of charge carriers during photocatalysis (Jiao et al., 2018).

2.2.4.4 Doping concentration

Shallow doping is often done in low concentration, this is because excessive doping of a shallow dopant can turn it into a deep dopant. For example, Murashkina et al. found that aluminium (Al) dopant formed a shallow level in TiO_2 when the Al doping concentration was low (0 to 0.5 wt%). The shallow doping of Al effectively improved the photoelectrochemical (PEC) performance. However, when the Al doping concentration was further increased (0.5 to 1.1 wt%), a deep level was formed. The deep level acted as a recombination centre, hence reducing the PEC activity (Murashkina et al., 2018). Likewise, Singh et al. found that doping TiO_2 with a low concentration of iron (Fe) dopant (0.1 – 0.2 wt%) increased the N_D and improved the PEC performance. Further excessive doping of Fe dopant (0.5 wt%) then created recombination centres, therefore enhancing the charge carrier recombination and reducing the PEC activity (Singh et al., 2008).

Choudhury et al. reported a study of doping TiO_2 with Cu donor dopant. It was found that doping of Cu introduced both a shallow non-radiative level and a deep radiative level in TiO_2. Increasing the doping concentration of Cu would increase the relative amount of deep radiative level. The shallow non-radiative level may trap electrons from the conduction band, and then migrate the trapped electrons to the photocatalyst's surface to participate in photocatalytic activity. In another word, the shallow non-radiative level

prevented charge carrier recombination. Meanwhile, the deep radiative level is an effective recombination centre that recombines charge carriers during photocatalysis. Therefore, to improve photocatalytic activity, the doping concentration of a photocatalyst should be optimized to maximize the shallow non-radiative level and minimize the deep radiative level (Choudhury et al., 2014).

Bloh et al. developed a model that predicted the optimal doping concentration of a photocatalyst by the particle size of the photocatalyst. The optimal doping is when there is at least one but not too many dopants per photocatalyst particle. This is because too many dopant atoms per particle of photocatalyst would result in recombination centres and diminish the photocatalytic activity (Bloh et al., 2012).

Tayebi et al. reported the doping of molybdenum (Mo) donor atoms on n-type bismuth vanadate (BVO). Mo-doping at 1 - 2 at% increased the N_D and PEC activity considerably. However, the further addition of Mo dopants up to 3 - 5 at% gradually reduced the N_D and PEC performance. The authors stated that at the higher doping concentration of Mo, some electrons at the donor level were used up to form unnecessary chemical bonds (i.e. Mo-O-Mo), hence decreasing the N_D and PEC activity (Tayebi et al., 2019).

Goel et al. found that a low doping concentration increases the N_D. However, after exceeding 5 mol% of doping, the N_D decreased. The authors deduced that the higher doping concentration had led to more static disorder and dopant precipitation, hence a lower N_D (Goel et al., 2020). Furthermore, the allowable doping concentration of a dopant into a semiconductor is also limited by the dopant solubility. A dopant would have precipitated on the surface of the host if the dopant solubility is exceeded. The formation of dopant precipitation is often unwanted, as the precipitation might reduce the performance and stability of the semiconductor (Bajaj et al., 2016).

In summary, the doping concentration on a semiconductor/photocatalyst must be controlled carefully as excessive doping can cause negative consequences such as (i) formation of deep recombination centres, (ii) formation of unnecessary chemical bonds, (iii) static disorder, and (iv) precipitation of dopants.

2.3 Removal of volatile organic compound via photocatalytic oxidation

2.3.1 The PCO process of VOCs removal

In 1971, Teichner et al. firstly reported the PCO of paraffin in gas-phase reaction (Formenti et al., 1971). Since then, the growing health concern from indoor air pollution has attracted a lot of attention to use the PCO technique to remove VOCs. The PCO process utilizes a photocatalyst to carry out the removal of VOCs. There are five major steps in a PCO process: (i) the adsorption of VOCs, oxygen, and water molecules on the photocatalyst's surface, (ii) light absorption and generation of photoinduced charge carriers in the photocatalyst, (iii) migration of charge carriers to the surface of the photocatalyst, (iv) generation of reactive oxygen species (ROS) at the photocatalyst's surface, and (v) oxidation of VOCs into CO_2 and H_2O.

During the adsorption step (i), the oxygen (O_2), water (H_2O), and VOC molecules from the ambient environment are adsorbed onto the surface of the photocatalyst. Next, steps (ii), (iii), and (iv) occur when a light source with an energy greater than the bandgap of the photocatalyst is irradiated onto the photocatalyst. By absorbing the light energy, an electron at the valence band is photoexcited, and its energy is elevated to the conduction band. This electron at the conduction band is now a free-electron and can participate in a reduction reaction. For instance, the free-electrons at the conduction band can be donated to an adsorbed O_2 to produce $\bullet O_2^-$ radicals. Meanwhile, a vacancy/void of an electron is left in the valence band after the photoexcited electron is elevated to the conduction band.

This void of the electron is the photoinduced hole. The photoinduced hole at the valence band can participate in an oxidation reaction. For example, hole carriers at the valence band can accept an electron from an adsorbed H_2O to oxidise the H_2O into H^+ and •OH radicals (Mamaghani et al., 2017; Zhao & Yang, 2003). The photogenerated electron and hole are also known as the photoinduced charge carriers, while the $\bullet O_2^-$ and •OH radicals are the reactive oxygen species (ROS). In step (v), the ROS and the hole carriers can break down harmful VOCs into simpler compounds. Hence, the ROS and the hole carriers are the common reactive species in a PCO process. The overall PCO process is summarized in Figure 2.9.

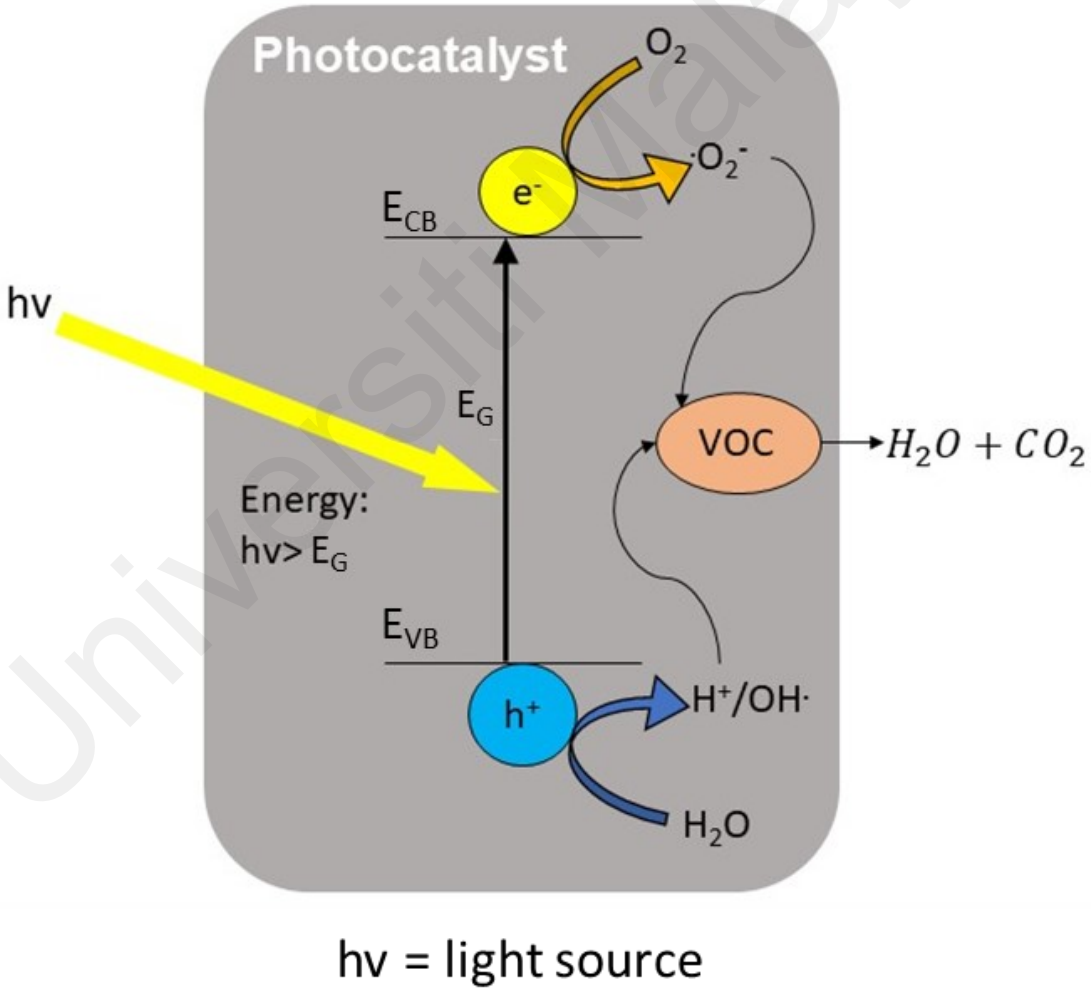

Figure 2.9: General pathway for PCO of VOCs.

The main limitation of a PCO process is the recombination of charge carriers. This unwanted recombination process would happen concurrently at step (iii), in which the photoexcited free-electron and hole carriers attract and recombine with each other instead of migrating to the surface of the photocatalyst. Since the charge carriers are recombined, the photocatalyst is unable to carry out the subsequent steps of PCO (Ni et al., 2007). The mechanism of recombination can be generally classified into two types, which are radiative and non-radiative recombination.

Radiative recombination is a recombination process that emits excess energy in the form of a photon. Meanwhile, non-radiative recombination occurs when the excess energy from recombination is not released as a photon, but instead is converted to vibrational energy (phonon) of the lattice atoms in the semiconductor. Therefore, the excess energy of non-radiative recombination is often released in the form of heat. One of the common causes of non-radiative recombination is the deep state/defect in the photocatalyst, such as native defects, foreign atoms, and dislocations. These deep defects act as recombination centres within the bandgap of the photocatalyst/semiconductor. In a non-radiative recombination process, the photogenerated electron is firstly trapped by the deep defect sites, then the electron falls into the valence band and recombines with a hole. A deep defect often has an energy level close to the middle of the bandgap (far from the conduction band). Conversely, if the photoexcited electron falls to a shallow defect level close to the conduction band, light energy can reemit the electron back to the conduction band and avoid recombination (Agrawal & Dutta, 1993).

The complete photodegradation (or mineralisation) of a VOC molecule into CO_2 and H_2O is usually through a chain of stepwise reactions. For example, Figure 2.10 shows a proposed mineralisation pathway of (a) methanol (Raillard et al., 2006) and (b) acetone (Bianchi et al., 2014).

(a)

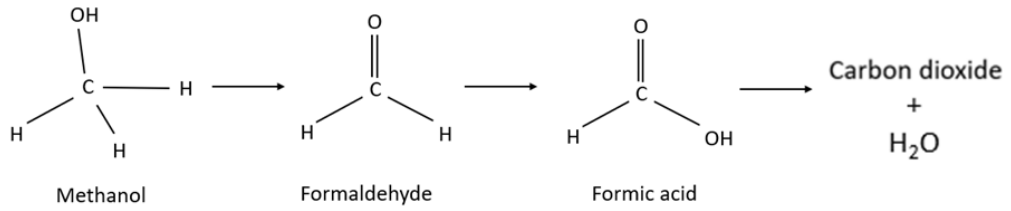

(b)

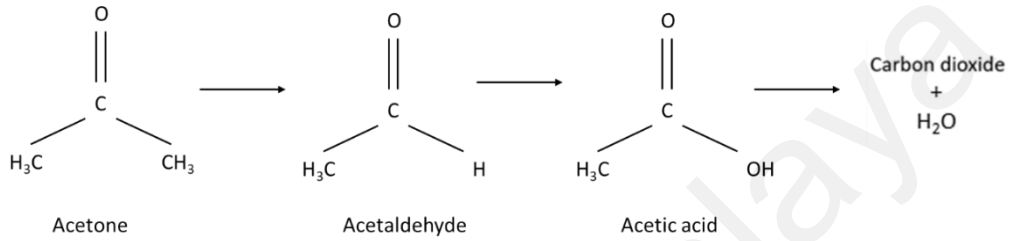

Figure 2.10: Mineralisation pathway of (a) methanol and (b) acetone.

2.3.2 Process parameters for PCO of VOCs

2.3.2.1 Light source

Light is the energy input for a PCO system, where the photon energy (E_{photon}) and light intensity can greatly affect the PCO performance. The E_{photon} of a light source needs to be greater than the bandgap of the photocatalyst to trigger the production of the photoinduced charge carriers. The E_{photon} is governed by the electromagnetic wavelength (λ) of the light source. Furthermore, the E_{photon} of a single wavelength can be calculated by Equation 2.1 (PVEducation, 2015):

$$E_{photon} = \frac{hc}{\lambda} \tag{2.1}$$

where h is the Planck's constant ($6.63 \times 10^{-34}\ m^2kg/s$) and c is the speed of light ($2.99 \times 10^{8}\ m/s$) in vacuum. From Equation 2.1, it is shown that the shorter the wavelength, the higher the energy of the light source.

As shown in Figure 2.11, the types of light used for PCO are categorized into infrared light (IR) (λ = 700 - 800 nm) (Kulathunga et al., 2016; Kulathunga et al., 2020), visible light (λ = 380 - 700 nm) (Inturi et al., 2014), UV-A (λ = 321 - 380 nm (Mull et al., 2017), UV-B (λ = 280 - 320 nm) (Malecha & Nizkorodov, 2016), and UV-C (λ = 200 - 280 nm) (Zhou et al., 2020). These light sources have different ranges of wavelength and energy. For a photocatalyst system designed to use sunlight or indoor light, the usage of a visible light active photocatalyst is more ideal. This is because sunlight and indoor light are mostly comprised of visible light (Newport, 2020). However, if the photocatalyst is designed to be used inside an enclosed UV photoreactor, using a UV active photocatalyst would be more effective. This is because UV carries higher energy and can potentially achieve a more effective PCO process. Among the UV lights, UV-A is more suitable to be used for indoor UV photoreactors. This is because accidental light exposure could happen, and UV-A is relatively harmless for short-term exposure, while exposures to UV-B and UV-C are immediately harmful to human skin and eyes (UVResources, 2020).

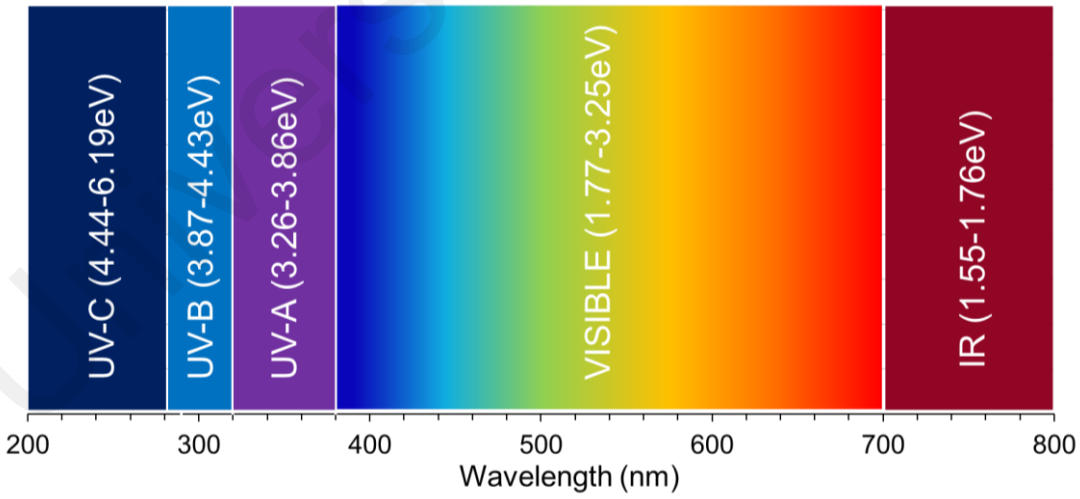

Figure 2.11: Light electromagnetic spectrum and the corresponding energy.

Several past studies about the effects of light sources on PCO efficiency are summarized in Table 2.5. Alberici et al. found that TiO_2 with an indirect bandgap of 3.2 eV, can be fully photoexcited under both UV-C (254 nm) and UV-A (365nm) lights.

Therefore, the PCO efficiency of VOCs under both UV-C and UV-A are similar (Alberici & Jardim, 1997). In contrast, another study found that an rGO-TiO_2 composite with a bandgap of 2.85 eV had a PCO efficiency of 100% under UV-A, but only 43% under visible light. This is because the lower photon energy of visible light could only partially photoexcite the photocatalyst (Ebrahimi & Fatemi, 2017). Similarly, other studies also found that the PCO performances of the photocatalysts were better under UV than visible light (Jo & Kang, 2013; Mull et al., 2017; Štengl et al., 2013). Therefore, it is important to choose a suitable light source according to the bandgap of the photocatalyst to achieve the best PCO performance.

The light intensity of a PCO system is usually measured in Lumens or mW/cm^2. Furthermore, to determine the utilization efficiency of photon energy, the quantum yield (Φ) of a PCO system can be calculated by Equation 2.2 (Serpone, 1997):

$$\Phi = \frac{N_{mol}}{N_{photon}} \tag{2.2}$$

Where, N_{mol} (mol s^{-1}) is the number of molecules of converted reactant/formation of product and N_{photon} (einstein s^{-1}) is the number of photons absorbed by the photocatalyst.

In Figure 2.12, Wang et al. found that the rate of photodegrading trichloroethylene (TCE) is enhanced with higher light intensity due to the generation of more photoinduced charge carriers. However, higher light intensity could also increase the probability of recombination of charge carriers, thus causing a decrease in the quantum yield (Wang et al., 1998). Likewise, Wang and co-workers found that higher light intensity led to a higher rate of PCO but with the cost of a lower quantum yield. The authors hypothesized that the surface area of the photocatalyst had limited the absorption of excessive photons, hence excess light intensity resulted in energy wastage and lower quantum yield (Wang & Ku, 2003).

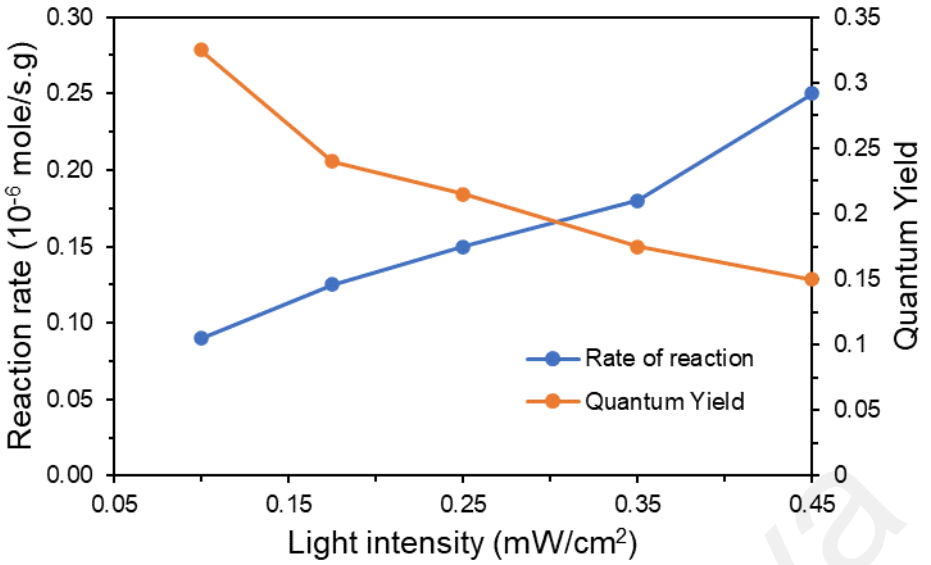

Figure 2.12: Reaction rate and quantum yield under different light intensity. Adapted from (Wang et al., 1998)

Besides quantum yield, the light intensity can also affect the rate of PCO. Qu et al. determined that higher light intensity could lead to a higher rate of PCO. However, the PCO rate became plateaued when the light intensity was >30,000 lux. This is because the amount of photoexcited charge carriers that can be produced had reached a maximum (Qu et al., 2009). Therefore, to avoid wastage of light energy, a photocatalytic system should be designed appropriately by maximizing quantum efficiency. As a rule of thumb, the greater the number of carbon and hydrogen atoms in a VOC, the higher the light intensity required to reach the maximum PCO rate (Tang & Yang, 2012).

Table 2.5: Effect of light source on efficiency of PCO of VOCs

Photocatalyst (bandgap)	**VOC and photoreactor**	**Light source**	**Efficiency**	**Reference**
TiO_2/0.5wt% rGO (2.85 eV)	500 ppm acetaldehyde in continuous flow reactor	15 W UV	100% > 90 min	(Ebrahimi & Fatemi, 2017)
		15 W daylight	43% > 90 min	
TiO_2/0.1wt% GO (~2.82 eV)	1 ppm BTEX in continuous flow reactor	8 W UV-A (352 nm)	65% > 1 h	(Jo & Kang, 2013)
		8 W daylight (> 400 nm)	41% in > 1 h	
TiO_2/GO (< 2.5 eV)	0.87 vol% butane in batch reactor	8 W UV-A (365 nm)	kinetic constant = 0.030 h^{-1}	(Štengl et al., 2013)
		8 Warm white (> 400 nm)	kinetic constant = 0.007 h^{-1}	

Table 2.5, continued

Photocatalyst (bandgap)	VOC and photoreactor	Light source	Efficiency	Reference
TiO_2/5wt% GO (N/A)	90 µg.m^{-3} toluene in batch reactor	UV-A LED (365 nm)	94% in 7 days	(Mull et al., 2017)
		Blue LED (455 nm)	0% in 7 days	
TiO_2 (3.2 eV)	572 ppm methanol in continuous reactor	30 W UV-C (254 nm) Light flux = 2.84 × 10^{-8} Einstein cm^{-2} s^{-1}	92.4% > 60 min	(Alberici & Jardim, 1997)
		30 W UV-A (365 nm) Light flux = 7.56 × 10^{-9} Einstein cm^{-2} s^{-1}	97.9% > 60 min	
	560 ppm isopropanol in continuous reactor	30 W UV-C (254 nm) Light flux = 2.84 × 10^{-8} Einstein cm^{-2} s^{-1}	83.5% > 60 min	
		30 W UV-A (365 nm) Light flux = 7.56 × 10^{-9} Einstein cm^{-2} s^{-1}	79.7% > 60 min	

2.3.2.2 Initial concentration of VOCs

The concentration of VOCs in the air can be expressed in metric units such as mg/m^3 or µg/m^3. Another way to express the concentration of VOCs is by using the unit of parts per million (ppm) or parts per billion (ppb) by volume or mole. 1 ppm is equivalent to 1 gas volume per 10^6 of gas volume, while 1 ppb is equivalent to 1 gas volume per 10^9 of gas volume. The conversion between mg/m^3 and ppm can be done by utilizing the ideal gas law (PV=nRT) as the Equation 2.3 (Boguski, 2006) below:

$$C[ppm] = \frac{RT(10^6)}{P\left(\frac{1000mg}{g}\right)} \times \frac{1}{MW} \times C\left[\frac{mg}{m^3}\right]$$
$$C\left[\frac{mg}{m^3}\right] = MW \times C[ppm] \times \frac{P\left(\frac{1000mg}{m^3}\right)}{RT(10^6)} \quad (2.3)$$

where MW is the molecular weight of the VOC (g/mol), P is the ambient pressure (atm), R is the universal gas constant (8.205×10^{-5} m^3.atm.mole^{-1}.K^{-1}), T is the ambient temperature (K), and C (mg/m$_3$ or ppm) is the concentration of the VOC.

The initial concentration of VOCs has a major effect on the PCO rate of reaction. As shown in Figure 2.13, a higher initial concentration of VOC resulted in a higher kinetic

rate of reaction until reaching a plateau (Noguchi et al., 1998). This is because the amount of VOC molecules that can be adsorbed and degraded on the surface of the photocatalyst increased with a higher initial VOC concentration (Monteiro et al., 2015).

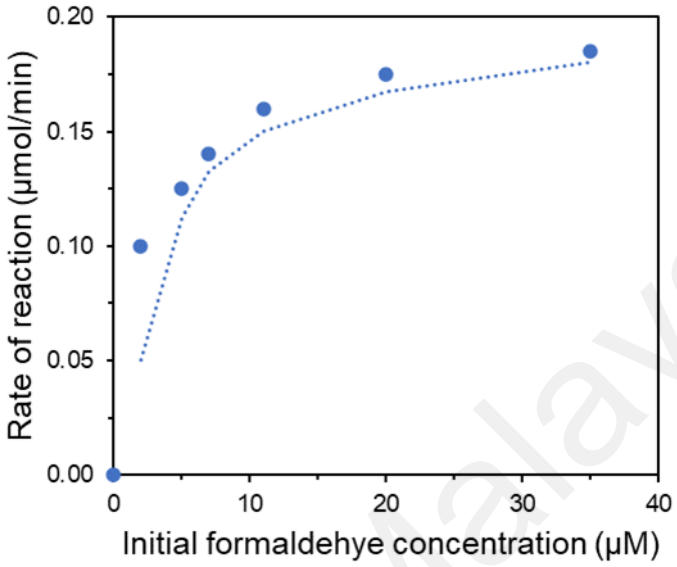

Figure 2.13: Dependence of reaction rates on the initial reactant concentrations. Adapted from (Noguchi et al., 1998).

Although increasing the initial concentration of VOCs can increase the rate of reaction, after the rate of reaction is at its peak, further increment of the initial concentration would result in a drop of the PCO removal% (Wu et al., 2015), as shown in Figure 2.14.

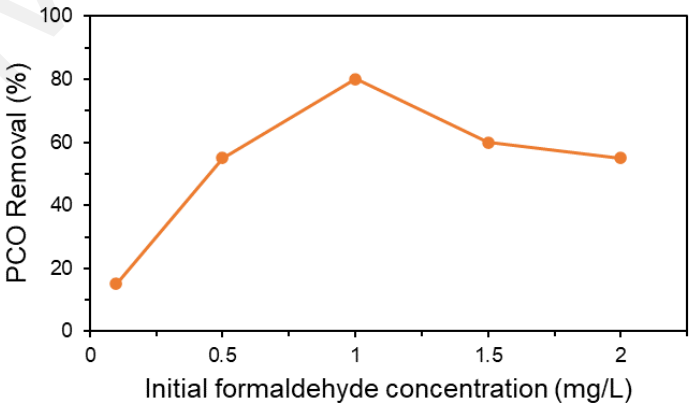

Figure 2.14: Effect of VOCs concentration on PCO removal%. Adapted from (Wu et al., 2015)

2.3.2.3 Humidity

Indoor humidity is usually at a range between 30 - 65 RH% (Mamaghani et al., 2018b), therefore PCO experiments to remove indoor VOC should be conducted within this range of humidity to mimic a realistic indoor condition. The effects of humidity on the PCO process of VOCs can be positive, negative, or no effect. This is because water vapour adsorbed on the photocatalyst can be oxidised into •OH radicals to boost PCO, but at the same time, water vapour can compete with VOC molecules for adsorption sites and hinder the PCO process. It is also noteworthy that •OH radicals can only be produced if the photocatalyst's valence band is positive enough to oxidise the water vapour (Demeestere et al., 2007). Hence, the effect of humidity on PCO is situational, depending on the type of VOCs, the concentration of VOCs, the photocatalyst's adsorption properties, and the position of the valence band of the photocatalyst (Mamaghani et al., 2017).

For example, the effect of humidity is more significant for non-polar VOCs than polar VOCs. This is because the adsorption competition between water vapour and VOC molecules is stronger for non-polar VOCs. As water vapour is firstly adsorbed on a photocatalyst, the wetted surface can accommodate polar VOCs, but it would greatly hinder the adsorption of non-polar VOCs (Mamaghani et al., 2018b).

Moreover, the effect of humidity is more prominent on low concentration VOCs than high concentration VOCs. For example, Ao et al. stated that the adsorption competition between VOC and water molecules is stronger for VOCs in the ppb range than VOCs in the ppm range (Ao & Lee, 2003). Even among the ppb range VOC, lower ppb concentration (7.5 – 250 ppb) is more significantly affected by humidity for adsorption than higher ppb concentration (113 – 800 ppb) (Geng et al., 2010; Mo et al., 2013). This is because at a lower concentration of VOCs, the small quantity of VOC molecules had lesser strength to compete with water vapour for adsorption sites.

Furthermore, the effect of humidity on PCO also depends on the surface absorptivity properties of the photocatalyst. The higher the hydrophilicity of a photocatalyst, the more sensitive it is to humidity. For example, a hydrophilic TiO_2 photocatalyst has a strong tendency to adsorb water vapour than VOCs. Therefore, the efficiency of the TiO_2 in degrading toluene was heavily limited by high humidity (Cao et al., 2000).

Humidity can also affect the reusability and mineralisation efficiency of a PCO process. For instance, Einaga et al. found that the presence of water vapour can prevent the deactivation of TiO_2 photocatalyst during PCO of benzene. This is because the water vapour could inhibit the formation of brownish carbonaceous materials on the TiO_2 during PCO. Conversely, the carbonaceous materials were precipitated on the TiO_2 during PCO under dry air, thus deactivating its photoactivity (Einaga et al., 2004). In addition, it was discussed that toluene and formaldehyde cannot be completely mineralised without the presence of water vapour (Wang et al., 2007).

In summary, every PCO process usually has an optimal humidity level to achieve the maximum amount of •OH radicals and the highest PCO rate. If the humidity exceeds the optimal level, the adsorption competition between water vapour and VOC molecules would then lower the PCO rate (Kim & Hong, 2002). The general effects of humidity on the performance of PCO are summarized in Figure 2.15.

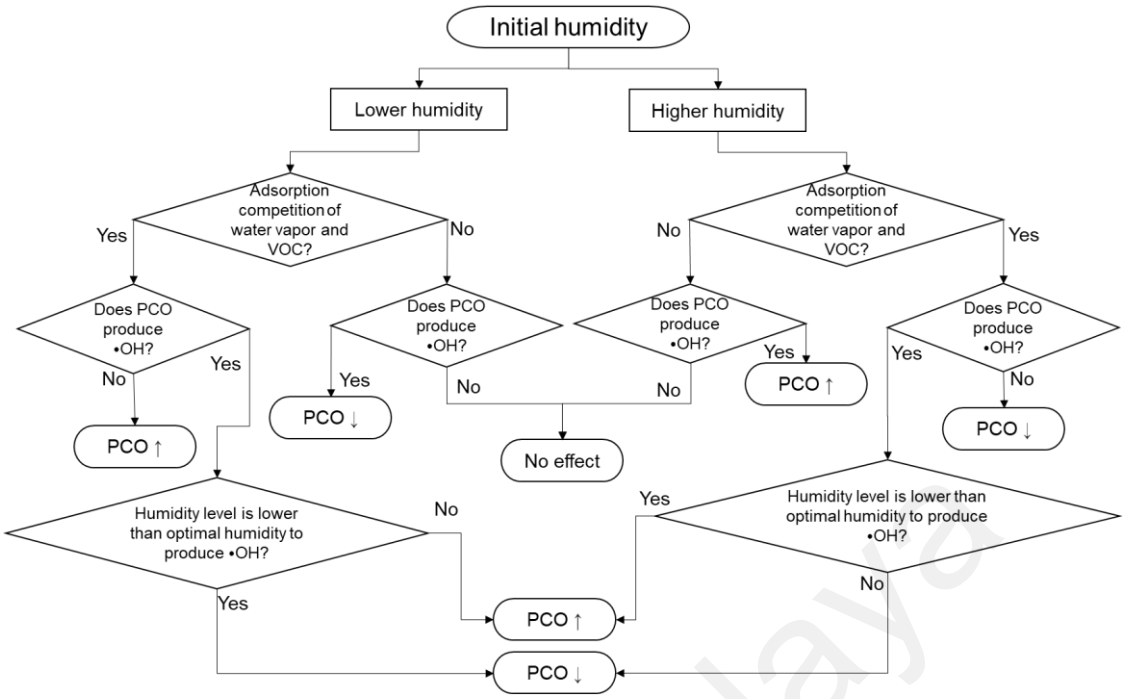

Figure 2.15: General effect of humidity on PCO performance.

2.3.3 Measurement of the concentration of VOCs

To measure the concentration of VOCs, one of the most common methods is through online sampling followed by a gas chromatography (GC) analysis. However, this analysis method is time-consuming, expensive, and required sophisticated operations (Spinelle et al., 2017). Alternatively, the concentrations of VOCs can be measured continuously via the usage of VOC detectors. There are many types of VOC detectors, such as photo-ionization detectors (PID), flame-ionization detectors (FID), and metal oxide sensors (Spinelle et al., 2017). These VOC detectors can detect VOCs in a wide range of concentrations in real-time (Spinelle et al., 2015). However, a VOC detector usually cannot differentiate between different types of VOCs, and can only measure the concentration of the total VOCs (TVOC) (Jian et al., 2013). Table 2.6 shows the past studies that utilized commercial VOC detectors to measure the concentrations of VOCs during PCO processes. The VOC detectors can detect various types of VOCs, such as toluene, MEK, benzene, ethylbenzene, acetone, benzene, formaldehyde, and isobutylene.

Table 2.6: Past PCO experiment with VOCs detector.

VOC detector	VOC detected	Initial concentration of VOC	Reference
Mini-RAE PLUS PGM-76	toluene	210 to 800 mg/m^3	(Wei et al., 2010)
ppbRAE Model PGM-7240	toluene	200 to 800 ppb	(Chen et al., 2011)
ppb3000 RAE PID	toluene, MEK	100 to 1000 ppb	(Mamaghani et al., 2018b)
MiniRAE Plus Professional PID	acetone	400 ppm	(Jimmy et al., 2002)
VOC-72 M gas analyser (Environment SA, FR),	benzene	80 to 260 µg/m^3	(Tobaldi et al., 2021)
PID-AH2 (Alphasense Pvt. Ltd., UK)	toluene	200 to 600 ppb	(SM & Maiya, 2019)
ppb3000 RAE PID	toluene, MEK	0.5 to 20 ppm	(Mamaghani et al., 2018a)
ppb3000 RAE PID	toluene	500 to 5200 mg/m^3	(Fang et al., 2016)
TVOC fixed PID Detector (Ion Science Ltd, Roystone, UK)	ethylbenzene	20 to 250 ppm	(Kamaei et al., 2018)
PID Scan-800 (GDS Instruments PTE. Ltd., Singapore)	acetone	500 to 1000 ppb	(Ho et al., 2019)
PhoCheck 5000 PID	toluene	50 to 200 ppm	(Jafari et al., 2019)
PhoCheck 5000 PID	formaldehyde	2.5 to 25 mg/m^3	(Rezaee et al., 2014)
PID-TECH Plus photoionization detector (Baseline-Mocon Inc.)	isobutylene	11 to 100 ppm	(Riley et al., 2014)
MiniRAE 2000	toluene	11 ppm	(Tokode et al., 2017)
MiniRAE Plus Professional PID	acetone	800 ppm	(Yu et al., 1998)

2.3.4 Investigation of reactive species involved in the PCO of VOCs

A photocatalyst system can still photodegrade VOCs even without producing both of the main radical species ($\bullet O_2^-$ and •OH radicals) (Han et al., 2013). Therefore, it is important to conduct a reactive species study to fully understand the PCO mechanism of a photocatalyst system. There are three main methods to determine the reactive species produced in a gas-phase PCO process: (1) aqueous phase electron spin resonance (ESR), (2) use scavengers to trap reactive species on the surface of photocatalyst during gas phase PCO, and (3) manipulate the oxygen and water concentration in the ambient air during gas-phase PCO.

For instance, Zou et al. used the ESR technique to determine the ROS produced by a cobalt oxide (CoO)-tungsten trioxide (WO_3) photocatalyst under visible light irradiation for the degradation of toluene (Zou et al., 2020). The trapping agent used was 5,5-dimethyl-1-pyrroline (DMPO), where •OH radicals were measured in an aqueous solution and $•O_2^-$ radicals was detected in methanol (Zou et al., 2020). The drawback of the ESR method is that the reactive species were measured in an aqueous phase, which could have resulted in some discrepancy with the actual gas-phase PCO.

The second method to identify reactive species is to adsorb scavenger or trapping agents onto the surface of the photocatalyst prior to gas-phase PCO. For example, Hu et al. immersed photocatalyst in aqueous solutions with 10mM of radical scavengers, such as tert-butanol (t-BuOH), 1,4-benzoquinone (BQ), and edentate disodium (EDTA-2Na) to trap •OH, $•O_2^-$ radicals, and hole carriers, respectively. The immersion process allowed the surface adsorption of radical scavengers onto the photocatalyst. Then, the photocatalyst was dried at room temperature, followed by gas-phase PCO to remove formaldehyde (Hu et al., 2020). Zhang et al. also used a similar scavenger method to trap reactive species, where 0.1 mM of $AgNO_3$, triethanolamine (TEOA), BQ, and isopropanol (IPA) were used to trap free-electron, hole carriers, $•O_2^-$, and •OH radicals, respectively for the photodegradation of VOCs (J. Zhang et al., 2020).

The third method to investigate the reactive species involved is by manipulating the concentrations of water and oxygen in the ambient air of the PCO reactor. For example, Lie et al. conducted PCO of VOCs in air, pure oxygen, pure nitrogen, air with high RH%, and air with low RH% to identify the involvement of $•O_2^-$and •OH radicals during PCO (P. Li et al., 2020).

2.3.5 Mineralisation of VOCs into CO_2

Generally, intermediates are produced during the photodegradation of VOCs (Debono et al., 2017) because the PCO process is usually a stepwise process (Figure 2.7). Therefore, it is important to study the rate of mineralisation of a PCO process to ensure that the VOCs are broken down into harmless CO_2, instead of other potentially harmful intermediates (Kovalevskiy et al., 2018). The mineralisation efficiency (M%) can be calculated by Equation 2.4 (Chen et al., 2020; I.-S. Kang et al., 2018; Sleiman et al., 2009):

$$Mineralization\% = \frac{[CO_2]_{evolved}}{[CO_2]_{theoretical}} \times 100\% \qquad (2.4)$$

$$[CO_2]_{theoretical} = n_C \times PCO\% \times C_0$$

where $[CO_2]$ is the experimental and theoretical concentration of CO_2, n_C is the stoichiometric number of carbon (C) of the targeted VOC, PCO% is the percentage of the VOC degraded by PCO, and C_0 is the concentration of VOC at the initial point (after the adsorption-desorption equilibrium). The concentrations of CO_2 can be measured by using instruments like GC (Debono et al., 2017) and infrared CO_2 detector (I.-S. Kang et al., 2018; Temerov et al., 2021). The reported mineralisation rates were rarely 100% (Chun & Jo, 2016; Xu et al., 2010) because some stable intermediates were formed during the PCO. The stable intermediates could be adsorbed onto the surface of the photocatalyst or reactor's wall and resist mineralisation (Debono et al., 2017).

2.3.6 Single photocatalyst for removal of VOCs

In the past reports on air purification, TiO_2 as a photocatalyst has been extensively investigated (Boyjoo et al., 2017). Besides TiO_2, there are also other single photocatalysts that have been developed to photodegrade VOCs (X. Zhang et al., 2016), such as ZnO, SnO_2, indium oxide (In_2O_3), bismuth oxide (Bi_2O_3), perovskite-structured photocatalyst (i.e. $CdSnO_3$), spinel structured photocatalyst (i.e. $BaAl_2O_4$, $ZnGa_2O_4$, and $MnFe_2O_4$),

metal hydrate photocatalyst (i.e. $MgSn(OH)_6$, $ZnSn(OH)_6$, and $SrSn(OH)_6$), and metal-free photocatalyst (i.e. graphitic carbon nitride (gCN)). Among them, the usage of metal-free photocatalyst to photodegrade VOCs has only been reported sparingly. Recently, gCN was used as a sole photocatalyst to photodegrade formaldehyde (Kong et al., 2021; Yao et al., 2019) and acetaldehyde (Baca et al., 2020). The gCN is a 2D nanosheet material, hence it has a large surface area and a short charge carrier diffusion distance to the surface (Yao et al., 2019). For instance, Baca et al. found that 2D gCN was able to photodegrade acetaldehyde up to 43% continuously with a mineralisation efficiency of 15% (Baca et al., 2020). Table 2.7 summarizes some of the recent reports of single photocatalysts for the removal of VOCs.

Table 2.7: Recent reports of single photocatalysts for the removal of VOCs.

Photocatalyst, band gap (eV)	**Application**	**Light Source**	**Performance**	**Ref.**
TiO_2	100 ppm acetylene, continuous flow: 500 ml/min	24 W UV-A (365 nm)	PCO = 75% M% = 85%	(Thevenet et al., 2014)
TiO_2	500 ppm acetone, 110 ppm benzene	500 W Xenon (UV-Vis)	PCO = 100% in 25 min and 100% in 110 min	(Xie et al., 2016)
TiO_2 (3.19)	400 ppm acetone, acetaldehyde, and toluene (each)	500 W UV (315-400 nm, 30W/m^2)	PCO = 100% in 60 min, 100% in 50 min, and 50% in 6 h	(Bianchi et al., 2014)
$Zr_xTi_{1-x}O_2$	1 mg/m^3 formaldehyde	45 W Energy saving lamp (UV-Vis)	PCO = 92% in 48 h	(Huang et al., 2013)
ZnO	100 ppm formaldehyde	UV-A LED (365 nm, 3.6 mW/cm^2) White LED (400-800 nm, 36 mW/cm^2)	PCO = ~33% in 60 min and ~14% in 60 min	(Liao et al., 2013)
SnO_2 (3.6)	580 ppb acetaldehyde, continuous flow: 0.26 L/min	15 W UV-C (254 nm)	PCO = ~95%	(Chu et al., 2011)
$1n_2O_3$ (2.9, direct)	4 uL in 120 mL of toluene	500W Xenon (>400nm, 40 mW/cm^2)	PCO = ~69% in 8h	(Zhang et al., 2015)
α-Bi_2O_3 (2.72, indirect)	2 ppm formaldehyde, continuous flow: 4 L/min	300 W halogen lamp (> 420nm)	PCO = 37.4%	(Ai et al., 2011)

Table 2.7, continued

Photocatalyst, band gap (eV)	Application	Light Source	Performance	Ref.
$CdSnO_3 \cdot 3H_2O$ (4.4, direct)	280 ppm acetone, continuous flow: 20 ml/min	4 W UV-C (254 nm)	PCO = 25% M% = 58%	(Chen et al., 2013)
Ag-doped $BaAl_2O_4$ (1.63)	750 mg/m^3 toluene, continuous flow: 20 ml/min	15 W UV-A (365 nm, 42 mW/cm^2)	PCO = 88%	(Zhu et al., 2015)
$ZnGa_2O_4$ (4.82)	300 ppm benzene, continuous flow: 20 ml/min	4 W UV-C (254 nm)	PCO = 41%	(Zhang et al., 2009)
$MnFe_2O_4$ (1.61, direct)	280 ppm benzene	Xenon (> 400 nm, 50 mW/cm^2)	CO_2 evolution detected by in situ FTIR during PCO	(Shen et al., 2015)
Zn_2SnO_4 (3.25 indirect)	2 ppm formaldehyde, continuous flow: 4 L/min	300 W halogen lamp	PCO = 26.4%	(Ai et al., 2010)
$MgSn(OH)_6$ $ZnSn(OH)_6$	250 ppm benzene, balanced with O_2	6 W UV-C (254 nm)	PCO = 89%, 66% M% = 68%, 68%	(D. Huang et al., 2015)
$CaSb_2O_5(OH)_2$ (4.6)	300 ppm benzene, continuous flow: 20 ml/min	4 W UV-C (254 nm)	PCO = 7.5% M% = 100%	(Huang et al., 2012)
$SrSn(OH)_6$ (3.86)	280 ppm benzene, balanced with O_2, continuous flow: 20 ml/min	4 W UV-C (254 nm)	PCO = 31% M% = 55%	(Luo et al., 2016)
$CaSn(OH)_6$ (4.4)	210 ppm benzene, balanced with O_2, continuous flow: 20 ml/min	4 W UV (254 nm)	PCO = 20% M% = 83%	(Meng et al., 2011)
Ag doped gCN (2.7)	700 ppm toluene, continuous flow: 100 ml/min	6 W daylight fluorescent lamp (> 390 nm)	Higher quantum efficiency than TiO_2	(Fontelles-Carceller et al., 2016)
gCN on textile (2.81, indirect)	2 mg/m^3 formaldehyde	300 W Xenon (> 420 nm), 50 W LED	PCO = 100% in 20 and 100% in 30 min	(Yao et al., 2019)
gCN (2.7, indirect)	0.45 mg/m^3 formaldehyde	Yellow LED (585 nm)	PCO = 56.3% in 30 h	(Kong et al., 2021)
gCN (2.71, indirect)	300 ppm acetaldehyde, continuous flow: 1 ml/min	20 W LED	PCO = 43% M% = 15%	(Baca et al., 2020)

(M% = Mineralisation efficiency)

2.4 Metal-free graphene oxide (GO)-based photocatalyst

First discovered in 2004, graphene is a monolayer of sp^2 carbon atoms structured in a 2D honeycomb shape (Novoselov et al., 2004). The discovery of graphene has intrigued a lot of attention due to the excellent mechanical, thermal, optical, and electrical properties of graphene (Geim & Novoselov, 2010). One branch of graphene research

focuses on functionalized graphene such as the oxygen-rich graphene oxide (GO). GO is a single or a few-layer of graphite oxide usually synthesized by the Hummers method, which involves the oxidation of graphite with strong acids and oxidants, then followed by an exfoliation process (Li & Bubeck, 2013). A monolayer of GO has a thickness of 1.0 – 1.3 nm (Liscio et al., 2011; Wilson et al., 2010). A few-layer GO has around 2 – 5 layers of GO, while a multilayer GO have 5 – 10 layers (Bianco et al., 2013; Kumar et al., 2021). GO is composed of two primary regions, namely the conducting hydrophobic π-conjugated sp^2 domain and the insulating hydrophilic sp^3 domain with oxygenated carbon groups (OCGs). Among the main OCGs on GO, the hydroxyl and epoxide groups are found on its basal plane, while the carboxylic groups are found at its edge (Gao, 2015). Pure graphene has a zero-bandgap, in which the valence band (filled C-C π (bonding) orbital) touches the conduction band (empty C-C π* (anti-bonding) orbital). Conversely, GO has a tuneable finite bandgap, therefore enabling GO to function as a semiconductor/photocatalyst (Putri et al., 2015).

The bandgap of GO can be direct, indirect, or both. In the direct bandgap of GO, the C-C π (bonding) and C-C π* (anti-bonding) orbitals act as the valence and conduction bands, respectively. Meanwhile, GO with a high oxygenated level (O/C > 0.5) may exhibit an indirect bandgap, where the oxygen (O) $2p_z$ and C-C π* (anti-bonding) orbitals are the valence and conduction bands, respectively (Ito et al., 2008). Besides that, the magnitude of the bandgap can be tuned by varying the relative amount of sp^2 and sp^3 domains in GO. For example, the lesser the OCGs on GO, the lesser the insulating sp^3 domain, and the larger the isolated conductive sp^2 domain, therefore this would lead to a narrower bandgap (Mathkar et al., 2012). It is also noteworthy that due to the random distributions and sizes of the OCGs, GO often has a range of bandgap (between 2.8 – 4.6 eV (Ito et al., 2008)) instead of a precise bandgap (Yeh et al., 2010). The relationships

between the bandgap, oxidation level, and sp^2/sp^3 domains of GO are summarized in Figure 2.16.

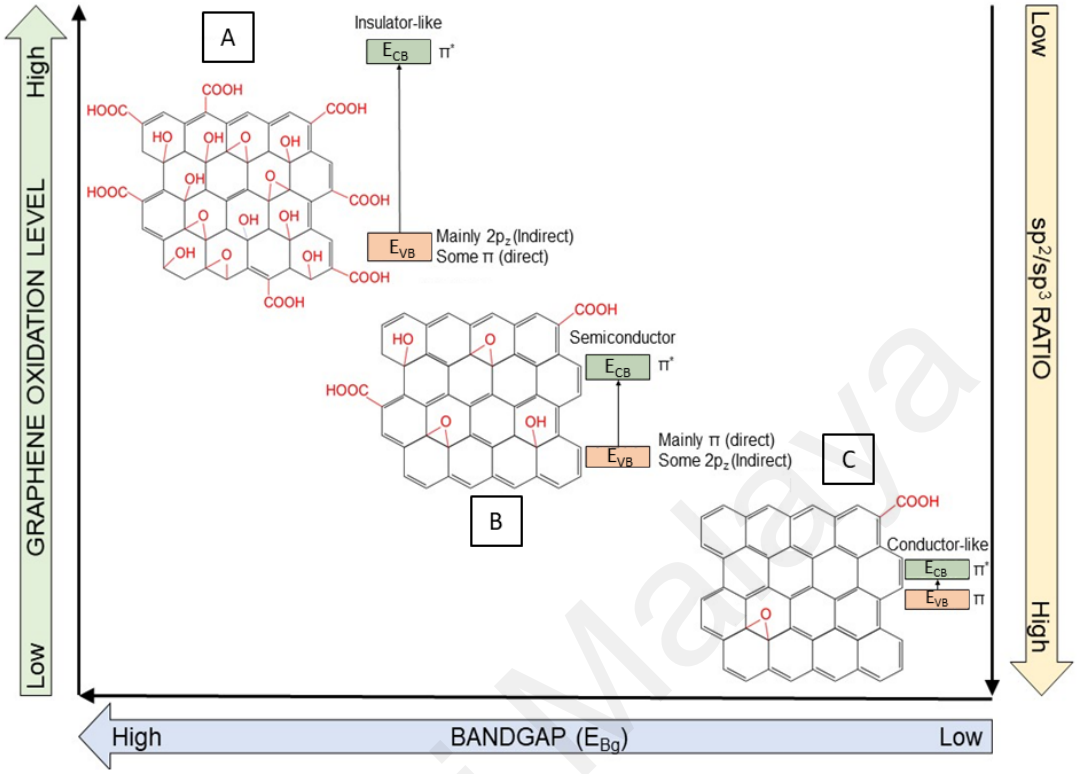

A – GO with higher oxidation level
B – Partially reduced GO with lower oxidation level
C – Fully reduced GO with very low oxidation level

Figure 2.16: Relationship of oxidation level, bandgap, and sp^2/sp^3 ratio of GO.

While various metal-based photocatalysts have been developed, the possibility of employing metal-free GO for photocatalysis is fascinating. Nevertheless, it should be noted that in the past studies, GO has mainly functioned as a support/cocatalyst for other photocatalysts (Xiang et al., 2012), while the study of GO as a sole photocatalyst is still lacking (Putri et al., 2016). For example, the utilization of GO as a standalone photocatalyst to degrade air pollutants has not been explored yet.

2.4.1 Undoped graphene oxide (GO)-based photocatalyst

Graphene and GO are 2D materials, for instance, the thickness of pure graphene and single-layer GO are approximately 0.3 and 1 nm, respectively (Putri et al., 2016). Theoretically, this 2D nature is beneficial for photocatalytic activity as the occurrence of volume charge carrier recombination is hindered. This is because photogenerated charge carriers can be rapidly transported to the surface of a 2D photocatalyst to participate in photocatalysis (Putri et al., 2016). Moreover, the massive specific surface area, presence of OCGs, and π-conjugation structures of GO can boost its ability to adsorb pollutants and reactive species for photocatalytic reactions (Putri et al., 2016). Recently, pristine GO had been used as a standalone photocatalyst in aqueous dye degradation (Bustos-Ramirez et al., 2015; Guardia et al., 2012), photoreduction of CO_2 (Hsu et al., 2013), photoreduction of toxic Cr (VI) (Wu et al., 2020), and generation of hydrogen peroxide (H_2O_2) (Hou & Wang, 2017). Despite the potential of GO as a standalone photocatalyst, it suffers from poor photostability (Kuang et al., 2019) and large bandgap (Yu et al., 2021). Additionally, it was reported that some of the highly electronegative OCGs on GO might act as recombination centres that recombine photogenerated charge carriers, therefore diminishing the photoactivity (Putri et al., 2015).

Plotnikov et al. found that pristine GO undergoes photolysis/photo-corrosion under light irradiation (Plotnikov et al., 2011). Due to photolysis, the chemical composition and properties of GO photocatalyst might change during photocatalysis (Kuang et al., 2019). Therefore, the poor photostability of GO had limited its practical usage as a stable photocatalyst. The photolysis of GO occurred due to the dissociation of some of the OCGs, such as the removal of C-OH, C-O-C, C=O, and O-C=O groups (Nia et al., 2017). The activation energies for the photolysis of the OCGs is between 0.7 – 4.0 eV (McDonald et al., 2015), which means that GO could undergo photolysis even under visible light irradiation.

Besides that, the photocatalytic activity of GO is also limited by its large bandgap (Pedrosa et al., 2020). Generally, a GO produced via the traditional Hummers method has a large direct bandgap between 3.3 – 4.4 eV (Wu et al., 2020; Yeh et al., 2010). Therefore, a pristine GO is only photoactive under the irradiation of a light source with a wavelength <375 nm.

To improve the photocatalytic activity of GO, various reduction methods were used to tune its photostability and bandgap. GO can be reduced through many methods such as thermal, chemical, and photoreduction (Low et al., 2015). In this thesis, GO reduced via photoreduction is dubbed as the photoreduced graphene oxide (PRGO), while GO reduced by the other traditional thermal/chemical methods are denoted as the reduced-graphene oxide (rGO). The photoreduction method is a more cost-effective, scalable, and environmentally benign method than the thermal/chemical methods (Gengler et al., 2013). This is because the photoreduction method eliminates the usage of toxic reducing agents and avoids reliance on high temperatures. It is also important to note that the PRGO and rGO photocatalysts should only be partially reduced. This is because a completely reduced GO would have a near-zero bandgap and thus behave like a conductor instead of a semiconductor.

The photoreduction process of GO is essentially the photolysis of GO under a constant light source for a certain duration. The constant light source emits constant photon energy, which is absorbed by the molecular resonance of the OCGs on GO (McDonald et al., 2015). The absorbed energy then dissociates some of the OCGs and releases them as either H_2O, O_2, CO_2, or carbon monoxide (CO) (Shulga et al., 2010), simultaneously, some sp^2 carbon networks are restored on the GO (Zhang et al., 2014). After a certain duration, the photoreduction of GO would reach a plateau (Kuang et al., 2019) because the constant photon energy from the light source is unable to remove the remaining stabler OCGs. In another word, a PRGO is able to withstand further photoinduced changes after

it reaches a saturated reduction state unless a higher amount of energy is used (Gan et al., 2011). This is useful because it signifies that PRGO as a photocatalyst can resist further photo-corrosion during photocatalysis (Kuang et al., 2019). Besides that, since OCGs are removed during photoreduction, the bandgap of the PRGO is narrower than the bandgap of pristine GO (Yu et al., 2021), which would improve the ability of PRGO to absorb light. In the past, PRGO had exhibited good performance and photostability for the applications of CO_2 photoreduction (Kuang et al., 2019), water splitting (Yeh et al., 2011), and Cr (VI) photoreduction (Yu et al., 2021). Nevertheless, PRGO photocatalyst has not been used to photodegrade air pollutants yet. Table 2.8 below summarizes the past applications of GO, rGO, and PRGO as sole photocatalyst.

Yeh et al. found that GO can be photoreduced into PRGO by 6 h of irradiation under a 400 W mercury lamp. The PRGO had a stabilized bandgap (2.4 - 3.5 eV), and the remaining OCGs were stable during the subsequent photocatalytic water splitting process (Yeh et al., 2010). Kuang et al. found that PRGO (photoreduced under a 500 W Xenon lamp for 8 h) had a slower photogenerated charge carrier recombination rate than pristine GO. This is because the PRGO had a larger π-conjugated sp^2 network and a higher defect density in the sp^2 network than GO. As a result, the PRGO performed better than GO in the photoreduction of CO_2 into CO. In addition, the OCGs contents in the C 1s of the PRGO before (79.96%) and after (79.81%) photocatalysis were similar, thus indicating good photostability (Kuang et al., 2019).

Through AFM measurements, Matsumoto et al. found that the GO nanosheet had a thickness ~1.2 nm, while the thickness of the PRGO (photoreduced under a 500 W Xenon lamp for 48 h) was about 0.9 nm. The decrease in thickness was due to the reduction of OCGs on the PRGO. The study shows that PRGO was able to maintain a 2D structure even after the photoreduction treatment (Matsumoto et al., 2011). This is important as the

2D structure is vital for the fast transportation of charge carriers during photocatalysis (Putri et al., 2016).

Table 2.8: Summary of GO, rGO, and PRGO as single photocatalysts.

Photocatalyst	**Application**	**Light Source**	**Band gap (eV)**	**Performance**	**Ref.**
PRGO (photoreduced by 400 W Hg lamp, 6 h)	Water splitting	400 W Hg-lamp (<400 nm)	2.4-3.5 (direct) 1.4-1.5 (indirect)	H_2 production rate of 17,000 µmol in 6 h	(Yeh et al., 2010)
PRGO (photoreduced by 450 W Hg lamp, 6 h)	Water splitting	450 W Hg-lamp (<400 nm)	3.2-4.2 (direct) 2.3-2.8 (indirect)	H_2 production rate of 11,000 µmol in 6 h	(Yeh et al., 2011)
PRGO (photoreduced by 500 W Xe lamp, 48 h)	Water splitting	500 W Xe lamp (UV-Vis)	2.8 (direct)	H_2 production rate of 0.013 µmol h^{-1}	(Matsumoto et al., 2011)
PRGO (photoreduced by 500 W Xenon, 8 h)	Photoreduction of CO_2	500 W Xe lamp (UV-Vis)	2.8 - 3.9 (direct)	CO production rate of 1.23 µmol/g-cat.h^{-1}	(Kuang et al., 2019)
PRGO (photoreduced by 8W UV-C, 1 h)	Photoreduction of toxic Cr(VI) to Cr(III)	500 W Xe lamp (420-760 nm)	1.95 – 2.95 (direct)	6.4 L^{-1} min^{-1}	(Yu et al., 2021)
rGO (reduced by hydrazine at 80 °C, 48 h)	Photodegradation of Reactive Black 5 (RB5) in water	96W UV-A lamp	N/A	49% photo-decolorization in 60 min	(Wong et al., 2015)
GO	Photodegradation of phenol in water	UV lamp (254 nm)	4.04 (direct) 1.87 (indirect)	38.6% removal in 2 h	(Bustos-Ramirez et al., 2015)
GO	Photodegradation of 4-chlorophenol in water	5.5W Pencil 254 nm UV-C lamp	4.0 (direct) 1.8 (indirect)	97% removal in 2 h	(Bustos-Ramírez et al., 2015)
GO	Photodegradation of rhodamine B (RhB) in water	50 W short arc Hg bulb (UV)	N/A	95% reduction in 4 h	(Guardia et al., 2012)
GO	Photodegradation of RhB in water	150 W solar simulator (UV-Vis)	2.40 (direct)	43% in 2 h	(Oh et al., 2016)
GO	Photoreduce resazurin (RZ) into resorufin (RF)	350 nm UV light	3.26 (direct)	44.1% reduction in 40 min	(Krishnamoorthy et al., 2011)
GO	Photodegradation of phenol in water	Visible light >400 nm (Vis)	N/A	95% in 90 min	(Pedrosa et al., 2020)
GO	Photoreduction of CO_2	300 W Halogen lamp (UV-Vis)	3.2 – 4.2 (direct)	CH_3OH production rate of 0.172 µmol/g-cat.h^{-1}	(Hsu et al., 2013)

Table 2.8, continued

Photocatalyst	Application	Light Source	Band gap (eV)	Performance	Ref.
GO	Photocatalytic generation of H_2O_2	765 W Xe lamp (UV-Vis)	-	rGO (1mM H_2O_2 in 6 h)	(Hou & Wang, 2017)
GO	Photoreduction of toxic Cr(VI) to Cr(III)	1500 W Xe lamp (>400 nm)	3.5 – 4.4 (direct)	3.3 L^{-1} min^{-1}	(Wu et al., 2020)
GO	Photodegradation of bisphenol A (BPA) in water	800 W Xe lamp (UV-Vis)	-	rGO (11.2% in 24 h)	(Adeleye et al., 2018)

2.4.2 Heteroatom-doped graphene oxide (GO)-based photocatalyst

Heteroatom-doping has been shown as an effective process to alter the properties of GO. It was found that heteroatom-doped GO often develop new or improved electromagnetic, physicochemical, optical, and structural properties (X. Wang et al., 2014). More recently, studies have found that heteroatom-doping is a promising strategy to modulate the photoactivity of GO photocatalyst (Mokhtar Mohamed et al., 2018; Putri et al., 2017). For example, B-doped rGO (BrGO) (Putri et al., 2017) and N-doped rGO (NrGO) (Mokhtar Mohamed et al., 2018) exhibited enhanced photoactivity in water splitting and aqueous dye degradation, respectively.

There are mainly two types of heteroatom-doping on GO, namely the surface-transfer doping and substitutional doping. In surface-transfer doping, foreign atoms are attached to the surface of GO. An electron-withdrawing surface-transfer dopant is an acceptor (p-type) dopant, while an electron-donating surface-transfer dopant is a donor (n-type) dopant. Meanwhile, in substitutional doping, a foreign atom is doped into the graphitic matrix of GO and may replace an original host C atom. Generally, a substitutional dopant atom with lesser valence electron than the host C atom is an acceptor (p-type) dopant, while a substitutional dopant atom with more valence electron than the host C atom is a donor (n-type) dopant (Liu et al., 2011). Notably, undoped GO, rGO, and PRGO usually have a p-type conductivity due to the oxygen atoms attached to their surface. The oxygen

atoms are more electronegative than the host C atoms, therefore they tend to withdraw electrons from C and act as p-type dopants (Wang et al., 2009). Studies found that heteroatom-doping of GO creates new chemical bonds (Q. Zhang et al., 2020) and tunes the charge carrier density (Q. Zhang et al., 2020), which could influence the subsequent photocatalytic performances. Figure 2.17 displays the summary of surface-transfer and substitutional doping on GO.

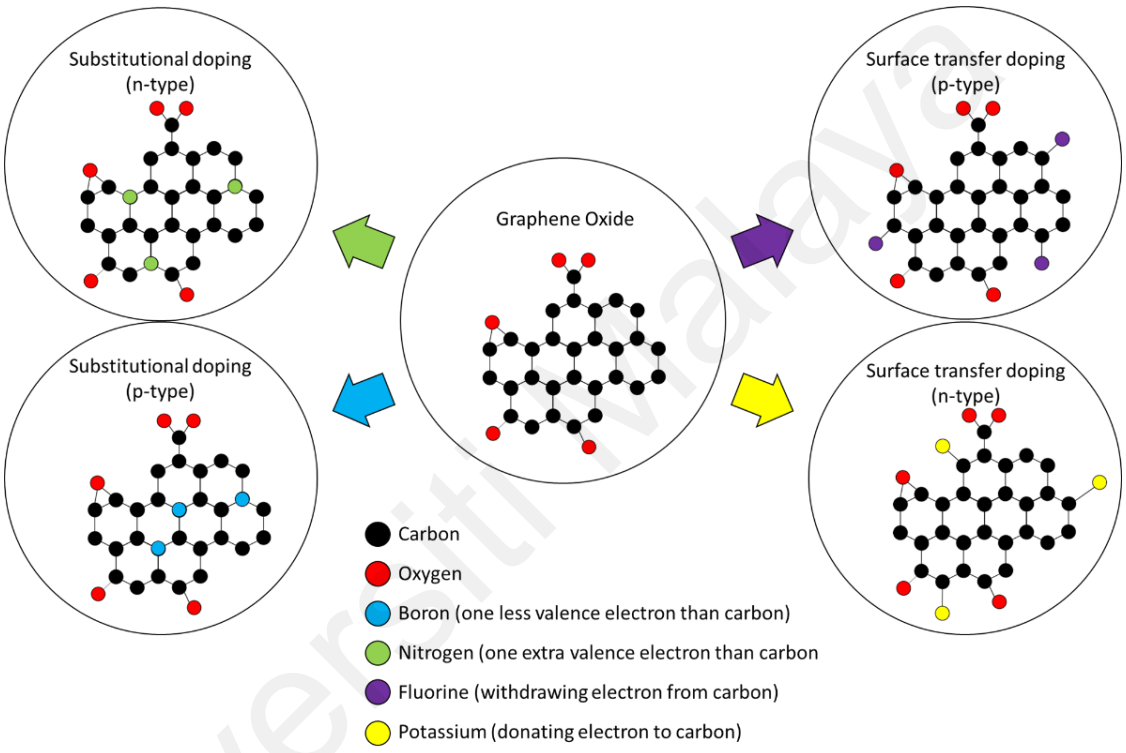

Figure 2.17: Surface-transfer and substitutional heteroatom-doping of GO.

Table 2.9 summarizes the previous studies about heteroatom-doped graphene-based photocatalysts. As shown in Table 2.9, most heteroatom-doping techniques simultaneously reduce and dope the initial GO into "X"-doped rGO, where "X" is the dopant atom. Moreover, most of the past studies used thermal-induced doping method such as calcination (Putri et al., 2017), hydrothermal (Yang et al., 2017), and pyrolysis (Das et al., 2019). However, these techniques are often tedious, energy-demanding, costly, and difficult to scale up (Del Pino et al., 2016; Kepić et al., 2017).

Among the heteroatoms, boron (B) and nitrogen (N) can be easily substitutionally-doped into GO, owing to their similar sizes to carbon (C) and their close proximity in the periodic table (Lee et al., 2021). N atom is an n-type dopant to GO because N atom has one valence electron more than C atom. Conversely, B atom has one valence electron less than C atom, thus B is a p-type dopant (X. Wang et al., 2014). Since the atomic sizes of N and B dopants are compatible to C atom, they do not cause much disturbance to the graphitic structure of GO (Putri et al., 2015). Despite the success of the past studies, the mass production of heteroatom-doped GO photocatalyst with a facile, scalable, and inexpensive process remains a great challenge. In addition, there is still a lack of study on the effect of dopant bonding configurations on the photocatalytic activity of heteroatom-doped GO photocatalyst.

Table 2.9: Summary of heteroatom-doped graphene-based photocatalyst

Photocatalyst	**Doping concentration (at%)**	**Precursor. Doping method**	**Application**	**Light source**	**Band gap (eV)**	**Performance**	**Ref.**
B doped rGO (BrGO)	B: 2.74, 2.93, 3.59 (XPS)	GO and B_2O_3. Calcination under Ar gas.	Water splitting	500 W Xe lamp (UV)	-	H_2 production rate of 64.6 μmol g^{-1} h^{-1}	(Putri et al., 2017)
B doped graphene aerogel	B: 3.37, 2.15, 1.68, 0.96, 0.14 (XPS)	GO and H_3BO_3. Hydrothermal.	Photodegradation of AO dye in water	11 W Xe lamp (>420 nm)	1.55 (direct)	Degraded 98% in 210 min	(Chowdhury et al., 2018)
BrGO	B: 10.1 (EDX)	GO and H_3BO_3. Calcination under vacuum.	Photodegradation of MO and MB dyes in water	175 W halide lamp (UV)	3.00 (indirect)	Degraded 98% of MO in 100 min and 99% of MB in 50 min.	(Singh et al., 2018)
BrGO	B: 1.2 (XPS)	GO and borane-tetrahydrofuran. Heated in oil bath.	Photodegradation of RhB dye in water	300 W Xe lamp (>420 nm)	-	Degraded 100% in 130 min.	(Tang et al., 2015)
B doped graphene nanoribbon (BGNR)	-	GO and H_3BO_3. Calcination under vacuum.	Photodegradation of RhB dye in water	300 W Hg lamp (UV)	-	Degraded 50% in 120 min.	(M. Xing et al., 2014)
BrGO	B: 8.4 (XPS)	GO and H_3BO_3. Calcination under Ar gas.	Photodegradation of MB dye in water	160 W light (mono wavelength at 420 nm)	1.90 (direct)	38.5% in 60 min.	(Mokhtar Mohamed et al., 2018)
N doped rGO (NrGO)	N: 8.26, 7.60, 6.51 (XPS)	GO and Urea. Calcination under Ar gas.	Water splitting	500 W Xe lamp with visible cut off (UV)	-	H_2 production rate of 66.7 μmol g^{-1} h^{-1}	(Putri et al., 2017)
NrGO	N: 2.93 (XPS)	GO and hydrazine. Hydrothermal	Photodegradation of RhB dye in water	300 W Xe lamp (>405 nm)	3.09 – 3.21 (direct). 2.43 – 3.05 (indirect).	Degraded 90% in 6 h.	(Yang et al., 2017)

Table 2.9, continued

Photocatalyst	Doping concentration (at%)	Precursor. Doping method	Application	Light source	Band gap (eV)	Performance	Ref.
N doped GO (NGO)	N: 4.13 (XPS)	Pyrolysis of lentil, followed by oxidation.	Photodegradation of MB dye in water	60 W tungsten bulb (Vis)	3.50	Degraded 100% in 80 min	(Das et al., 2019)
N doped graphene	N wt%: 16.2, 15.8, 15.1, 8.1, 5.4 (combustion analysis)	Pyrolysis of chitosan aerogel bead.	Water splitting	100 W solar simulator (UV-Vis)	-	H_2 production rate of 82.8 µmol/3 h	(Lavorato et al., 2014)
NGO	N/C atomic ratio: 0.13 (XPS)	GO under ammonia gas (25 °C)	Water splitting.	450 W Hg lamp (>420 nm)	2.60 (direct) 2.30 (indirect)	H_2 production rate of 2000 µmol/6 h	(Yeh et al., 2013)
N doped graphene quantum dot (NGQD)	N/C atomic ratio: 2.9 (XPS)	GO calcination under ammonia gas, then oxidation with Hummers' method.	Water splitting.	300W Xe lamp (>420 nm)	2.20 (direct).	H_2 production rate of 5 µmol after 10 h.	(Yeh et al., 2014)
N doped GO dot	N/C atomic ratio: 10 (XPS)	GO calcined under ammonia gas. Oxidation to get GO dot and then hydrothermal with ammonia.	Water splitting.	300 W Xe lamp (>420 nm)	2.10 (direct).	H_2 production rate of 12 µmol h^{-1}.	(Nguyen et al., 2018)
NrGO	N: 2.7 (XPS)	GO and urea. Calcination under Ar gas	Photodegradation of MB dye in water	160 W light (mono wavelength at 420 nm)	1.68 (direct)	Degraded 93% in 60 min.	(Mokhtar Mohamed et al., 2018)
NGQD	N: 2.26, 3.93, 6.85, 4.39, 4.18 (XPS)	GO and urea. Hydrothermal.	Water splitting.	AM 1.5G (100 mW/cm^2)	2.29 (direct)	H_2 production rate of ~50 µmol 6 h^{-1}. g^{-1}	(Tsai et al., 2020)

Table 2.9, continued

Photocatalyst	Doping concentration (at%)	Precursor. Doping method	Application	Light source	Band gap (eV)	Performance	Ref.
S doped graphene quantum dot (SGQD)	S: 1.91 (EDX) S: 1.90 (XPS)	Citric acid and NaHS. Hydrothermal	Water splitting.	500 W Xe lamp (UV-Vis)	2.19 (direct) 2.34 (linear potential scan)	H_2 production rate of 30,519 μmol h^{-1} g^{-1}	(Gliniak et al., 2017)
SGQD	S: 1.69 (XPS)	1,3,6-trinitropyrene and Na_2S. Hydrothermal.	Photodegradation of basic fuchsin	300 W Xe lamp with <420 nm cut off (Vis)	2.53	Degraded 81% in 2 h.	(Huang et al., 2018)
N and S codoped GO dot	N/C atomic ratio: 12 S/C atomic ratio: 5.4 (XPS)	GO and sulfur calcined under ammonia gas. Oxidation into GO dot and then hydrothermal with ammonia.	Water splitting.	300 W Xe lamp (>420 nm)	1.90 (direct)	H_2 production rate of 20 μmol h^{-1}.	(Nguyen et al., 2018)
P doped Pt-graphene	C/P atomic ratio: 17.16, 13.86, 13.95, 12.73	Pyrolysis of H_2PO_4-modified alginate, followed by photodeposition of Pt from H_2PtCl_6.	Water splitting.	Xe lamp (1.3W/m^2) (UV-Vis)	2.85	H_2 production rate of 282 mmol $g^{-1}h^{-}$	(Latorre‐Sánchez et al., 2013)
N and S codoped graphene aerogel	N: 2.42, 1.73, 2.38, 1.44 S: 1.69, 1.24, 1.49, 1.37 (XPS)	GO and NH_4SCN. Hydrothermal	Photodegradation of AO dye in water	4 units of 11W Xe (>420 nm)	1.42	Degraded 100% in 300 min.	(Jiang et al., 2019)
N and B codoped rGO	N: 7 B: 8 (XPS)	GO, H_3BO_3, and urea. Calcination under Ar gas.	Photodegradation of MB dye in water	160 W light (mono wavelength at 420 nm)	2.04 (direct)	Degraded 25% in 60 min.	(Mokhtar Mohamed et al., 2018)

2.4.2.1 Boron-doped graphene oxide (GO)-based photocatalyst

As shown in Table 2.9, boron (B) with one less valence electron than carbon (C) was widely reported as a suitable p-type and acceptor dopant for GO (Chowdhury et al., 2018). B atoms can be easily doped into GO due to the atomic radii size compatibility of B (85 pm) and C (70 pm) (Ngidi et al., 2020). Numerous studies had reported that B-doping can increase the hole carrier density of GO (Sarkar et al., 2021; Q. Zhang et al., 2020). This means that B dopants can form a shallow acceptor level that accepts electrons from the valence band, therefore forming new hole carriers in the valence band (Chen, 2004; Lin et al., 2011). It was reported that each B dopant contributes ca. 0.5 hole carrier to the GO (Zhao et al., 2013). The increment of charge carrier density is beneficial for photoactivity, as it may retard the recombination of photogenerated electrons and holes (Huang et al., 2020). Furthermore, the B-doping of GO can result in various B bonding. For instance, the BC_3 groups are doped on the basal plane, while the oxygenated boron groups (OBGs) such as the BC_2O and BCO_2 groups are located at the edges or defect sites (Chowdhury et al., 2018; Q. Zhang et al., 2020). Different B-doping concentrations and bonding can result in B-doped GO (BGO) with varying properties and catalytic performances (Cheng et al., 2018; Q. Zhang et al., 2020). For instance, BrGO with a higher content of BC_2O and BCO_2 groups performed better in the electrocatalytic oxidation of acetaminophen (Q. Zhang et al., 2020), while BC_3 groups acted as the active sites of BrGO for nitrogen reduction reaction (Yu et al., 2018).

In the past, many strategies have been developed to fabricate BGO for various applications. Putri et al. fabricated BrGO via pyrolysis (1000 °C, 2 h) for hydrogen evolution reaction (Putri et al., 2017). Singh et al. prepared BrGO by a two steps oven heating (60 °C, 12 h) and vacuum thermal annealing (300 °C, 3 h) method for the photodegradation of dyes (Singh et al., 2018). Chowdhury et al. studied the efficiency of B-doped graphene aerogel prepared via hydrothermal (180 °C, 12 h) for the

photodegradation of acridine orange (AO) dye (Chowdhury et al., 2018). Xing et al. (M. Xing et al., 2014) and Tang et al. (Tang et al., 2015) synthesized BrGO via vacuum thermal heating (300 °C, 3 h) and oil bath heating (100 °C, 96 h), respectively for the photodegradation of Rhodamine B (RhB) dye. Cha et al. developed a flash irradiation method on GO sheet with boric acid (H_3BO_3) to produce BrGO for nitrogen dioxide (NO_2) gas sensing (Cha et al., 2020). Nevertheless, the mass production of BGO photocatalyst with a facile, scalable, and inexpensive process remains a great challenge. In addition, there is a lack of study on the effect of B bonding on the photocatalytic activity of BGO photocatalyst, especially for the removal of VOCs. Figure 2.18 exhibits the common structure of a BGO.

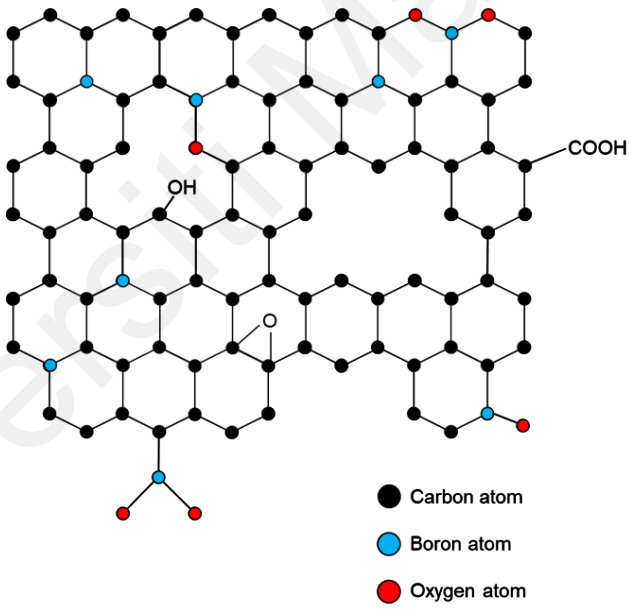

Figure 2.18: Schematic structure of B-doped GO.

2.4.2.2 Nitrogen-doped graphene oxide (GO)-based photocatalyst

The N atoms can be introduced into GO for many photocatalytic applications, owing to the similar atomic radii of N and carbon (C) (Yang et al., 2015). The N-dopants with one valence electron more than C tend to produce shallow donor levels near the conduction band (CB) (Joucken et al., 2015; Yu et al., 2009), therefore transitioning the

conductivity of a GO from p-type to n-type behaviour (Y.-S. Chang et al., 2021; Lu et al., 2013). Notably, an n-type rGO is reported to be more favourable for photocatalysis than its p-type counterpart (Mokhtar Mohamed et al., 2018). This is attributed to the better charge carrier transportation (Mokhtar Mohamed et al., 2018) and electron-donating ability (Bie et al., 2021) of the n-type graphene-based photocatalyst. The N-doping of GO can form three major N-bonding groups, which are the pyridinic-N, pyrrolic-N, and graphitic-N groups (Witjaksono et al., 2021). Many efforts have been made to achieve control over the formation of the N groups in order to tune the charge carrier density and catalytic activity of the N-doped GO (Talukder et al., 2021). For example, pyridinic-N groups acted as the catalytic centre for the electrochemical oxygen reduction reaction (ORR) (T. Xing et al., 2014), pyrrolic-N groups induced high capacitance and good supercapacitor characteristics (Tian et al., 2020), while graphitic-N groups were effective in increasing the free-electron charge carrier density (Guo et al., 2014). It was reported that a large free-electron carrier density can suppress the recombination of photoexcited electron/hole pairs and subsequently enhanced the photocatalytic reaction (Tsai et al., 2020). Since graphitic-N can provide more free-electron carriers than the other N groups (Guo et al., 2014; Scardamaglia et al., 2016), an N-doped GO (NGO) with a higher proportion of graphitic-N groups could demonstrate a better photocatalytic activity (del Pino et al., 2018).

In the past, Putri et al. synthesized NrGO via pyrolysis of GO with urea (600 °C, 2 h) for water splitting (Putri et al., 2017). Yang et al. fabricated NrGO by hydrothermal of GO with sodium hydroxide (NaOH) and hydrazine (100 °C, 12 h) for the photodegradation of RhB dye (Yang et al., 2017). Yeh et al. and Nguyen et al. made N doped graphene quantum dot (NGQD) by calcinating GO with ammonia gas for water splitting (Nguyen et al., 2018; Yeh et al., 2014). To date, the synthesis of NGO

photocatalysts with desired doping concentration and N groups in a cost-effective way is still challenging.

Recently, photoirradiation had emerged as a solution-based method to simultaneously reduce and N-dope GO (Del Pino et al., 2016). In comparison to the thermal N-doping strategies, the photoirradiation method is simpler, faster, and more energy-efficient (Kepić et al., 2017). For example, Kepić et al. conducted N-doping via photoirradiation of GO in ammonia solution with pulsed lasers (Kepić et al., 2017). Del Pino et al. also successfully utilized ammonia (Del Pino et al., 2016) and N-containing ionic liquid (del Pino et al., 2018) solutions under laser irradiation to achieve N-doping of GO. Nevertheless, scaling up the laser photoirradiation N-doping process is still a difficult task. This is because the laser-induced changes were limited to a small area (1 – 64 mm^2) on the surface of GO irradiated with the laser focus at once (del Pino et al., 2018; Del Pino et al., 2016; Guo et al., 2014). Despite the efforts to date, the investigation of N-doped GO photocatalyst and its N configuration for VOCs removal have not been well studied yet. Figure 2.19 exhibits the common structure of an NGO.

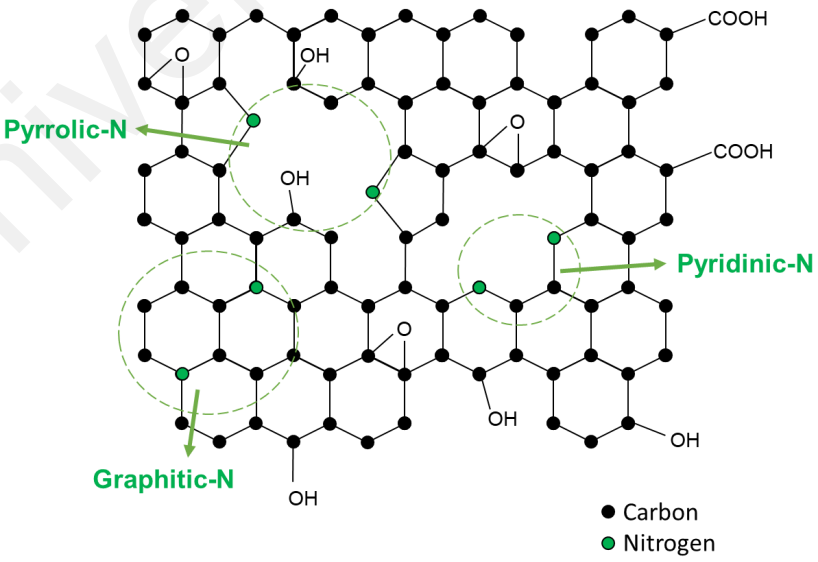

Figure 2.19: Schematic structure of N-doped GO.

2.4.2.3 Other heteroatom-doped graphene oxide (GO) photocatalyst

Besides B and N, a few other dopants of GO have also been studied for photocatalysis. Gliniak et al. and Huang et al. created sulfur (S)-doped graphene quantum dots (SGQD) for water splitting (Gliniak et al., 2017) and basic fuchsin dye degradation (Huang et al., 2018), respectively. Nguyen et al. co-doped GO with N and S atoms for water splitting (Nguyen et al., 2018). Mokhtar et al. synthesized N and B co-doped GO for MB dye degradation (Mokhtar Mohamed et al., 2018). Other than the aforementioned heteroatoms, there are also other potential GO dopants such as the fluorine (F) (Park & Lee, 2016), phosphorus (P) (Zegao Wang et al., 2014), and chlorine (Cl) (Savva et al., 2014) atoms, but their capability for photocatalysis were rarely explored.

2.4.3 Fluorine-doped graphene oxide (GO)

Among the potential heteroatoms, fluorine has the strongest electronegativity and can greatly polarize the carbon (C) atoms on a GO (Kim et al., 2018). The substitutional doping of the F atom into the graphitic lattice of GO is impossible due to the much larger atomic size of F than C (X. Wang et al., 2014). Therefore, the F atom is doped on the surface of GO via the surface-transfer mechanism, where the C-F bonds stick out from the basal plane (X. Wang et al., 2014; Wu et al., 2011). It was calculated that F-doping stretches the nearby C-C bond length from 1.42 Å (Yu et al., 2020) to 1.58 Å (X. Wang et al., 2014; Zbořil et al., 2010), therefore causing significant changes in the structure and properties of the host GO. The F atom acts as a p-type acceptor dopant (Saha et al., 2018) because it is an electron-withdrawing dopant on the surface of the GO (Liu et al., 2011). Wu et al. reported that each F atom of a C-F bond withdraws ca. 0.62 electrons from the attached C atom (Wu et al., 2010). Moreover, it was found that p-type F-doping shifted the fermi level of graphene towards the valence band (VB) (Nguyen et al., 2019) and increased the hole carrier density in the VB of the host semiconductor (Park et al., 2016).

Different fluorination conditions can result in various types of C-F bonds, such as the covalent, semi-ionic, and ionic C-F bonds. The covalent C-F bond is a F atom connected to a sp^3-hybridized C atom, the ionic C-F bond is a F atom joined to a sp^2-hybridized C atom, while the semi-ionic C-F bond is an intermediate state between the covalent and ionic bonds (Feng et al., 2016). Since F is the most electronegative element, it greatly polarizes the carbon (C) atoms of the GO (Kim et al., 2018). In general, the semi-ionic C-F bond has a higher polarity than the covalent and ionic C-F bonds (Y. Chang et al., 2021; Kim et al., 2018; Peera et al., 2015). A highly polarized p-type dopant can greatly increase the hole carrier concentration of the host semiconductor (Simon et al., 2010). Large hole carrier density is beneficial for photocatalysis because it promotes the separation of charge carriers (Huang et al., 2020; Siong et al., 2020). Therefore, the systematic introduction of semi-ionic C-F bond is desirable to enhance the photocatalytic activity of a F-doped GO (FGO).

Several research groups have employed FGO in sensor applications, such as ammonia sensor (Park et al., 2016), heavy-metal sensor (Thiruppathi et al., 2017), caffeic acid sensor (Manikandan et al., 2019), and histamine sensor (Shahzad et al., 2017). Besides sensors, Sim et al. synthesized FGO for supercapacitor (Sim et al., 2022), while Zhang et al. fabricated FGO for electrochemical catalytic oxidation of acetaminophen (Zhang et al., 2022). Nevertheless, there is lack of study on the photocatalytic activity of FGO to date.

In the past, many strategies have been developed to fabricate FGO in harsh conditions. Park and co-workers fabricated FGO semiconductors by pressurizing GO with fluorine gas (F_2) (Park et al., 2016). Thiruppathi et al. synthesized FGO by adding hydrofluoric acid (HF) during the Hummers' process (Thiruppathi et al., 2017). Shahdzad et al. fabricated F-doped rGO (FrGO) via hydrothermal with hexafluorophosphoric acid (Shahzad et al., 2017). Interestingly, Gong et al. reported a UV-assisted photoirradiation

method that successfully F-doped GO, though the usage of toxic HF was still required (Gong et al., 2013). Besides that, trifluoroacetic acid (TFA), which is a less toxic F precursor than the common precursors like HF and F_2 (Fujihara et al., 1998; Sun & Corbett, 2018) was also used to dope GO with a hydrothermal route (Musico et al., 2019). Despite these efforts, there is no report on the preparation of F-doped GO by photoirradiation technique with TFA precursor. Most reported techniques of F-doping GO were complicated, costly, energy-intensive, and possibly polluting due to the high chemical reactivity of the fluorination precursors (T. Jin et al., 2020). Figure 2.20 exhibits the common structure of a FGO.

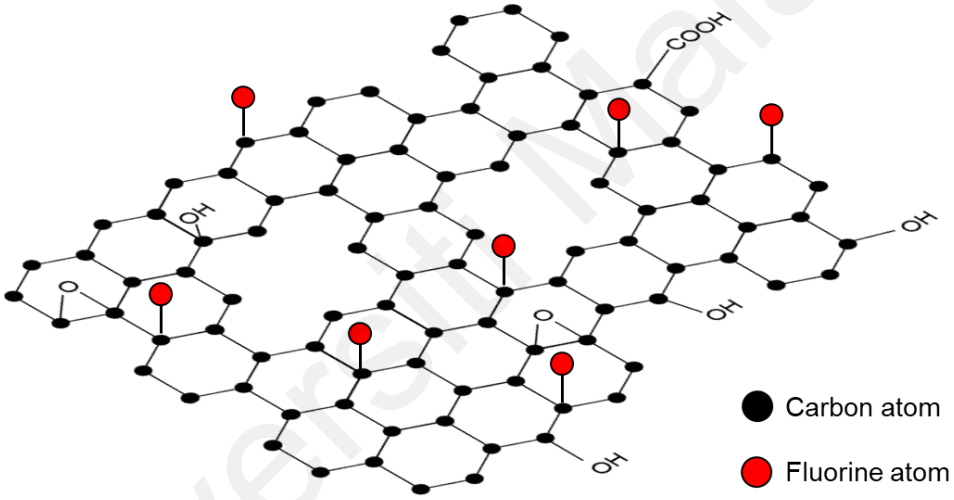

Figure 2.20: Schematic structure of F-doped GO.

2.5 Photoreduced graphene oxide (PRGO)

2.5.1 Undoped PRGO

As mentioned in section 2.4.1, photoreduction is a versatile technique to reduce GO in a controllable manner. Owing to the flexibility of the photoreduction technique, PRGO had performed well in photocatalysis. Besides photocatalysis, PRGO had also been used as sensors (Han et al., 2017; Hasani et al., 2015; He et al., 2017), actuators (Han et al., 2018; Liu et al., 2017), electronic devices (Chen et al., 2018; Chen et al., 2019; Takehira

et al., 2017; Zhao et al., 2018), photocatalyst supports (Fan et al., 2011; Lu et al., 2019; Lv et al., 2019; Mangadlao et al., 2017; Xue & Zou, 2018; Yadav et al., 2019), film membrane (Amadei et al., 2017; Nam et al., 2017; Tu, Utsunomiya, Kokufu, et al., 2017), supercapacitors (S. H. Kang et al., 2018; R. Li et al., 2017; Li et al., 2018), electrocatalysis (Ching et al., 2019; Hu et al., 2017), and pollutant absorbents (Zhang et al., 2019).

It was found that various light sources can be used to photoreduce GO and produce PRGO, such as artificial sunlight (Lu et al., 2019; Wu et al., 2018), sunlight (Han et al., 2017; F. Wang et al., 2017), UV (Hu et al., 2017; Mangadlao et al., 2017), VUV (Tu, Nakamoto, et al., 2017; Tu, Utsunomiya, Ichii, et al., 2017; Tu, Utsunomiya, Kokufu, et al., 2017), camera flash (He et al., 2017; S. H. Kang et al., 2018), and laser (Sokolov et al., 2010). Since a constant light source can produce a constant emission of energy, the control over the light wavelength, light intensity, light distribution, and exposure duration can lead to controllable photoreduction of GO (Tu, Utsunomiya, Kokufu, et al., 2017; Zhang et al., 2014).

The process of GO photoreduction can be carried out in different ambient phases. For instance, in ambient air (Han et al., 2017; He et al., 2017), aqueous phase (Mangadlao et al., 2017; Todorova et al., 2017), organic solvents (Ching et al., 2019; Hasani et al., 2015; Xue & Zou, 2018), and even in vacuum condition (Amadei et al., 2017; Tu, Nakamoto, et al., 2017). As compared to thermal or chemical GO reduction method, the photoreduction method is a green method. Besides that, the photoreduction method shows promising potential to be scaled up in large volume under ambient conditions (Zhang et al., 2014).

2.5.2 Heteroatom-doped PRGO

As mentioned in section 2.4.2, doping GO with heteroatoms is a sensible way to enhance its photocatalytic properties. To date, heteroatom-doping of GO is mostly performed by chemical means at elevated temperatures (Jiang et al., 2020). Hence, the mass production of heteroatom-doped GO in an easy and cost-effective way is still a big challenge. As briefly discussed in section 2.4.2.2, recently, photoinduced-doping has emerged as a technique to simultaneously photoreduce and dope GO (Del Pino et al., 2016). The photoinduced-doping method is carried out by irradiating GO with the presence of a dopant precursor in either solid/gas or solid/liquid phase (Kepić et al., 2017). In comparison to the traditional chemical-doping strategies, the photoinduced-doping method is simpler, faster, and more energy-efficient (Kepić et al., 2017). Furthermore, during the photoinduced-doping process, the reduction and doping level of GO can be controlled via the variation of irradiation time (Savva et al., 2014). Table 2.10 summarizes the recent studies of heteroatom-doped PRGO.

As shown in Table 2.10, the photoinduced heteroatom-doping of GO can be carried out by using many different light sources such as mercury lamp (Li et al., 2015b), xenon flash lamp (Cha et al., 2020), UV (Imamura & Saiki, 2013), and lasers (Kepić et al., 2017). For instance, Li et al. and Liu et al. synthesized N-doped PRGO (NPRGO) by irradiating GO with a mercury lamp (UV light) under NH_3 gas atmosphere (Li et al., 2015a, 2015b; F. Liu et al., 2013). Meanwhile, Guo et al. simultaneously photoreduced and N-doped GO by irradiating GO with an 800 nm femtosecond pulse laser under nitrogen gas (N_2) atmosphere (Guo et al., 2014). Kepić et al. doped GO with N atoms by irradiating GO/NH_3 solution with several laser sources. It was found that lasers with different energy resulted in different N-doping concentrations. For instance, a UV (266 nm) laser was able to dope more N atoms than a green laser (532 nm) and infrared laser (1064 nm) because UV laser emitted a higher amount of energy (Kepić et al., 2017).

Imamura et al. discovered that under the irradiation of UV light, ammonia precursor decomposed into nitrogen-containing radicals and subsequently reacted with graphene to achieve N-doping (Imamura & Saiki, 2013). The same group later found that photoinduced-doping of N atoms could increase the free-electron carrier density of graphene since the N atoms were donor dopants (Imamura & Saiki, 2015).

Angel Pérez del Pino et al. compared the photoinduced-N-doping of GO under ammonia gas atmosphere and in liquid ammonia solution. It was determined that GO irradiated under ammonia gas was significantly photoreduced but only a small amount of N atoms (1.5 at%) were doped. Conversely, GO irradiated in ammonia solution exhibited a lower reduction degree but a higher amount of N dopants (6.4 at%). The study suggested that photoinduced-doping in a solid/liquid phase is able to achieve a higher doping concentration than a in solid/gas phase (Del Pino et al., 2016). Besides that, the same research group found that nitrogen-containing ionic liquids can also be used as N-precursors to achieve photoinduced-N-doping of GO. Interestingly, the NPRGO showed remarkably higher photoactivity in water splitting than that of pure GO (del Pino et al., 2018).

Other than NPRGO, other studies have also successfully doped B (Cha et al., 2020), F (Lee et al., 2012), and Cl (Savva et al., 2014) atoms via the photoirradiation-doping method. Cha et al. synthesized B-doped PRGO (BPRGO) by irradiating GO film with H_3BO_3 under a xenon flash lamp. The BPRGO displayed better NO_2 gas sensing than undoped PRGO and pristine GO (Cha et al., 2020). Besides that, Lee et al. achieved F-doping on graphene by using a laser photoirradiation-doping method. It was found that the laser energy decomposed the F-containing precursor and produced F radicals. These F radicals then reacted with the sp^2 domain of graphene to form sp^3 C-F bonds (Lee et al., 2012). Gong et al. reported a photoirradiation-F-doping method of GO at room temperature by using HF as the precursor (Gong et al., 2013). Despite the conveniences,

scalability, and effectiveness of the photoirradiation-doping method, the application of heteroatom-doped PRGO in photocatalysis is not well studied and understood yet.

Table 2.10: Recent studies of heteroatom-doped PRGO

Material. Doping density (at%)	**Starting material and precursor**	**Light source, duration**	**Photoirradiation phase and method**	**Application**	**Ref.**
NPRGO (N: 13.92)	GO and NH_3 gas	500 W Hg lamp, 10 min	Solid/gas. UV-Vis irradiation of GO under NH_3 atmosphere.	Enhance conductivity	(Li et al., 2015b)
NPRGO (N: 12.75)	GO and NH_3 gas	500 W Hg lamp, 60 min	Solid/gas. UV-Vis irradiation of GO under NH_3 atmosphere.	Fabrication of n-type transistor	(Li et al., 2015a)
NPRGO (N: 13.62)	GO and NH_3 gas	500 W Hg lamp, 10 min	Solid/gas. UV-Vis irradiation of GO under NH_3 atmosphere.	PL enhancement	(F. Liu et al., 2013)
NPRGO (N: 4.9, 3.3, 2.4)	GO and NH_3 solution	266, 532, 1064 nm lasers	Solid/liquid. Laser irradiation of GO/NH_3 solutions.	-	(Kepić et al., 2017)
NPRGO membrane (N: 1.5)	GO and N_2/NH_3 gas	266 nm pulse laser	Solid/gas. Laser irradiation of GO membrane under N_2/NH_3 atmosphere.	Create free-standing NrGO membrane	(Del Pino et al., 2016)
NPRGO membrane (N: 6.4)	GO and NH_3 solution	266 nm pulse laser	Solid/liquid. Laser irradiation on GO membrane/NH_3 solutions.	Create free-standing NrGO membrane	(Del Pino et al., 2016)
NPRGO (N: 5)	GO and nitrogen-containing ionic liquids	266 nm pulse laser	Solid/liquid. Laser irradiation of GO/precursor solutions.	Water splitting	(del Pino et al., 2018)
NPRGO (N: 10.3)	GO and N_2 gas	800 nm pulse femtosecond laser	Solid/gas. Laser irradiation of GO under N_2 atmosphere.	Fabrication of n-type transistor	(Guo et al., 2014)
N-doped graphene (N-graphene) (N: 24)	Graphene and NH_3 gas	30 W UV (150 & 200 nm), 2 h	Solid/gas. UV irradiation of graphene under NH_3 atmosphere.	-	(Imamura & Saiki, 2013)
N-graphene	Graphene and N_2 gas	400 nm laser pulse, 8h	Solid/gas. Laser irradiation on graphene under N_2 atmosphere.	Tune the p- and n- type conductivity	(H. I. Wang et al., 2017)
N-graphene	Graphene and NH_3 gas	30 W UV (150 & 200 nm), 3 h	Solid/gas. UV irradiation of graphene under NH_3 atmosphere.	Increase free electron charge carrier density	(Imamura & Saiki, 2015)

Table 2.10, continued

Material. Doping density (at%)	**Starting material and precursor**	**Light source, duration**	**Photoirradiation phase and method**	**Application**	**Ref.**
BPRGO (B: 3.6)	GO and boric acid	Xenon flash (300 -1000 nm), <10 ms	Solid/gas. Flash irradiation of GO adsorbed with boric acid under ambient air.	NO_2 gas sensor	(Cha et al., 2020)
F-doped graphene	Graphene and fluoropolymer	488 nm laser	Solid/solid. Laser irradiation of graphene placed on fluoropolymer.	Graphene fluorination patterning	(Lee et al., 2012)
F-doped rGO	GO and hydrofluoric acid (HF)	150 W Mercury lamp (UV), 46 h	Solid/liquid. UV irradiation of GO/HF solutions.	Develop new method to F-dope GO	(Gong et al., 2013)
Cl-doped rGO (Cl: 11.3)	GO and Cl_2 gas	248 nm pulse laser	Solid/gas. Laser irradiation of graphene under Cl_2 atmosphere.	Fabrication of field effect transistor	(Savva et al., 2014)

In summary, this chapter reviews the potential of metal-free graphene-based material in photocatalytic applications. Meanwhile, heteroatom-doping is an effective method in boosting the photocatalytic activity of undoped GO. Nevertheless, there is a lack of study of graphene-based photocatalyst for the removal of VOCs. Therefore, it is important to explore the capability of graphene-based photocatalyst for removal of VOCs.

CHAPTER 3: METHODOLOGY

In this chapter, the methodology of this thesis is categorized into four sections. An overview of the procedure flowchart is shown in Figure 3.1. The materials and chemicals used in this work were listed in Section 3.1. Section 3.2 provides the steps to synthesize the photocatalysts. Section 3.3 discusses the photocatalyst characterization techniques used in this work. Lastly, Section 3.4 shows the procedures of conducting experiments in the photoreactor.

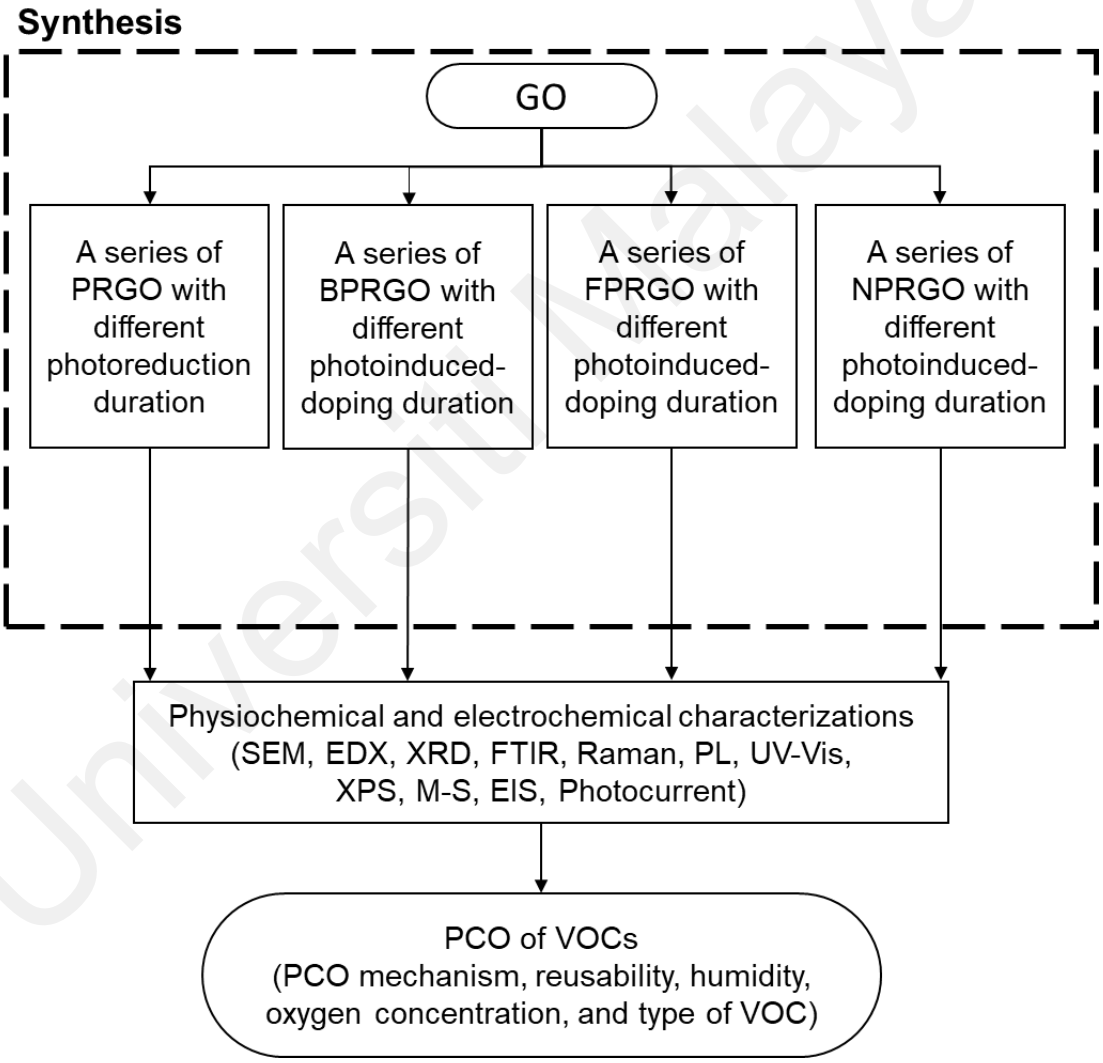

Figure 3.1: Overview of the research methodology.

3.1 Materials

Natural Graphite flake (100 mesh size) was purchased from XFNANO Ltd. All chemicals used in this work were reagent grade. Sulphuric acid, H_2SO_4 (95-97%), phosphoric acid, H_3PO_4 (85%), potassium permanganate, $KMnO_4$ (>99%), hydrogen peroxide, H_2O_2 (30%), hydrochloric acid, HCl (37%), isopropanol, IPA (>99.5%), sodium sulphate, Na_2SO4 (>99%), ammonia solution (25%), ethanol (96%), H_3BO_3 (>99.5%), and TFA (99%) were all purchased from Sigma-Aldrich. The polyester fabrics were purchased from Selladurai Textile Ltd.

3.2 Synthesis of photocatalysts

3.2.1 Synthesis of GO

The synthesis process of GO was modified from the Tour's method (Marcano et al., 2010). Firstly, 3 g of graphite flakes were dispersed in a mixture of 300 ml H_2SO_4 and H_3PO_4 (9:1 volume ratio) under constant stirring. Then, 18 g of $KMnO_4$ was added slowly into the suspension and was heated to 50°C for 12 hours before being transferred into an ice bath for reaction stopping. To stop the reaction, 50 ml of deionized (DI) water was dripped dropwise into the suspension, followed by pouring in 250 ml of DI water quickly. Then, 6 ml of H_2O_2 was added dropwise into the suspension, and the colour changed from purplish-brown into yellowish-brown, indicating the endpoint. The suspension was washed with 1 M HCl and DI water alternately via centrifugation until reaching pH 3-4. The GO was dispersed in DI water for storage after the washing process**.** The schematic procedure is shown in Figure 3.2.

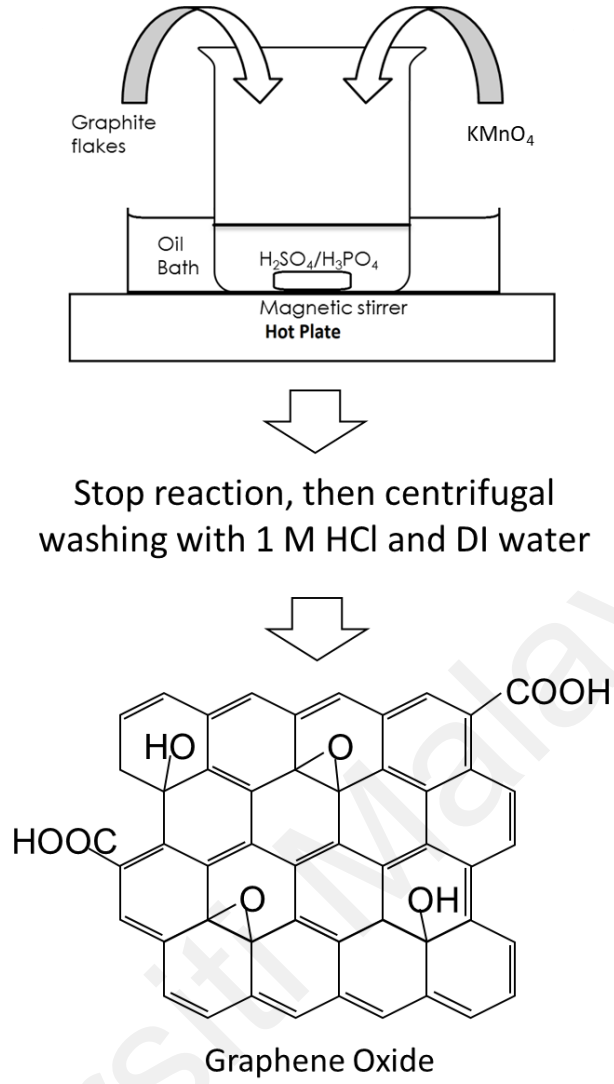

Figure 3.2: Synthesis of GO.

3.2.2 Synthesis of PRGO with different photoreduction duration

GO suspension was coated onto a 12 × 10 cm polyester fabric by repeatedly drop-casting and drying. The weight of the deposited GO was ~30 mg each. The deposited GO fabric was then irradiated with a light source of 4 W UV-A (λ_{peak} = 365 nm, I = 0.6 mW/cm^2) for a specific time to undergo photoreduction. The as-prepared PRGO samples are denoted as PRGO-x, where x represents the UV-A irradiation time of 2, 4, 6, 8, and 10 hours. The procedure of 3.2.2 is shown in Figure 3.3.

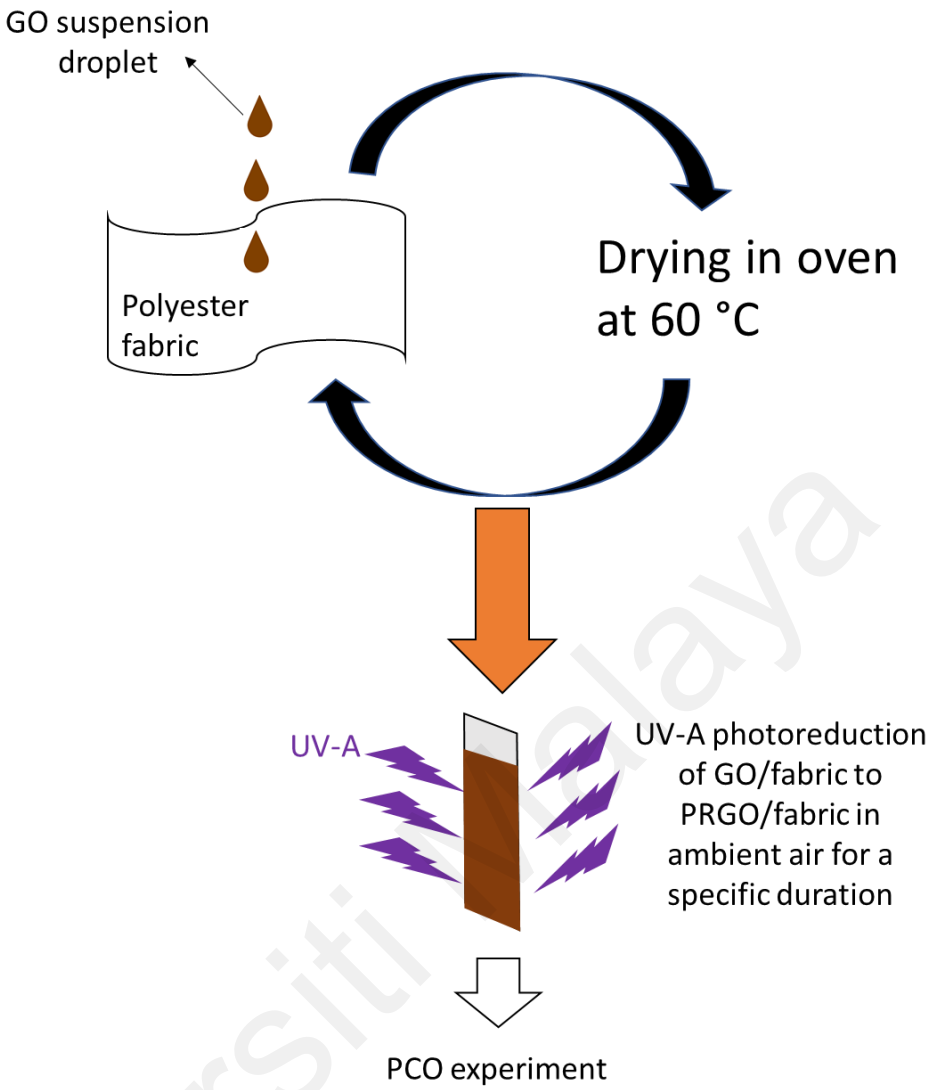

Figure 3.3: Synthesis of PRGO with different photoreduction duration.

3.2.3 Synthesis of BPRGO with different photoinduced doping duration

GO (0.5 mg/ml) was dispersed in a suspension of DI water and IPA (1:1 volume ratio) with 0.6 M of boric acid. The as-prepared suspension was constantly stirred and irradiated under a light source of 20 W UV-C (λ_{peak} = 253 nm, I = 2.4 mW/cm^2) for a specific time to undergo simultaneous doping and photoreduction. Appendix A shows the light spectrum of the UV-C light source. After photoirradiation, the suspensions were repeatedly washed by DI water (4 times) via centrifuge to remove unreacted boric acid. The samples were dispersed in DI water after the washing process**.** The as-prepared samples are denoted as BPRGO-x, where x represents the photoinduced doping time of

0.5, 1, 2, and 4 h. Then, the BPRGO suspensions were each coated on a 12 × 10 cm polyester fabric by repeatedly drop-casting and drying. The weight of the deposited BPRGO was ~30 mg each. The procedure of 3.2.3 is shown in Figure 3.4. Control experiments conducted to determine the ideal weight of photocatalyst deposited and concentration of boric acid are shown in Appendix D and E, respectively.

3.2.4 Synthesis of FPRGO with different photoinduced doping duration

GO (0.5 mg/ml) was dispersed in a suspension of DI water and IPA (1:1 volume ratio) with 0.1 M of TFA. The as-prepared suspension was constantly stirred and irradiated under a light source of 20 W UV-C (λ_{peak} = 253 nm, I = 2.4 mW/cm^2) for a specific time to undergo simultaneous doping and photoreduction. After photoirradiation, the suspensions were repeatedly washed by DI water (4 times until pH 4 - 5) via centrifuge to remove unreacted TFA. The samples were dispersed in DI water after the washing process**.** The as-prepared samples are denoted as FPRGO-y, where y represents the photoinduced doping time of 0.25, 0.5, 1, and 2 h. Then, the FPRGO suspensions were each coated on a 12 × 10 cm polyester fabric by repeatedly drop-casting and drying. The weight of the deposited FPRGO was ~30 mg each. The procedure of 3.2.4 is shown in Figure 3.4. Control experiments conducted to determine the ideal concentration of TFA is shown in Appendix G.

3.2.5 Synthesis of NPRGO with different photoinduced doping duration

GO (0.5 mg/ml) was dispersed in a suspension of DI water and IPA (1:1 volume ratio) with 1.0 M of ammonia. The as-prepared suspension was constantly stirred and irradiated under a light source of 20 W UV-C (λ_{peak} = 253 nm, I = 2.4 mW/cm^2) for a specific time to undergo simultaneous doping and photoreduction. After photoirradiation, the

suspensions were repeatedly washed by DI water (4 times until pH 4 - 5) via centrifuge to remove unreacted ammonia. The samples were dispersed in DI water after the washing process**.** The as-prepared samples are denoted as NPRGO-z where z represents the photoinduced doping time of 0.25, 0.5, 1, and 2 h. For comparison, GO (0.5 mg/ml) was also irradiated by the 20 W UV-C in a water/IPA suspension without ammonia. Then, the photocatalyst suspensions were each coated on a 12 × 10 cm polyester fabric by repeatedly drop-casting and drying. The weight of the deposited coated photocatalyst was ~30 mg each. The procedure of 3.2.5 is shown in Figure 3.4. Control experiments conducted to determine the ideal concentration of ammonia is shown in Appendix I.

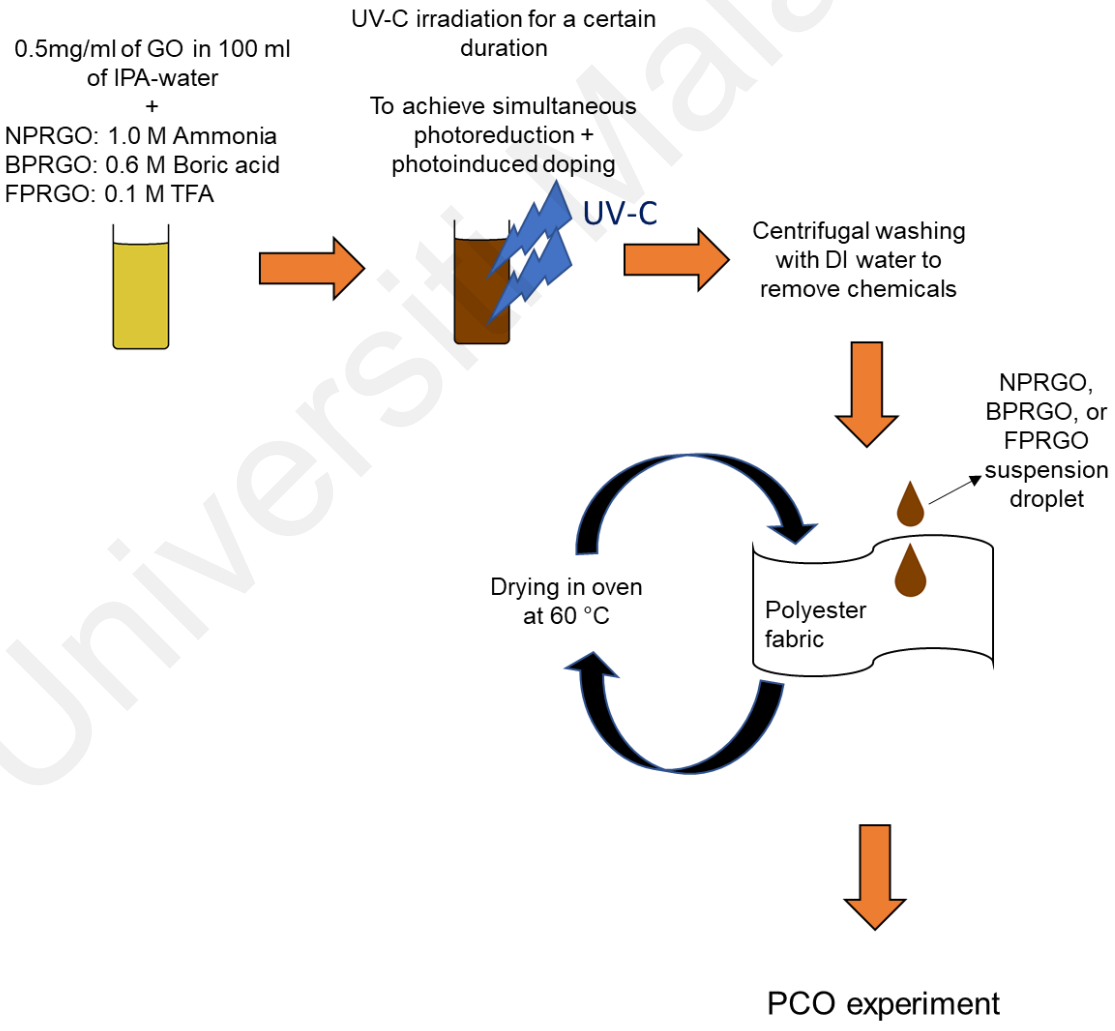

Figure 3.4: Synthesis of NPRGO, BPRGO, and FPRGO with different photoirradiation doping duration.

3.3 Characterization techniques

3.3.1 Scanning Electron Microscopy (SEM)

A Scanning electron microscope (SEM) was used to visualise the morphology of the sample with a magnified image. In contrast to an optical microscope, the SEM utilizes electrons as the imaging source instead of light. As shown in Figure 3.5, SEM was equipped with a high-energy electron source that beams electrons. To ensure good quality images, the SEM column was operated under vacuum condition to prevent contaminations, vibrations, and background noises. The emitted electrons were attracted and accelerated by the positively-charge anode to the desired accelerating voltage (kV). Since electrons are sensitive to magnetic fields, two electromagnetic lenses (condenser and objective lens) with modulating currents were used to control the pathway of the electrons. The electrons were then directed onto the sample and generated reflected electrons. Finally, detectors were used to collect the reflected electron signals to generate the image of the sample (Nanakoudis, 2019).

In this study, a FEI Quanta FEG 450 Field Emission Scanning Electron Microscope unit was used to capture the images of the synthesized samples. To prepare the samples for SEM characterisation, the samples were firstly dispersed in IPA, assisted by 30 min of ultrasonic bath sonication. A few drops of the suspension were dropped onto an aluminium sheet (1 cm × 1 cm) and allowed to dry in an oven (60 °C) before imaging.

This study also imaged the samples with AFM technique as shown in Appendix B.

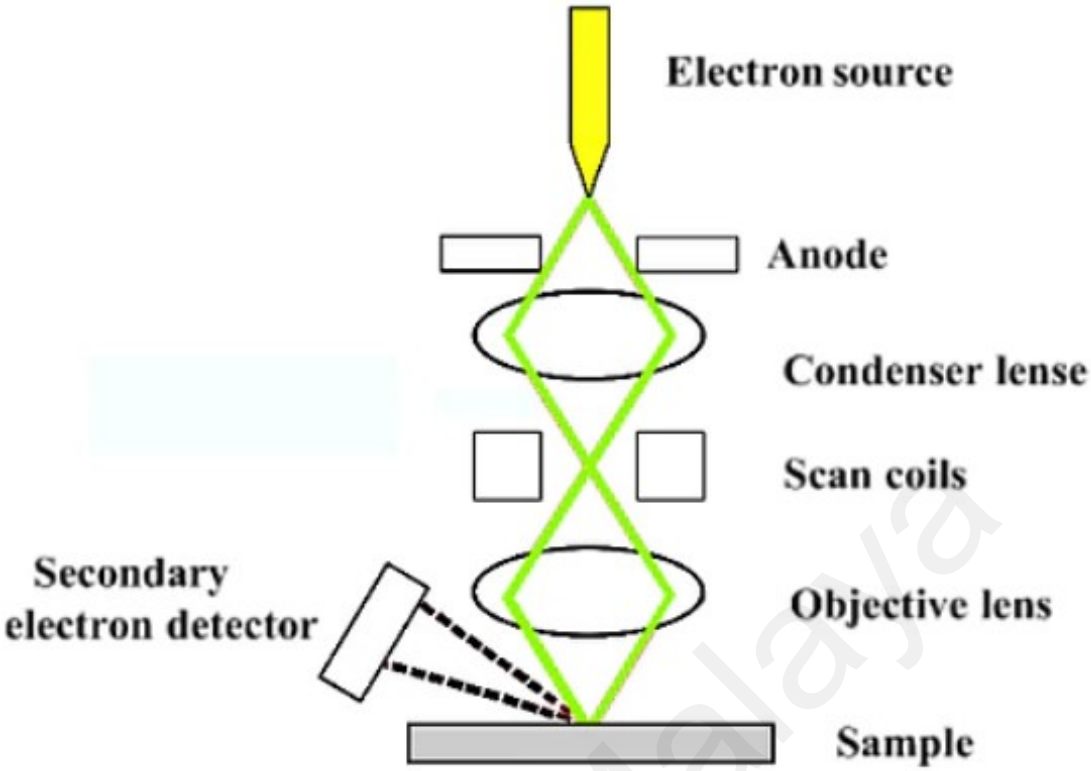

Figure 3.5: Basic working principle of a SEM.
(Nanakoudis, 2019)

3.3.2 Energy-dispersive X-ray spectroscopy (EDX)

An Energy dispersive X-ray (EDX) coupled to the SEM instrument was used to analyse and image the elemental composition/distribution of a sample. The sample preparation method for EDX was the same as SEM.

During EDX analysis, electrons were beamed on the surface of the sample to produce X-ray emissions. A detector was used to identify the energy of the emitted X-rays, and then to interpret the detected elements. The elemental composition/mapping was determined by using an EDX software (Colpan et al., 2018). A schematic diagram illustrating the EDX spectroscopy is shown in Figure 3.6.

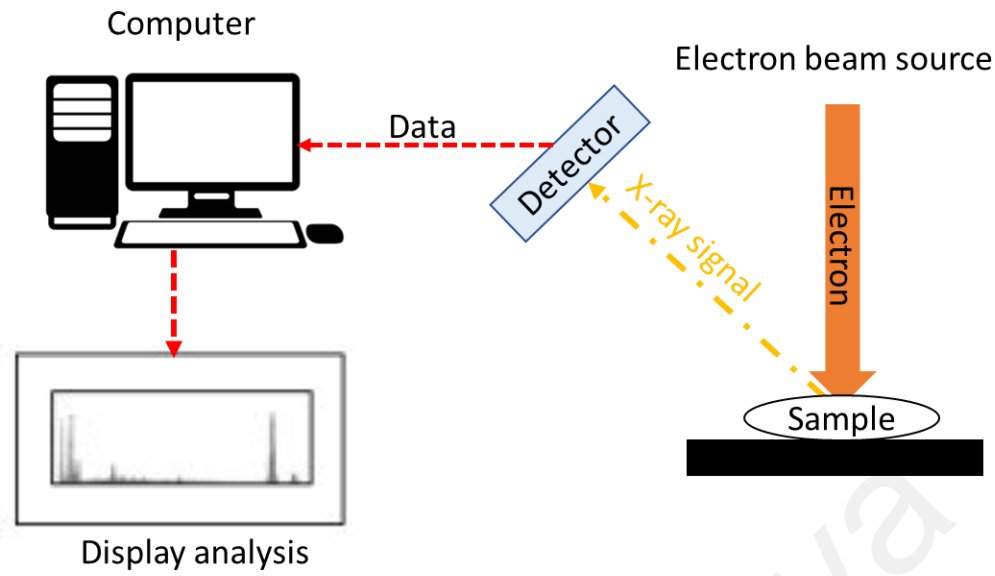

Figure 3.6: Basic working principle of an EDX.
Adapted from (Colpan et al., 2018)

3.3.3 X-ray diffraction (XRD)

XRD was used to analyse the crystallinity and crystal phases of the samples. XRD was conducted by a PANalytical Empyrean XRD at 45 kV and 40 mA with CuKα radiation (λ = 1.5406 Å). The diffraction angle (2θ) was between 5° to 80°, with a scan rate of 0.1 $°s^{-1}$. To prepare the samples for XRD scans, the samples were firstly dispersed uniformly in IPA, assisted by ultrasonic bath sonication. A few drops of the suspension were dropped onto an aluminium sheet (2 cm × 2 cm) and allowed to dry in an oven (60 °C).

The XRD contained three basic components, which were the X-ray source, a sample stage, and a detector. During analysis, the sample was gradually rotated while being bombarded with X-rays to produce diffraction patterns. The emitted X-rays struck the sample on the sample stage at a range of angle θ, while the detector detected the diffracted X-rays at a range of angle 2θ from the source. The diffraction patterns were indexed to obtain the phase information, structural properties, and "fingerprint" of the sample

(Bishnoi et al., 2017). Figure 3.7 demonstrates the basic components and working principles of the XRD.

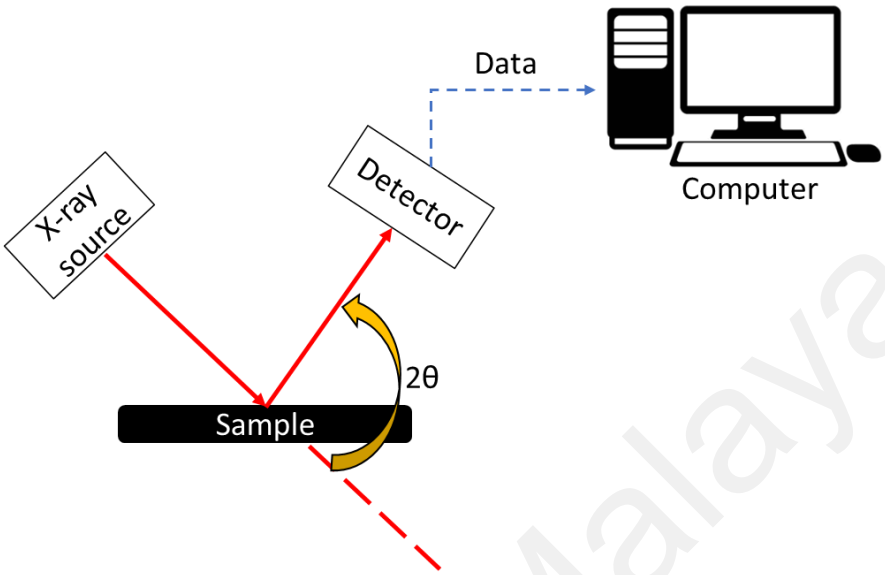

Figure 3.7: Basic working principle of an XRD.
Adapted from (Bishnoi et al., 2017)

3.3.4 Fourier-transform infrared spectroscopy (FTIR)

FTIR was used to determine the functional groups on the samples based on the characteristic absorptions of infrared radiation. A PerkinElmer FTIR-Spectrum 400 spectrometer was used to obtain the FTIR spectrum for frequency between 800 to 4000 cm^{-1}. The samples were dried and ground into fine powders, then mixed with some potassium bromide (KBr) powder. The mixtures were then pressed into thin pellets by a hydraulic press.

A FTIR generally consisted of an infrared source, beam splitter, sample compartment, moving mirror, fixed mirror, and detector. During analysis, the infrared source was split to pass through the sample pellet and the reference chamber for analytical comparison. The emitted infrared then reached the detector and generated electrical signals as responses (Titus et al., 2019). Figure 3.8 demonstrates the basic components and working principle of the FTIR.

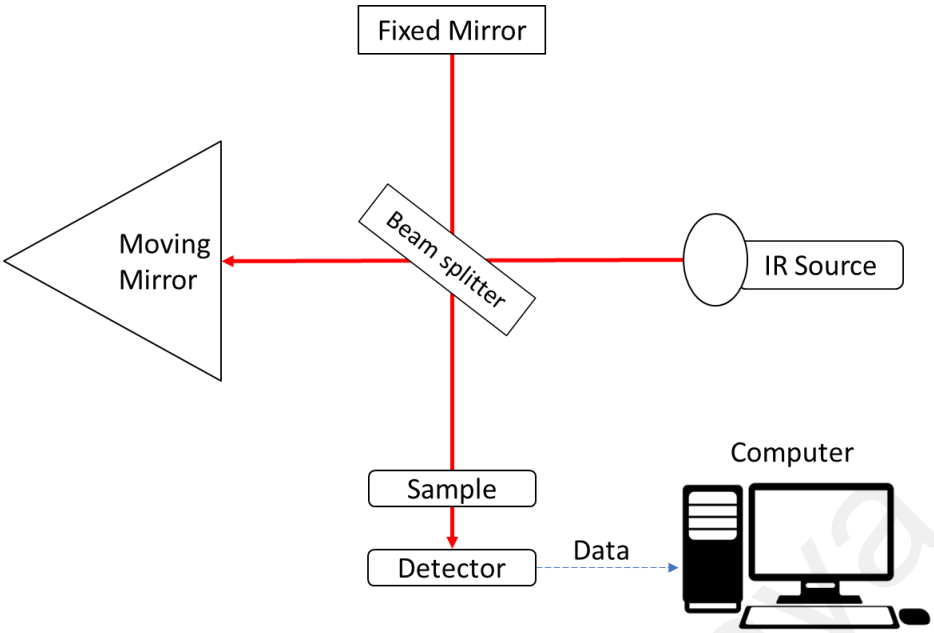

Figure 3.8: Basic working principle of a FTIR.
Adapted from (Titus et al., 2019)

3.3.5 Raman spectroscopy

Raman was carried out to investigate the graphitic structures and defects of graphitic carbon materials. It can also be used to identify the phases of some samples. The Raman spectra were analysed on a Renishaw inVia using a 514 nm laser. The scan range was between 1000 – 3200 cm^{-1}. To prepare the samples for Raman scans, the samples were firstly dispersed uniformly in IPA, assisted by ultrasonic bath sonication. A few drops of the suspension were dropped onto an aluminium sheet (1 cm × 2 cm) and allowed to dry in an oven (60 °C).

During analysis, the sample was irradiated with a monochromatic laser beam. The laser was scattered in all directions after the interaction with the sample molecules. Much of the scattered light had the frequency same as the incident radiation (Rayleigh scattering), while some scattered light had a different frequency from the incident light (Raman scattering). A notch filter was used to separate the Raman scattered lights from the Rayleigh scattered lights. Finally, the Raman scattered lights were detected by a detector

and plotted as a spectrum (Bumbrah & Sharma, 2016; Thirumalainambi et al., 2005). Figure 3.9 shows the basic component and working principle of a Raman spectroscopy.

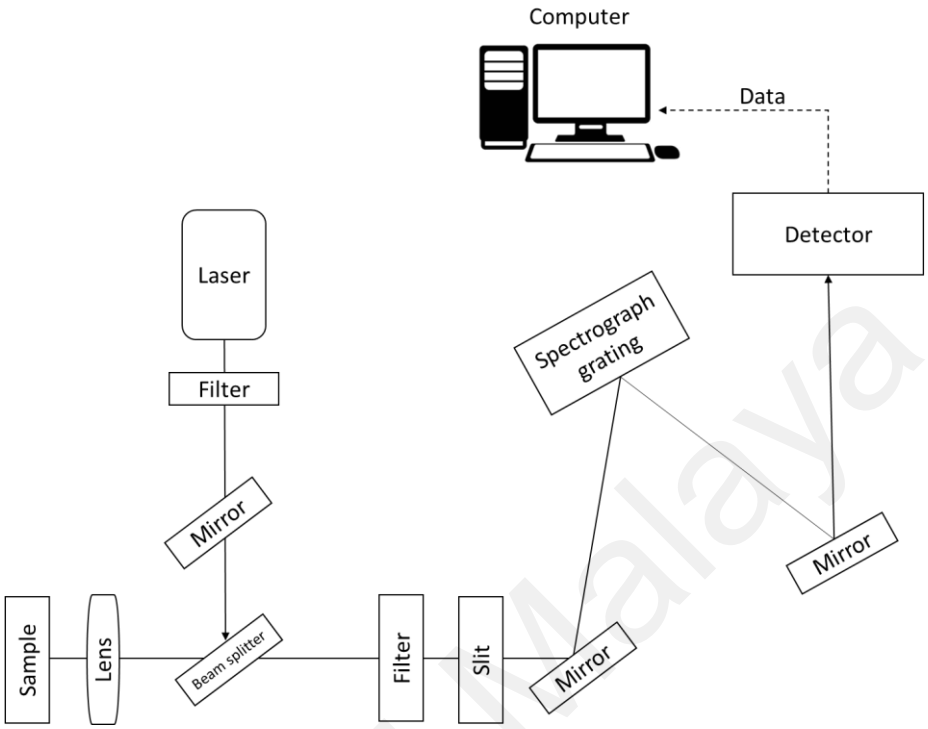

Figure 3.9: Basic working principle of a Raman spectroscopy. Adapted from (Thirumalainambi et al., 2005)

3.3.6 Photoluminescence (PL)

PL analysis was used to evaluate the rate of recombination rate of photoexcited electrons and holes. A Renishaw inVia with an excitation wavelength of 325 nm laser was used. The scan range was between 400 to 950 nm. The instrumentation components (Figure 3.9) and the sample preparation of the PL scan were similar to that of Raman with the addition of a fluorescent detector. During analysis, the laser source elevated the energy of the electrons on the samples. When the excited electron was returned to its original energy state, a photoluminescence signal was emitted and detected by the detector.

3.3.7 UV-Vis spectroscopy

UV-Vis absorption spectroscopy was used to measure the light absorption properties of the samples. UV-Vis tests were carried out by a Perkin Elmer Lambda 35 UV-Vis spectrophotometer, for wavelengths between 200 to 800 nm. The samples were prepared by dispersion in DI water. The main components of the UV-Vis spectrophotometer are light sources, a monochromator, sample compartments, and a detector (Figure 3.10). After the light source passed through the monochromator, it was split into two beams to the reference cuvette and the sample cuvette. Then, the detectors measured the transmitted light and processed the data to generate a spectrum (Rocha et al., 2018).

The optical band gaps of the samples were determined via the Tauc plot, according to Equation 3.1:

$$(\alpha h\upsilon)^{\frac{1}{n}} = \beta(h\upsilon - E_g) \quad 3.1$$

Where α is the absorption coefficient of the sample, h is the Planck's constant (6.626×10^{-34}J.s), υ is the frequency (s^{-1}), β is the band tailing parameter constant, E_g is the energy of the optical band gap (eV), and n is the power factor of the transition mode (n = ½ for direct transition). The bandgap was estimated from the x-axis interception point of the linear portion of the $(\alpha h\upsilon)^{\frac{1}{n}}$ versus hυ Tauc plot.

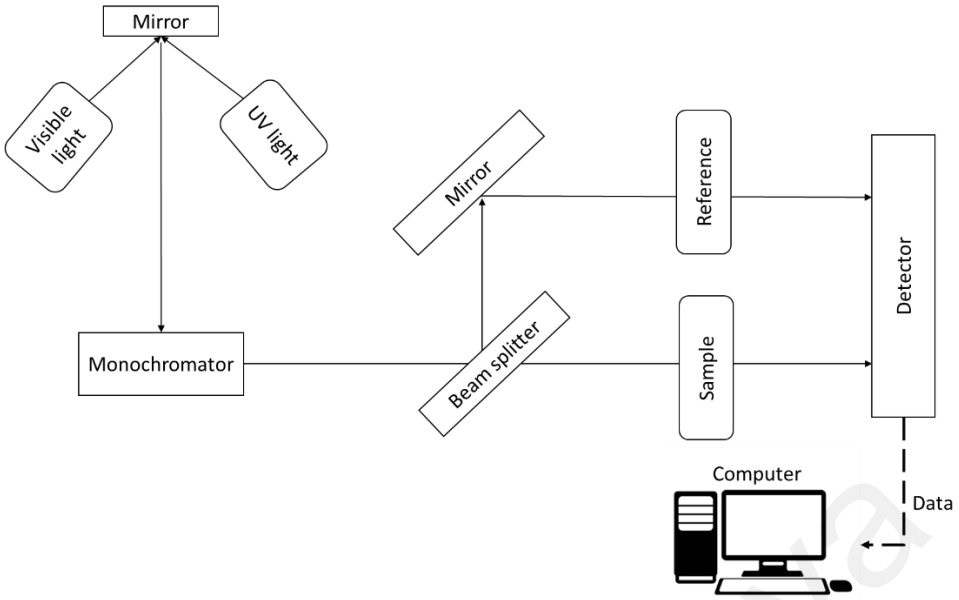

Figure 3.10: Basic working principle of a UV-Vis absorbance spectroscopy. Adapted from (Rocha et al., 2018)

3.3.8 X-ray photoelectron spectroscopy (XPS)

XPS was used to determine the surface chemical composition and bonding states of the elements in the samples. The XPS instrument used was a JEOL JPS-9030 equipped with a MgKα (1253.6 eV) X-ray source. The sample preparation method was similar to that of the SEM samples. As shown in Figure 3.11, an XPS instrument has three main components, which are the X-ray source, the electron energy analyser, and the sample compartment. During analysis, the photon energy of the X-ray source was absorbed by the electrons of the sample. Then, these photoelectrons (electrons that absorbed photon energy) were ejected with a certain level of kinetic energy (KE). An electron analyser measured the KE of the photoelectrons and converted the measurement to binding energy (BE). A computer then produced a spectrum based on the data. The XPS measurements were conducted under an ultra-high vacuum condition to avoid contamination (Greczynski & Hultman, 2020). The reference of the BE position was the C1s (284.5 eV) peak for all scans in this study.

For example, if a sample has C, O, and B atoms, the atomic fractions of each of the elements can be calculated with Equation 3.2:

$$C\ atomic\ fraction = \frac{\frac{A_{C\ 1s}}{C_{rsf}}}{\frac{A_{O\ 1s}}{O_{rsf}} + \frac{A_{C\ 1s}}{C_{rsf}} + \frac{A_{B\ 1s}}{B_{rsf}}}$$

$$O\ atomic\ fraction = \frac{\frac{A_{O\ 1s}}{O_{rsf}}}{\frac{A_{O\ 1s}}{O_{rsf}} + \frac{A_{C\ 1s}}{C_{rsf}} + \frac{A_{B\ 1s}}{B_{rsf}}} \quad (3.2)$$

$$B\ atomic\ fraction = \frac{\frac{A_{B\ 1s}}{C_{rsf}}}{\frac{A_{O\ 1s}}{O_{rsf}} + \frac{A_{C\ 1s}}{C_{rsf}} + \frac{A_{B\ 1s}}{B_{rsf}}}$$

Where $A_{C\ 1s}$, $A_{O\ 1s}$, and $A_{B\ 1s}$ are the integrated areas of the C 1s, O 1s, and B 1s peaks respectively. While the C_{rsf}, O_{rsf}, and B_{rsf} are the relative sensitive factor (rsf) of the C 1s, O 1s, and B 1s, respectively.

The ratio of the oxygenated carbon groups (OCGs) in a C 1s was calculated by Equation 3.3:

$$OCGs/C = \frac{A_{C-O} + A_{C=O} + A_{O=C-O}}{A_{C\ 1s}} \quad (3.3)$$

where A_{C-O}, $A_{c=O}$, and $A_{O=C-O}$ were the areas for the peaks ascribed to the C-O, C=O, and O=C-O bonds, respectively in C 1s.

Meanwhile, the ratio of oxygenated boron groups (OBGs) in the B 1s of a BPRGO was determined by Equation 3.4:

$$OBGs/B = \frac{A_{BCO_2} + A_{BC_2O}}{A_{B\ 1s}} \quad (3.4)$$

where $A_{BCO_2}$and A_{BC_2O} were the peak areas for BCO_2 and BC_2O, respectively in B 1s.

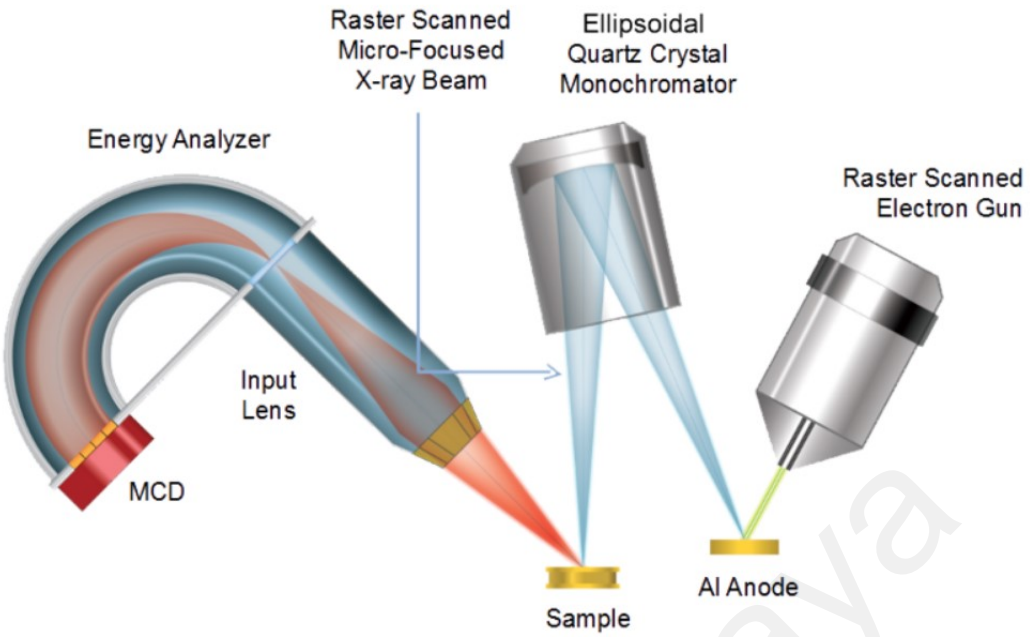

Figure 3.11: Basic working principle of a XPS spectroscopy.
(Physical Electronics, 2022)

3.3.9 Electrochemical measurements

Electrochemical measurements were carried out by a Metrohm Autolab (PGSTAT302N) potentiometer in a three-electrode setup (Figure 3.12a). The electrochemical measurements conducted for this study were transient photocurrent, electrochemical impedance spectroscopy (EIS), and Mott-Schottky (M-S). The reference electrode was Ag/AgCl, while the counter electrode was platinum (Pt). Fluorine-doped tin oxide (FTO) glass slides (active area of 1 cm × 1 cm) were used as the substrates of the working electrode. The samples were coated on the FTO glass via a doctor-blade coating method, where glass rod and scotch tape were used as the frame and spacer, respectively (Figure 3.12b). For sample preparation, the sample was firstly dispersed in ethanol, then the dispersion was drop-casted onto the FTO glass slide. A glass rod was used to roll out any excess sample, while scotch tapes were used to shape the droplet into the desired size. The coated FTO glass slides were dried in an oven at 60°C overnight. In all analyses, an aqueous solution of 0.5 M Na_2SO_4 (pH 6.5) was used as the electrolyte.

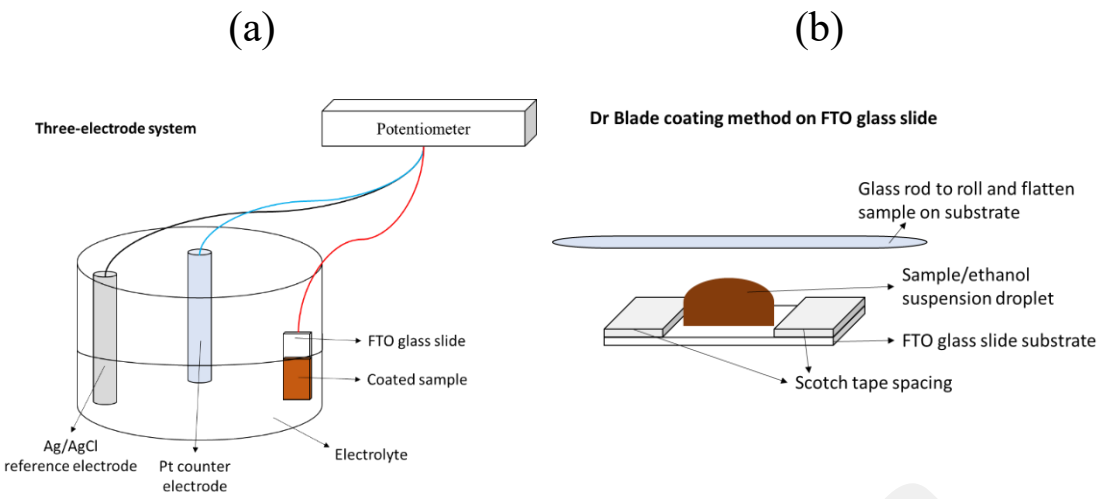

Figure 3.12: (a) Three-electrode system setup. (b) Doctor Blade coating method.

3.3.9.1 Photocurrent

The transient photocurrent was conducted to measure the photocurrent density and stability of the samples upon light illumination. The samples were coated on FTO glass slides, and the three-electrode setup was used. The light source used was a 150 W Xenon lamp (ZOLIX GLORIA-X150A) at 0.3 V bias. The interval for light on and off was 10 s. The setup of the photocurrent experiment is shown in Figure 3.13.

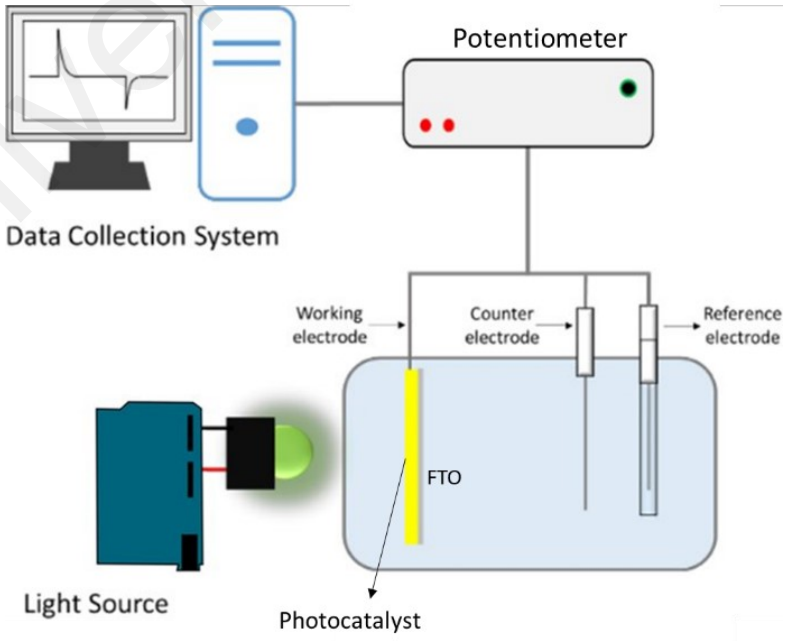

Figure 3.13: Setup for transient photocurrent measurement.

3.3.9.2 Electrochemical Impedance Spectroscopy (EIS)

EIS was measured to determine the resistance of charge carrier transportation in the samples. The Nyquist plots were plotted from the EIS results. The samples were coated on FTO glass slides, and the three-electrode setup was used (Figure 3.12a). The setting of AC amplitude was 5 mV, at the frequency range between 0.01 Hz to 10 kHz.

3.3.9.3 Mott-Schottky (M-S)

M-S was conducted to determine the type of conductivity of the samples. The samples were coated on FTO glass slides, and the three-electrode cell setup was used (Figure 3.12a). M-S plots were measured at 100 Hz frequency. The potentials were converted from versus Ag/AgCl, pH 6.5 to versus NHE, pH 7 by Equation 3.5 (Giannakopoulou et al., 2017):

$$V_{(vs.NHE,pH\ 7)} = V_{(vs.Ag/AgCl,pH\ 6.5)} + 0.21\,V - 0.059 \times (7.0 - 6.5) \quad (3.5)$$

The M-S equations for p-type and n-type semiconductors are Equation 3.6 and 3.7 respectively:

$$\frac{1}{C^2} = \frac{2}{e\varepsilon_0\varepsilon_r N_A}\left[(-V + V_{FB}) - \frac{kT}{e}\right] \quad (3.6)$$

$$\frac{1}{C^2} = \frac{2}{e\varepsilon_0\varepsilon_r N_D}\left[(V - V_{FB}) - \frac{kT}{e}\right] \quad (3.7)$$

Where, C is the capacitance, e is the electron charge (1.602×10^{-19} C), ε_0 is the permittivity of vacuum (8.854×10^{-12} F m^{-1}), ε_r is the dielectric constant of the material, V is applied bias potential, V_{FB} is the flat band potential, k is the Boltzmann constant, T is the temperature (K), N_A is the ionised acceptor density (cm^{-3}), and N_D is the ionised donor density (cm^{-3}). According to previous reports, the ε_r of GO at 100 Hz was ~770 (Hong et al., 2016). By determining the slope of a extrapolated straight line from a M-S plot, the N_A and N_D could be determined according to Equation 3.8 (P. Wang et al., 2017):

$$N_A = -\frac{2}{e\varepsilon_0\varepsilon_r} / \frac{d(1/C^2)}{dV}$$
$$N_D = \frac{2}{e\varepsilon_0\varepsilon_r} / \frac{d(1/C^2)}{dV} \quad (3.8)$$

Where $\frac{d(1/C^2)}{dV}$ is the slope of the M-S plot extrapolated straight line (F^{-2} cm^4/V). The hole carrier density is approximately equal to the ionised acceptor density, N_A (cm^{-3}) of a p-type semiconductor, while the free-electron carrier density is roughly equal to the ionised donor density, N_D (cm^{-3}) of an n-type semiconductor (Tai et al., 2022)

3.4 Photoreactor for PCO of VOC

3.4.1 PCO of VOC at ambient condition

A custom-made VOC PCO chamber with a total volume of 12 L was designed to simulate an enclosed indoor environment under ambient conditions (Figure 3.14). A diaphragm pump was connected to the chamber to provide air circulation. The concentrations of VOCs were monitored continuously by an Extech VFM200 VOC detector inside the chamber. Photocatalyst coated on polyester fabric substrate was placed at the middle of the PCO chamber, with the light source located 5 cm away. The light source was 4 W UV-A (λ_{peak} = 365 nm, I = 0.6 mW/cm^2). A certain concentration of VOCs (e.g., methanol, 1.52 µl, 100 mg/m^3) was dropped into the chamber and then quickly sealed to be airtight, allowing the VOCs to vaporize inside the chamber. After the dark adsorption-desorption equilibrium was achieved, the light source was switched on to begin the PCO test. The PCO experiment was carried out at room temperature (25°C) with an indoor humidity of 65 RH%. The ambient temperature and RH% were measured with a digital thermo-hygrometer (ETP 101).

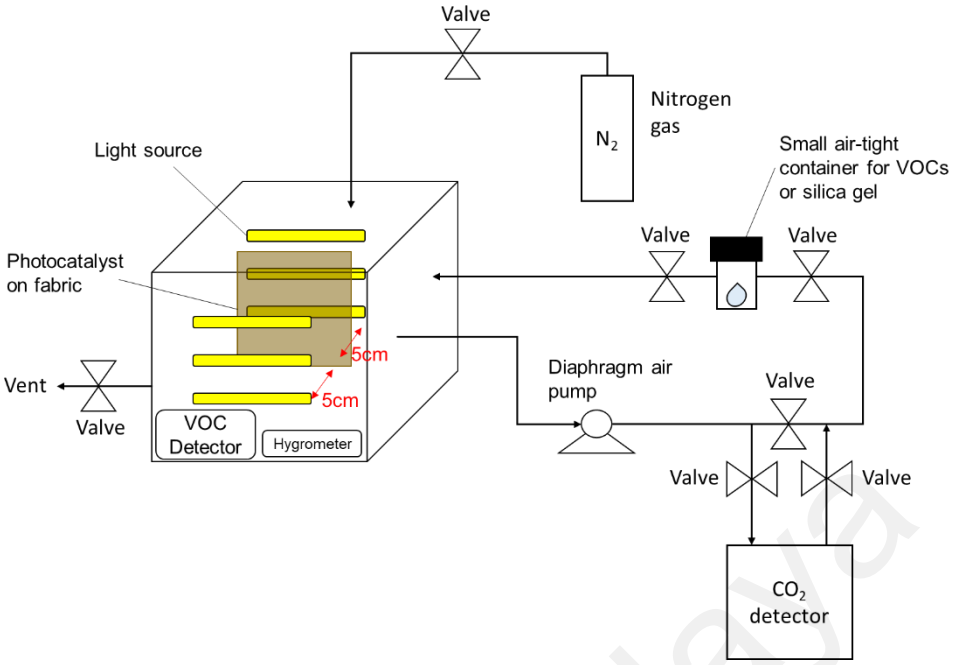

Figure 3.14: VOCs PCO Chamber.

3.4.2 Effects of humidity on PCO

The optimal ambient humidity for PCO was determined by conducting PCO at 85, 65 (room), 48, 36, and 30 RH%. The humidity of 85 RH% was created by introducing 55 µl of deionised water into the photoreactor, as the initial humidity was 65 RH%. Besides that, the air in the photoreactor was circulated through dry silica gel for 0, 0.5, and 1 h to create humidity of 65, 48, and 36 RH%, respectively.

3.4.3 Investigation of active species participated in the PCO process

In gas phase PCO, most •OH radicals are generated from water vapour, while $\bullet O_2^-$ radicals are generated from oxygen (P. Li et al., 2020; Rao et al., 2022). The active species involved in PCO were studied by comparing three different ambient atmospheric conditions according to a previous study (Rao et al., 2022). The three ambient conditions were air with optimal humidity (contained •OH, $\bullet O_2^-$ radicals, and the photogenerated hole carries at VB (h_{VB}^+)), nitrogen gas (N_2) atmosphere with optimal humidity (contained •OH radicals and h_{VB}^+), and dry N_2 (contained h_{VB}^+ only). The N_2 atmospheres

were created by flushing pure N_2 throughout the photoreactor, while moisture was reintroduced into the photoreactor by vaporising deionised water.

3.4.4 Photocatalyst recyclability

To study the recyclability, photocatalysts coated of fabrics were repeatedly used for PCO reactions up to 5 cycles to evaluate its stability. Before each cycle, the photocatalyst was dried in an oven (60 °C) to remove any adhering VOCs.

3.4.5 PCO reaction kinetics calculation

The $\%R_{adsorption}$ and $\%R_{PCO}$ removal efficiencies were calculated based on Equation 3.9 and 3.10:

$$\%R_{adsorption} = \frac{C_{initial} - C_0}{C_{initial}} \times 100\% \tag{3.9}$$

$$\%R_{PCO} = \frac{C_0 - C_t}{C_0} \times 100\% \tag{3.10}$$

Where $C_{initial}$, C_0, and C_t are the concentration of VOCs (mg/m^3) at initial, adsorption-desorption equilibrium, and time, t (h). The data of the removal of VOCs versus time was fitted to the pseudo-first order kinetics as described by the Langmuir–Hinshelwood kinetic model, Equation 3.11:

$$\ln\left(\frac{C_t}{C_0}\right) = -kt \tag{3.11}$$

Where k (h^{-1}) is the pseudo-first order rate constant.

3.4.6 Mineralisation rate

Since the complete mineralisation of 1 mole of the model VOCs (methanol) should lead to the formation of 1 mole of CO_2, the mineralisation efficiency (M%) of the PCO process was calculated by Equation 3.12 (Sleiman et al., 2009):

$$M\% = \frac{CO_{2_{actual}}\left[\frac{mole}{m^3}\right]}{CO_{2_{theoretical}}\left[\frac{mole}{m^3}\right]} \times 100\%$$

$$CO_{2_{actual}}\left[\frac{mole}{m^3}\right] = \frac{CO_{2_{actual}}[ppm] \times P}{RT \times 10^6} \quad (3.12)$$

$$CO_{2_{theoretical}}\left[\frac{mole}{m^3}\right] = C_{initial}\left[\frac{mg}{m^3}\right] \times \frac{C_0}{C_{initial}} \times \frac{C_0 - C_t}{C_0} \times \frac{1}{MW\left[\frac{g}{mol}\right]} \times \frac{g}{1000\,mg}$$

Where $CO_{2_{actual}}$ is the actual measured concentration of CO_2 in the unit of mole/m^3 or ppm, $CO_{2_{theoretical}}$ is the theoretical concentration of CO_2 evolved from PCO after the adsorption-desorption equilibrium, P is the ambient pressure (atm), R is the universal gas constant (8.205×10^{-5} m^3.atm.$mole^{-1}$.K^{-1}), T is the ambient temperature (K), and MW is the molar weight of the VOC (g.$mole^{-1}$).

CHAPTER 4: Photoreduced graphene oxide (PRGO) photocatalyst for the removal of VOCs

In this chapter, a series of PRGO samples with different photoreduction duration was synthesized from GO. The GO and PRGO samples were characterized to determine their physicochemical and electrochemical properties (Section 4.1). Then, PCO experiments were carried out to investigate the effects of photoreduction on the photoactivity of the PRGO samples (Section 4.2). Lastly, the band structures and PCO mechanism of the PRGO photocatalyst were determined (Section 4.3).

4.1 Characterizations of GO and PRGO samples

A set of characterization tests were conducted on the PRGO samples to determine their physicochemical properties, which include XRD, Raman, FTIR, UV-Vis, XPS, and PL. Furthermore, the electrochemical properties of the PRGO samples were investigated by M-S, EIS, and photocurrent techniques.

4.1.1 Physicochemical properties of GO and PRGO

Figure 4.1a shows the colour of PRGO changed from brown to black with a longer photoreduction time. The change of colour suggested the occurrence of photoreduction. This colour darkening effect was commonly observed in past GO photoreduction studies (Kim et al., 2009; Xue et al., 2017). UV-vis absorbance analysis was carried out to investigate the optical properties of the as-synthesized GO and PRGO samples (Figure 4.1.1a). All of them showed a peak around 230 nm (π-π^* transition of C=C) and the appearance of a small shoulder near 300 nm (n-π^* transition of C=O). After photoreduction, the peak was not significantly shifted, while the shoulder at 300 nm was broadened. The non-shifting peak is in contrast with some GO reduction studies, where

the peak was gradually red-shifted to 260-270 nm after reduction (Muthoosamy et al., 2015; Türk et al., 2018). This implies that the UV-A photoreduction method was a milder reduction method, in which GO was only partially reduced. This is important as PRGO is a semiconductor with a finite bandgap, while a greatly reduced GO will have a near-zero bandgap and behave more like a conductor (Mathkar et al., 2012). In addition, the broadened area between 300 - 800 nm indicated that sp^2 hybridization carbon atom fraction was partially recovered and the π electron concentration was increased after photoreduction (Ding et al., 2011; Hou et al., 2015). As shown in Figure 4.1b, Tauc plot linear extrapolation technique was used to determine the bandgaps of the GO and PRGO samples. GO-based materials have a cluster of collective band structures due to graphene of different oxygenated levels, giving them a range of bandgaps instead of an absolute value (Gan et al., 2011; Loh et al., 2010). After photoreduction, the bandgap was reduced and stabilized, where PRGO-8 and PRGO-10 had the lowest bandgap at 3.10 - 4.00 eV. The bandgap energy was sufficient to overcome the theoretical energy requirement of 2.71 eV to produce the ROS pair, namely $\bullet O_2^-$ and •OH radicals under UV-A excitation for VOCs photodegradation (Saison et al., 2013).

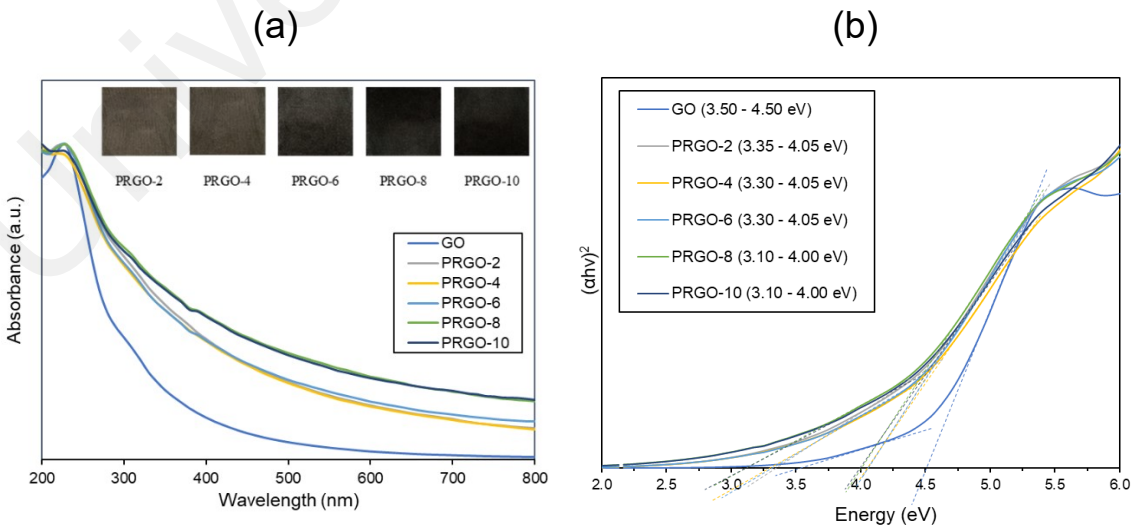

Figure 4.1: (a) UV-vis absorbance spectra and (b) Tauc plot derived bandgaps of GO and PRGO samples.

Figure 4.2a presents the Raman spectra of the GO and PRGO samples, where all exhibited two strong peaks at the D (~1350cm^{-1}) and G (~1600cm^{-1}) modes. Two smaller peaks at 2D (~2722cm^{-1}) and S3 (~2930cm^{-1}) appeared after photoreduction. The D band represented the disordered structure of graphene; G band was from the scattering of E_{2g} phonon of sp^2 carbon atoms; 2D was the second-order of D band, which is used to evaluate the stacking order of the c-axis orientation; while S3 band was from the imperfect activated grouping of phonons (Li et al., 2016). The peak intensity ratio of D to G (I_D/I_G ratio) and 2D to G (I_{2D}/I_G) increased steadily after photoreduction, from 0.88 and 0.08 (GO) to 0.98 and 0.11 (PRGO-10). The increase of I_D/I_G ratio indicated that there was formation of new smaller graphitic domain upon photoreduction, which reduce the average size of the sp^2 fraction (Amieva et al., 2015; Stankovich et al., 2007). Meanwhile, the increase of I_{2D}/I_G ratio was due to the reinstallation of the sp^2 domain (Mortazavi et al., 2018). The Raman analysis is well agreed with the UV-vis results, in which the sp^2 domain was partially recovered after photoreduction and had reduced disorder-induced fraction.

Photoluminescence (PL) spectra results are shown in Figure 4.2b. All GO and PRGO samples exhibited a broad peak, suggesting a wide bandgap structure (Luo et al., 2009), which supported the bandgap results derived from Tauc plots. The relative PL peak intensity decreased with a longer photoreduction time. The PRGO-8 and PRGO-10 had the lowest peak intensity, indicating that the rate of recombination of photogenerated electrons and holes was reduced with longer photoreduction. This could be due to the partial restoration of the sp^2 domain during photoreduction, which led to better electrical conductivity and charge carriers' mobility. This is in agreement with previous studies (Choi et al., 1994; Liu et al., 2010), where higher conductivity had led to better charge separation, hence lowering the rate of electron recombination. In addition, the PL peak location was shifted slightly from 600 - 610 nm to 590 - 600 nm as photoreduction time

increased. These findings concorded with others (Chien et al., 2012; Chuang et al., 2014), where the blue-shifting of PL was caused by the partial deoxygenation of GO, which led to more sp^2 cluster and lesser disorder-induced fraction within the π-π^* gap.

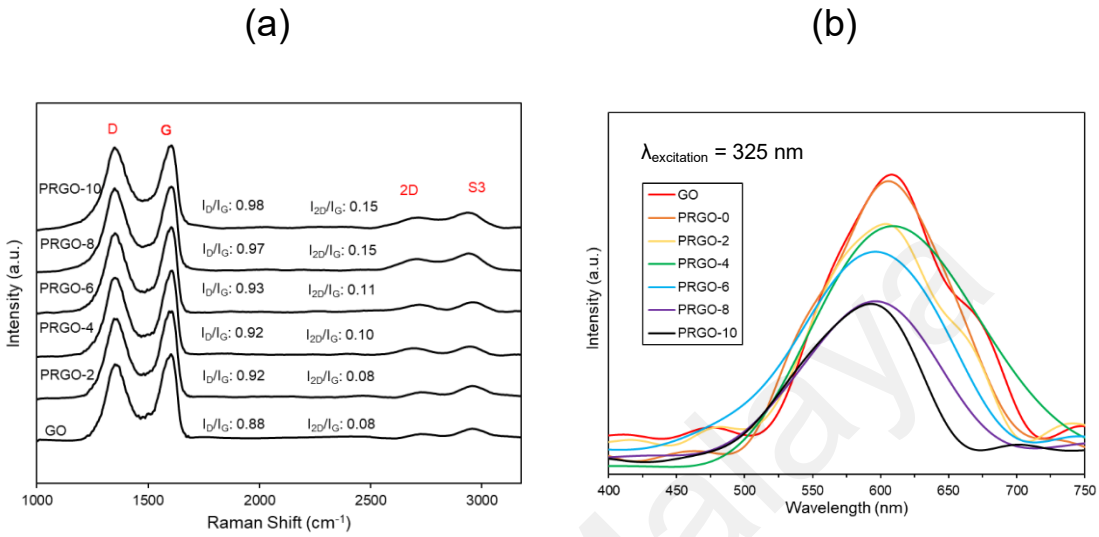

Figure 4.2: (a) Raman and (b) Photoluminescence spectra of GO and PRGO samples.

Figure 4.3 shows that the XRD pattern of GO had a diffraction peak at $2\theta = 10.04°$, which is typical for exfoliated GO. After photoreduction, the peak at 10.04° disappeared, while a broad peak at 24.5° appeared. This is because GO was photoreduced, hence part of the interlayer-spacing collapsed. The 24.5° peak is a typical pattern of lowered stacking order between the graphene layers (Amer et al., 2017; Díez et al., 2015). The XRD patterns of PRGO-2 to PRGO-10 were similar, this suggested that the interlayer-spacing structure of the PRGO samples were unchanged after extended photoreduction treatment. In addition, a peak was present at 44° for all PRGO samples, this indicates a short-range order of stacked graphene layers (Stobinski et al., 2014).

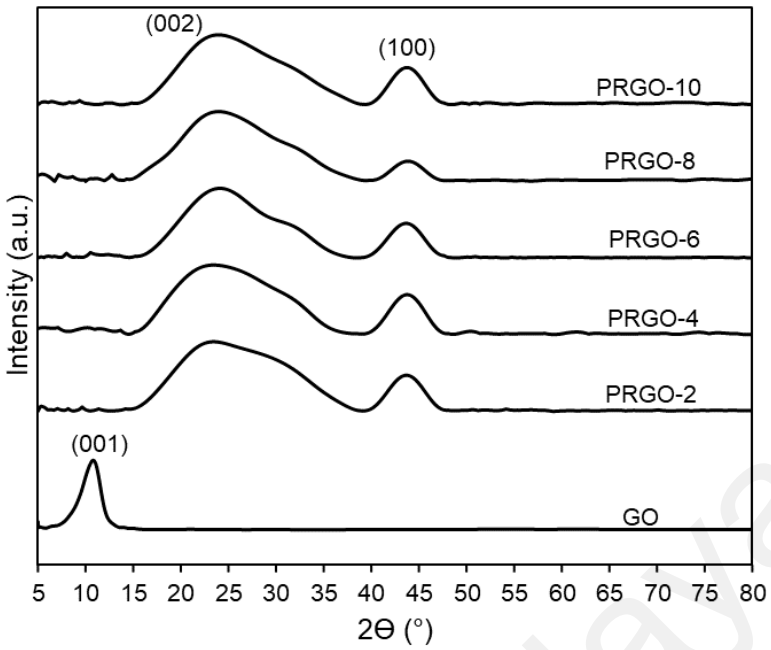

Figure 4.3: XRD patterns of GO and PRGO samples.

XPS study was used to analyse the elemental composition and oxygen functionalities of the GO and PRGO samples. Figure 4.4 (a and b) display the high-resolution scan of XPS spectra C 1s (284.5 eV) and O 1s (532.4 eV) results. The C 1s spectra were deconvoluted into four peaks C-C/C=C (284.5 eV), C-O (286.6 eV), C=O (287.7 eV), and C(O)(OH) (289.6 eV), and then fitted using a symmetric Gaussian function (Stobinski et al., 2014). Table 4.1 summarizes the composition of the functionalities analysed from the C 1s spectra and the O/C atomic ratios. The proportion of the C-C/C=C group showed a gradual intensity increase with photoreduction time, where PRGO-10 had the largest composition of 73%. In contrast, the other three oxygenated carbon groups (OCGs) became less intense but in fluctuating trends with photoreduction. The fluctuating reducing trend suggested that the UV-A irradiation photoreduction method was random and did not target a specific carbon-oxygen group. From Figure 4.4b, it was found that the O 1s peak relative area reduced with photoreduction. Quantitative analysis was carried out to determine the O and C concentrations, the atomic ratio of O/C gradually decreased

from 0.49 to 0.25 with longer photoreduction. These results reflect the reduction of PRGO is responsible for the decrease of oxygen content with photoreduction time. In addition, the O/C ratios of PRGO-8 to PRGO-10 were similar even after further light irradiation. This indicated that the material might have resisted photoreduction and drastic oxygen functional groups reduction after 8 hours. This is in concordance with a previous study, where PRGO can resist further light-induced reduction, unless a higher amount of energy is used (Hou et al., 2015).

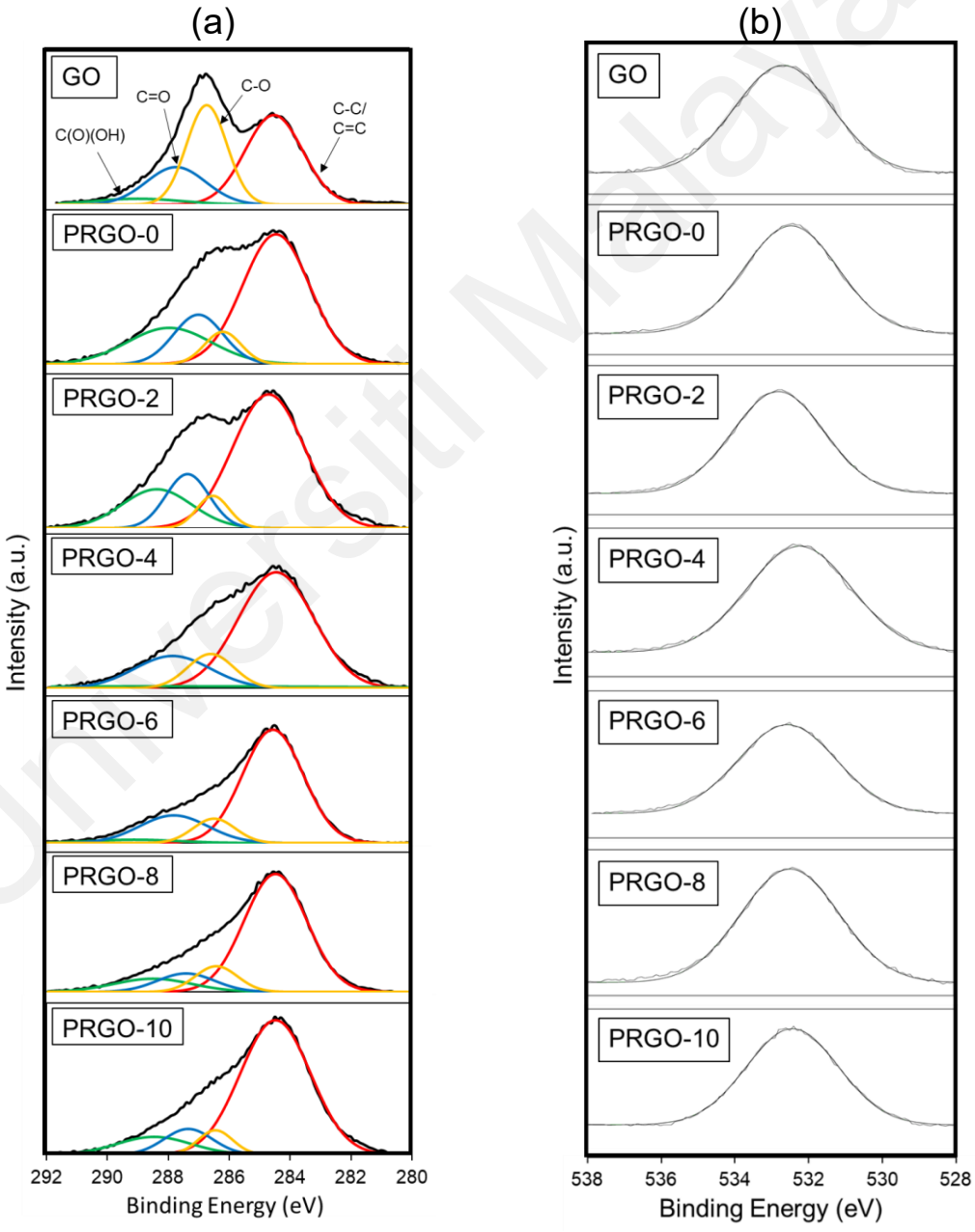

Figure 4.4: (a) C1s and (b) O1s XPS spectra of GO and PRGO samples.

Table 4.1: Summary of XPS compositions for GO and PRGO samples

Material	XPS (at%)			C 1s (at%)				OCGs/C
	C	O	O/C	C-C /C=C	C-O	C=O	O=C-O	
GO	67	33	0.49	43	34	19	4	0.57
PRGO-0	71	29	0.42	57	8	16	20	0.44
PRGO-2	72	28	0.38	61	7	15	17	0.39
PRGO-4	73	27	0.37	66	12	18	4	0.34
PRGO-6	77	23	0.31	68	10	19	3	0.32
PRGO-8	79	21	0.26	70	10	10	10	0.30
PRGO-10	80	20	0.25	73	7	10	10	0.27

The FTIR results of GO and PRGO samples are shown in Figure 4.5. It was found that all the major oxygen functional groups were present despite after photoreduction. The peaks of C=O stretching, C=C (sp^2 of aromatic ring), C-OH group, C-O-C (epoxy), C-O stretching at 1730, 1630, 1380, 1260, and 1040 cm^{-1}, respectively were noticed. Only the C-OH group had a relatively significant reduction of intensity. These results agreed well with XPS analysis, where the oxygen groups were still present even after photoreduction. The $C-H_2$ group at 2930 cm^{-1} appeared after photoreduction, which might be due to the reaction of carbon atoms with the hydrogen ions produced during photoreduction. The formation of hydrogen during the photoreduction of GO was also observed in previous studies (Mohandoss et al., 2017).

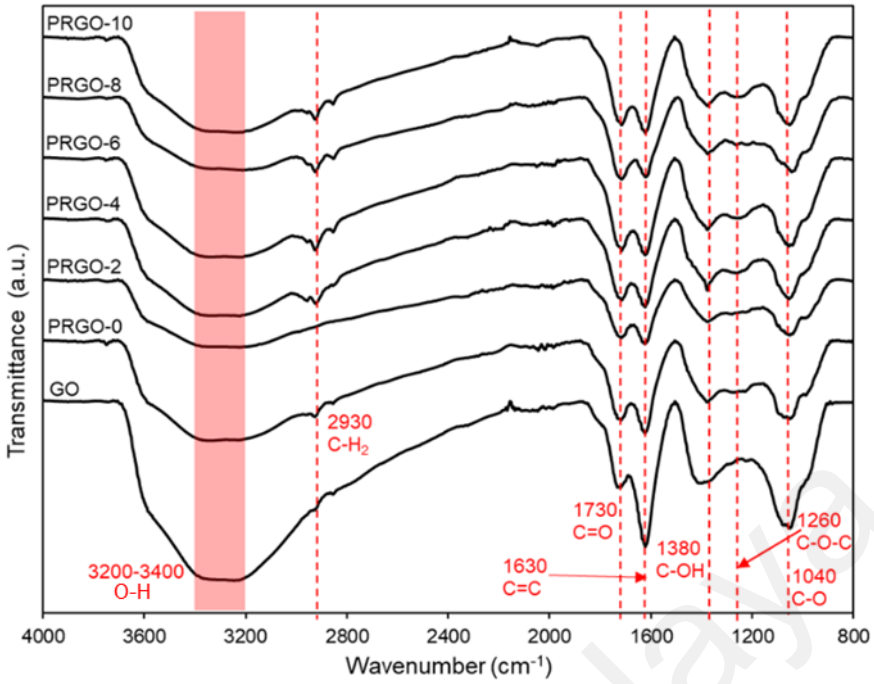

Figure 4.5: FTIR spectra of GO and PRGO samples.

4.1.2 Electrochemical properties of GO and PRGO

Figure 4.6a shows the M-S plots of the GO and PRGO samples. All samples exhibited negative slopes, indicating that they were p-type semiconductors. The p-type conductivities of GO and PRGO were attributed to the presence of oxygen atoms on their surfaces, which were more electronegative than the basal carbon atoms (Wang et al., 2009). From the x-axis intersection points of the M-S plots, the flat band potentials (V_{FB}) of GO, PRGO-2, PRGO-4, PRGO-6, PRGO-8, and PRGO-10 were found to be +1.08, +1.10, +1.11, +1.11, +1.14, and +1.14 V vs. Ag/AgCl, pH 6.5, respectively. After the conversion to vs. NHE, pH 7, the V_{FB} of the samples were +1.26 V (GO), +1.28 V (PRGO-2), +1.29 V (PRGO-4), +1.29 V (PRGO-6), +1.32 V (PRGO-8), and +1.32 V (PRGO-10). Generally, the VBM is approximately +0.3 V away from the V_{FB} of p-type semiconductors (Yin et al., 2016). Therefore, the VBM were determined to be +1.56 V (GO), +1.58 V (PRGO-2), +1.59 V (PRGO-4), +1.59 V (PRGO-6), +1.62 V (PRGO-8), and +1.62 V (PRGO-10). In addition, the hole carrier density can be derived from the M-

S plots to determine the hole carrier density of the samples. The hole carrier density of GO was 1.03×10^{16} cm^{-3}, while among the PRGO samples, PRGO-8 had the largest hole carrier density at 1.45×10^{16} cm^{-3} (1.41 times higher than GO). The PRGO-8 exhibited a larger hole carrier density than GO because of the partial removal of OCGs after photoreduction. This is because excessive OCGs would have acted as trap centres that diminish the charge carrier density (Putri et al., 2015; Tu et al., 2015).

The electrochemical impedance spectroscopy (EIS) of the samples were determined by the Nyquist plot (Figure 4.6b). In a Nyquist plot, the arc radius of the semi-circle signifies the resistance in transporting charge carriers (Putri et al., 2020). It was found that PRGO-8 had the smallest arc radius, hence the best conductivity to transport charge carriers. This is because PRGO-8 had the largest hole carrier density, which led to a higher p-type conductivity (Lin et al., 2011; Yeom et al., 2015). Moreover, the partial restoration of the conducting sp^2 fractions in PRGO-8 after photoreduction also contributed to the increase of conductivity (Mortazavi et al., 2018).

In Figure 4.6c, transient photocurrent experiments with five on-off cycles of light irradiation were conducted. All GO and PRGO samples exhibited photocurrent values instantaneously upon light irradiation. The photocurrent densities were in the order of PRGO-8 ≈ PRGO-10 > PRGO-6 > PRGO-4 > PRGO-2 > GO. The highest photocurrent density of PRGO-8 indicated that it had the slowest charge carrier recombination, which agreed with the PL results. Slow charge carrier recombination rate is beneficial for photocatalytic activity, as the availability of more photoexcited electron-hole pairs can produce more reactive species for PCO.

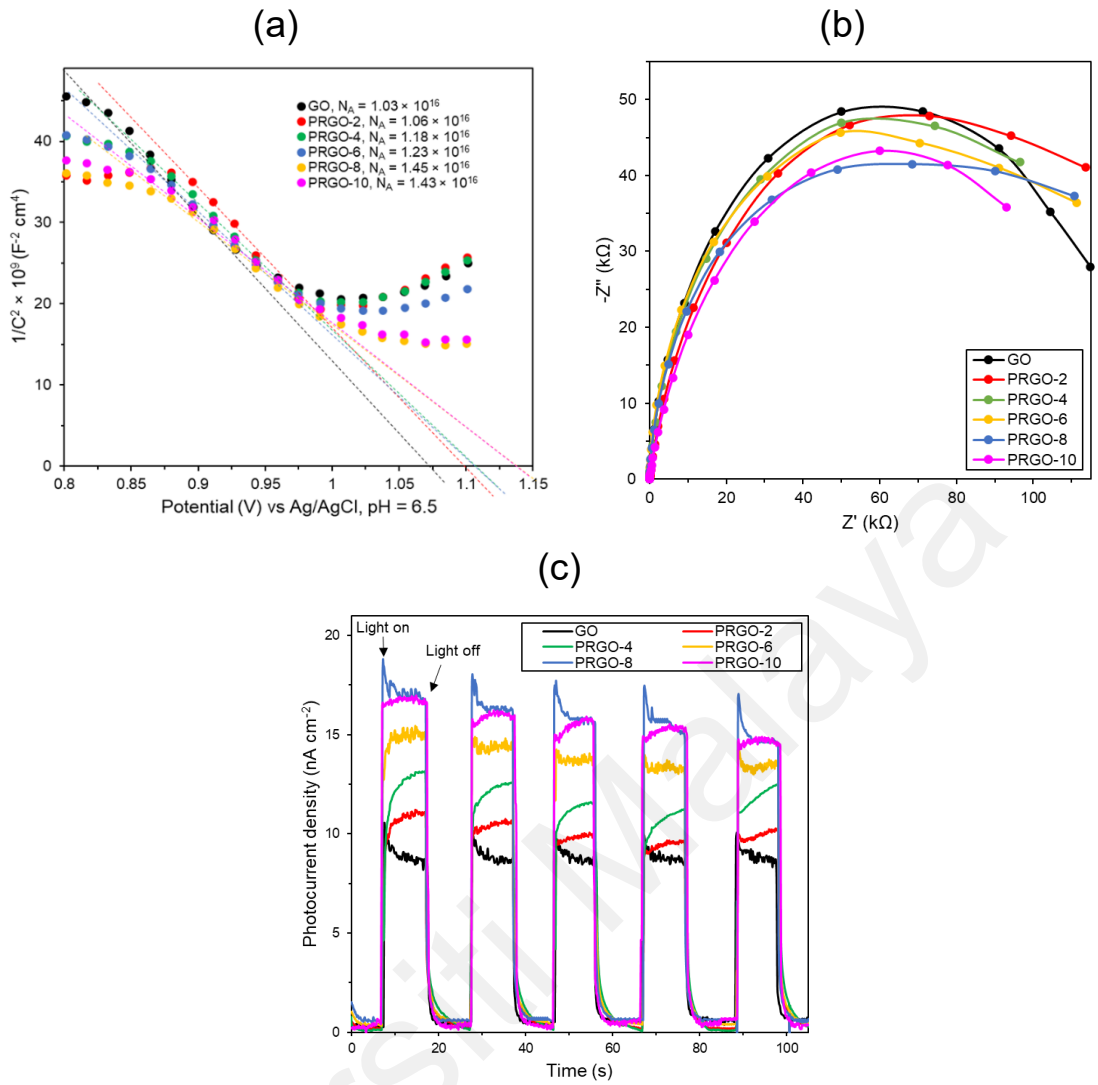

Figure 4.6: (a) M-S plot, (b) EIS analysis, and (c) photocurrent of GO and PRGO samples.

4.2 PCO performances of GO and PRGO samples

Methanol was successfully removed by the GO and PRGO samples via PCO. No methanol was removed by photolysis at the absence of photocatalyst (Appendix C). The photocatalysts had similar VOCs adsorption efficiencies between 10 – 14%. In Figure 4.7 (a and b), the photocatalytic activity of methanol degradation was found to follow the order of PRGO-8 ≈ PRGO-10 > PRGO-6 > PRGO-4 > PRGO-2 > GO. After GO photoreduction, the PCO performance was improved by more than two-fold, where PRGO-8 had the highest methanol PCO at 23.4% and the highest pseudo-first order rate constant, k at 0.066 h^{-1}. The lower PL peak intensity of PRGO-8 indicated a lower charge

recombination rate. This could have led to better photocatalytic activity (Chien et al., 2012) as more photogenerated electrons and holes can be utilized for reactive species production. Figure 4.7c and Appendix L show the correlation between hole carrier density and PCO rate of the GO and PRGO photocatalysts. It was shown that a higher hole carrier density enhanced the rate of PCO. This is because the high hole carrier density had led to slow recombination of photogenerated charge carriers. Another possible factor affecting methanol PCO was the bandgap of the PRGO. The bandgap before photoreduction was too wide to be fully photoexcited by the UV-A light source, then the bandgap was reduced after photoreduction. Hence, more PRGO molecules would become photoactive under UV-A, thus contributing to a higher photoactivity. This finding is in agreement with a previous study, where the bandgap of GO was found to be a limiting factor affecting its photoactivity of water splitting (Yeh et al., 2011). Figure 4.7d shows that after five cycles, the performance of PRGO-8 was almost the same without any drastic decrease. The results indicated that PRGO-8 was a stable photocatalyst with good reusability.

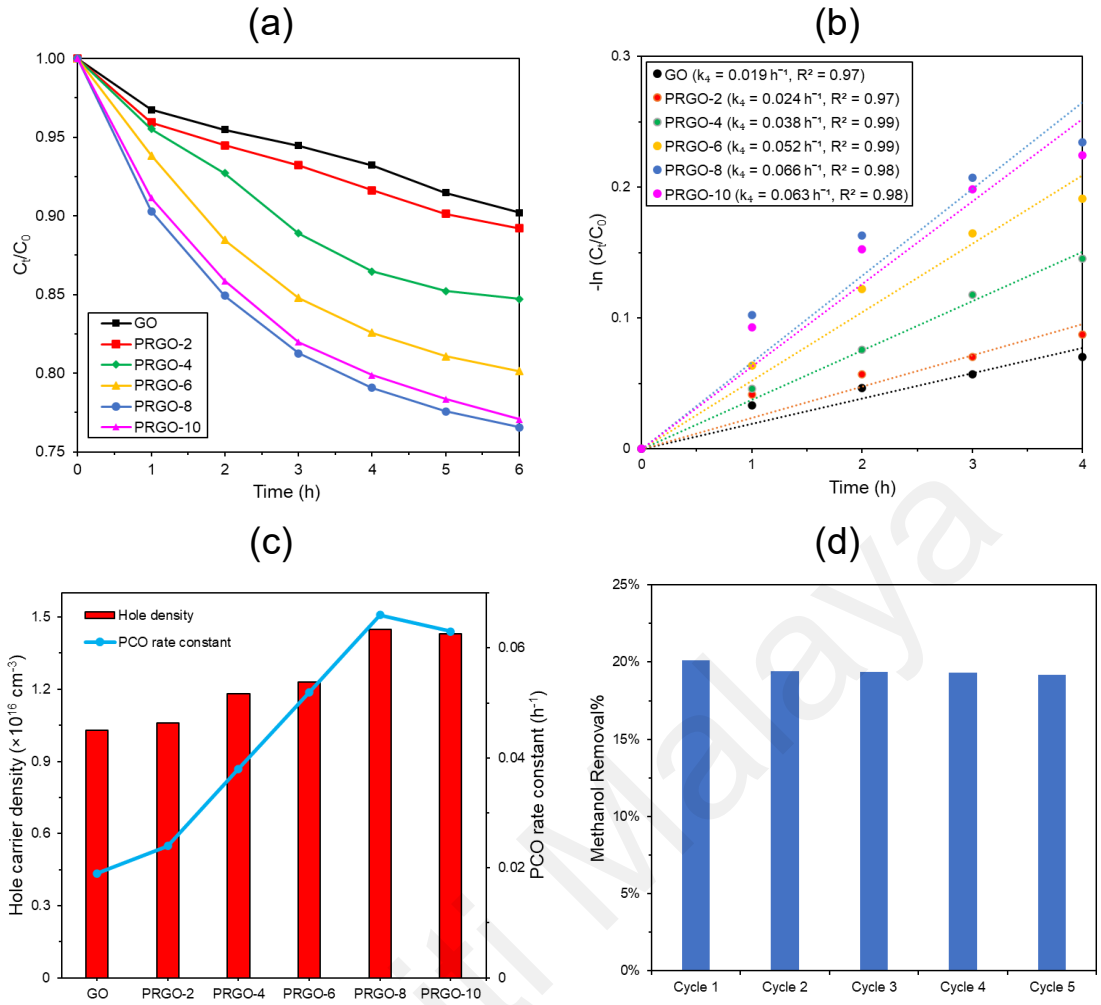

Figure 4.7: (a) PCO of methanol, (b) pseudo-first order kinetic by PRGO samples, (c) correlation of hole carrier density and PCO rate, and (d) PCO recyclability test of PRGO-8.

It is important to investigate the effect of ambient humidity on gas-phase PCO. The presence of water vapour can affect both the adsorption of VOCs and the generation of •OH radicals (Mamaghani et al., 2017). From Figure 4.8 (a and b), the optimal humidity for the PCO by PRGO-8 was 36 RH%, where 29.4% of methanol was degraded in 6 h, with a rate constant of 0.07 h^{-1}. Besides that, it was also found that the adsorption efficiency was increased from 14% (65 RH%) to 20% (36 RH%). This is because at lower humidity, fewer water molecules were present in the air to compete with VOCs for adsorption. However, the PCO efficiency was reduced at lower humidity (30 RH%) because the low quantity of water molecules in the air had limited the generation of •OH.

Figure 4.8c exhibits the concentration of CO_2 evolved from the PCO process by GO and PRGO-8 at 36 RH%. No CO_2 was formed in the absence of photocatalyst or VOCs. After 6 h, the M% was calculated to be 58% and 62% for GO and PRGO-8, respectively. The results indicate that both the GO and PRGO-8 were able to partially mineralise VOCs into harmless CO_2. The incomplete M% suggested that some VOCs have been broken down into stabler intermediates and were probably re-adsorbed onto the surface of the photocatalyst or reactor (Debono et al., 2017).

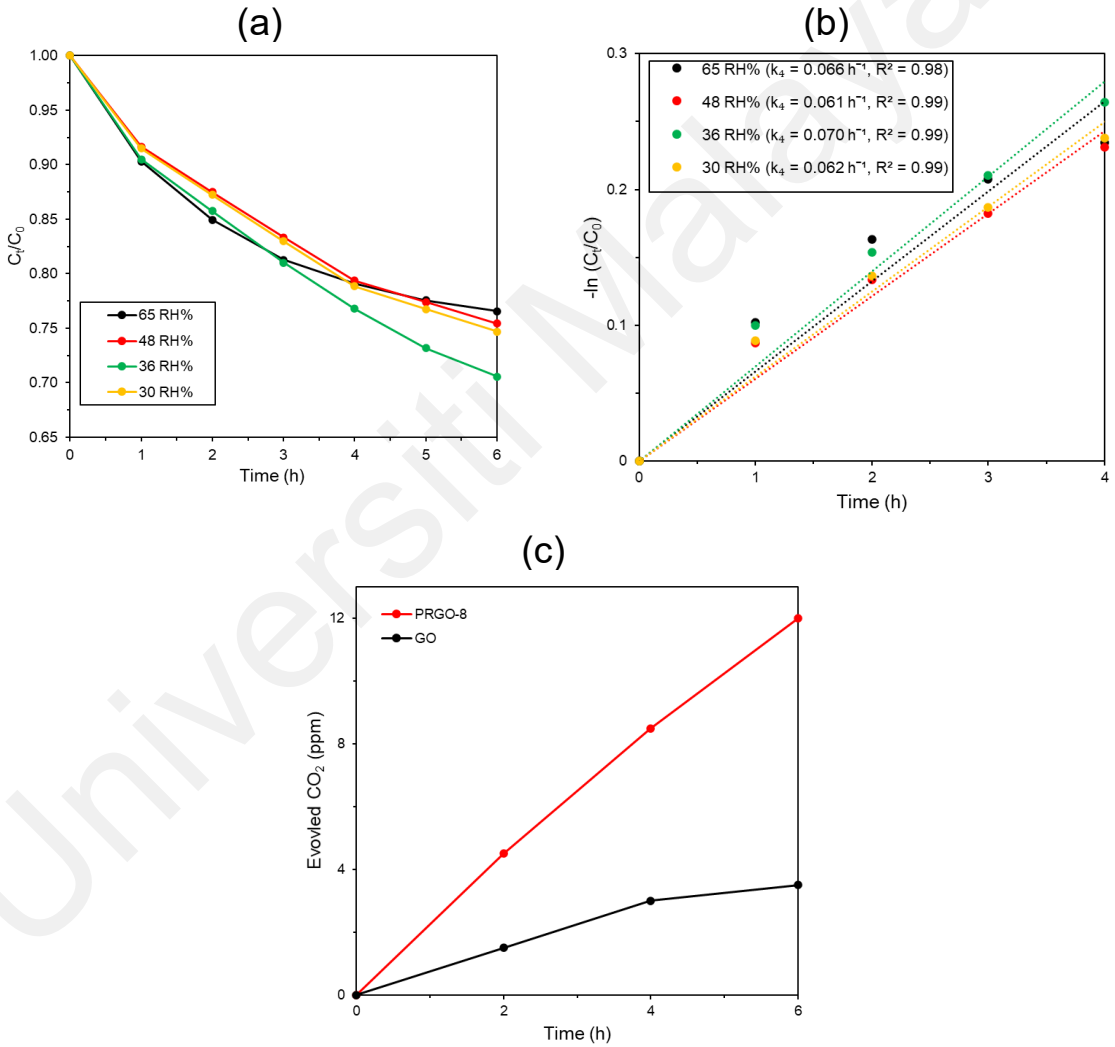

Figure 4.8: (a) PCO by PRGO-8 at different RH% and the corresponding, (b) pseudo-first order kinetic, and (c) CO_2 evolution during PCO by GO and PRGO-8.

4.3 Reactive species and mechanism of PCO by PRGO

In Figure 4.9a, the PCO performance of PRGO-8 was compared under three different types of ambient atmospheres to investigate the relative PCO contributions of the three reactive species, namely $\bullet O_2^-$, •OH radicals, and hole carriers at the valence band (h_{VB}^+). It was found that PRGO-8 was able to remove 29.4%, 25.0%, and 18.2% of methanol under humid air (36 RH%), humid N_2 (36 RH%), and dry N_2 (0 RH%), respectively. The findings suggested that all three reactive species contributed to the PCO process, in which their relative contributions were as such h_{VB}^+ (18.2%) > •OH (6.7%) > $\bullet O_2^-$ (4.5%).

Based on the results of M-S and bandgaps, the band structures of the GO and PRGO samples were constructed in Figure 4.9b. Besides that, Figure 4.9b also exhibits the mechanism of VOCs removal by PRGO-8. Under UV-A irradiation, free-electron (e_{CB}^-) and h_{VB}^+ were generated at the CB and VB of PRGO-8, respectively. The CB was negative enough to reduce oxygen (O_2) into $\bullet O_2$ radicals (-1.48 V vs. NHE, pH 7), while the VB was positive enough to oxidise water vapour into •OH radicals (+2.52 V vs. NHE, pH 7). The h_{VB}^+ in tandem with the $\bullet O_2^-$ and •OH radicals then mineralised VOC molecules into harmless CO_2.

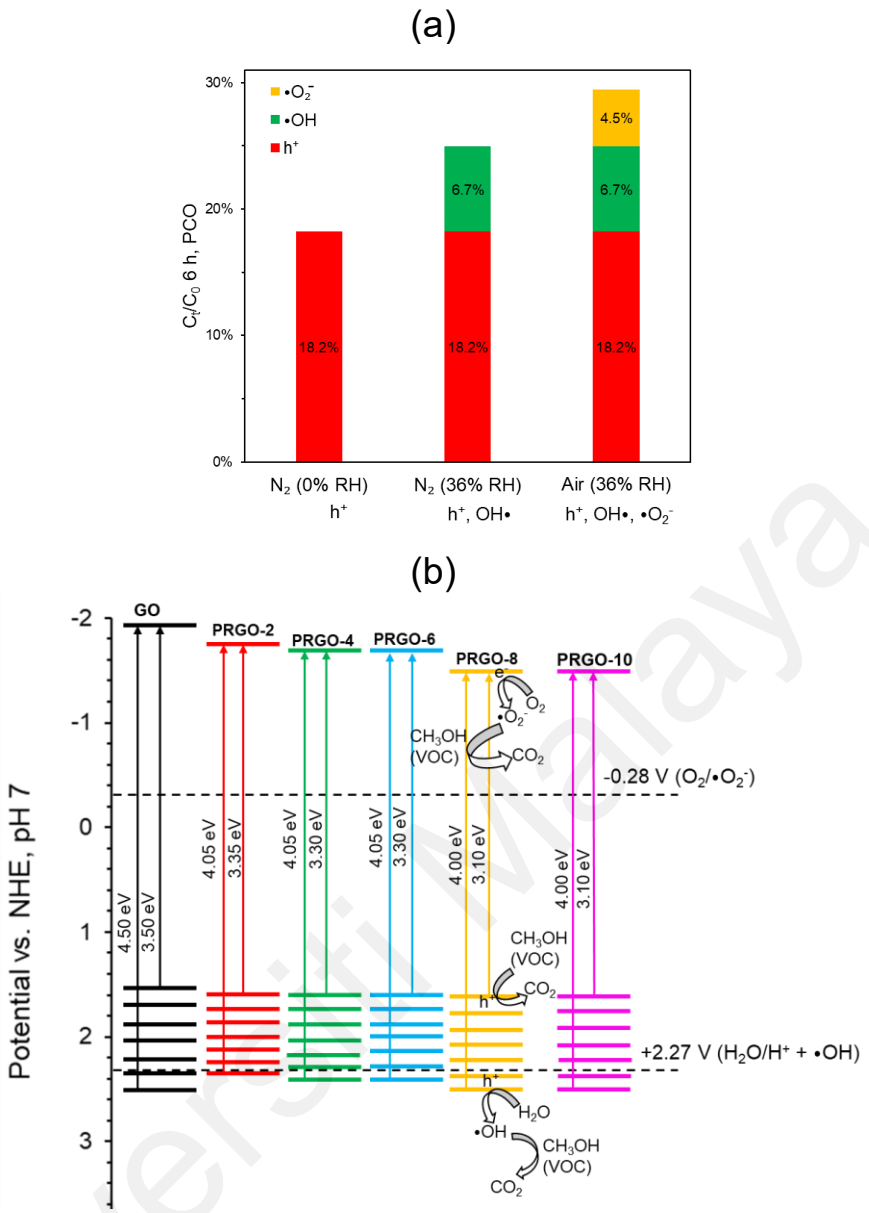

Figure 4.9: (a) PCO by PRGO-8 under different ambient atmosphere and (b) Band structures and PCO mechanism by PRGO photocatalysts

In summary, PRGO photocatalysts were successfully synthesized via photoreduction technique without using any harmful reducing agent or solvent. This study shows that PRGO is a potential low cost, eco-friendly, and metal-free photocatalyst to carry out indoor PCO of methanol under UV-A irradiation. The methanol photodegradation was boosted up to 29.4% with a rate constant of 0.07 h^{-1} by using PRGO-8 at 36 RH%. This enhancement was mainly due to its smaller bandgap and slower electron recombination. The photocatalyst was stable and no significant loss of performance was observed even after five cycles of PCO.

CHAPTER 5: Boron-doped photoreduced graphene oxide (BPRGO) photocatalyst for the removal of VOCs

In this chapter, a series of BPRGO samples with different photoirradiation duration was synthesized from GO. After the photoirradiation process in the presence of H_3BO_3, the GO was simultaneously photoreduced and B-doped. The samples were characterized to determine their physicochemical and electrochemical properties (Section 5.1). Then, PCO experiments were carried out to investigate the effect of photoreduction on the photoactivity of the BPRGO samples (Section 5.2). Lastly, the band structures and PCO mechanism of the BPRGO photocatalyst were determined (Section 5.3).

5.1 Characterizations of BPRGO samples

A set of characterization tests were conducted on the BPRGO samples to determine their physicochemical properties, which include XRD, Raman, FTIR, UV-Vis, XPS, and PL. Furthermore, the electrochemical properties of the BPRGO samples were investigated by M-S, EIS, and photocurrent techniques.

5.1.1 Physicochemical properties of BPRGO samples

Figure 5.1 demonstrates the FESEM images and elemental mappings of the GO and BPRGO samples. Wrinkles were found on the surfaces of all the as-synthesized GO and BPRGO samples. This observation concurred with previous studies (Putri et al., 2017; Van Khai et al., 2012), in which the morphology of GO was not changed after B doping. Additionally, the elemental mapping of BPRGO samples show the presence of B, therefore suggesting that B was successfully and homogenously doped on the GO.

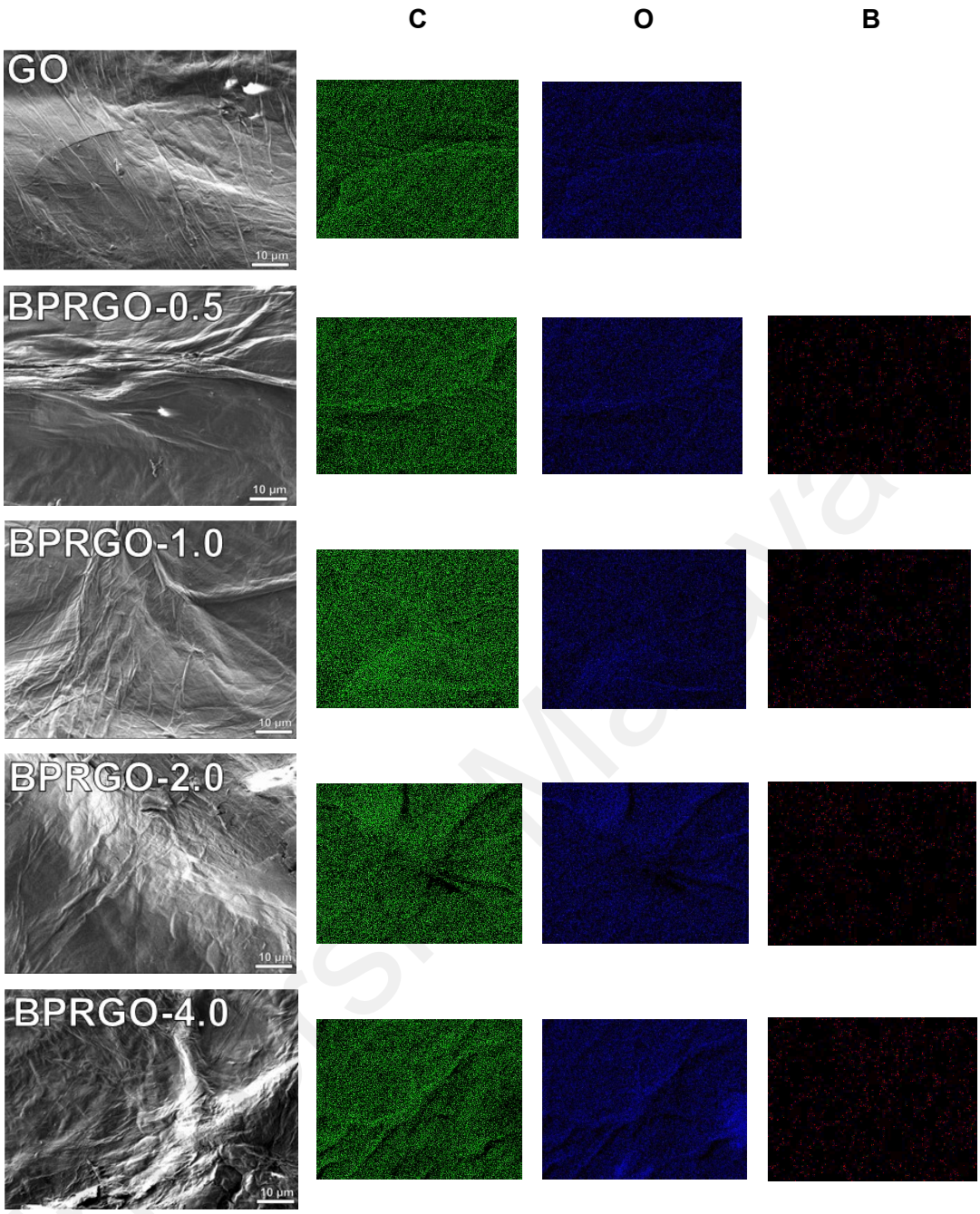

Figure 5.1: SEM and elemental mapping images of GO and BPRGO samples.

In Figure 5.2a, the detection of XPS B 1s peak affirmed that B atoms were introduced into the GO after the photoirradiation process. Besides that, the absence of a H_3BO_3 peak at 194.0 eV (Okazaki et al., 1999) indicated the absence of any adhering or adsorbed H_3BO_3 precursor. The B 1s of the BPRGO samples were deconvoluted into three peaks at 191.7, 192.5, and 193.2 eV, which were ascribed to the BC_3, BC_2O, and BCO_2 groups,

respectively (Mannan et al., 2018; Singh et al., 2018). The schematic B bonding configuration of BPRGO is illustrated in Figure 5.2d. This is similar to the structure of BrGO reported by Putri and coworkers (Putri et al., 2017). The BC_3 groups originated from the B atoms substituted into the graphitic basal of GO. Meanwhile the BC_2O and BCO_2 groups were the oxygenated boron groups (OBGs) doped at the edges or defect sites (Chowdhury et al., 2018). As shown in Table 5.1, the B at% gradually increased from 2.2 at% to 3.0 at% for the photoirradiation duration between 0.5 to 2 h but decreased to 1.9% after 4 h. Meanwhile, the OBGs/B ratio increased from 0.21 (BPRGO-0.5) to 0.57 (BPRGO-1.0), and then gradually decreased to 0.29 (BPRGO-4.0). This suggested that longer photoirradiation duration induced more doping of B atoms but excessive photoirradiation caused some B dopants especially those OBGs at the edges or defect sites to detach from the BPRGO. Similar to the previous nitrogen doping on GO (Tsai et al., 2020), the excessive nitrogen doping caused the nitrogen atoms at the edges or defect sites of the graphene to break off due to lattice stress.

In the C 1s spectra of the samples (Figure 5.2b), the four peaks detected at 284.5, 286.5, 287.7, and 289.2 eV corresponded to the C-C/C=C, C-O, C=O, and O=C-O groups, respectively (Siong et al., 2020). Based on Table 5.1, BPRGO samples displayed a reduction in OCGs/C ratio after photoirradiation as compared to that of GO. The observation implied that the photoirradiation process simultaneously doped B atoms and reduced the OCGs on GO. Meanwhile, Figure 5.2c displays a peak at 532.4 eV, which corresponded to the O-C groups in the O 1s spectra (Moreira et al., 2020). Table 5.1 shows that the oxygen at% of the BPRGO samples were lesser than that of GO, which was similar to the OCGs/C ratios. Intriguingly, BPRGO-1.0 had a higher content of OCGs and oxygen at% than BPRGO-0.5 due to the higher content of OBGs in BPRGO-1.0. The formation of more OBGs could introduce new C-O bonds at the edges or defect sites of

the graphitic structure of BPRGO. The formation of new C-O bonds by OBGs on BPRGO-1.0 is illustrated in Figure 5.2e.

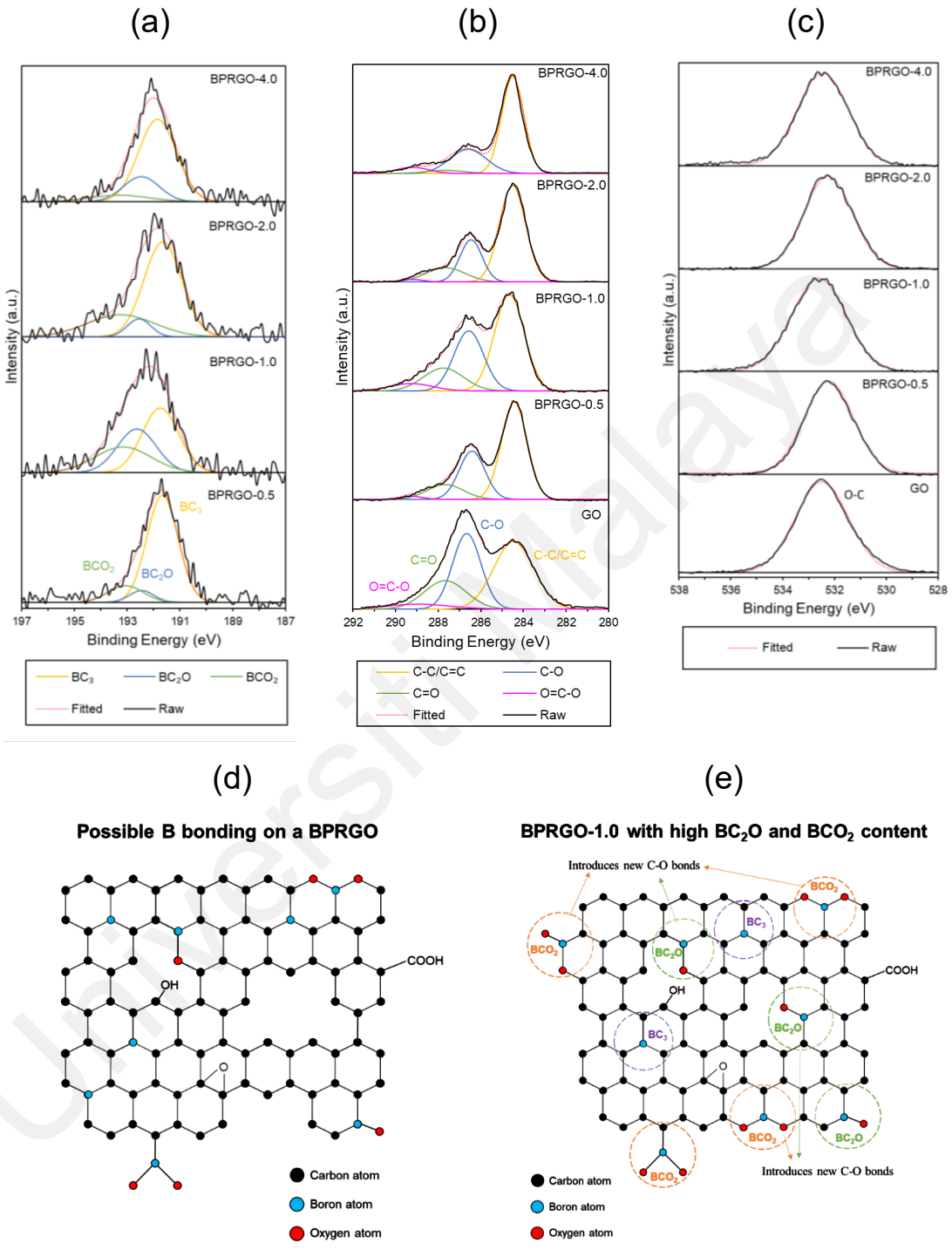

Figure 5.2: XPS spectra of GO and BPRGO samples for (a) B 1s, (b) C 1s, (c) O 1s, (d) Possible boron bonding configurations of BPRGO, and (e) Structure of BPRGO-1.0 with a high content of OBGs with BC_2O and BCO_2 groups.

Table 5.1: Summary of XPS compositions for GO and BPRGO samples

Sample	XPS (at%)			C 1s (at%)				$\frac{OCGs}{C}$	B 1s (at%)			$\frac{OBGs}{B}$
	C	O	B	C-C/ C=C	C-O	C=O	O=C -O		BC_3	BC_2O	BCO_2	
GO	66.8	33.2	0.0	43.2	33.9	18.7	4.3	0.57	-	-	-	-
BPRGO-0.5	69.6	28.2	2.2	57.2	28.5	12.5	1.8	0.43	79.5	6.6	13.9	0.21
BPRGO-1.0	64.4	33.1	2.6	48.9	30.2	15.5	5.4	0.51	43.0	26.0	31.0	0.57
BPRGO-2.0	69.9	27.1	3.0	62.0	23.0	13.7	1.3	0.38	64.7	7.8	27.5	0.35
BPRGO-4.0	74.3	23.9	1.9	64.5	26.2	3.4	5.8	0.36	70.8	20.6	8.6	0.29

Figure 5.3a displays the FTIR spectra of the GO and BPRGO samples. GO showed several characteristic peaks at 1040, 1390, 1630, 1730, and 3200-3400 cm^{-1}, which corresponded to the C-O stretching modes, C-OH groups, C=C groups, C=O stretching, and surface adsorbed water (Ţucureanu et al., 2016). The BPRGO samples exhibited similar FTIR patterns as GO, though with a new peak at 1190 cm^{-1}, which was attributed to the B-C bands (Van Khai et al., 2012). Additionally, the wide surface adsorbed water peaks of the BPRGO samples became sharp at 3200 cm^{-1}, which corresponded to the presence of B-OH stretching modes (Mannan et al., 2018; Romanos et al., 2013). The findings were well agreed with the XPS results, where B groups were doped on the BPRGO samples.

Figure 5.3b shows the Raman patterns of the GO and BPRGO samples. All samples displayed two prominent peaks at 1350 cm^{-1} (D band) and 1600 cm^{-1} (G band). The D band represented the defects and disorders in the graphitic structure, while the G band was related to the in-plane stretching modes of sp^2 bonds (Q. Zhang et al., 2020). The intensity ratio of D and G bands (I_D/I_G) increased from 0.88 (GO) to 0.94 (BPRGO-2.0 and BPRGO-4.0). This increment of I_D/I_G ratio was due to the lattice distortion from B-doping (Putri et al., 2017) because the B-C bond (1.49 Å) is longer than the pristine C-C bond (1.41 Å) (Rani & Jindal, 2013). Additionally, the samples exhibited two smaller

bands at ~2736 and ~ 2930 cm^{-1}, which were referred to the 2D (second order of D band) and S3 (imperfect activated grouping of phonon) bands (Li et al., 2016). Among the BPRGO samples, BPRGO-1.0 had the highest intensity ratio of 2D and G (I_{2D}/I_G) at 0.22. The high I_{2D}/I_G ratio suggested a high amount of restored conjugated graphitic domains (Mortazavi et al., 2018) in the BPRGO-1.0 after photoirradiation.

The XRD patterns were shown in Figure 5.3c. The GO exhibits a characteristic peak at $2\theta = 10^{\circ}$, which was attributed to the exfoliated basal planes (Putri et al., 2017). After the photoirradiation process, the GO peak was still present in the BPRGO samples, but the peak intensity was gradually reduced. This indicated that the BPRGO samples were only partially reduced, which was in concordance with the XPS and FTIR analysis.

Figure 5.3 (d and e) display the UV-Vis absorbance spectra and the corresponding Tauc plot of the samples. The GO exhibited a peak at 230 nm and a shoulder at ~300 nm. The peak represented the $\pi \rightarrow \pi^*$ transitions of the C=C bond, while the shoulder was the $n \rightarrow \pi^*$ transitions of the C=O bond (Hsu et al., 2013). After photoirradiation treatment, the absorbance peaks of the BPRGO samples were not shifted, while the shoulders were gradually widened. From the Tauc plot, the bandgap was gradually narrowed from 3.50 – 4.50 eV (GO) to 3.30 – 4.0 eV (BPRGO-4.0). The reduction of bandgap was attributed to the synergistic effects of B-doping and OCGs removal during the photoirradiation process. The p-type B-doping introduces new acceptor levels between the VB and conduction band (CB) (Srikanth et al., 2012). The acceptor levels could act as intermediate energy levels and reduce the overall E_{BG} (Hu et al., 2019; Luo et al., 2017) of the BPRGO. Besides that, the reduction of OCGs restored some sp^2 graphitic domains in the BPRGO and also led to a narrower bandgap.

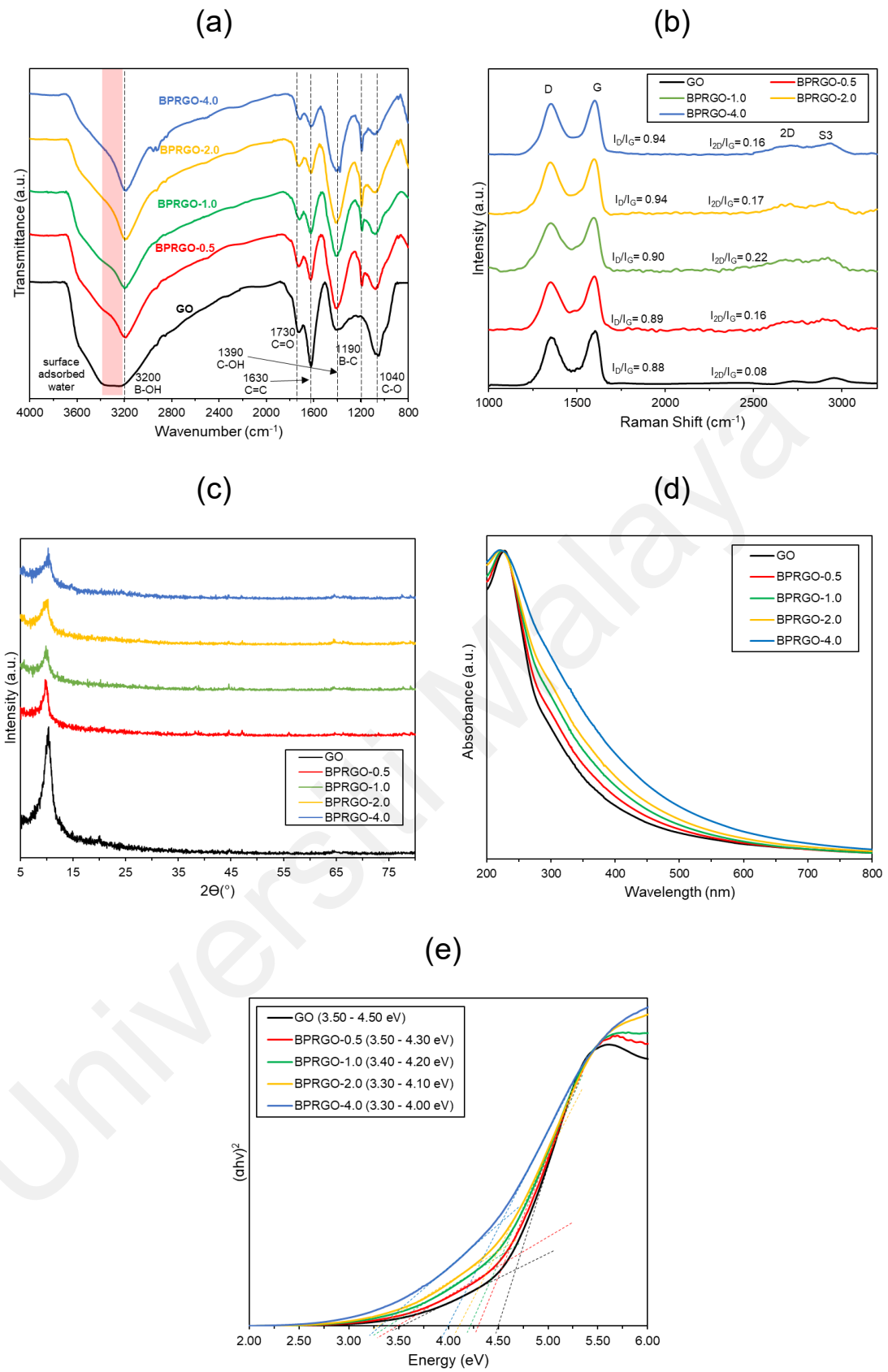

Figure 5.3: (a) FTIR spectra, (b) Raman spectra, (c) XRD diffractogram, (d) UV-Vis absorbance, and (e) Tauc plot of GO and BPRGO samples.

5.1.2 Electrochemical properties of BPRGO samples

Figure 5.4a displays the M-S plots of GO and BPRGO samples. Since the samples exhibit negative M-S slopes, they were p-type semiconductors. The V_{FB} of GO, BPRGO-0.5, BPRGO-1.0, BPRGO-2.0, and BPRGO-4.0 were +1.26, +1.28, +1.46, +1.30, and +1.28 V vs. NHE at pH 7, respectively. Since the VBM is roughly +0.3 V from the V_{FB} of a p-type semiconductor (Yin et al., 2016), therefore the VBM of GO, BPRGO-0.5, BPRGO-1.0, BPRGO-2.0, and BPRGO-4.0 were calculated to be +1.56, +1.58, +1.76, +1.60, and +1.58 V vs. NHE at pH 7, respectively. The shifting of the energy band levels was probably due to the changes in OCGs and OBGs (Ngidi et al., 2020; Siong et al., 2020) after photoirradiation. It was reported that the VBM of GO could be shifted up to 1.08 eV after B-doping (Ngidi et al., 2020). All BPRGO samples had a larger hole carrier density than that of GO and thus proved that B atoms were doped as shallow acceptors. Shallow acceptor dopants are able to accept electrons from the VB of the host semiconductor, therefore introducing extra hole carriers to the VB (Chen, 2004; Lin et al., 2011). Among the BPRGO samples, BPRGO-1.0 had the largest hole carrier density of 2.3×10^{16} cm^{-3}, which was 2.3 times higher than that of GO. This was attributed to the relatively high B doping concentration (2.6 at%) with the highest content of OBGs (0.57). Based on previous studies, the BC_2O and BCO_2 groups were indeed able to induce more hole carriers than the BC_3 groups (Sarkar et al., 2021; Q. Zhang et al., 2020). This affirmed that BPRGO-1.0 with the highest amount of OBGs had higher hole carrier density, which can be beneficial for photocatalytic activity.

Figure 5.4b displays the EIS of the samples in the form of a Nyquist plot. A smaller arc radius of the Nyquist plot indicates a better conductivity (Siong et al., 2020). It was found that BPRGO-1.0 had the smallest arc radius, hence exhibiting the highest conductivity. This phenomenon was because BPRGO-1.0 had the largest hole carrier density as shown in the M-S analysis. A p-type semiconductor with a larger hole carrier

density has a higher p-type conductivity, which leads to the better transportation of charge carriers (Lin et al., 2011; Yeom et al., 2015).

PL (Figure 5.4c) and photocurrent (Figure 5.4d) were carried out to compare the photogenerated charge carrier recombination rate of the samples. Among the samples, the BPRGO-1.0 exhibited the lowest PL peak intensity and the highest photocurrent density. This signified that BPRGO-1.0 had the slowest photogenerated charge carrier recombination rate (Siong et al., 2019; Siong et al., 2020). The finding was due to the good ability of BPRGO-1.0 in transporting charge carriers, which subsequently eased the separation of the photogenerated free electrons and holes. Generally, a better ability to transport charge carriers could retard the recombination rate of photoinduced charge carriers (Huang et al., 2020).

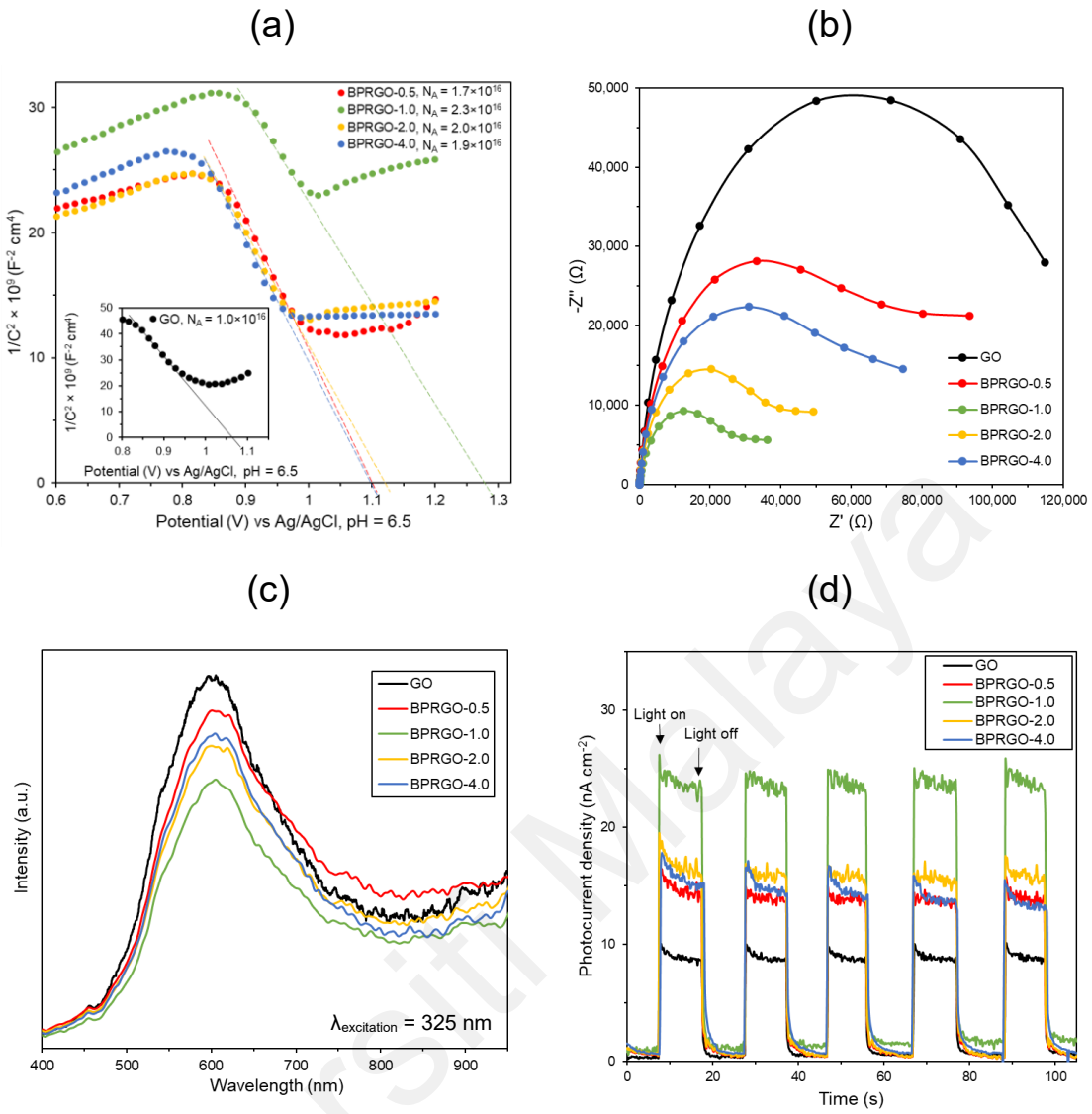

Figure 5.4: (a) M-S plot, (b) EIS, (c) photoluminescence, and (d) photocurrent of GO and BPRGO samples.

5.2 PCO performances of BPRGO samples

The PCO of gaseous methanol by the photocatalysts were examined. In control experiments, methanol was not degraded without light or photocatalyst after 6 h. All samples were able to remove a similar amount of methanol (10 – 12%) after the 1 h of dark adsorption (Appendix F). Figure 5.5 (a and b) display the PCO performance of the samples at room conditions. It was found that all BPRGO samples were able to remove more methanol than GO. Among them, the BPRGO-1.0 exhibited the best PCO performance at 62.0% (in 6 h) with a rate constant of 0.195 h^{-1}, which was 10 times more effective than the GO. The enhancement of PCO performance of BPRGO-1.0 was

attributed to its relatively high B-doping concentration with high OBGs content, which led to a large hole carrier density and a slow charge carrier recombination rate. The availability of more photogenerated charge carriers led to the production of more reactive species to degrade pollutants (Siong et al., 2020). Figure 5.5c and Appendix L demonstrate the correlation between the hole carrier density and photocatalytic activity of the BPRGO photocatalysts. It was shown that a higher density of hole carrier indeed significantly improved the rate of PCO. This new insight signifies the importance of OBGs to induce more charge carriers and active radicals for better VOCs removal. Additionally, BPRGO-1.0 did not have a significant drop (only ~4%) in PCO effectiveness even after five cycles, therefore indicating good recyclability (Figure 5.5d).

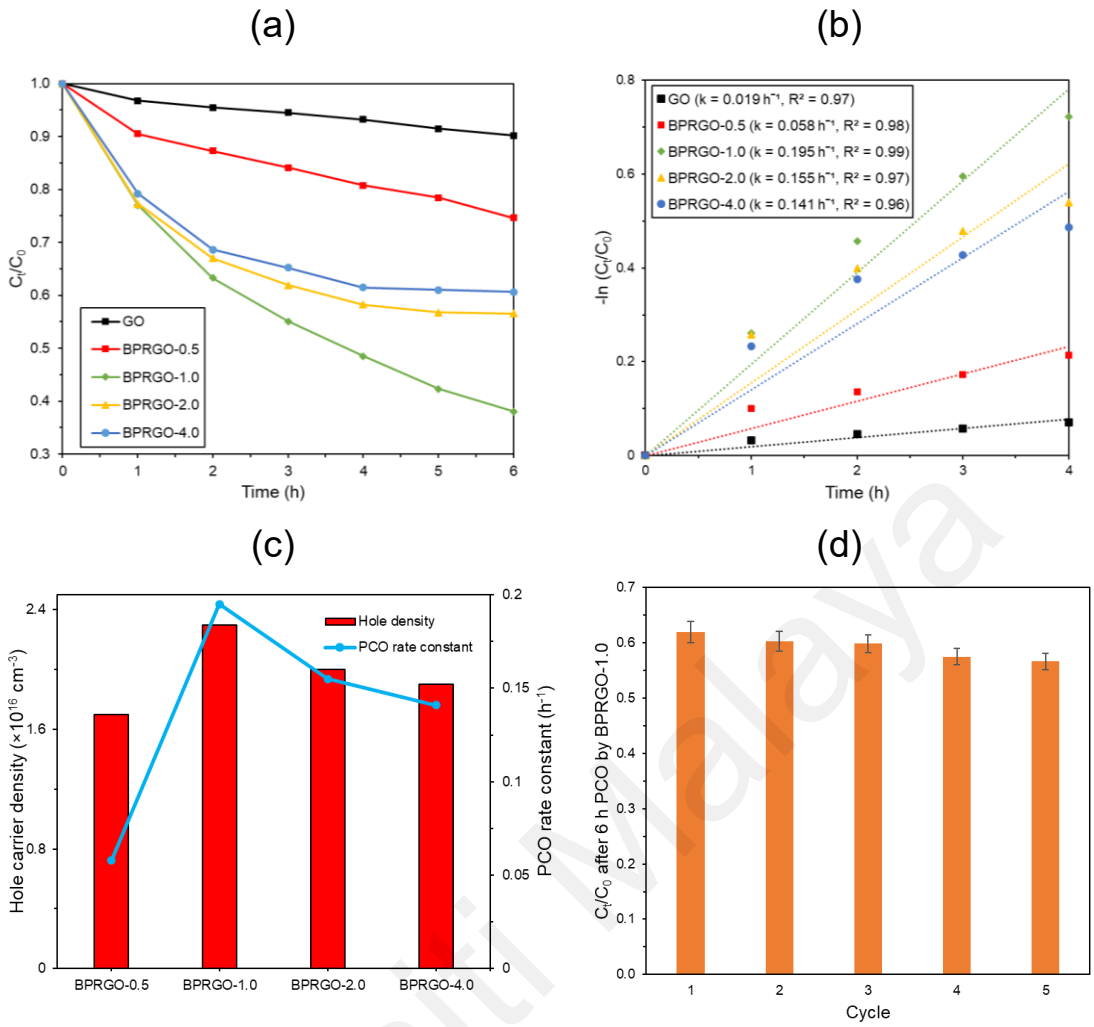

Figure 5.5: (a) PCO removal, (b) pseudo-first order kinetic plot, (c) Correlation of hole carrier density and the rate of PCO, and (d) Recyclability test of BPRGO-1.0.

Ambient humidity is an important factor for the photodegradation of VOCs because water vapour can affect the processes of VOCs adsorption and •OH radicals generation (Mamaghani et al., 2017). The sample with the highest PCO performance, namely BPRGO-1.0 was used as the model photocatalyst for the ambient humidity study. It was found that the 1 h Ads% (12-16%) was not significantly changed by the varying ambient humidity. From Figure 5.6 (a and b), the optimal humidity for the PCO by BPRGO-1.0 was 36 RH%, where 79.9% of methanol was removed in 6 h with a rate constant of 0.283 h^{-1}. At 36 RH%, there were sufficient adsorption sites for VOCs and a good amount of water molecules to produce •OH radicals for PCO. However, the rate of photodegradation

was reduced at lower humidity (30 RH%) because the low quantity of water molecules in the air had limited the generation of •OH radicals.

Figure 5.6c shows the concentration of CO_2 evolved from the PCO process by BPRGO-1.0 at 36 RH%. No CO_2 was formed in the absence of photocatalyst or methanol. After 6 h, the M% was calculated to be 90.8%. The findings indicated that BPRGO-1.0 was capable of mineralising toxic methanol into harmless CO_2, therefore purifying the air. Nevertheless, the incomplete mineralisation suggested that some methanol molecules were re-adsorbed onto the surface of the photocatalyst (Debono et al., 2017).

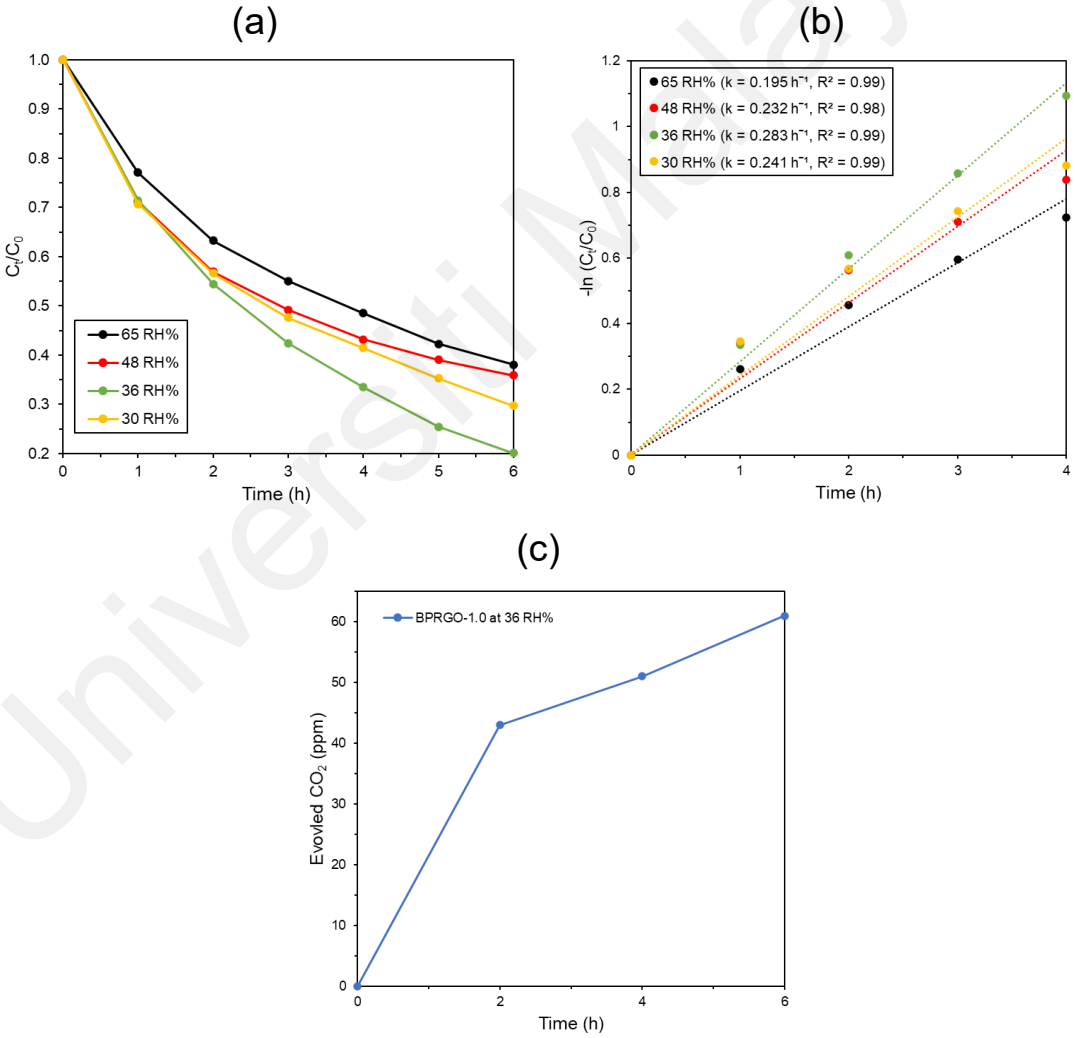

Figure 5.6: (a) PCO performance of BPRGO-1.0 under varying humidity, (b) pseudo-first order kinetic plot of BPRGO-1.0 under varying humidity, and (c) Evolution of CO_2 during the PCO process by BPRGO-1.0 at 36 RH%.

5.3 Reactive species and mechanism of PCO by BPRGO

In gas-phase PCO, most •OH radicals are converted from water vapour, while $\bullet O_2^-$ radicals are generated from oxygen (P. Li et al., 2020; Rao et al., 2022). The active species involved in PCO were determined by comparing three different ambient atmospheric conditions, which were air at 36 RH% (contained •OH, $\bullet O_2^-$ radicals, and the photogenerated hole at VB (h_{VB}^+)), N_2 at 36 RH% (contained •OH radicals and h_{VB}^+), and dry N_2 (contained h_{VB}^+ only). As shown in Figure 5.7a, BPRGO-1.0 was able to remove 47.5%, 70.0%, and 79.9% of methanol under humid air (36 RH%), humid N_2 (36 RH%), and dry N_2 (0 RH%), respectively. The findings suggested that all three reactive species contributed to the PCO process, in which their relative contributions were as such h_{VB}^+ (~48%) > •OH (~23%) > $\bullet O_2^-$ (~10%).

Based on the results of M-S and bandgap, the band structures of the BPRGO samples are shwon in Figure 5.7b. The free-electron (e^-) and h_{VB}^+ charge carriers were generated under UV-A irradiation at the CB and VB of BPRGO-1.0, respectively. The CB and VB potential is related to the redox reaction of a photocatalyst. For BPRGO-1.0, the potential of CB is at a sufficiently negative value to reduce the oxygen (O_2) into $\bullet O_2^-$ radicals (-1.64 V vs. NHE, pH 7). Meanwhile, the potential of VB is at a highly positive value to oxidise the water vapour into •OH radicals (+2.56V vs. NHE, pH 7). The h_{VB}^+ in tandem with the $\bullet O_2^-$ and •OH radicals then mineralised the VOCs molecules into harmless CO_2 and water.

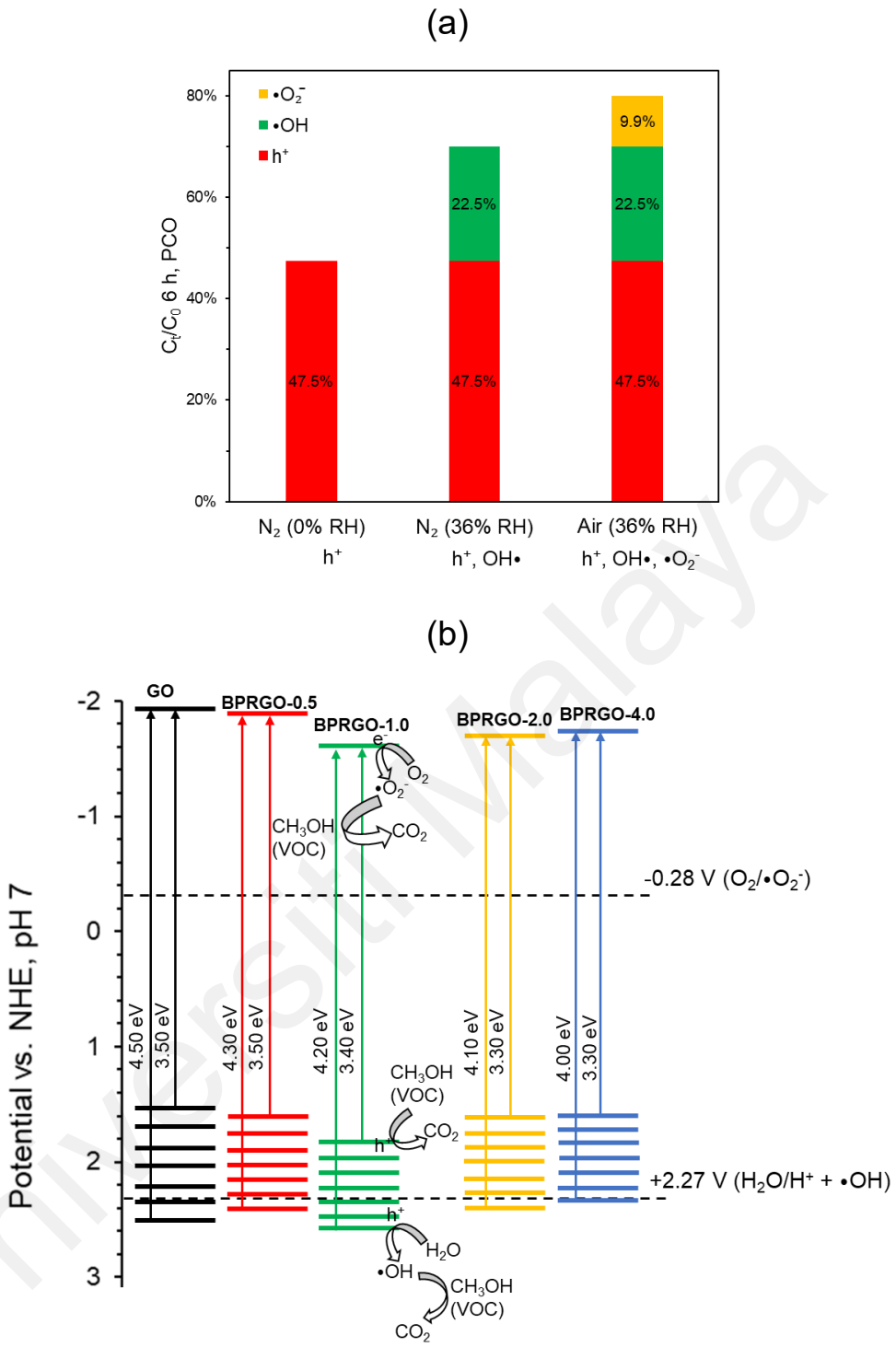

Figure 5.7: (a) Reactive species study of BPRGO-1.0 for 6 h of PCO and (b) band structures and PCO mechanism of BPRGO.

In summary, the photoirradiation of GO with the presence of H_3BO_3 is a facile, scalable, and solution-based method to produce effective metal-free BPRGO photocatalysts. This photoirradiation method allows control over the B doping and bonding configuration of GO. For instance, BPRGO-1.0 exhibited high amount of B concentration (2.6 at%) and

OBGs content (0.57). The high amount of OBGs group had increased the hole carrier density and conductivity of p-type BPRGO-1.0 photocatalyst. This had suppressed the recombination of photogenerated free-electrons and holes. As a result, BPRGO-1.0 was capable of removing up to 79.9% of methanol with a mineralisation efficiency of 90.8% under UV-A irradiation. Among the three reactive species, the h_{VB}^{+} species was the most important reactive species in the PCO process by BPRGO-1.0.

CHAPTER 6: Fluorine-doped photoreduced graphene oxide (FPRGO) photocatalyst for the removal of VOCs

In this chapter, a series of FPRGO samples with different photoirradiation duration was synthesized from GO. After the photoirradiation process in the presence of TFA, the GO was simultaneously photoreduced and F-doped. The samples were characterized to determine their physicochemical and electrochemical properties (Section 6.1). Then, PCO experiments were carried out to investigate the effect of photoreduction on the photoactivity of the FPRGO samples (Section 6.2). Lastly, the band structures and PCO mechanism of the FPRGO photocatalyst were determined (Section 6.3).

6.1 Characterizations of FPRGO samples

A set of characterization tests were conducted on the FPRGO samples to determine their physicochemical properties, which include XRD, Raman, FTIR, UV-Vis, XPS, and PL. Furthermore, the electrochemical properties of the FPRGO samples were investigated by M-S, EIS, and photocurrent techniques.

6.1.1 Physicochemical properties of FPRGO samples

Figure 6.1 displays the FESEM and elemental mapping images of the GO and FPRGO samples. It was observed that the surfaces of the FPRGO samples were more crumpled and corrugated than GO. The observations coincided with previous reports, in which F-doping caused wrinkling effects on the surface of GO (An et al., 2016; Musico et al., 2019). In addition, the detection of uniformly distributed F atoms on the FPRGO samples by the elemental mapping analysis indicated that F was successfully doped on the GO.

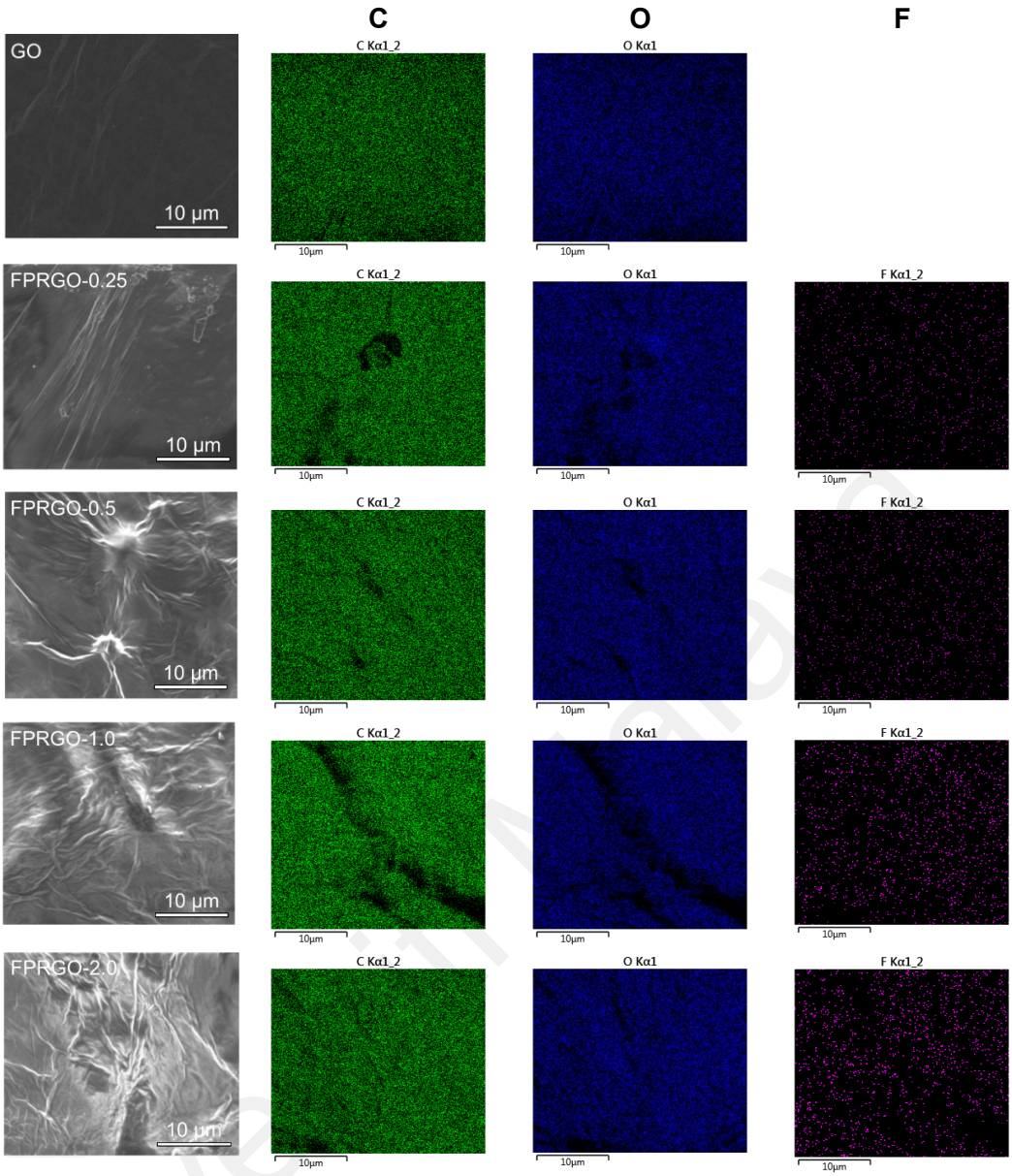

Figure 6.1: SEM and elemental mapping images of GO and FPRGO samples.

Figure 6.2 shows the XPS results of the GO and FPRGO samples. The detection of F 1s peaks indicated that F dopants were successfully introduced into GO by the photoirradiation method (Figure 6.2a). In Table 6.1, the concentration of F dopants increased gradually with photoirradiation time, which was from 0.15 at% (0.25 h) to 0.47 at% (2 h). The F dopant concentrations of the FPRGO samples were comparable to the concentrations reported in previous F-doped graphene-based material studies (0.10 – 0.83 at%) (Jiang et al., 2015; Parthiban et al., 2019; Qiao et al., 2016; Sun et al., 2013). Notably, all FPRGO samples exhibited a single F 1s peak at 688.3 eV corresponding to the semi-

ionic C-F bonds (Y. Chang et al., 2021; Nakajima et al., 2000; Peera et al., 2015). It is noteworthy that, the other two possible F 1s peaks between 686 – 687 eV (ionic C-F bonds (Y. Chang et al., 2021; Nakajima et al., 2000)) and 689 – 691 eV (covalent C-F bonds (Feng et al., 2016; Nakajima et al., 2000)) were not detected. Notably, the semi-ionic C-F bond was reported to have higher polarity (Y. Chang et al., 2021; Peera et al., 2015), faster charge carrier transportation (Sim et al., 2022), and higher electrocatalytic performance (Y. Chang et al., 2021; Kim et al., 2018; Peera et al., 2015) than the ionic and covalent C-F bonds. Therefore, the success of inducing semi-ionic C-F bonds on FPRGO potentially enables a high photocatalytic activity.

The C 1s scans of the samples (Figure 6.2b) were deconvoluted into four main peaks at 284.5, 286.5, 287.7, and 289.2 eV ascribed to the C-C/C=C, C-O, C=O, and O=C-O groups, respectively (Stobinski et al., 2014). Besides that, the FPRGO samples exhibited an extra peak at 288.5 eV ascribed to the semi-ionic C-F bonds formed after F-doping (H. Zhang et al., 2016). The content of the semi-ionic C-F bonds increased from 0.0 to 5.5 at%, while the OCGs ratio decreased from 0.57 to 0.17 with longer photoirradiation time (Table 1). The oxygen content (at%) of O 1s spectra (Figure 6.2c) also decreased gradually after photoirradiation. The results affirmed that the photoirradiation treatment simultaneously doped and reduced GO. Figure 6.2d illustrates the structure of FPRGO with semi-ionic C-F bonds.

Table 6.1: Summary of XPS compositions for GO and FPRGO samples

Sample	XPS (at%)			C 1s (at%)					$\frac{OCGs}{C}$
	C	O	F	C-C/ C=C	C-O	C=O	C-F	O=C-O	
GO	66.80	33.20	0.0	43.1	33.9	18.7	0.0	4.3	0.57
FPRGO-0.25	71.97	27.87	0.15	51.4	37.2	8.2	1.1	2.1	0.47
FPRGO-0.5	73.30	26.54	0.16	52.8	32.3	12.4	1.1	1.4	0.46
FPRGO-1.0	73.99	25.83	0.18	54.0	34.5	7.5	1.3	2.7	0.45
FPRGO-2.0	82.30	17.23	0.47	77.6	11.9	4.3	5.5	0.7	0.17

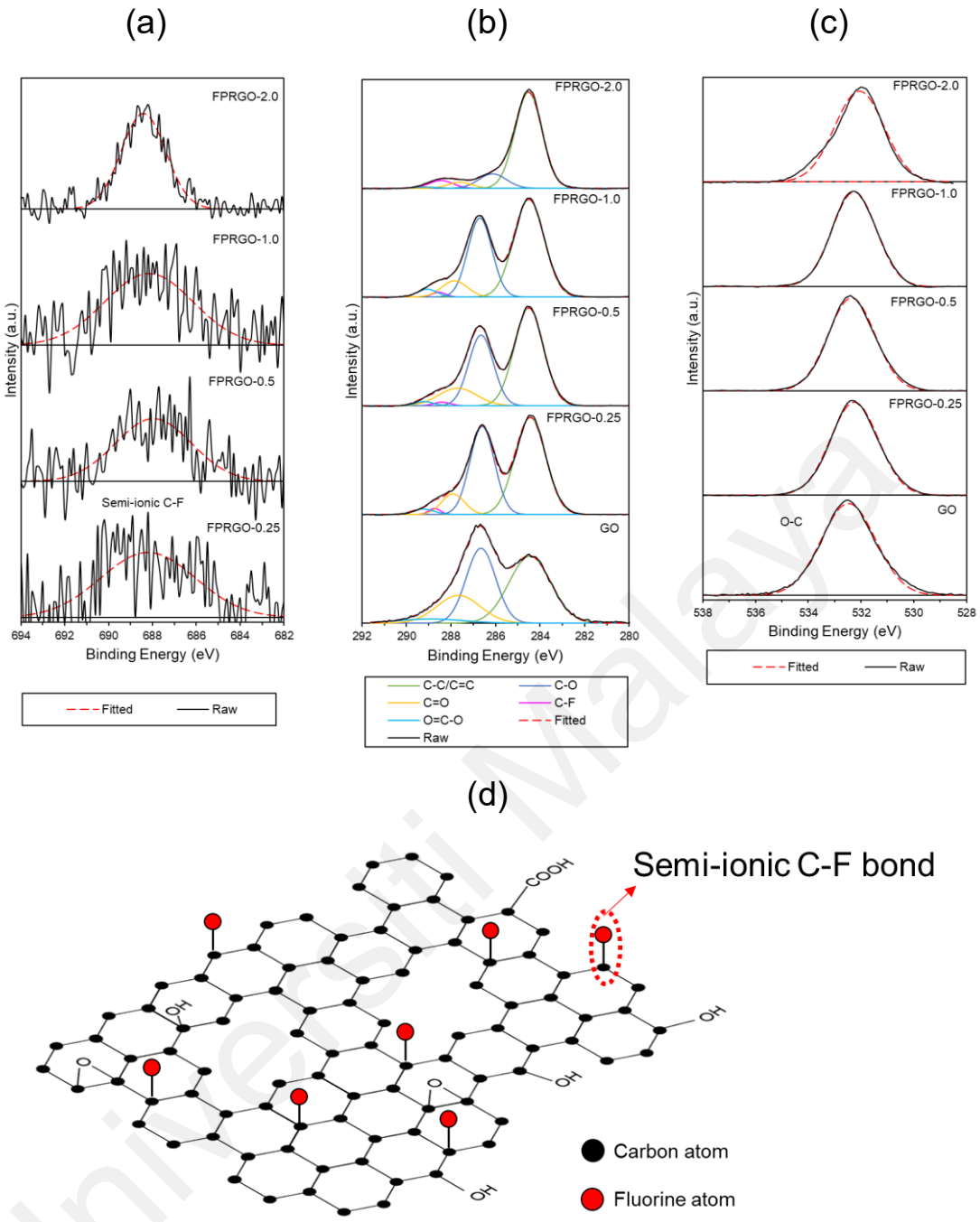

Figure 6.2: XPS spectrum of (a) F 1s, (b) C 1s, (c) O 1s of GO and FPRGO samples, and (d) Schematic structure of FPRGO.

Figure 6.3a demonstrates the FTIR spectra of the GO and FPRGO samples. GO exhibited several peaks at 1040, 1390, 1630, 1730, and 3000-3600 cm^{-1} corresponded to the C-O stretching modes, C-OH groups, C=C groups, C=O stretching, and surface adsorbed water/OH group (Chong et al., 2018). The FPRGO samples showed two new peaks at 1220 and 1260 cm^{-1} ascribed to the C-F bonds (Shahzad et al., 2017), which

aligned with the XPS analysis. Besides that, the FPRGO-0.25 sample contained a peak at 2925 cm^{-1} attributed to the C-H bonds (Sandoval et al., 2016), which disappeared after longer doping duration due to the conversion of the C-H bonds into C-F bonds (Li et al., 2004).

Figure 6.3b displays the Raman peaks of the GO and FPRGO samples. All samples exhibited two main peaks at 1350 (D band) and 1600 cm^{-1} (G band). The D and G bands are ascribed to the defects/distortion in the graphitic structure and the in-plane stretching modes of the C=C sp^2 bonds (Q. Zhang et al., 2020). Besides that, the samples also exhibited two smaller bands at ~2736 and ~ 2930 cm^{-1}, which were referred to the 2D (second order of D band) and S3 (imperfect activated grouping of phonon) bands (Li et al., 2016). After photoirradiation, the intensity ratio I_D/I_G gradually increased from 0.88 (GO) to 0.91 (FPRGO-2.0) because of GO reduction and F-doping. Generally, a higher F-doping concentration shows a higher I_D/I_G ratio (An et al., 2016). This is because the formation of C-F bonds caused lattice distortions to the nearby C-C bonds. It was reported that the C-F bond on F-doped graphene-based material could stretch the C-C bond length from 1.41 Å up to 1.58 Å (X. Wang et al., 2014).

The XRD spectra of GO and FPRGO samples are shown in Figure 6.3c. The GO exhibited a typical peak at $2\theta = \sim 10^{\circ}$, which was attributed to the exfoliated GO sheets (Putri et al., 2017). Although the GO peak was still intact in the FPRGO samples after photoirradiation, the peak intensity was depleted. This indicated that the FPRGO was photoreduced, which concorded with the XPS analysis.

Figure 6.3 (d and e) demonstrate the UV-Vis absorbance patterns and Tauc plot analysis of the GO and FPRGO samples. The GO exhibited a peak at 230 nm and a shoulder at ~300 nm. The peak represented the $\pi \rightarrow \pi^*$ transitions of the C=C bond, while the shoulder was the $n \rightarrow \pi^*$ transitions of the C=O bond (Hsu et al., 2013). After

photoirradiation, the FPRGO samples exhibited gradually more absorbance in the 300 – 800 nm region. From the Tauc plot, it was determined that the bandgap was gradually narrowed from 3.50 – 4.50 eV (GO) to 3.25 – 4.0 eV (FPRGO-2.0). This was mainly due to the reduction of OCGs and the restoration of conjugated graphitic domains (Olumurewa et al., 2020) of FPRGO after photoirradiation.

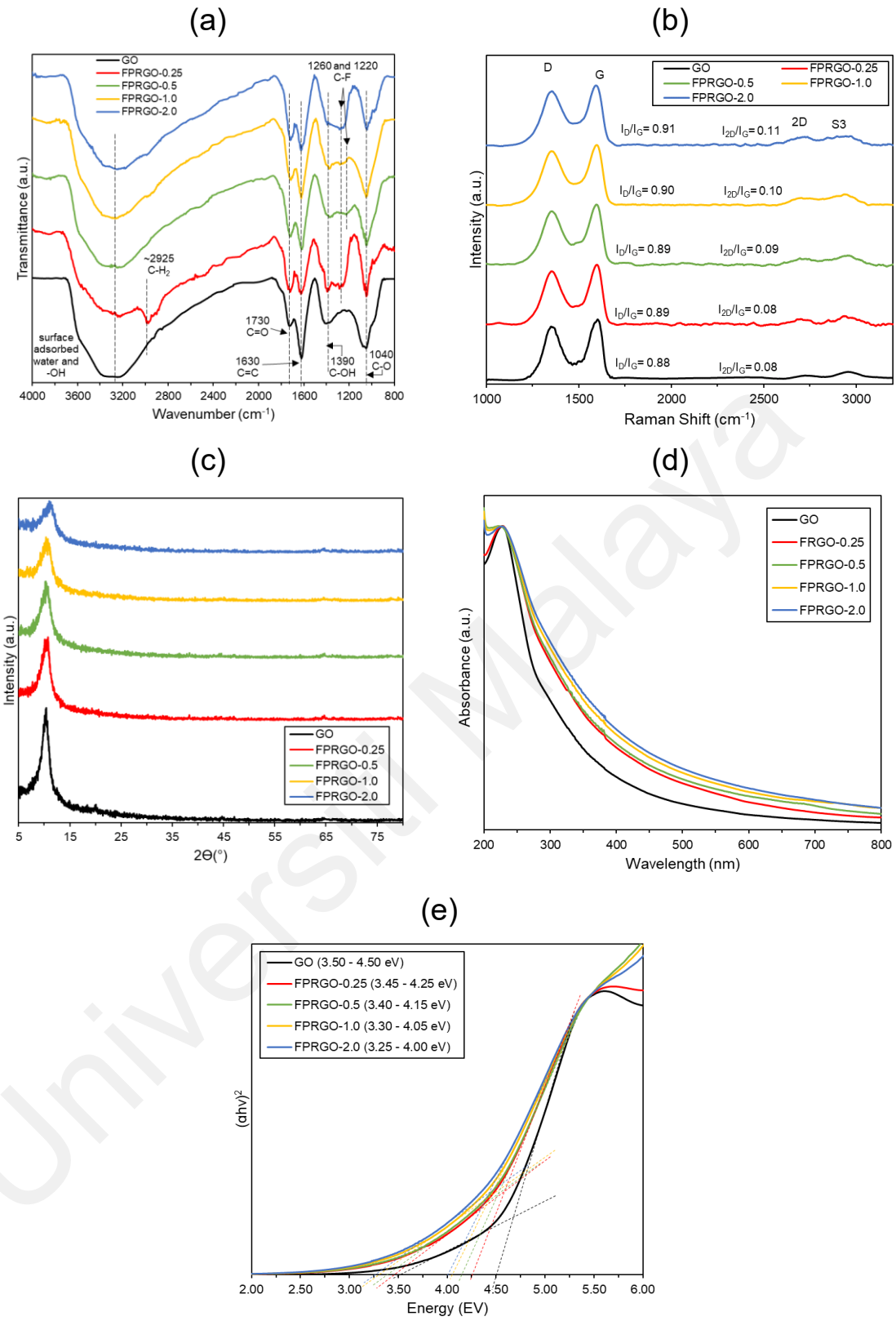

Figure 6.3: (a) FTIR spectra, (b) Raman spectra, (c) XRD diffractogram, (d) UV-Vis absorbance spectra, and (e) Tauc plot of GO and FPRGO samples.

6.1.2 Electrochemical properties of FPRGO samples

Figure 6.4a exhibits the M-S plots of the samples. The GO and FPRGO samples displayed negative slopes corresponded to p-type conductivities. Their p-type properties were induced by the presence of electron-withdrawing oxygen (O) and F atoms on the surfaces of GO and FPRGO samples. This is because both O and F atoms had stronger electronegativity than the host C atoms (Putri et al., 2015; X. Wang et al., 2014). The V_{FB} of GO, FPRGO-0.25, FPRGO-0.5, FPRGO-1.0, and FPRGO-2.0 were +1.26, +1.29, +1.31, +1.19 and +1.19 V vs. NHE at pH 7, respectively. Since the VBM is approximately +0.3 V from the V_{FB} of a p-type semiconductor (Yin et al., 2016), therefore the VBM of GO, FPRGO-0.25, FPRGO-0.5, FPRGO-1.0, and FPRGO-2.0 were calculated to be +1.56, +1.59, +1.61, +1.49, and +1.49 V vs. NHE, pH 7, respectively.

It was found that all FPRGO samples had a larger hole carrier density than GO, which indicated that F-doping was able to increase the p-type conductivity of GO. Among the FPRGO samples, FPRGO-0.5 had the largest hole carrier density of 6.9×10^{16} cm^{-3}, which was remarkably seven folds higher than that of GO. The enlargement of hole carrier density was attributed to the semi-ionic C-F bonds on the FPRGO samples. It was reported that the semi-ionic C-F bond induced a high polarization effect (Y. Chang et al., 2021; Kim et al., 2018; Peera et al., 2015). A highly polarized acceptor dopant could greatly increase the hole carrier density of the host semiconductor. Notably, despite their higher F at%, both FPRGO-1.0 (0.18 at% F) and FPRGO-2.0 (0.47 at% F) had smaller hole carrier densities than that of FPRGO-0.5 (0.16 at% F). This indicated that 0.16 at% was the ideal concentration for shallow F-doping, while the excessive F-dopants in FPRGO-1.0 and FPRGO-2.0 became deep acceptor dopants. Shallow acceptor dopants are able to accept electrons and create extra hole carriers in the VB of the host semiconductor (Chen, 2004; Lin et al., 2011). Conversely, deep dopants cannot be ionised easily and thus unable to induce extra hole carriers (Aroutiounian et al., 2007). This is in

concordance with previous reports, where excessive doping could cause the formation of deep dopants and diminish the charge carrier density (Murashkina et al., 2018; Singh et al., 2008).

Figure 6.4b displays the EIS of the samples in the form of a Nyquist plot. A smaller arc radius indicates a smaller charge carrier transport resistance, which also signifies a higher conductivity (Siong et al., 2020). The FPRGO samples demonstrated smaller arc radii and thus their conductivities were higher than that of GO. This is due to the formation of semi-ionic C-F bonds on the FPRGO samples, which possessed low resistance and facilitated the diffusion of charge carriers (Sim et al., 2022). Among the FPRGO samples, the FPRGO-0.5 had the highest conductivity, attributed to its largest hole carrier density. It was reported elsewhere (Lin et al., 2011; Yeom et al., 2015) that a p-type semiconductor with a larger hole carrier density has a higher p-type conductivity. Notably, the excessive deep F-dopants in FPRGO-1.0 and FPRGO-2.0 were not fully ionised, therefore they had diminished hole carrier densities and conductivities.

PL (Figure 6.4c) and photocurrent (Figure 6.4d) were conducted to investigate the rate of recombination of photoinduced charge carriers in the photocatalysts. The FPRGO-0.5 displayed the lowest PL peak intensity and the highest photocurrent density, which signified that FPRGO-0.5 had the slowest photoinduced charge carrier recombination rate (Siong et al., 2019; Siong et al., 2020). This is because FPRGO-0.5 had the highest conductivity to ease the transportation and separation of charge carriers (Huang et al., 2020). Meanwhile, the FPRGO-1.0 and FPRGO-2.0 with higher F-dopant concentrations than FPRGO-0.5 had faster charge carrier recombination rates. As expected, the excessive deep F-dopants in FPRGO-1.0 and FPRGO-2.0 acted as recombination sites and trapped the photoinduced charge carriers. This concorded with others, in which excessive electronegative (Putri et al., 2015) and deep (Murashkina et al., 2018) dopants such as oxygen (O) and aluminium (Al) would act as recombination sites of charge carriers.

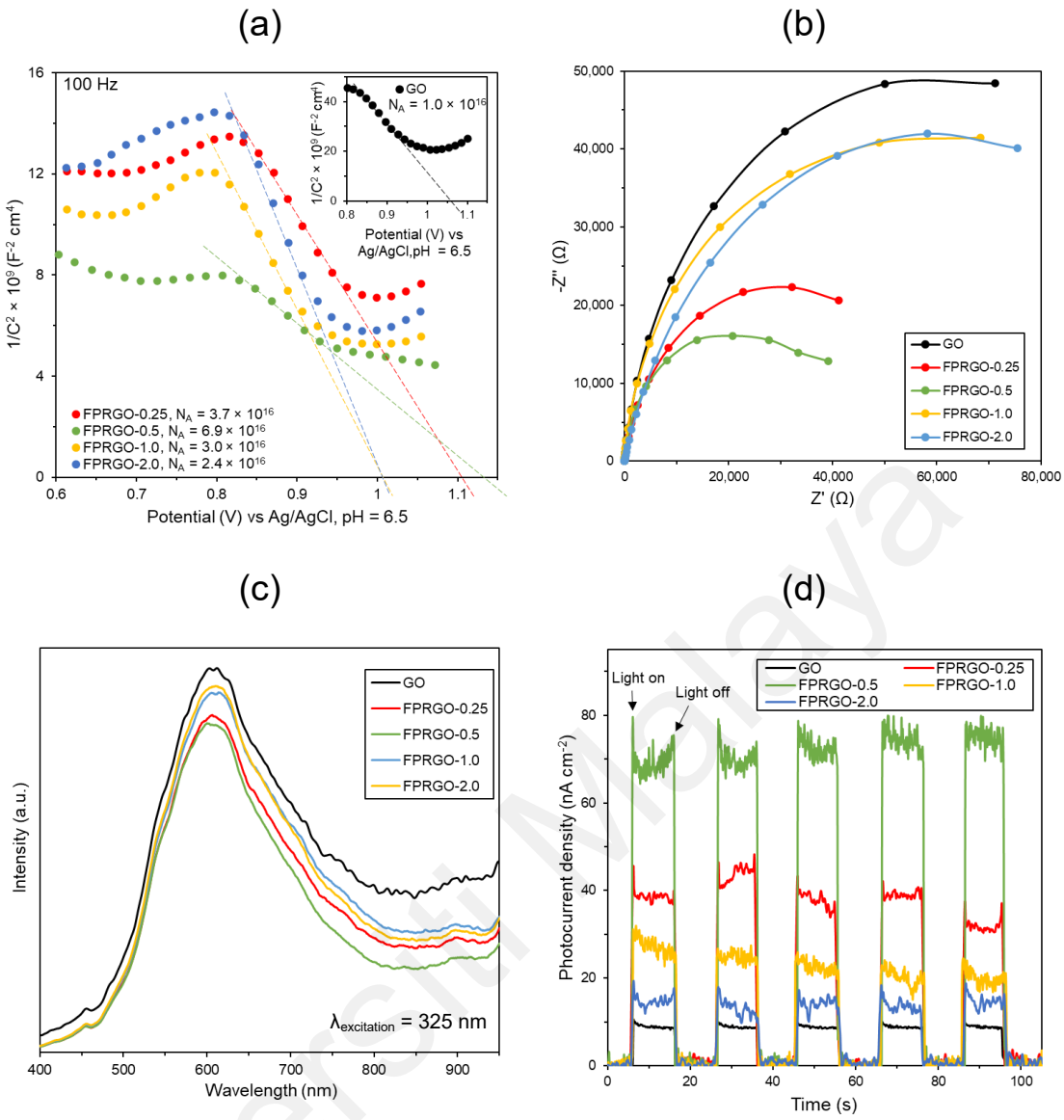

Figure 6.4: (a) M-S plot, (b) EIS, (c) photoluminescence, and (d) photocurrent of GO and FPRGO samples.

6.2 PCO performances of FPRGO samples

The photodegradation of gaseous methanol as the model VOCs by the photocatalysts was studied. In a set of control experiments, no methanol was degraded without the presence of light or photocatalyst within 6 h. All FPRGO samples were able to remove a similar amount of methanol (16 – 22%) after 1 h of dark adsorption (Appendix H). Figure 6.5 (a and b) display the PCO performance of the samples under room conditions. It was found that all FPRGO samples were able to remove more methanol than GO. Among them, the FPRGO-0.5 exhibited the best PCO performance at 73.1% after 6 h with a rate constant of 0.27 h^{-1}. This photodegradation rate is 14 times more effective than that of GO. The outstanding performance of FPRGO-0.5 was attributed to its ideal F-doping concentration of 0.16 at% with the formation of semi-ionic C-F bonds, which had led to high hole carrier density, high p-type conductivity, and slow recombination of photoinduced charge carriers. The slow recombination of charge carriers allowed the creation of more reactive species to photodegrade methanol. Figure 6.5c and Appendix L exhibit the correlation between the hole carrier density and photocatalytic activity of the FPRGO photocatalysts. It was shown that a higher density of hole carrier had a strong positive impact on the rate of PCO. Notably, the FPRGO-2.0 was only able to photodegrade 38.1% of methanol due to its excessive deep F-dopants that diminished the hole carrier density and trapped photoinduced charge carriers. The findings signify that the photoirradiation method is an effective method to introduce F dopant on GO. Additionally, the PCO of FPRGO-0.5 showed good reusability with only ~8% reduction even after five cycles (Figure 6.5d).

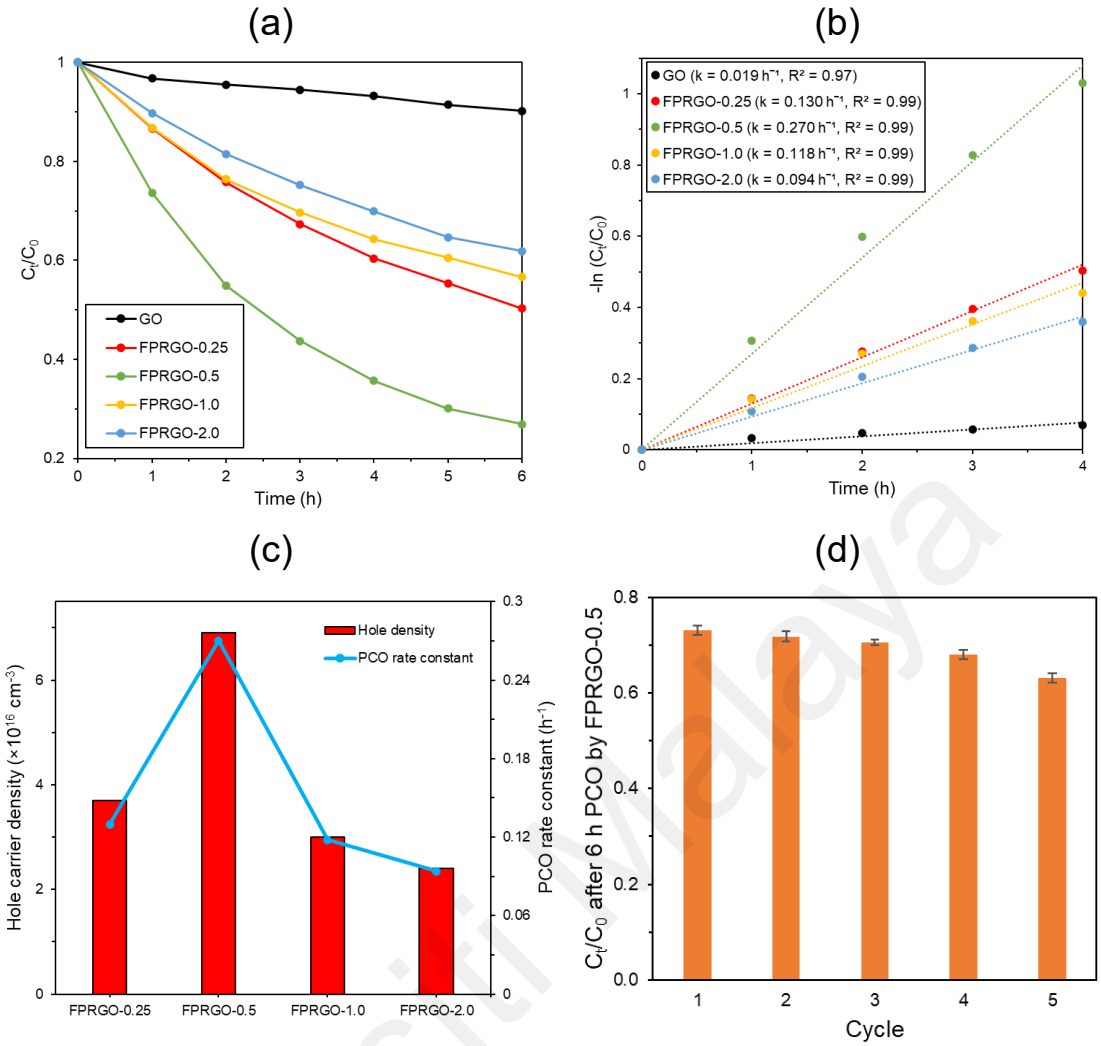

Figure 6.5: (a) PCO removal, (b) pseudo-first order kinetic plot, (c) Correlation of hole carrier density and rate of PCO, and (d) Recyclability test of FPRGO-0.5.

Humidity is an important factor in the photodegradation of VOCs because water vapour influences the VOCs adsorption and •OH radicals generation (Mamaghani et al., 2017). Based on FPRGO-0.5 which exhibited the highest PCO, a similar amount of methanol (18 – 22%) was removed after 1 h of dark adsorption despite the varying ambient humidity. In Figure 6.6 (a and b), the highest PCO performance of FPRGO-0.5 was at 48 RH%, in which 93.5% of methanol was photodegraded within 6 h following a pseudo-first order rate of 0.493 h^{-1}. At 48 RH%, there were adequate adsorption sites for VOCs and sufficient water molecules to produce •OH radicals for PCO. However, the

rate of photodegradation was reduced at lower humidity (36 and 30 RH%) because the low quantity of water molecules in the air had limited the generation of •OH radicals.

Figure 6.6c shows the concentration of CO_2 evolved from the PCO process by FPRGO-0.5 at 48 RH%. There is an absence of CO_2 evolution without the existence of photocatalyst or methanol. After 6 h, the M% of FPRGO was 91.7%, which signified that FPRGO was capable of mineralising toxic methanol into harmless CO_2.

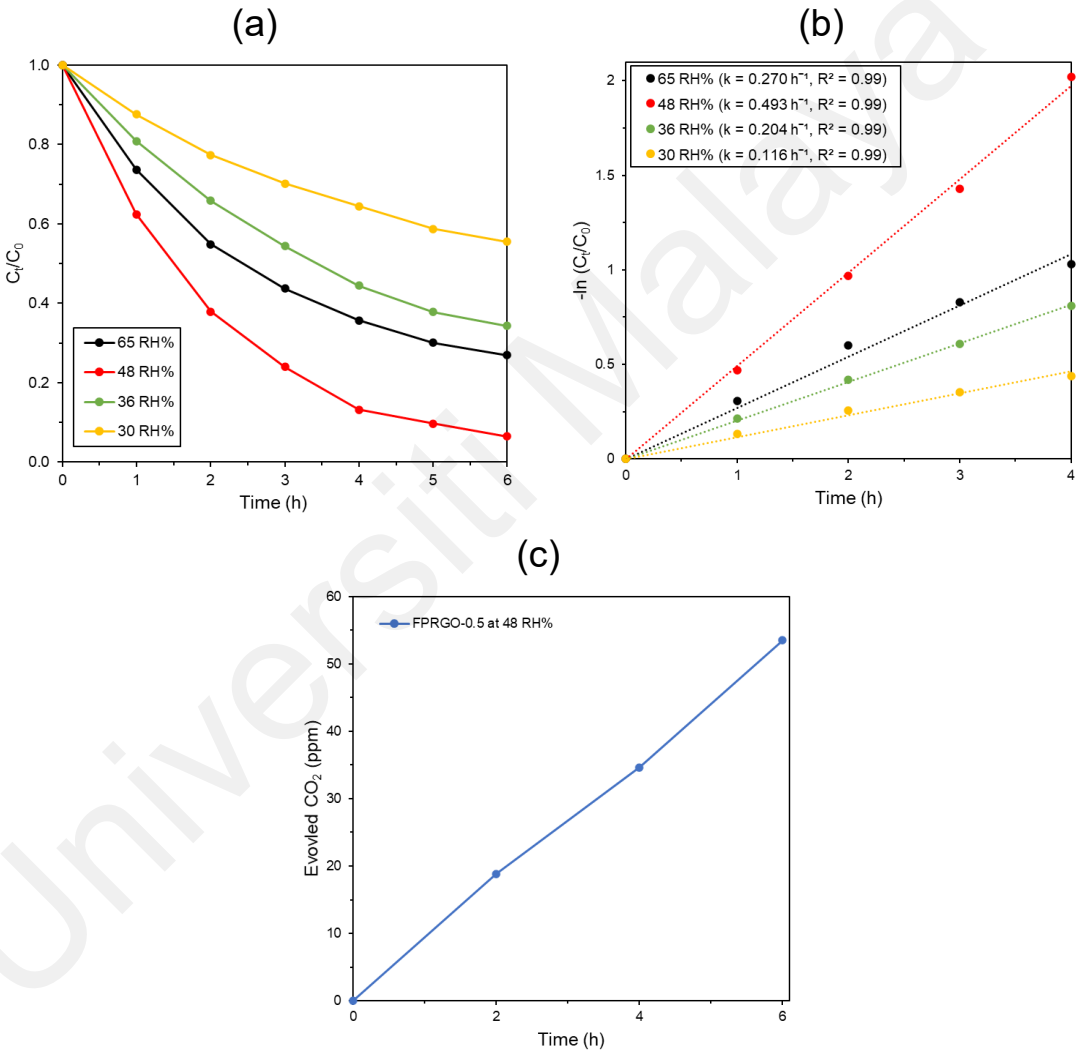

Figure 6.6: (a) PCO performance of FPRGO-0.5 under varying humidity, (b) pseudo-first order kinetic plot of FPRGO-0.5 under varying humidity, and (c) Evolution of CO_2 during the PCO process by FPRGO-0.5 at 48 RH%.

6.3 Reactive species and mechanism of PCO by FPRGO

It is widely known that $\bullet O_2^-$, •OH radicals, and h_{VB}^+ are the main reactive species in the photodegradation of VOCs. In gas-phase PCO, most •OH radicals are converted from water vapour, while $\bullet O_2^-$ are generated from oxygen (P. Li et al., 2020; Rao et al., 2022). The active species involved in the PCO by FPRGO-0.5 were determined by comparing three different ambient atmospheric conditions, which were air at 48 RH% (contained •OH, $\bullet O_2^-$ radicals, and the photogenerated hole at VB (h_{VB}^+)), N_2 at 48 RH% (contained •OH radicals and h_{VB}^+), and dry N_2 (contained h_{VB}^+ only). In Figure 6.7a, it was found that FPRGO-0.5 was able to remove 93.5%, 76.4%, and 42.2% of methanol under humid air (48 RH%), humid N_2 (48 RH%), and dry N_2 (0 RH%), respectively. The findings suggested that all three reactive species were generated in the PCO process, in which their relative contributions were as such h_{VB}^+ (~42%) > •OH (~34%) > $\bullet O_2^-$ (~17%).

Based on the results of M-S and bandgap, the band structures and PCO mechanism of the FPRGO samples were illustrated in Figure 6.7b. For example, free-electron (e^-) and h_{VB}^+ charge carriers were produced from FPRGO-0.5 under UV-A irradiation at the conduction band (CB) and VB, respectively. Notably the potential of CB was negative enough (-1.79 V vs. NHE, pH 7) to reduce O_2 into $\bullet O_2^-$ radicals, while the potential of VB was positive enough (+2.36 V vs. NHE, pH 7) to oxidise water vapour into •OH radicals. The h_{VB}^+ in tandem with the $\bullet O_2^-$ and •OH radicals mineralised the methanol molecules into harmless CO_2 and water.

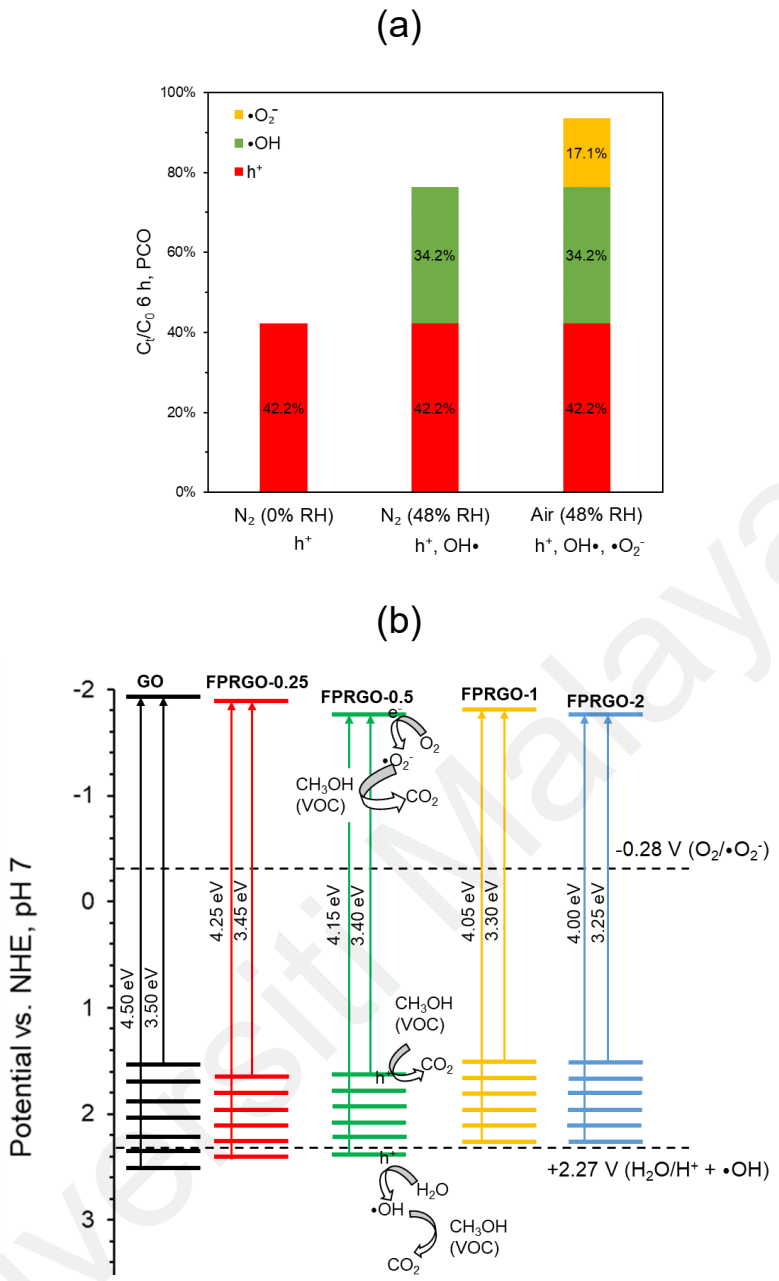

Figure 6.7: (a) Reactive species of FPRGO-0.5 during 6 h of PCO, (b) Band structures and PCO mechanism of FPRGO-0.5.

In summary, the photoirradiation of GO with the presence of TFA is a facile, scalable, and solution-based method to produce an efficient FPRGO photocatalyst with semi-ionic C-F bonds. The FPRGO-0.5 exhibited the ideal F dopant concentration at 0.16 at% for effective photodegradation of methanol. For example, FPRGO-0.5 was able to remove 93.5% of methanol with a mineralisation efficiency of 91.7% under UV-A irradiation and 48 RH%. Through manipulation of the band structures, •O_2^-, •OH radicals, and h_{VB}^+ reactive species are responsible for the PCO process by FPRGO-0.5. This work is a new

finding in utilizing F-doped graphene-based material as a standalone photocatalyst in VOCs removal. Future work may explore the viability of tuning F-doped graphene-based photocatalyst for other photocatalytic applications such as water splitting.

CHAPTER 7: Nitrogen-doped photoreduced graphene oxide (NPRGO) photocatalyst for the removal of VOCs

In this chapter, a series of NPRGO samples with different photoirradiation duration was synthesized from GO. After the photoirradiation process in the presence of ammonia, the GO was simultaneously photoreduced and N-doped. The samples were characterized to determine their physicochemical and electrochemical properties (Section 7.1). Then, PCO experiments were carried out to investigate the effect of photoreduction on the photoactivity of the NPRGO samples (Section 7.2). The band structures and PCO mechanism of the NPRGO photocatalyst were determined (Section 7.3). Lastly, Section 7.4 compares the PCO performance of GO, PRGO, BPRGO, FPRGO, and NPRGO.

7.1 Characterizations of NPRGO samples

A set of characterization tests were conducted on the NPRGO samples to determine their physicochemical properties, which include XRD, Raman, FTIR, UV-Vis, XPS, and PL. Furthermore, the electrochemical properties of the NPRGO samples were investigated by M-S, EIS, and photocurrent techniques.

7.1.1 Physicochemical properties of NPRGO samples

Figure 7.1 exhibits the FESEM images and elemental mapping of the GO and NPRGO samples. The surfaces of NPRGO samples were more wrinkled than GO. This observation agrees with a past study (Witjaksono et al., 2021), in which simultaneous reduction and N-doping processes induced wrinkling on the surface of GO. Besides that, the detection of uniformly distributed N atoms on the NPRGO samples by the elemental mapping analysis indicated that N was successfully doped on the GO.

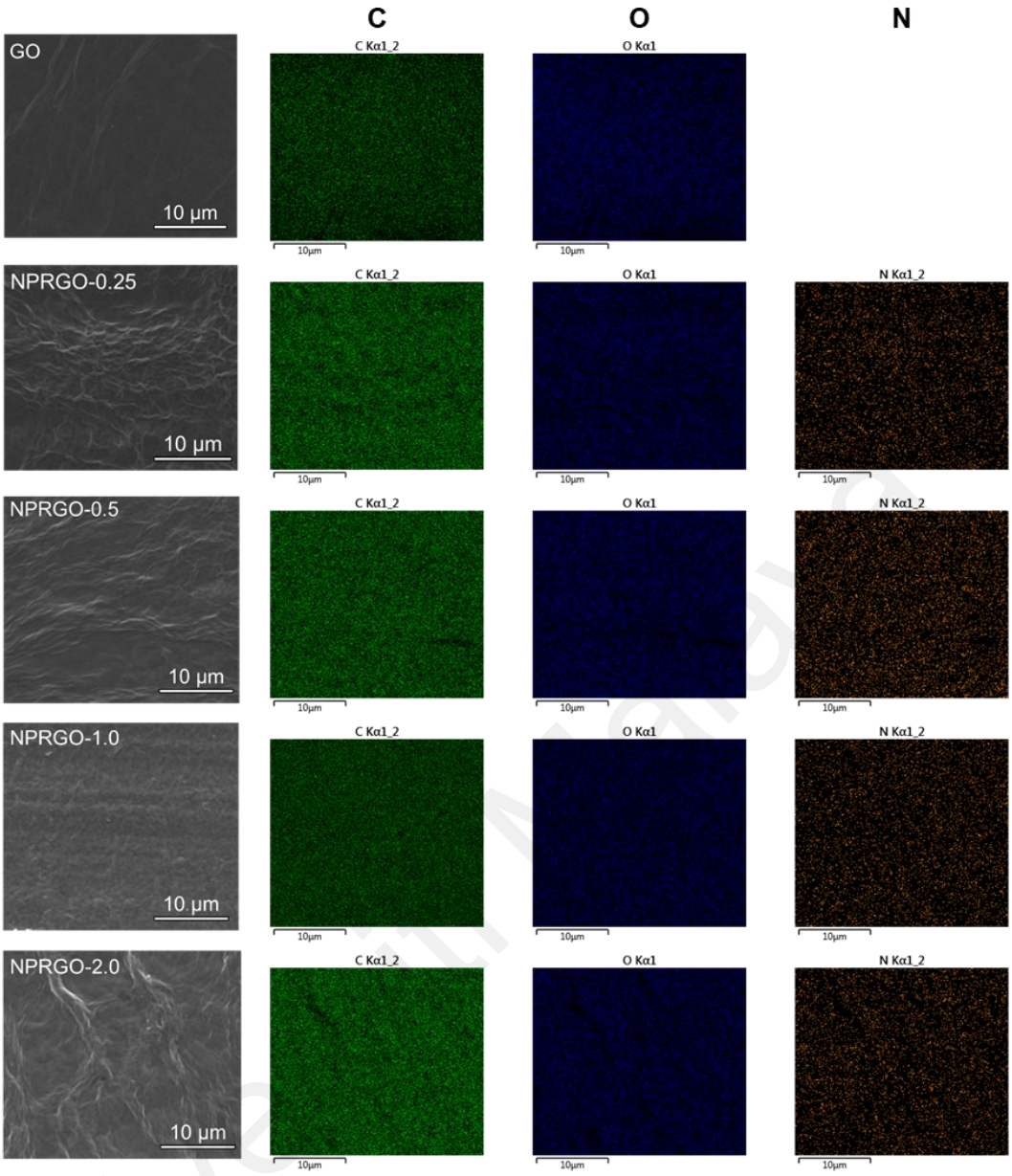

Figure 7.1: SEM and elemental mapping images of GO and NPRGO samples

In Figure 7.2a, the detection of XPS N 1s peak confirmed that N atoms were doped on GO after the photoirradiation process. The N 1s spectra of the NPRGO samples were deconvoluted into three peaks of pyridinic-N, pyrrolic-N, and graphitic-N groups at 398.7, 399.7, and 401.3 eV, respectively (del Pino et al., 2018; Yang et al., 2017). As shown in Figure 7.2d, the pyridinic-N (five-membered ring) and pyrrolic-N (six-membered ring) configurations can only be formed at the edges or defects of the graphitic structure, while the graphitic-N was doped on the graphitic basal plane connected to three carbon atoms

(Putri et al., 2017; Yang et al., 2017). The N dopants would cause some graphitic lattice distortion to the GO because the bond lengths of the pyridinic (1.32 Å), pyrrolic (1.37 Å), and graphitic (1.40 Å) N-C bonds are different from the original graphitic C-C bond (1.41 Å) (Matsoso et al., 2016; Rani & Jindal, 2013; Yang et al., 2015).

Besides that, the C 1s spectra of the samples (Figure 7.2b) exhibit four main peaks at 284.5, 286.5, 287.7, and 289.2 eV attributed to the C-C/C=C, C-O, C=O, and O=C-O groups, respectively [38]. Additionally, the NPRGO samples had an extra peak at 285.8 eV corresponding to the C-N groups (Zhiyu Wang et al., 2014). According to Table 7.1, the NPRGO-0.5 (0.5 h photoirradiation) contained the highest N concentration (4.8 at%) with the highest content of graphitic-N (41.2 at%). Notably, it was found that prolonged duration of photoirradiation led to a decrease in the N at% and C-N bonds. This suggested that C-N bonds were destructed as a result of excessive lattice distortion stress after exposure to long hours of photoirradiation. Besides that, it is noteworthy that the graphitic-N content of NPRGO-0.5 was higher than that of those previously reported N-doped graphene-based photocatalysts synthesised via calcination and hydrothermal methods. The amount of graphitic-N produced from the calcination (Putri et al., 2017; Yeh et al., 2014) and hydrothermal (Tsai et al., 2020; Yang et al., 2017) techniques were only 12 – 22 at% and 29 – 31 at%, respectively. This exemplifies the success of forming a higher amount of graphitic-N via the photoirradiation method.

Meanwhile, the O 1s of the samples displayed one main peak at 532.4 eV (Figure 7.2c). This peak is corresponding to the O-C groups from the remaining OCGs, as shown in Table 7.1. After photoirradiation, the NPRGO samples displayed a gradual reduction of the OCGs content in C 1s and the overall oxygen (O) at% content. The OCGs decreased from 0.57 to 0.33, while the O at% decreased from 33.2% to 18.6% with longer photoirradiation duration (Table 7.1). As expected, the photoirradiation process simultaneously reduced and N-doped the GO.

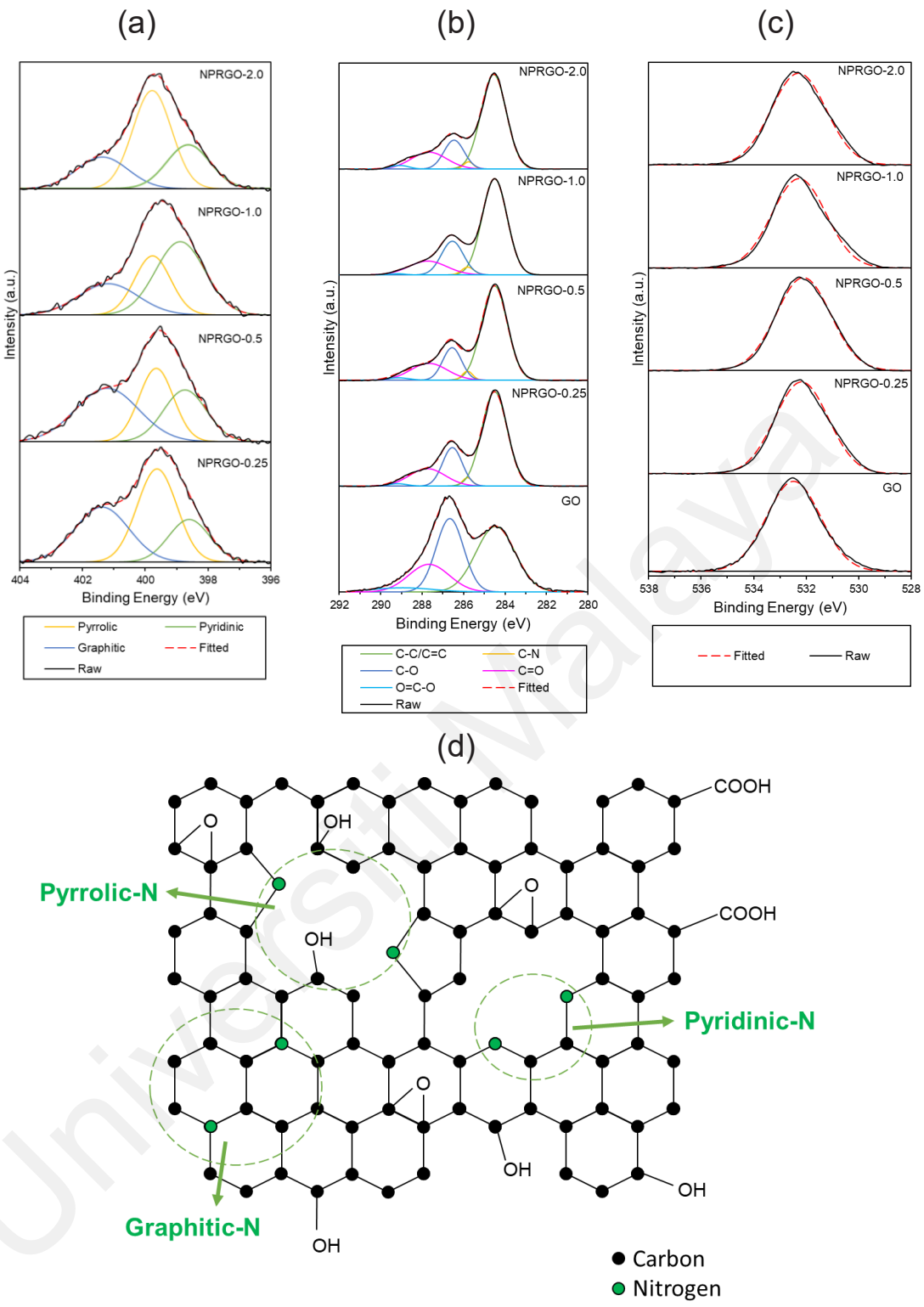

Figure 7.2: XPS (a) N 1s, (b) C 1s, and (c) O 1s of GO and NPRGO samples, and (d) Schematic structure of NPRGO.

Table 7.1: Summary of XPS compositions for GO and NPRGO samples

Sample	XPS (at%)			C 1s (at%)					$\frac{OCGs}{C}$	N 1s (at%)		
	C	O	N	C-C/ C=C	C-N	C-O	C=O	O=C -O		Pyridinic	Pyrrolic	Graphitic
GO	66.8	33.2	0.0	43.1	0	33.9	18.7	4.3	0.57	-	-	-
NPRGO-0.25	73.8	22.0	4.2	61.7	2.1	19.3	15.9	1.0	0.36	20.8	43.9	35.3
NPRGO-0.5	73.4	21.8	4.8	63.4	2.4	16.1	16.6	1.5	0.34	27.5	31.3	41.2
NPRGO-1.0	75.8	19.7	4.5	63.8	2.4	19.5	14.0	0.3	0.34	47.5	28.0	24.5
NPRGO-2.0	77.2	18.6	4.2	64.8	1.8	15.9	15.9	1.6	0.33	25.8	51.9	22.3

Figure 7.3a displays the FTIR spectra of the GO and NPRGO samples. GO displayed several peaks at 1040, 1390, 1630, 1730, and 3000-3600 cm^{-1}, which were assigned to the C-O stretching modes, C-OH groups, C=C groups, C=O stretching, and surface adsorbed water/OH groups (Ţucureanu et al., 2016). In comparison with GO, some of the peaks of NPRGO samples such as the surface adsorbed water, C-O, and C=O peaks had lower intensities. A new peak that appeared at 1575 cm^{-1} in NPRGO samples was attributed to the C=C bands overlapping with the C=N bonds (Xue et al., 2012). Besides that, another new peak emerged at 1225 cm^{-1} in NPRGO samples corresponded to the C-N stretching (Das et al., 2019). These observations affirmed that the NRPGO samples were simultaneously reduced and doped with N, which agreed with the XPS findings. Additionally, a small peak ascribed to C-H bonds (2925 cm^{-1}) appeared in NPRGO-0.5, which was commonly observed after the doping of GO with ammonia precursor (Sandoval et al., 2016).

Figure 7.3b displays the Raman peaks of the GO and NPRGO samples. All samples exhibited two main peaks at 1350 (D band) and 1600 cm^{-1} (G band). The D and G bands were ascribed to the defects or disorders of graphitic structure and also in-plane stretching modes of the C=C sp^2 bonds (Q. Zhang et al., 2020). Besides that, all samples exhibited two smaller bands at ~2736 and ~ 2930 cm^{-1}, which were referred to the 2D (second order

of D band) and S3 (imperfect activated grouping of phonon) bands (Li et al., 2016). Among the NPRGO samples, the NPRGO-0.5 exhibited the highest I_D/I_G ratio (0.95), which was 1.1 times higher than that of GO (0.88). The introduction of N dopants had induced defects and distortion to the graphitic structure of GO, therefore increasing the I_D/I_G ratio (L. Wang et al., 2014). Meanwhile, the I_{2D}/I_G ratio was used to estimate the N doping concentration on an N-doped graphene-based material (Zhang et al., 2011). Since all NPRGO samples demonstrated a I_{2D}/I_G ratio (0.093 – 0.114) lower than the value of 0.6 (Das et al., 2008; Zhang et al., 2011), this suggested that a considerable amount of N dopant ($> 4 \times 10^{13}$ cm^{-2}) had been introduced on the samples (Liu et al., 2016).

Figure 7.3c demonstrates the XRD patterns of the samples. The GO exhibited a characteristic peak at $2\theta = \sim 10^{\circ}$ (Putri et al., 2017). After photoirradiation, the peak at $2\theta = \sim 10^{\circ}$ gradually diminished and then disappeared due to the reduction of OCGs (Siong et al., 2020). In addition, the peak at $2\theta = \sim 25^{\circ}$ that usually appears after GO reduction (Siong et al., 2020) was absent in all NPRGO samples. This suggested that the graphitic sheets of the NPRGO samples had a minimal stacking effect (Chen et al., 2010). The minimum stacking effect ensured a high electrical conductivity in the graphitic sheet (Worsley et al., 2014), which is beneficial for the transportation of photogenerated charge carriers during photocatalysis (Huang et al., 2020).

Figure 7.3 (d and e) show the UV-Vis absorbance and Tauc plots of the samples. The GO possessed a peak at 230 nm originated from the $\pi \rightarrow \pi^*$ transitions of the C=C bonds and a shoulder at ~300 nm attributed to the $n \rightarrow \pi^*$ transitions of the C=O bonds (Hsu et al., 2013). Upon photoirradiation, the absorbance between 250 – 800 nm was gradually broadened. From the Tauc plot analysis, it was found that the bandgap was gradually reduced from 3.50 – 4.50 (GO) to 3.10 – 3.40 eV (NPRGO-2.0). These changes signified the restoration of sp^2 conjugated structure after the removal of OCGs (Mohandoss et al.,

2017; Rabchinskii et al., 2016). Furthermore, the potentials of the conduction band minimum (CBM) and valence band maximum (VBM) could have been shifted after N-doping, which would have also contributed to the reduction in bandgap (Loh et al., 2010). The potentials of the CBM and VBM play an important role in governing the type of radicals (e.g., •OH and $\bullet O_2^-$ radicals) that can be produced during the PCO process.

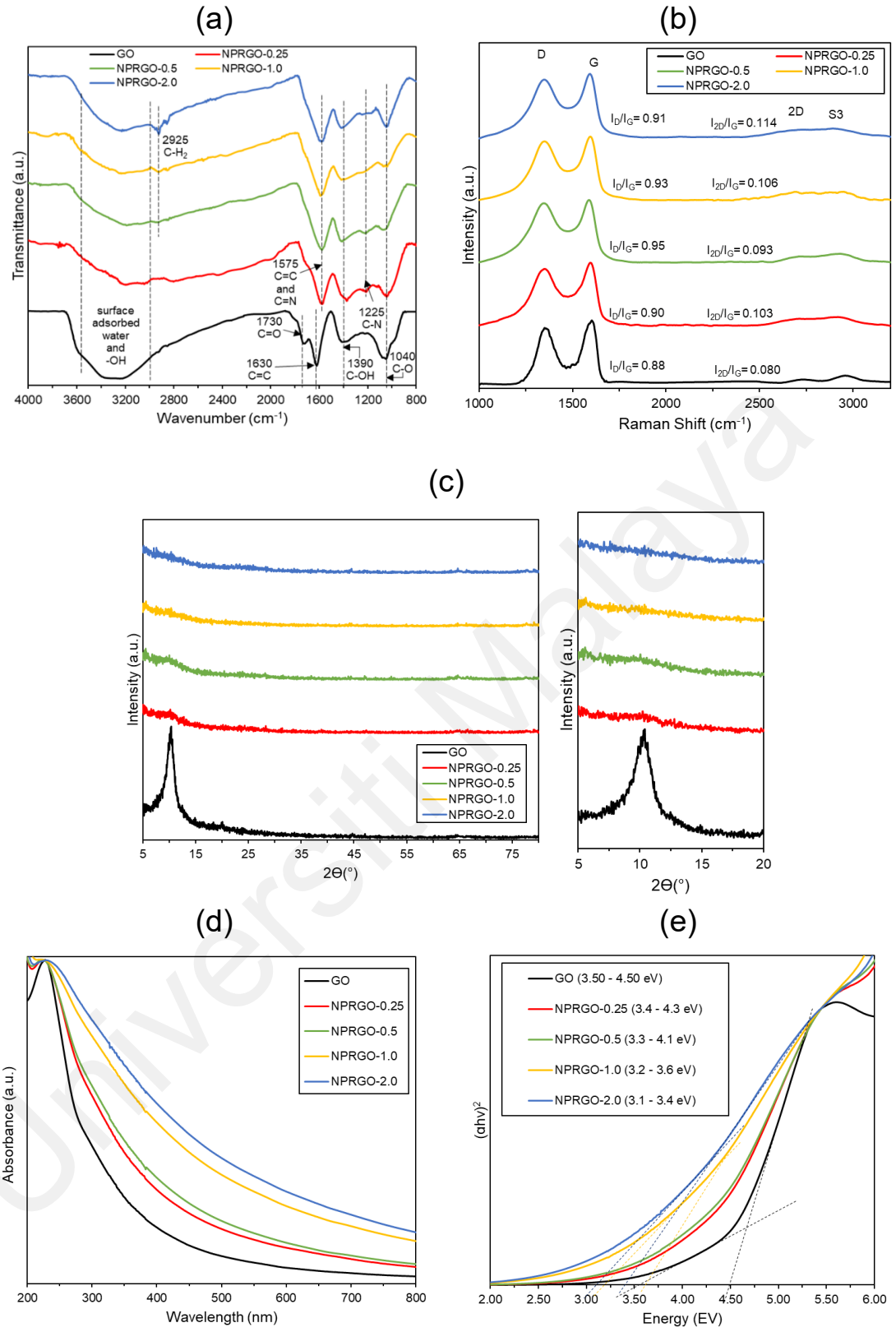

Figure 7.3: (a) FTIR spectra, (b) Raman spectra, and (c) XRD diffractogram, (d) UV-Vis absorbance spectra, and (e) Tauc plot of GO and NPRGO samples.

7.1.2 Electrochemical properties of NPRGO

Figure 7.4 (a and b) display the M-S plots of the samples. The GO displayed a negative slope corresponding to a p-type conductivity because of the presence of electron-withdrawing O atoms on its surface (Wang et al., 2009). Meanwhile, the NPRGO samples exhibited positive slopes that represent n-type conductivity. This is because the ionised N dopants donated electrons to the CB of the GO and thus increased the n-type (free-electron) carrier density. It was reported in previous studies as well that the transformation of GO from p-type to n-type conductivity was achieved by doping with N (Bie et al., 2021; Lu et al., 2013) and K (Liu et al., 2011) atoms. In contrast to the p-type GO, the majority charge carrier of the n-type NPRGO samples was free-electron instead of hole. Besides that, the V_{FB} of GO, NPRGO-0.25, NPRGO-0.5, NPRGO-1.0, and NPRGO-2.0 were +1.26, -1.14, -1.12, -1.11, and -1.10 V vs. NHE at pH 7, respectively. Since the VBM and CBM are approximately ±0.3 V away from the V_{FB} of a p-type and n-type semiconductor (Yin et al., 2016), the CBM of NPRGO-0.25, NPRGO-0.5, NPRGO-1.0, and NPRGO-2.0 were -1.44, -1.42, -1.41, and -1.40 V vs. NHE at pH 7, respectively. Meanwhile, the VBM of GO was +1.56 V vs. NHE at pH 7.

The free-electron densities of NPRGO-0.25, NPRGO-0.5, NPRGO-1.0, and NPRGO-2.0 were determined as 4.3×10^{15}, 2.5×10^{16}, 1.6×10^{16}, and 1.5×10^{16} cm^{-3}, respectively. Among the NPRGO samples, the NPRGO-0.5 exhibited the highest free-electron carrier density. This is because NPRGO-0.5 had the highest concentration of graphitic-N. As a group 15 element, each of the N dopant contains five valence electrons. Three of the valence electrons of a graphitic-N formed σ bonds, one electron formed a π bond, and the remaining one electron enters the π^* state in the CB. Consequently, the graphitic-N induced a strong n-type doping effect. Meanwhile, two of the valence electrons of the pyrrolic-N and pyridinic-N formed σ bonds, one electron formed a π bond, and two electrons were left as a lone pair (Robertson & Davis, 1995). One of the electrons

from the lone pair can form a N-H bond with a hydrogen atom, therefore forcing the last electron into the CB and inducing a weak n-type doping effect (Schiros et al., 2012). Intriguingly, it was computed that the n-type electron-donating ability of the graphitic-N is around 27 times stronger than that of pyrrolic-N and pyridinic-N (Lu et al., 2013; Schiros et al., 2012). Hence the graphitic-N is more effective for the increment of free-electron carrier density than pyrrolic-N and pyridinic-N.

Figure 7.4c demonstrates the EIS of the samples. A smaller arc radius of the Nyquist plot indicates a lower resistance and a higher conductivity (Putri et al., 2020). It was observed that the n-type NPRGO samples demonstrated dramatically higher conductivities than the p-type GO. The higher conductivity of an n-type semiconductor is attributed to its better electron-donating ability than the p-type counterpart (Mokhtar Mohamed et al., 2018). It is important to note that a photocatalyst with high conductivity is essential for photocatalysis because it facilitates the transportation of photoinduced charge carriers (Shi et al., 2016). Among the NPRGO samples, NPRGO-0.5 exhibited the highest conductivity due to the formation of a substantial amount of graphitic-N from the N dopants. As explained earlier, the graphitic-N induced a strong n-type doping effect, thus it is able to significantly increase the free-electron carrier density. It was reported (Guo et al., 2014; Tsai et al., 2020) that an n-type semiconductor with a higher free-electron carrier density has a higher n-type conductivity.

Figure 7.4 (d and e) show the PL and photocurrent measurements of the GO and NPRGO samples. The NPRGO-0.5 exhibited the lowest PL peak intensity and highest photocurrent density, therefore suggesting that NPRGO-0.5 had the slowest recombination rate of photogenerated charge carriers. The finding was due to the high n-type conductivity of NPRGO-0.5, which eased the transportation and separation of the photogenerated charge carriers (Huang et al., 2020). The N dopants formed shallow donor levels (Tsai et al., 2020) near the CB of the NPRGO-0.5. Under light excitation, if a

photoexcited electron falls from the CB, the shallow donor levels can trap and re-emit the electron back to the CB easily, therefore preventing the photoexcited electron from recombining with a hole carrier at the valence band (VB) (Agrawal & Dutta, 1993).

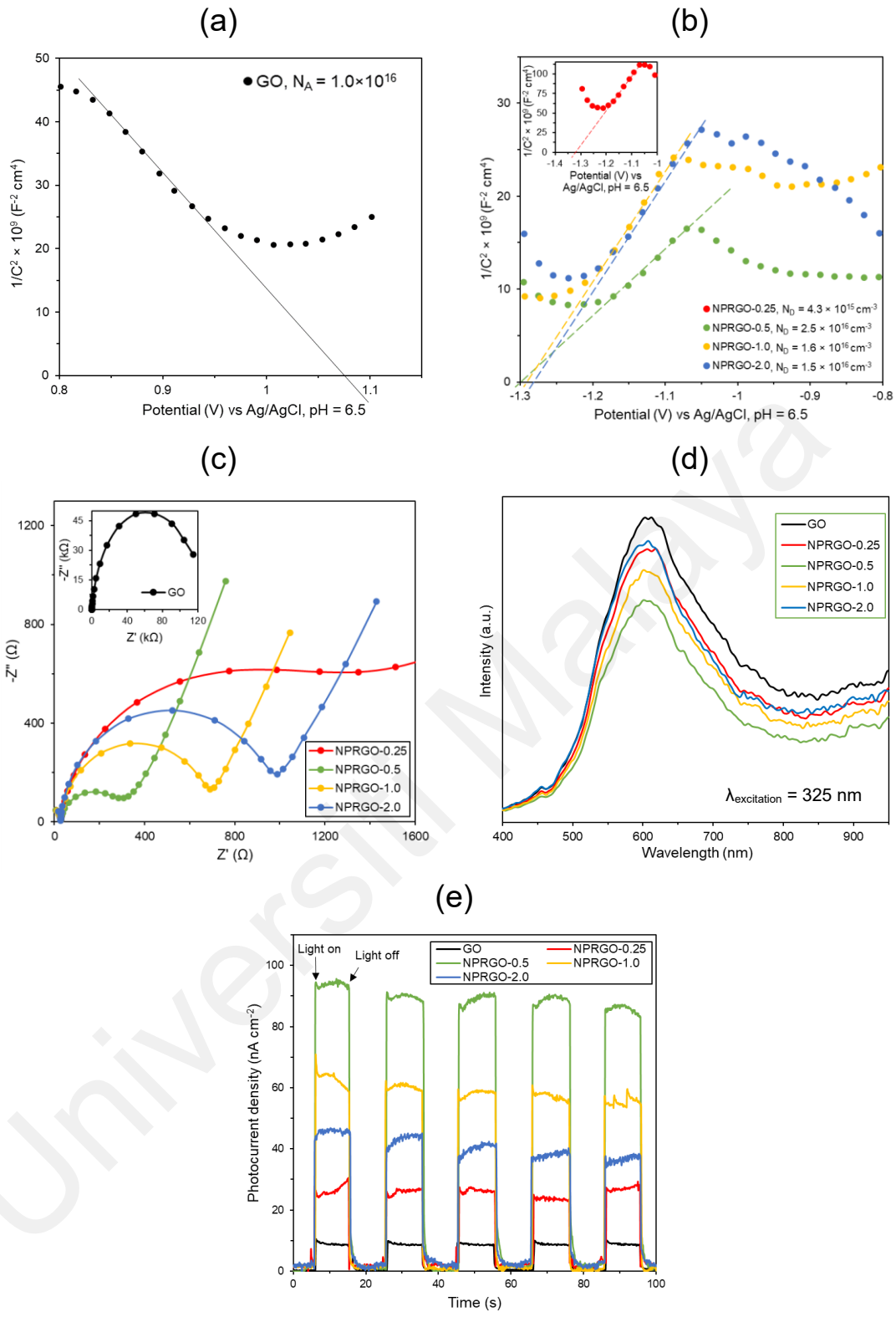

Figure 7.4: M-S plot of (a) GO and (b) NPRGO samples. (c) EIS, (d) photoluminescence, and (e) photocurrent of GO and NPRGO samples.

7.2 PCO performances of NPRGO samples

The photocatalytic degradation of gaseous methanol as the model VOCs was examined under UV-A irradiation. No methanol was degraded without light or photocatalyst in the control experiments within 6 h. All NPRGO samples were able to remove a similar amount of methanol (16 – 20%) after the 1 h of dark adsorption (Appendix J). Figure 7.5a and Figure 7.5b display the PCO performance of the samples at room conditions. All NPRGO samples were able to photodegrade more methanol than GO. Among them, the NPRGO-0.5 exhibited the best PCO performance with 95.6% photodegradation within 6 h (0.376 h^{-1}), which was 20 times more effective than that of GO. Figure 7.5c and Appendix L demonstrate the correlation between the free-electron density and photocatalytic activity of the NPRGO photocatalysts. It was shown that a higher density of free-electron carrier had a significant positive impact on the rate of PCO. Therefore, the remarkable PCO performance of NPRGO-0.5 was attributed to the high content of graphitic-N. This is because the strong electron-donating ability of graphitic-N increased the free-electron carrier density, improved the conductivity, and retarded the photogenerated charge carrier recombination. As a result, more charge carriers were available to participate in the photocatalytic reaction. It was also reported (del Pino et al., 2018) that higher graphitic-N content had improved the photoactivity of an NPRGO in water splitting. Additionally, NPRGO-0.5 showed good recyclability with just a minor drop of 5% in photocatalytic activity even after five cycles (Figure 7.5d).

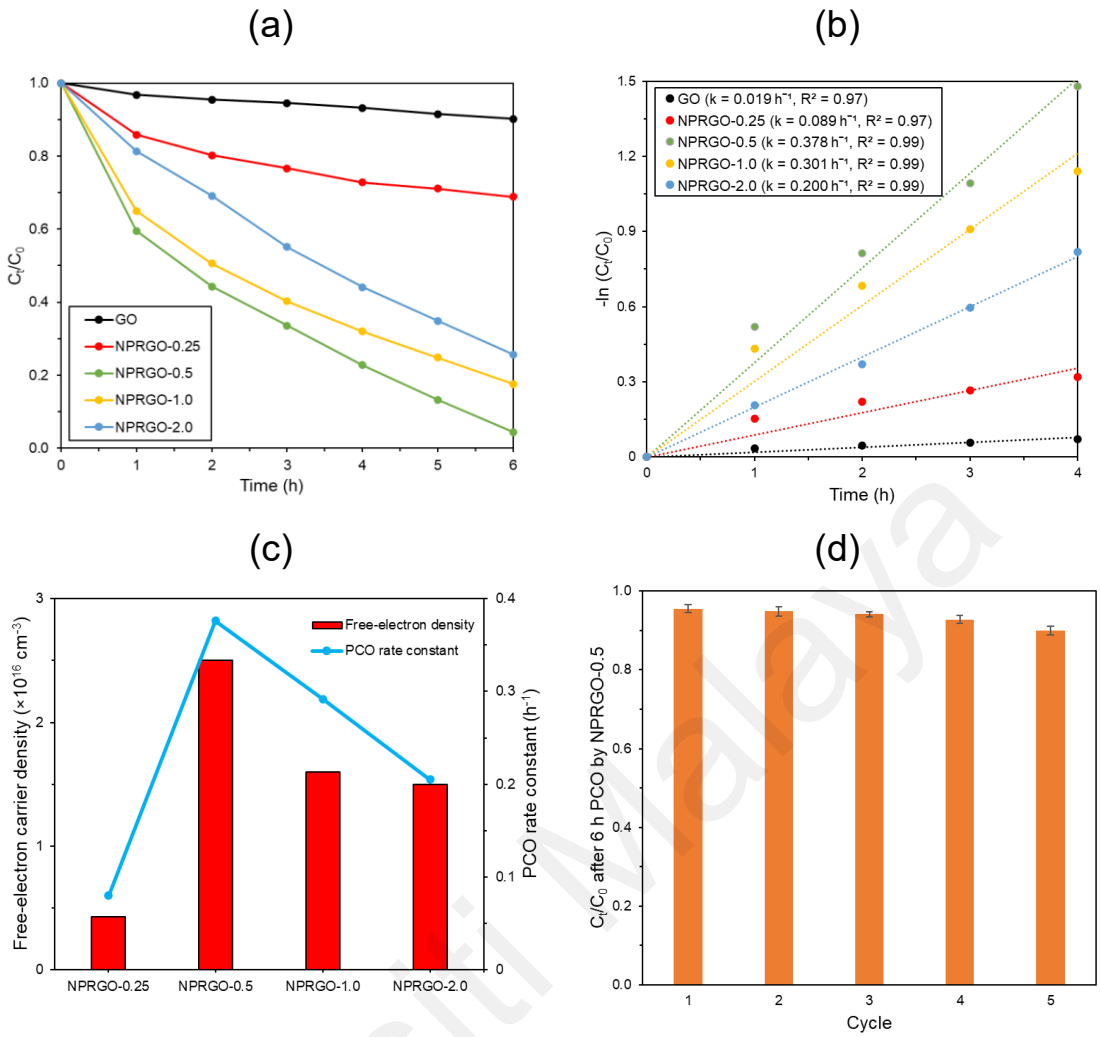

Figure 7.5: (a) PCO removal, (b) pseudo-first order kinetic plot, (c) Correlation of free-electron carrier density and PCO rate, and (d) Recyclability test of NPRGO-0.5.

It is vital to investigate the effects of ambient humidity during PCO because the concentration of water vapour affects both the processes of VOCs adsorption and •OH radicals production (Mamaghani et al., 2017). For NPRGO-0.5, the humidity did not significantly affect the 1 h adsorption removal (20-22%). As refer to Figure 7.6a and Figure 7.6b, the ideal humidity was 65 RH% for the PCO process of NPRGO-0.5. This indicated that a humidity of 65 RH% was adequate for adsorption of methanol and possessed enough water molecules to generate •OH radicals for PCO. However, excessive water vapour at 85 RH% would compete for the adsorption sites with methanol molecules and thus hampering the PCO process. Meanwhile, at lower humidity (36 - 48

RH%) conditions, the insufficient amount of water vapour had limited the generation of •OH radicals during PCO.

Figure 7.6c shows the concentration of CO_2 evolved from the PCO process by NPRGO-0.5 at 65 RH%. Without photocatalyst or methanol, no evolution of CO_2 was detected. After 6 h of PCO, up to 96.3% of toxic methanol was mineralised into harmless CO_2. The findings indicated that NPRGO-0.5 is an excellent photocatalyst that not only degrade but also mineralise VOCs such as methanol into harmless CO_2.

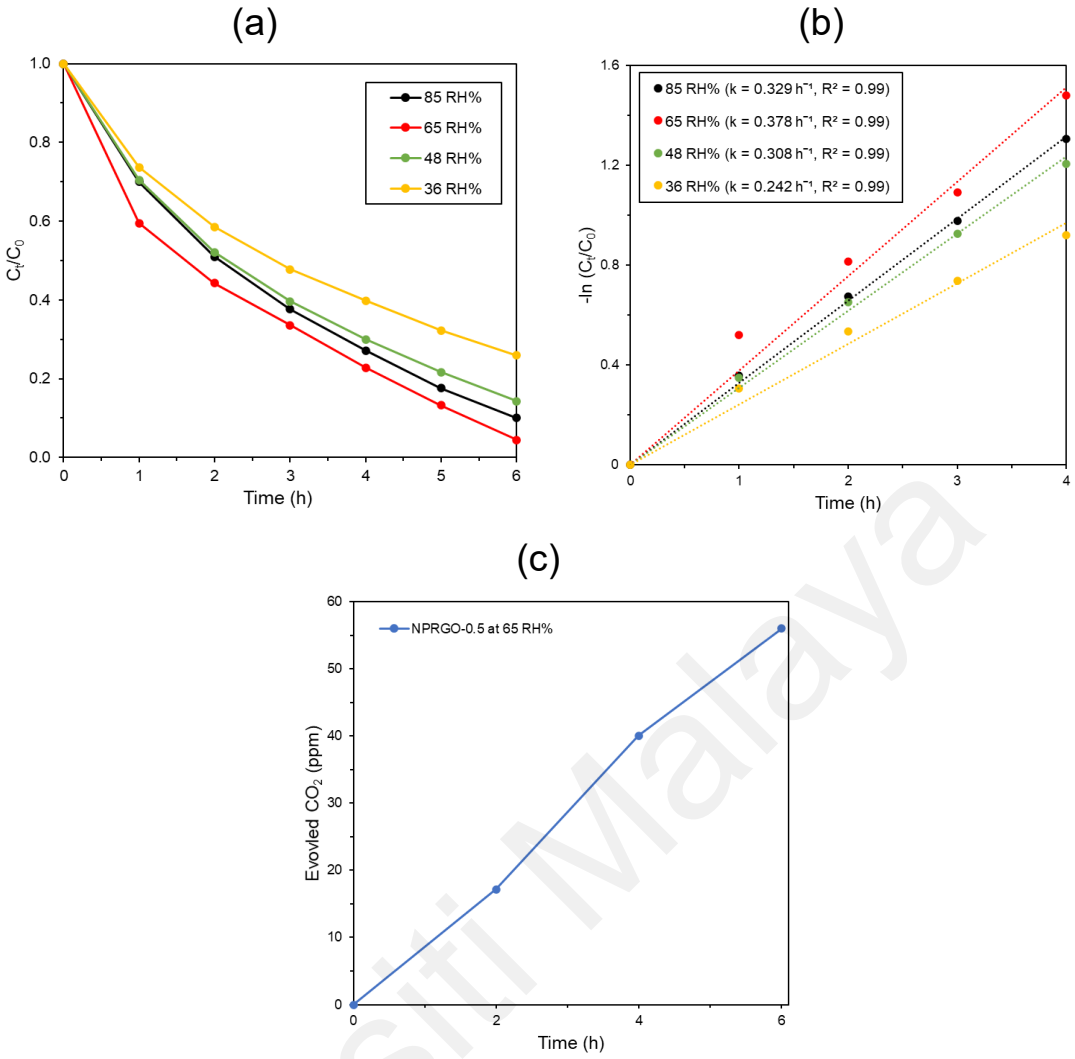

Figure 7.6: (a) PCO performance of NPRGO-0.5 under varying humidity, (b) pseudo-first order kinetic plot of NPRGO-0.5 under varying humidity, and (c) Evolution of CO_2 during the PCO process by NPRGO-0.5 at 65 RH%.

7.3 Reactive species and mechanism of PCO by NPRGO

It is widely known that the hole carrier at the VB (h_{VB}^+), •OH radicals, and $•O_2^-$ radicals are the major reactive species for a PCO process. In gas-phase PCO, most of the •OH radicals are converted from water vapour, while $•O_2^-$ radicals are generated from oxygen (P. Li et al., 2020; Rao et al., 2022). The reactive species produced during the PCO process of NPRGO-0.5 were determined by comparing three different ambient atmospheric conditions, namely (i) humid air (65 RH%) for •OH radicals, $•O_2^-$ radicals, and h_{VB}^+, (ii) humid N_2 (65 RH%) for •OH radicals and h_{VB}^+, and (iii) dry N_2 (0 RH%)

for h_{VB}^+ only. As shown in Figure 7.7a, NPRGO-0.5 removed 95.6%, 77.3%, and 54.0% of methanol under humid air (65 RH%), humid N_2 (65 RH%), and dry N_2 (0 RH%), respectively. The findings suggested that all three reactive species were produced in the PCO process, in which their relative contributions were h_{VB}^+ (54%) > •OH (~23%) > $•O_2^-$ (~18%). The main reactive species, namely h_{VB}^+ is capable of accepting electron from the adsorbed methanol molecules, therefore directly oxidising the methanol into CO_2.

Figure 7.7b constructed the band structures of the NPRGO photocatalysts based on the M-S and bandgap. For instance, the free-electron (e^-) and h_{VB}^+ carriers were produced by NPRGO-0.5 under UV-A irradiation at the CB and VB, respectively. The potential of the CB was negative enough (-1.42 V vs. NHE at pH 7) to reduce oxygen (O_2) into $•O_2^-$, while the potential of the VB was positive enough (+2.68 V vs. NHE at pH 7) to oxidise water vapour into •OH radicals. The h_{VB}^+ in tandem with the $•O_2^-$ and •OH then completely mineralised the methanol completely into harmless CO_2 and water.

(a)

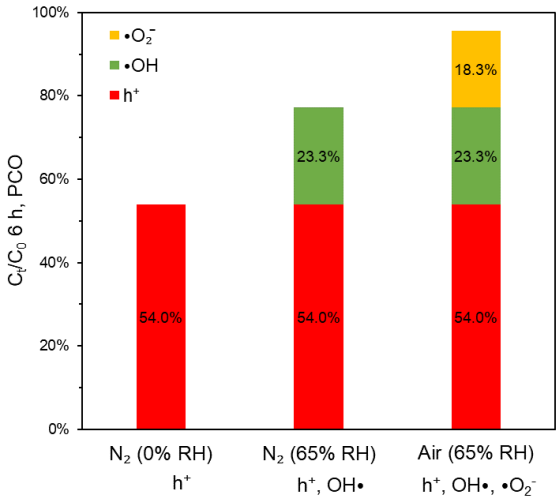

(b)

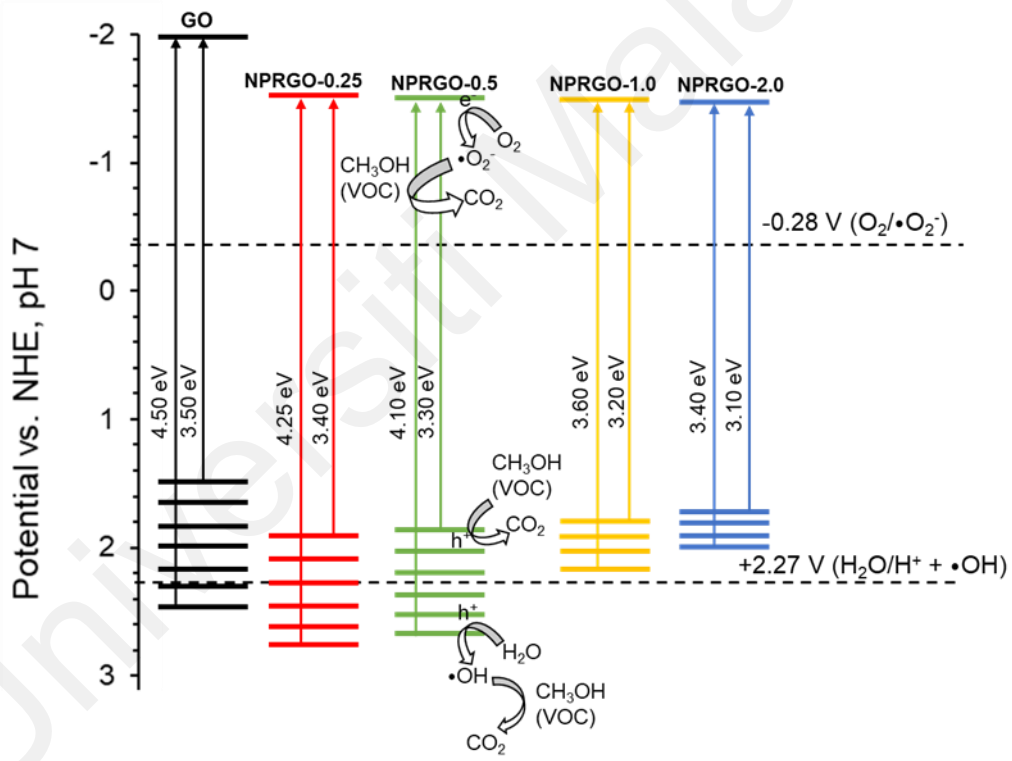

Figure 7.7: (a) Reactive species study of NPRGO-0.5 for 6 h of PCO and (b) Band structures and PCO mechanism of NPRGO-0.5.

In summary, the photoirradiation of GO in the presence of ammonia is a facile, scalable, and solution-based method to produce effective metal-free NPRGO photocatalysts. The photoirradiation method successfully controlled the concentration and configuration of N dopant on GO. For instance, NPRGO-0.5 possessed 41.2 at% of graphitic-N among 4.7

at% of N dopant after 0.5 h of photoirradiation. This favourable N doping of NPRGO-0.5 increased its free-electron carrier density and n-type conductivity, which in turn suppressed the recombination of photogenerated charge carriers. As a result, NPRGO-0.5 was able to degrade 95.6% of methanol under UV-A irradiation at 65 RH%. Based on the band structures and PCO mechanism, the main h_{VB}^{+} species along with the $\bullet O_2^{-}$ and •OH radicals were involved in the PCO process by NPRGO-0.5. This work reforms the ability of N-doped graphene-based material to be used as a highly effective photocatalyst for VOCs removal.

7.4 Comparison of GO, PRGO-8, BPRGO-1.0, FPRGO-0.5, and NPRGO-0.5

7.4.1 Electrochemical properties of GO, PRGO-8, BPRGO-1.0, FPRGO-0.5, and NPRGO-0.5

Figure 7.8a compares the EIS Nyquist plots of GO, PRGO-8, BPRGO-1.0, FPRGO-0.5, and NPRGO-0.5. The heteroatom-doped PRGO samples had significantly smaller arc radii than the undoped GO and PRGO samples. The inset in Figure 7.8a is the proposed equivalent circuit of the Nyquist plots, while the fitted charge carrier transfer resistance (R_{ct}) values are shown in Table 7.2. The observations suggested that heteroatom-doping is an effective method to reduce the charge carrier transportation resistance in PRGO. This is because the heteroatom-dopants increased the charge carrier density and conductivity of the PRGO, as discussed in Chapter 5 - 7. Among the heteroatom-doped PRGO samples, the n-type NPRGO-0.5 exhibited the lowest R_{ct} at 300 Ω/cm^2. Notably, NPRGO-0.5 had a smaller R_{ct} than FPRGO-0.5, despite that FPRGO-0.5 had a higher charge carrier density (Table 7.2). This is in concordance with previous reports, where an n-type semiconductor exhibited a lower resistance than its p-type counterpart because of the strong n-type electron-donating ability (Mokhtar Mohamed et al., 2018; Shi et al., 2016).

Figure 7.8b and Table 7.2 display that the transient photocurrent densities of the samples were in the order of NPRGO-0.5 > FPRGO-0.5 > BPRGO-1.0 > PRGO-8 > GO. The results suggested that NPRGO-0.5 had the best ability in separating photoexcited electron and hole charge carriers. It was shown in Section 7.1 that N-dopants formed a shallow donor level near the conduction band of NPRGO-0.5. If a photoexcited electron falls from the conduction band of NPRGO-0.5, the shallow dopant level can trap the electron and reemit it back to the conduction band easily, therefore preventing the electron from recombining with a hole at the valence band (Agrawal & Dutta, 1993). Moreover, the EIS also showed that NPRGO-0.5 had the smallest R_{ct}, therefore photoexcited electron and hole carriers could be transported and separated more easily.

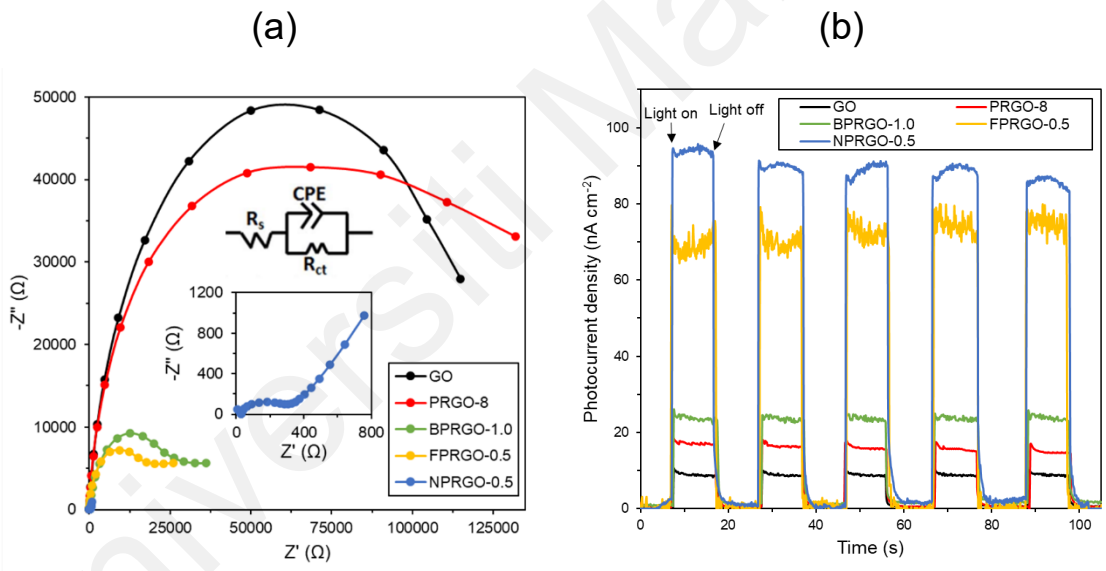

Figure 7.8: (a) EIS and (b) photocurrent of GO, PRGO-8, BPRGO-1.0, FPRGO-0.5, and NPRGO-0.5

Table 7.2: Comparison of PRGO, BPRGO, FPRGO, and NPRGO

Photocatalyst	Dopant	Conductivity	Charge carrier density (cm^{-3})	Charge transfer resistance, R_{ct} (Ω/cm^2)	Photocurrent density (nA/cm^2)	PCO rate (h^{-1})
GO	-	p-type	1.0×10^{16}	118,260	10	0.026
PRGO-8	-	p-type	1.5×10^{16}	104,240	19	0.064
BPRGO-1.0	2.6 at% B	p-type	2.3×10^{16}	31,117	22	0.190
FPRGO-0.5	0.16 at% F	p-type	6.9×10^{16}	22,451	70	0.260
NPRGO-0.5	4.7 at% N	n-type	2.5×10^{16}	300	95	0.376

7.4.2 PCO of PRGO-8, BPRGO-1.0, FPRGO-0.5, and NPRGO-0.5

Figure 7.9 (a and b) exhibit the methanol photodegradation performance of the GO, PRGO-8, BPRGO-1.0, FPRGO-0.5, and NPRGO-0.5 at 65 RH%. All photocatalysts had suitable CB and VB levels to produce both the •OH and $\bullet O_2^-$ radicals for effective PCO. The BPRGO with 2.6 B at% and high OBGs content (57%), FPRGO with 0.16 F at% of semi-ionic C-F bonds, and NPRGO with 4.7 N at% and 41.2% of graphitic-N demonstrated 10, 14, and 20 times higher photoactivity than GO, respectively. Remarkably, the NPRGO-0.5 exhibited the highest PCO efficiency, where 100% of the 100 mg/m^3 methanol was degraded within 9 h and the mineralisation efficiency was up to 100% after 10 h (Figure 7.9c). It was observed that the order of the PCO performance was similar to the sequence of the photocurrent densities (Table 7.2). Therefore, the high performance of NPRGO-0.5 is attributed to its ability to effectively separate photoexcited electrons and holes. The findings highlight the excellent PCO performance of NPRGO with adequate N dopant concentration and high content of graphitic-N groups.

In addition, Figure 7.9d shows the ability of NPRGO-0.5 to photodegrade other types of VOCs such as a ketone (acetone) and an aldehyde (formaldehyde). It is clearly shown that 44% of acetone and 64% of formaldehyde were successfully degraded by NPRGO-0.5 within 9 h. The results indicated that NPRGO-0.5 is a versatile photocatalyst in photodegrading various types of VOCs. Besides that, the capability of NPRGO-0.5 to

photodegrade methanol under indoor white light (visible light) was also explored in Appendix K. All the findings in Section 7.4 are summarized into Fig. 7.10.

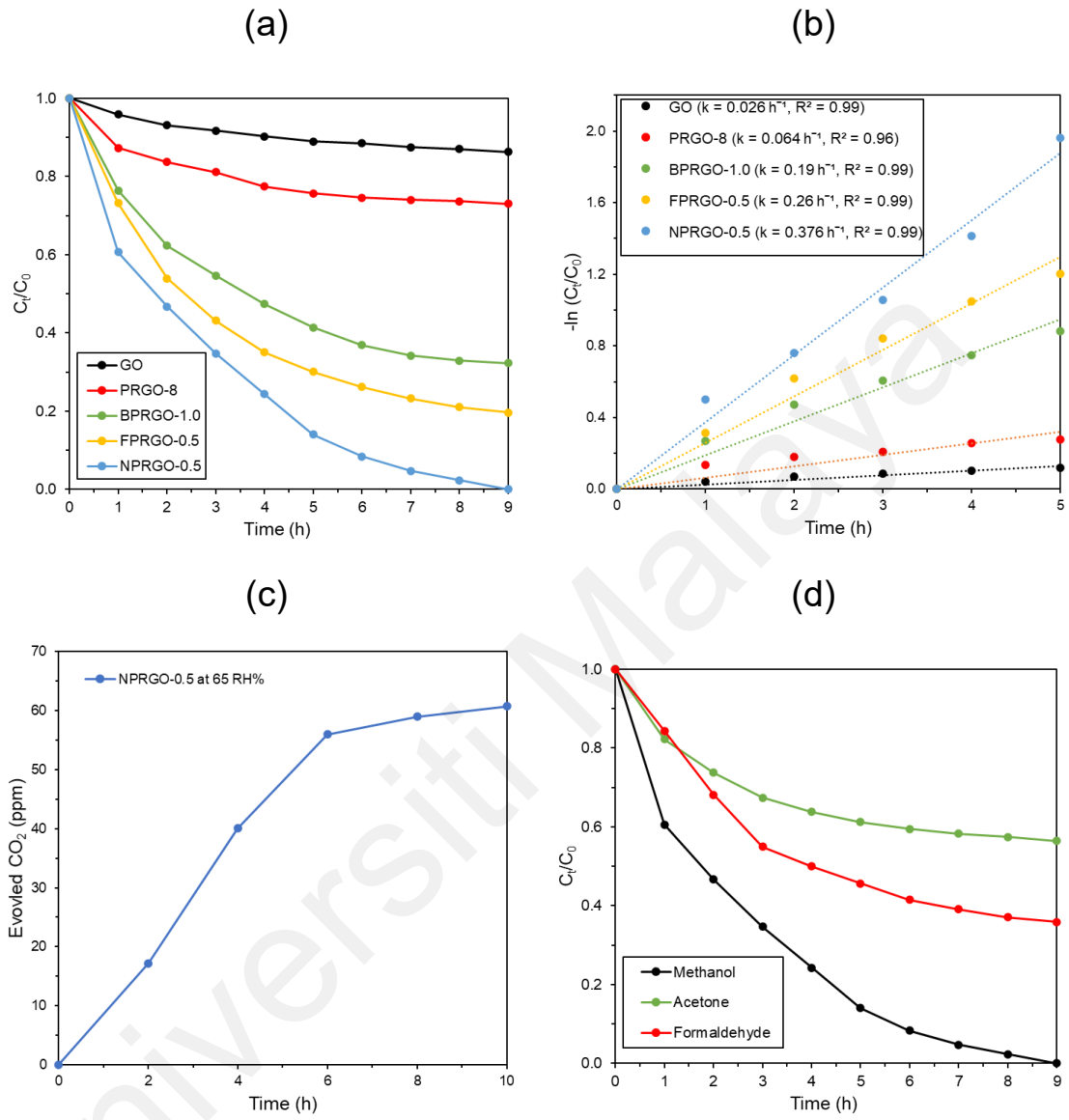

Figure 7.9: (a) PCO performance and the (b) respective pseudo-first order kinetic of GO, PRGO-8, BPRGO-1.0, FPRGO-0.5, and NPRGO-0.5 in 9 h, (c) CO_2 evolution during PCO by NPRGO-0.5 at 65 RH% in 10 h, and (d) PCO of 100 mg/m^3 of methanol, acetone, and formaldehyde by NPRGO-0.5 at 65 RH%.

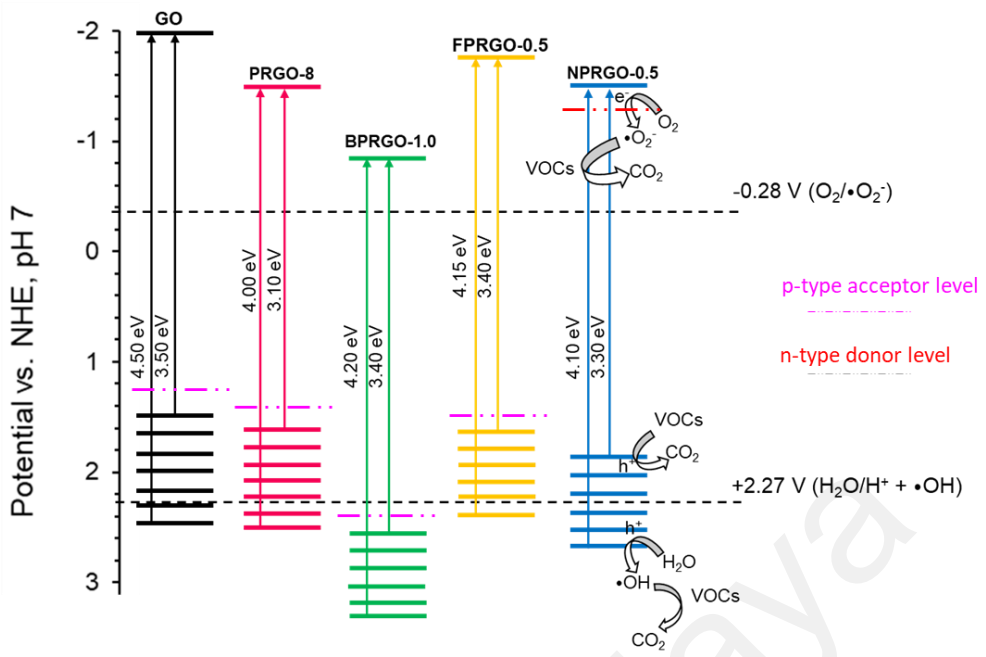

Figure 7.10: Summary of the comparison between PRGO, BPRGO, FPRGO, and NPRGO.

CHAPTER 8: CONCLUSION

8.1 Conclusion

In conclusion, metal-free heteroatom-doped PRGO such as BPRGO, FPRGO, and NPRGO photocatalysts were successfully synthesized with the photoirradiation method. The solution-based photoirradiation synthesis methods are scalable, facile, and green. By controlling the photoirradiation duration, the dopant concentrations and bonding configurations could be tuned to increase the charge carrier density. The NPRGO photocatalyst exhibited the highest PCO activity where toxic VOCs such as methanol was completely mineralised into harmless CO_2 in 10 h. The outstanding photocatalytic activity of NPRGO was attributed to its excellent ability to separate photogenerated charge carriers. The efficient charge carrier separation of NPRGO photocatalyst was reflected by its low R_{ct} value (300 Ω/cm^2) and high photocurrent density (95 nA/cm^2). The NPRGO photocatalyst mineralised VOCs through the active species $\bullet O_2^-$ radicals, •OH radicals, and h_{VB}^+ species. Moreover, NPRGO photocatalyst demonstrated good PCO recyclability up to five cycles. This study provides new insights into a scalable green method for producing effective metal-free heteroatom-doped PRGO photocatalysts for air purification. This work also revolutionised the potential of GO-based material as standalone photocatalyst in photodegrading VOCs by transforming GO into effective heteroatom-doped PRGO photocatalysts.

8.2 Recommendations for Future Research

For future study, the heteroatom-doped PRGO photocatalysts especially NPRGO are highly potential for the photodegradation of aqueous phase pollutants. This is attributed to the adequate CB and VB positions of the heteroatom-doped PRGO for the generation of reactive species even in aqueous phase photodegradation.

Moreover, there are a few strategies that could be deployed to further study the heteroatom-doped PRGO photocatalysts for air purification. It is well known that heterojunction formation is an effective strategy to improve the overall photoactivity of a photocatalyst. Therefore, it is recommended that heteroatom-doped PRGO can be coupled with other metal-free photocatalysts such as gCN, SiC, and black phosphorus to obtain a metal-free heterojunction photocatalyst. For example, p-type FPRGO could be coupled with an n-type NPRGO or gCN to form a p-n heterojunction photocatalyst. The p-n heterojunction photocatalyst contains a built-in potential at its p-n interface, which could generate a powerful electrical field to separate charge carriers. Besides that, n-type NPRGO could be combined with an n-type gCN to form an n-n z-scheme photocatalyst. The z-scheme photocatalyst contains a larger redox potential than its p-n heterojunction counterpart, therefore a z-scheme photocatalyst could generate more radicals during a PCO process. Besides that, a continuous flow reactor can be built to test the photocatalytic activity of the heteroatom-doped PRGO photocatalysts in an open-loop system.

REFERENCES

Abdul-Wahab, S. A., En, S. C. F., Elkamel, A., Ahmadi, L., & Yetilmezsoy, K. (2015). A review of standards and guidelines set by international bodies for the parameters of indoor air quality. *Atmospheric Pollution Research*, *6*(5), 751-767.

Adam, M. G., Tran, P. T., & Balasubramanian, R. (2021). Air quality changes in cities during the COVID-19 lockdown: A critical review. *Atmospheric Research*, 105823.

Adeleye, A. S., Wang, X., Wang, F., Hao, R., Song, W., & Li, Y. (2018). Photoreactivity of graphene oxide in aqueous system: Reactive oxygen species formation and bisphenol A degradation. *Chemosphere*, *195*, 344-350.

Afroz, K., Moniruddin, M., Bakranov, N., Kudaibergenov, S., & Nuraje, N. (2018). A heterojunction strategy to improve the visible light sensitive water splitting performance of photocatalytic materials. *Journal of Materials Chemistry A*, *6*(44), 21696-21718.

Agrawal, G. P., & Dutta, N. K. (1993). Recombination mechanisms in semiconductors. In *Semiconductor Lasers* (pp. 74-146). Springer.

Ai, Z., Huang, Y., Lee, S., & Zhang, L. (2011). Monoclinic α-Bi_2O_3 photocatalyst for efficient removal of gaseous NO and HCHO under visible light irradiation. *Journal of Alloys and Compounds*, *509*(5), 2044-2049.

Ai, Z., Lee, S., Huang, Y., Ho, W., & Zhang, L. (2010). Photocatalytic removal of NO and HCHO over nanocrystalline Zn_2SnO_4 microcubes for indoor air purification. *Journal of Hazardous Materials*, *179*(1-3), 141-150.

Alberici, R. M., & Jardim, W. F. (1997). Photocatalytic destruction of VOCs in the gas-phase using titanium dioxide. *Applied Catalysis B: Environmental*, *14*(1-2), 55-68.

Albero, J., Mateo, D., & García, H. (2019). Graphene-based materials as efficient photocatalysts for water splitting. *Molecules*, *24*(5), 906.

Amadei, C. A., Montessori, A., Kadow, J. P., Succi, S., & Vecitis, C. D. (2017). Role of oxygen functionalities in graphene oxide architectural laminate subnanometer spacing and water transport. *Environmental Science & Technology*, *51*(8), 4280-4288.

Amano, F., Tosaki, R., Sato, K., & Higuchi, Y. (2018). Effects of donor doping and acceptor doping on rutile TiO_2 particles for photocatalytic O_2 evolution by water oxidation. *Journal of Solid State Chemistry*, *258*, 79-85.

Amer, A. A., Reda, S., Mousa, M., & Mohamed, M. M. (2017). Mn_3O_4/graphene nanocomposites: outstanding performances as highly efficient photocatalysts and microwave absorbers. *RSC Advances*, *7*(2), 826-839.

Amieva, E. J.-C., Fuentes-Ramirez, R., Martinez-Hernandez, A., Millan-Chiu, B., Lopez-Marin, L. M., Castaño, V., & Velasco-Santos, C. (2015). Graphene oxide and reduced graphene oxide modification with polypeptide chains from chicken feather keratin. *Journal of Alloys and Compounds*, *643*, S137-S143.

An, H., Li, Y., Long, P., Gao, Y., Qin, C., Cao, C., Feng, Y., & Feng, W. (2016). Hydrothermal preparation of fluorinated graphene hydrogel for high-performance supercapacitors. *Journal of Power Sources*, *312*, 146-155.

Ao, C., & Lee, S. (2003). Enhancement effect of TiO_2 immobilized on activated carbon filter for the photodegradation of pollutants at typical indoor air level. *Applied Catalysis B: Environmental*, *44*(3), 191-205.

AO Smith. (2020). *VOC and Formaldehyde, Why It's Bad For Indoor Air, and What To Do About It*. Retrieved May 1, 2022 from https://www.aosmith.com.ph/blog/voc-and-formaldehyde-why-its-bad-indoor-air-and-what-do-about-it

Aranzabal, A., Pereda-Ayo, B., González-Marcos, M., González-Marcos, J., López-Fonseca, R., & González-Velasco, J. (2014). State of the art in catalytic oxidation of chlorinated volatile organic compounds. *Chemical Papers*, *68*(9), 1169-1186.

Aroutiounian, V., Arakelyan, V., Shahnazaryan, G., Hovhannisyan, H., Wang, H., & Turner, J. A. (2007). Photoelectrochemistry of tin-doped iron oxide electrodes. *Solar Energy*, *81*(11), 1369-1376.

Ashurst, J. V., & Nappe, T. M. (2018). *Methanol toxicity*. StatPearls Publishing.

Ayoko, G. A., & Wang, H. (2014). Volatile organic compounds in indoor environments. *Indoor Air Pollution*, 69-107.

Baca, M., Rychtowski, P., Wróbel, R., Mijowska, E., Kaleńczuk, R., & Zielińska, B. (2020). Surface properties tuning of exfoliated graphitic carbon nitride for multiple photocatalytic performance. *Solar Energy*, *207*, 528-538.

Bajaj, S., Wang, H., Doak, J. W., Wolverton, C., & Snyder, G. J. (2016). Calculation of dopant solubilities and phase diagrams of X–Pb–Se (X= Br, Na) limited to defects with localized charge. *Journal of Materials Chemistry C*, *4*(9), 1769-1775.

Bianchi, C., Gatto, S., Pirola, C., Naldoni, A., Di Michele, A., Cerrato, G., Crocellà, V., & Capucci, V. (2014). Photocatalytic degradation of acetone, acetaldehyde and toluene in gas-phase: comparison between nano and micro-sized TiO_2. *Applied Catalysis B: Environmental*, *146*, 123-130.

Bianco, A., Cheng, H.-M., Enoki, T., Gogotsi, Y., Hurt, R. H., Koratkar, N., Kyotani, T., Monthioux, M., Park, C. R., & Tascon, J. M. (2013). All in the graphene family–A recommended nomenclature for two-dimensional carbon materials. In (Vol. 65, pp. 1-6): Elsevier.

Bie, C., Yu, H., Cheng, B., Ho, W., Fan, J., & Yu, J. (2021). Design, fabrication, and mechanism of nitrogen‐doped graphene‐based photocatalyst. *Advanced Materials*, *33*(9), 2003521.

Bishnoi, A., Kumar, S., & Joshi, N. (2017). Wide-angle X-ray diffraction (WXRD): technique for characterization of nanomaterials and polymer nanocomposites. In *Microscopy methods in nanomaterials characterization* (pp. 313-337). Elsevier.

Bloh, J. Z., Dillert, R., & Bahnemann, D. W. (2012). Designing optimal metal-doped photocatalysts: correlation between photocatalytic activity, doping ratio, and particle size. *The Journal of Physical Chemistry C*, *116*(48), 25558-25562.

Bobrow, L. S. (1996). *Fundamentals of electrical engineering*. Oxford University Press, USA.

Boguski, T. (2006). *Understanding Units of Measurement*. Kansas State University. Retrieved 2021, January 5th from https://cfpub.epa.gov/ncer_abstracts/index.cfm/fuseaction/display.files/fileid/14285

Boobis, A., Dearman, R., Foster, J., & Harrison, D. (2010). *Committee on Toxicity of Chemicals in Food, Consumer Products and the Environment* Health Protection Agency].

Boyjoo, Y., Sun, H., Liu, J., Pareek, V. K., & Wang, S. (2017). A review on photocatalysis for air treatment: From catalyst development to reactor design. *Chemical Engineering Journal*, *310*, 537-559.

Brochen, S., Granier, C., Feuillet, G., & Pernot, J. (2012). Role of deep and shallow donor levels on n-type conductivity of hydrothermal ZnO. *Applied Physics Letters*, *100*(5), 052115.

Brown, S. (1997). National State of the Environment Report: Indoor Air Quality.

Bumbrah, G. S., & Sharma, R. M. (2016). Raman spectroscopy–Basic principle, instrumentation and selected applications for the characterization of drugs of abuse. *Egyptian Journal of Forensic Sciences*, *6*(3), 209-215.

Bustos-Ramírez, K., Barrera-Díaz, C. E., De Icaza-Herrera, M., Martínez-Hernández, A. L., Natividad-Rangel, R., & Velasco-Santos, C. (2015). 4-chlorophenol removal from water using graphite and graphene oxides as photocatalysts. *Journal of Environmental Health Science and Engineering*, *13*(1), 33.

Bustos-Ramirez, K., Barrera-Diaz, C. E., De Icaza, M., Martínez-Hernández, A. L., & Velasco-Santos, C. (2015). Photocatalytic activity in phenol removal of water from graphite and graphene oxides: effect of degassing and chemical oxidation in the synthesis process. *Journal of Chemistry*, *2015*.

Cao, L., Gao, Z., Suib, S. L., Obee, T. N., Hay, S. O., & Freihaut, J. D. (2000). Photocatalytic oxidation of toluene on nanoscale TiO_2 catalysts: studies of deactivation and regeneration. *Journal of Catalysis*, *196*(2), 253-261.

Cha, J. H., Kim, D. H., Park, C., Choi, S. J., Jang, J. S., Yang, S. Y., Kim, I. D., & Choi, S. Y. (2020). Low‐Thermal‐Budget Doping of 2D Materials in Ambient Air Exemplified by Synthesis of Boron‐Doped Reduced Graphene Oxide. *Advanced Science*, *7*(7), 1903318.

Chang, Y.-S., Chen, F.-K., Tsai, D.-C., Kuo, B.-H., & Shieu, F.-S. (2021). N-doped reduced graphene oxide for room-temperature NO gas sensors. *Scientific Reports*, *11*(1), 1-12.

Chang, Y., Chen, J., Jia, J., Hu, X., Yang, H., Jia, M., & Wen, Z. (2021). The fluorine-doped and defects engineered carbon nanosheets as advanced electrocatalysts for oxygen electroreduction. *Applied Catalysis B: Environmental*, *284*, 119721.

Chen, J., Kou, S.-c., & Poon, C.-s. (2011). Photocatalytic cement-based materials: Comparison of nitrogen oxides and toluene removal potentials and evaluation of self-cleaning performance. *Building and Environment*, *46*(9), 1827-1833.

Chen, P., Chen, L., Dong, X. a., Wang, H., Li, J., Zhou, Y., Xue, C., Zhang, Y., & Dong, F. (2020). Enhanced Photocatalytic VOCs Mineralization via Special Ga-OH

Charge Transfer Channel in α-Ga_2O_3/MgAl-LDH Heterojunction. *ACS ES&T Engineering*, *1*(3), 501-511.

Chen, Q. (2009). Ventilation performance prediction for buildings: A method overview and recent applications. *Building and Environment*, *44*(4), 848-858.

Chen, W., Yan, L., & Bangal, P. R. (2010). Preparation of graphene by the rapid and mild thermal reduction of graphene oxide induced by microwaves. *Carbon*, *48*(4), 1146-1152.

Chen, W. K. (2004). *The electrical engineering handbook*. Elsevier.

Chen, X., Pan, J., Fu, J., Zhu, X., Zhang, C., Zhou, L., Wang, Y., Lv, Z., Zhou, Y., & Han, S. T. (2018). Polyoxometalates‐Modulated Reduced Graphene Oxide Flash Memory with Ambipolar Trapping as Bidirectional Artificial Synapse. *Advanced Electronic Materials*, *4*(12), 1800444.

Chen, X., Zhu, X., Zhang, S. R., Pan, J., Huang, P., Zhang, C., Ding, G., Zhou, Y., Zhou, K., & Roy, V. A. (2019). Controlled Nonvolatile Transition in Polyoxometalates‐Graphene Oxide Hybrid Memristive Devices. *Advanced Materials Technologies*, *4*(3), 1800551.

Chen, Y., Li, D., Chen, J., Wang, J., Meng, S., Xian, J., Fu, X., & Shao, Y. (2013). A promising new photocatalyst $CdSnO_3 \cdot 3H_2O$ for air purification under ambient condition. *Applied Catalysis B: Environmental*, *129*, 403-408.

Cheng, W., Liu, X., Li, N., Han, J., Li, S., & Yu, S. (2018). Boron-doped graphene as a metal-free catalyst for gas-phase oxidation of benzyl alcohol to benzaldehyde. *RSC Advances*, *8*(20), 11222-11229.

Chien, C. T., Li, S. S., Lai, W. J., Yeh, Y. C., Chen, H. A., Chen, I. S., Chen, L. C., Chen, K. H., Nemoto, T., & Isoda, S. (2012). Tunable photoluminescence from graphene oxide. *Angewandte Chemie International Edition*, *51*(27), 6662-6666.

Ching, K., Fang, T., Chen, X., Liu, S., & Zhao, C. (2019). One-Step Photochemical Synthesis of Transition Metal-Graphene Hybrid for Electrocatalysis. *ACS Sustainable Chemistry & Engineering*.

Choi, W., Termin, A., & Hoffmann, M. R. (1994). The role of metal ion dopants in quantum-sized TiO_2: correlation between photoreactivity and charge carrier recombination dynamics. *The Journal of Physical Chemistry*, *98*(51), 13669-13679.

Chong, K. Y., Chia, C. H., Chook, S. W., Zakaria, S., & Lucas, D. (2018). Simplified production of graphene oxide assisted by high shear exfoliation of graphite with controlled oxidation. *New Journal of Chemistry*, *42*(6), 4507-4512.

Choudhury, B., Dey, M., & Choudhury, A. (2014). Shallow and deep trap emission and luminescence quenching of TiO_2 nanoparticles on Cu doping. *Applied Nanoscience*, *4*(4), 499-506.

Chowdhury, S., Jiang, Y., Muthukaruppan, S., & Balasubramanian, R. (2018). Effect of boron doping level on the photocatalytic activity of graphene aerogels. *Carbon*, *128*, 237-248.

Chu, D., Mo, J., Peng, Q., Zhang, Y., Wei, Y., Zhuang, Z., & Li, Y. (2011). Enhanced Photocatalytic Properties of SnO_2 Nanocrystals with Decreased Size for ppb‐level Acetaldehyde Decomposition. *ChemCatChem*, *3*(2), 371-377.

Chuang, C.-H., Wang, Y.-F., Shao, Y.-C., Yeh, Y.-C., Wang, D.-Y., Chen, C.-W., Chiou, J., Ray, S. C., Pong, W., & Zhang, L. (2014). The effect of thermal reduction on the photoluminescence and electronic structures of graphene oxides. *Scientific Reports*, *4*, 4525.

Chun, H.-H., & Jo, W.-K. (2016). Adsorption and photocatalysis of 2-ethyl-1-hexanol over graphene oxide–TiO_2 hybrids post-treated under various thermal conditions. *Applied Catalysis B: Environmental*, *180*, 740-750.

Colpan, C. O., Nalbant, Y., & Ercelik, M. (2018). 4.28 Fundamentals of Fuel Cell Technologies.

Commandeur, D., Brown, G., McNulty, P., Dadswell, C., Spencer, J., & Chen, Q. (2019). Yttrium-doped ZnO nanorod arrays for increased charge mobility and carrier density for enhanced solar water splitting. *The Journal of Physical Chemistry C*, *123*(30), 18187-18197.

Control, C. f. D., & Prevention. US Department of Housing and Urban Development (2006) Healthy housing reference manual. *US Department of Health and Human Services, Atlanta*.

Darlington, A., Chan, M., Malloch, D., Pilger, C., & Dixon, M. (2000). The biofiltration of indoor air: implications for air quality. *Indoor Air*, *10*(1), 39-46.

Darlington, A. B., Dat, J. F., & Dixon, M. A. (2001). The biofiltration of indoor air: air flux and temperature influences the removal of toluene, ethylbenzene, and xylene. *Environmental Science & Technology*, *35*(1), 240-246.

Das, A., Pisana, S., Chakraborty, B., Piscanec, S., Saha, S. K., Waghmare, U. V., Novoselov, K. S., Krishnamurthy, H. R., Geim, A. K., & Ferrari, A. C. (2008). Monitoring dopants by Raman scattering in an electrochemically top-gated graphene transistor. *Nature Nanotechnology*, *3*(4), 210-215.

Das, G. S., Tripathi, K. M., Kumar, G., Paul, S., Mehara, S., Bhowmik, S., Pakhira, B., Sarkar, S., Roy, M., & Kim, T. (2019). Nitrogen-doped fluorescent graphene nanosheets as visible-light-driven photocatalysts for dye degradation and selective sensing of ascorbic acid. *New Journal of Chemistry*, *43*(36), 14575-14583.

Debono, O., Hequet, V., Le Coq, L., Locoge, N., & Thevenet, F. (2017). VOC ternary mixture effect on ppb level photocatalytic oxidation: Removal kinetic, reaction intermediates and mineralization. *Applied Catalysis B: Environmental*, *218*, 359-369.

del Pino, A. P., González-Campo, A., Giraldo, S., Peral, J., György, E., Logofatu, C., deMello, A. J., & Puigmartí-Luis, J. (2018). Synthesis of graphene-based photocatalysts for water splitting by laser-induced doping with ionic liquids. *Carbon*, *130*, 48-58.

Del Pino, A. P., György, E., Cotet, C., Baia, L., & Logofatu, C. (2016). Laser-induced chemical transformation of free-standing graphene oxide membranes in liquid and gas ammonia environments. *RSC Advances*, *6*(55), 50034-50042.

Demeestere, K., Dewulf, J., & Van Langenhove, H. (2007). Heterogeneous photocatalysis as an advanced oxidation process for the abatement of chlorinated, monocyclic aromatic and sulfurous volatile organic compounds in air: state of the art. *Critical Reviews in Environmental Science and Technology*, *37*(6), 489-538.

Department of Occupational Safety and Health. (2022). *Indoor Air Quality*. Retrieved April 26, 2022 from https://www.dosh.gov.my/index.php/chemical-management-v/indoor-air-quality

Díez, N., Śliwak, A., Gryglewicz, S., Grzyb, B., & Gryglewicz, G. (2015). Enhanced reduction of graphene oxide by high-pressure hydrothermal treatment. *RSC Advances*, *5*(100), 81831-81837.

Ding, Y., Zhang, P., Zhuo, Q., Ren, H., Yang, Z., & Jiang, Y. (2011). A green approach to the synthesis of reduced graphene oxide nanosheets under UV irradiation. *Nanotechnology*, *22*(21), 215601.

Djurišić, A. B., He, Y., & Ng, A. M. (2020). Visible-light photocatalysts: Prospects and challenges. *APL Materials*, *8*(3), 030903.

Ebrahimi, A., & Fatemi, S. (2017). Titania-reduced graphene oxide nanocomposite as a promising visible light-active photocatalyst for continuous degradation of VVOC in air purification process. *Clean Technologies and Environmental Policy*, *19*(8), 2089-2098.

Einaga, H., Ibusuki, T., & Futamura, S. (2004). Photocatalytic oxidation of benzene in air. *Journal of Solar Energy Engineering*, *126*(2), 789-793.

Fan, W., Lai, Q., Zhang, Q., & Wang, Y. (2011). Nanocomposites of TiO_2 and reduced graphene oxide as efficient photocatalysts for hydrogen evolution. *The Journal of Physical Chemistry C*, *115*(21), 10694-10701.

Fang, P., Tang, Z.-j., Chen, X.-b., Tang, Z.-x., Chen, D.-s., Huang, J.-h., Zeng, W.-h., & Cen, C.-p. (2016). Experimental study on the absorption of toluene from exhaust gas by paraffin/surfactant/water emulsion. *Journal of Chemistry*, *2016*.

Feng, W., Long, P., Feng, Y., & Li, Y. (2016). Two‐dimensional fluorinated graphene: synthesis, structures, properties and applications. *Advanced Science*, *3*(7), 1500413.

Fleck, R., Gill, R., Pettit, T., Irga, P., Williams, N., Seymour, J., & Torpy, F. (2020). Characterisation of fungal and bacterial dynamics in an active green wall used for indoor air pollutant removal. *Building and Environment*, *179*, 106987.

Fontelles-Carceller, O., Muñoz-Batista, M. J., Fernández-García, M., & Kubacka, A. (2016). Interface effects in sunlight-driven Ag/g-C_3N_4 composite catalysts: study of the toluene photodegradation quantum efficiency. *ACS Applied Materials & Interfaces*, *8*(4), 2617-2627.

Formenti, M., Juillet, F., Meriaudeau, P., & Teichner, S. (1971). Heterogeneous photocatalysis for partial oxidation of paraffins. *Chemical Technology*(NNOV), 680-+.

Fujihara, S., Kusakado, J., & Kimura, T. (1998). Fluorine doping in transparent conductive ZnO thin films by a sol-gel method using trifluoroacetic acid. *Journal of Materials Science Letters*, *17*(9), 781-783.

Fujishima, A., & Honda, K. (1972). Electrochemical photolysis of water at a semiconductor electrode. *Nature*, *238*(5358), 37-38.

Gan, Z., Xiong, S., Wu, X., He, C., Shen, J., & Chu, P. K. (2011). Mn2+-bonded reduced graphene oxide with strong radiative recombination in broad visible range caused by resonant energy transfer. *Nano Letters*, *11*(9), 3951-3956.

Gao, W. (2015). The chemistry of graphene oxide. *Graphene Oxide*, 61-95.

Gao, Y., Wang, Y., & Wang, Y. (2007). Photocatalytic hydrogen evolution from water on SiC under visible light irradiation. *Reaction Kinetics and Catalysis Letters*, *91*(1), 13-19.

GB/T 18883-. (2002). Indoor air quality standard. In: Ministry of Environmental Protection of the People's Republic of China.

Geim, A. K., & Novoselov, K. S. (2010). The Rise of Graphene. In *Nanoscience and Technology: a Collection of Reviews from Nature Journals* (pp. 11-19). World Scientific.

Geng, Q., Guo, Q., & Yue, X. (2010). Adsorption and photocatalytic degradation kinetics of gaseous cyclohexane in an annular fluidized bed photocatalytic reactor. *Industrial & Engineering Chemistry Research*, *49*(10), 4644-4652.

Gengler, R. Y. N., Badali, D. S., Zhang, D., Dimos, K., Spyrou, K., Gournis, D., & Miller, R. J. D. (2013). Revealing the ultrafast process behind the photoreduction of graphene oxide. *Nature Communications*, *4*.

Ghahramanifard, F., Rouhollahi, A., & Fazlolahzadeh, O. (2018). Electrodeposition of Cu-doped p-type ZnO nanorods; effect of Cu doping on structural, optical and photoelectrocatalytic property of ZnO nanostructure. *Superlattices and Microstructures*, *114*, 1-14.

Giannakopoulou, T., Papailias, I., Todorova, N., Boukos, N., Liu, Y., Yu, J., & Trapalis, C. (2017). Tailoring the energy band gap and edges' potentials of g-C_3N_4/TiO_2 composite photocatalysts for NO_x removal. *Chemical Engineering Journal*, *310*, 571-580.

Gliniak, J., Lin, J. H., Chen, Y. T., Li, C. R., Jokar, E., Chang, C. H., Peng, C. S., Lin, J. N., Lien, W. H., & Tsai, H. M. (2017). Sulfur‐Doped Graphene Oxide Quantum Dots as Photocatalysts for Hydrogen Generation in the Aqueous Phase. *ChemSusChem*, *10*(16), 3260-3267.

Goel, M., Siegert, M., Krauss, G., Mohanraj, J., Hochgesang, A., Heinrich, D. C., Fried, M., Pflaum, J., & Thelakkat, M. (2020). HOMO‐HOMO Electron Transfer: An Elegant Strategy for p‐Type Doping of Polymer Semiconductors toward Thermoelectric Applications. *Advanced Materials*, *32*(43), 2003596.

Gong, P., Wang, Z., Li, Z., Mi, Y., Sun, J., Niu, L., Wang, H., Wang, J., & Yang, S. (2013). Photochemical synthesis of fluorinated graphene via a simultaneous fluorination and reduction route. *RSC Advances*, *3*(18), 6327-6330.

Grand View Research, I. (2017). *Photocatalyst Market Analysis By Material (Titanium Dioxide, Zinc Oxide), By Application (Self-cleaning, Air Purification, Water Purification), By Region, And Segment Forecasts, 2018 - 2025*. Retrieved May 5, 2022 from https://www.grandviewresearch.com/industry-analysis/photocatalyst-market

Greczynski, G., & Hultman, L. (2020). X-ray photoelectron spectroscopy: towards reliable binding energy referencing. *Progress in Materials Science*, *107*, 100591.

Guardia, L., Villar-Rodil, S., Paredes, J., Rozada, R., Martínez-Alonso, A., & Tascón, J. (2012). UV light exposure of aqueous graphene oxide suspensions to promote their direct reduction, formation of graphene–metal nanoparticle hybrids and dye degradation. *Carbon*, *50*(3), 1014-1024.

Guo, L., Zhang, Y. L., Han, D. D., Jiang, H. B., Wang, D., Li, X. B., Xia, H., Feng, J., Chen, Q. D., & Sun, H. B. (2014). Laser‐mediated programmable N doping and simultaneous reduction of graphene oxides. *Advanced Optical Materials*, *2*(2), 120-125.

Han, D. D., Liu, Y. Q., Ma, J. N., Mao, J. W., Chen, Z. D., Zhang, Y. L., & Sun, H. B. (2018). Biomimetic Graphene Actuators Enabled by Multiresponse Graphene Oxide Paper with Pretailored Reduction Gradient. *Advanced Materials Technologies*, *3*(12), 1800258.

Han, D. D., Zhang, Y. L., Ma, J. N., Liu, Y., Mao, J. W., Han, C. H., Jiang, K., Zhao, H. R., Zhang, T., & Xu, H. L. (2017). Sunlight‐Reduced Graphene Oxides as Sensitive Moisture Sensors for Smart Device Design. *Advanced Materials Technologies*, *2*(8), 1700045.

Han, Z., Chang, V.-W., Wang, X., Lim, T.-T., & Hildemann, L. (2013). Experimental study on visible-light induced photocatalytic oxidation of gaseous formaldehyde by polyester fiber supported photocatalysts. *Chemical Engineering Journal*, *218*, 9-18.

Hasani, A., Sharifi Dehsari, H., Amiri Zarandi, A., Salehi, A., Taromi, F. A., & Kazeroni, H. (2015). Visible light-assisted photoreduction of graphene oxide using CdS nanoparticles and gas sensing properties. *Journal of Nanomaterials*, *2015*.

He, F., Jeon, W., & Choi, W. (2021). Photocatalytic air purification mimicking the self-cleaning process of the atmosphere. *Nature Communications*, *12*(1), 1-4.

He, F., Weon, S., Jeon, W., Chung, M. W., & Choi, W. (2021). Self-wetting triphase photocatalysis for effective and selective removal of hydrophilic volatile organic compounds in air. *Nature Communications*, *12*(1), 1-12.

He, Y., Liu, Y.-Q., Ma, J.-N., Han, D.-D., Mao, J.-W., Han, C.-H., & Zhang, Y.-L. (2017). Facile fabrication of high-performance humidity sensors by flash reduction of GO. *IEEE Sensors Journal*, *17*(16), 5285-5289.

Heeley-Hill, A. C., Grange, S. K., Ward, M. W., Lewis, A. C., Owen, N., Jordan, C., Hodgson, G., & Adamson, G. (2021). Frequency of use of household products containing VOCs and indoor atmospheric concentrations in homes. *Environmental Science: Processes & Impacts*, *23*(5), 699-713.

Hernandez, G., Wallis, S. L., Graves, I., Narain, S., Birchmore, R., & Berry, T.-A. (2020). The effect of ventilation on volatile organic compounds produced by new furnishings in residential buildings. *Atmospheric Environment: X*, *6*, 100069.

Ho, C.-C., Kang, F., Chang, G.-M., You, S.-J., & Wang, Y.-F. (2019). Application of recycled lanthanum-doped TiO_2 immobilized on commercial air filter for visible-light photocatalytic degradation of acetone and NO. *Applied Surface Science*, *465*, 31-40.

Hoffmann, M. R., Martin, S. T., Choi, W., & Bahnemann, D. W. (1995). Environmental applications of semiconductor photocatalysis. *Chemical Reviews*, *95*(1), 69-96.

Hong, X., Yu, W., Wang, A., & Chung, D. (2016). Graphite oxide paper as a polarizable electrical conductor in the through-thickness direction. *Carbon*, *109*, 874-882.

Hou, W.-C., Chowdhury, I., Goodwin Jr, D. G., Henderson, W. M., Fairbrother, D. H., Bouchard, D., & Zepp, R. G. (2015). Photochemical transformation of graphene oxide in sunlight. *Environmental Science & Technology*, *49*(6), 3435-3443.

Hou, W.-C., & Wang, Y.-S. (2017). Photocatalytic generation of H_2O_2 by graphene oxide in organic electron donor-free condition under sunlight. *ACS Sustainable Chemistry & Engineering*, *5*(4), 2994-3001.

Hsu, H.-C., Shown, I., Wei, H.-Y., Chang, Y.-C., Du, H.-Y., Lin, Y.-G., Tseng, C.-A., Wang, C.-H., Chen, L.-C., & Lin, Y.-C. (2013). Graphene oxide as a promising photocatalyst for CO_2 to methanol conversion. *Nanoscale*, *5*(1), 262-268.

Hu, B., Hu, M., Guo, Q., Wang, K., & Wang, X. (2019). In-vacancy engineered plate-like $In(OH)_3$ for effective photocatalytic reduction of CO_2 with H_2O vapor. *Applied Catalysis B: Environmental*, *253*, 77-87.

Hu, J., Wu, X., Zhang, Q., Gao, M., Qiu, H., Huang, K., Feng, S., Yang, Y., Liu, Z., & Zhao, B. (2017). Preparation of a highly active palladium nanoparticle/polyoxometalate/reduced graphene oxide nanocomposite by a

simple photoreduction method and its application to the electrooxidation of ethylene glycol and glycerol. *Electrochemistry Communications*, *83*, 56-60.

Hu, X., Li, C., Sun, Z., Song, J., & Zheng, S. (2020). Enhanced photocatalytic removal of indoor formaldehyde by ternary heterogeneous $BiOCl/TiO_2$/sepiolite composite under solar and visible light. *Building and Environment*, *168*, 106481.

Huang, B., He, J., Bian, S., Zhou, C., Li, Z., Xi, F., Liu, J., & Dong, X. (2018). S-doped graphene quantum dots as nanophotocatalyst for visible light degradation. *Chinese Chemical Letters*, *29*(11), 1698-1701.

Huang, D., Fu, X., Long, J., Jiang, X., Chang, L., Meng, S., & Chen, S. (2015). Hydrothermal synthesis of $MSn(OH)_6$ (M= Co, Cu, Fe, Mg, Mn, Zn) and their photocatalytic activity for the destruction of gaseous benzene. *Chemical Engineering Journal*, *269*, 168-179.

Huang, H., Xu, Y., Feng, Q., & Leung, D. Y. (2015). Low temperature catalytic oxidation of volatile organic compounds: a review. *Catalysis Science & Technology*, *5*(5), 2649-2669.

Huang, J., Lv, T., Huang, Q., Deng, Z., Chen, J., Liu, Z., & Wang, G. (2020). Effect of Rh valence state and doping concentration on the structure and photocatalytic H_2 evolution in (Nb, Rh) codoped TiO_2 nanorods. *Nanoscale*, *12*(43), 22082-22090.

Huang, Q., Ma, W., Yan, X., Chen, Y., Zhu, S., & Shen, S. (2013). Photocatalytic decomposition of gaseous HCHO by $ZrxTi1- xO_2$ catalysts under UV–vis light irradiation with an energy-saving lamp. *Journal of Molecular Catalysis A: Chemical*, *366*, 261-265.

Huang, R., Xu, X., Zhu, J., Liu, W., Yuan, R., Fu, X., Zhang, Y., & Li, Z. (2012). Nanocrystalline $CaSb_2O_5(OH)_2$ and $Ca_2Sb_2O_7$: Controlled syntheses, electronic structures and photocatalytic activity. *Applied Catalysis B: Environmental*, *127*, 205-211.

Huang, Y., Ho, S. S. H., Lu, Y., Niu, R., Xu, L., Cao, J., & Lee, S. (2016). Removal of indoor volatile organic compounds via photocatalytic oxidation: a short review and prospect. *Molecules*, *21*(1), 56.

IKEA. (2019). *Meet GUNRID – the air purifying curtain*. Retrieved May 5, 2022 from https://about.ikea.com/en/sustainability/healthy-and-sustainable-living/meet-gunrid--the-air-purifying-curtain

Imamura, G., & Saiki, K. (2013). UV-irradiation induced defect formation on graphene on metals. *Chemical Physics Letters*, *587*, 56-60.

Imamura, G., & Saiki, K. (2015). Effect of UV light-induced nitrogen doping on the field effect transistor characteristics of graphene. *RSC Advances*, *5*(86), 70522-70526.

Institute of Environmental Epidemiology. (1996). Guidelines for good indoor air quality in office premises. In: Ministry of the Environment Singapore.

Inturi, S. N. R., Boningari, T., Suidan, M., & Smirniotis, P. G. (2014). Visible-light-induced photodegradation of gas phase acetonitrile using aerosol-made transition metal (V, Cr, Fe, Co, Mn, Mo, Ni, Cu, Y, Ce, and Zr) doped TiO_2. *Applied Catalysis B: Environmental*, *144*, 333-342.

Irga, P., Abdo, P., Zavattaro, M., & Torpy, F. (2017). An assessment of the potential fungal bioaerosol production from an active living wall. *Building and Environment*, *111*, 140-146.

Ito, J., Nakamura, J., & Natori, A. (2008). Semiconducting nature of the oxygen-adsorbed graphene sheet. *Journal of Applied Physics*, *103*(11), 113712.

Jaakkola, J., Tuomaala, P., & Seppänen, O. (1994). Air recirculation and sick building syndrome: a blinded crossover trial. *American Journal of Public Health*, *84*(3), 422-428.

Jafari, A. J., Arfaeinia, H., Ramavandi, B., Kalantary, R. R., & Esrafily, A. (2019). Ozone-assisted photocatalytic degradation of gaseous toluene from waste air stream using silica-functionalized graphene oxide/ZnO coated on fiberglass: performance, intermediates, and mechanistic pathways. *Air Quality, Atmosphere & Health*, *12*(10), 1181-1188.

Jantunen, M., Jaakkola, J. J., & Krzyzanowski, M. (1997). *Assessment of exposure to indoor air pollutants*. WHO Regional Office Europe.

Jian, R.-S., Huang, Y.-S., Lai, S.-L., Sung, L.-Y., & Lu, C.-J. (2013). Compact instrumentation of a μ-GC for real time analysis of sub-ppb VOC mixtures. *Microchemical Journal*, *108*, 161-167.

Jiang, H., Zhao, B., Liu, Y., Li, S., Liu, J., Song, Y., Wang, D., Xin, W., & Ren, L. (2020). Review of photoreduction and synchronous patterning of graphene oxide toward advanced applications. *Journal of Materials Science*, 1-18.

Jiang, S., Sun, Y., Dai, H., Hu, J., Ni, P., Wang, Y., Li, Z., & Li, Z. (2015). Nitrogen and fluorine dual-doped mesoporous graphene: a high-performance metal-free ORR electrocatalyst with a super-low HO 2− yield. *Nanoscale*, *7*(24), 10584-10589.

Jiang, Y., Chowdhury, S., & Balasubramanian, R. (2019). Nitrogen and sulfur codoped graphene aerogels as absorbents and visible light-active photocatalysts for environmental remediation applications. *Environmental Pollution*, *251*, 344-353.

Jiao, D., Zhong, X., Qiu, W., Zhang, H., Liu, Z., & Zhang, G. (2018). Structure and electric conduction in pulsed laser-deposited ZnO thin films individually doped with N, P, or Na. *Journal of Electronic Materials*, *47*(7), 3521-3528.

Jimmy, C. Y., Tang, H. Y., Yu, J., Chan, H., Zhang, L., Xie, Y., Wang, H., & Wong, S. (2002). Bactericidal and photocatalytic activities of TiO_2 thin films prepared by sol–gel and reverse micelle methods. *Journal of Photochemistry and Photobiology A: Chemistry*, *153*(1-3), 211-219.

Jin, S., Li, X., Yang, W., Zhao, Y., Bian, L., & Lu, S. (2020). Electrical and Optical Properties of Beryllium Deep Acceptors in GaN. *Journal of Electronic Materials*, *49*(12), 7472-7478.

Jin, T., Chen, J., Wang, C., Qian, Y., & Lu, L. (2020). Facile synthesis of fluorine-doped graphene aerogel with rich semi-ionic C–F bonds for high-performance supercapacitor application. *Journal of Materials Science*, *55*, 12103-12113.

Jo, W.-K., & Kang, H.-J. (2013). Titanium dioxide–graphene oxide composites with different ratios supported by Pyrex tube for photocatalysis of toxic aromatic vapors. *Powder Technology*, *250*, 115-121.

Joucken, F., Tison, Y., Le Fèvre, P., Tejeda, A., Taleb-Ibrahimi, A., Conrad, E., Repain, V., Chacon, C., Bellec, A., & Girard, Y. (2015). Charge transfer and electronic doping in nitrogen-doped graphene. *Scientific Reports*, *5*(1), 1-10.

Kabir, E., & Kim, K.-H. (2012). A review of some representative techniques for controlling the indoor volatile organic compounds. *Asian Journal of Atmospheric Environment*, *6*(3), 137-146.

Kahn, A. (2016). Fermi level, work function and vacuum level. *Materials Horizons*, *3*(1), 7-10.

Kamaei, M., Rashedi, H., Dastgheib, S. M. M., & Tasharrofi, S. (2018). Comparing photocatalytic degradation of gaseous ethylbenzene using N-doped and pure TiO_2 nano-catalysts coated on glass beads under both UV and visible light irradiation. *Catalysts*, *8*(10), 466.

Kamal, M. S., Razzak, S. A., & Hossain, M. M. (2016). Catalytic oxidation of volatile organic compounds (VOCs)–A review. *Atmospheric environment*, *140*, 117-134.

Kamarulzaman, N., Kasim, M. F., & Rusdi, R. (2015). Band gap narrowing and widening of ZnO nanostructures and doped materials. *Nanoscale Research Letters*, *10*(1), 346.

Kang, I.-S., Xi, J., & Hu, H.-Y. (2018). Photolysis and photooxidation of typical gaseous VOCs by UV Irradiation: Removal performance and mechanisms. *Frontiers of Environmental Science & Engineering*, *12*(3), 8.

Kang, S. H., Kim, I. G., Kim, B. N., Sul, J. H., Kim, Y. S., & You, I. K. (2018). Facile Fabrication of Flexible In‐Plane Graphene Micro‐Supercapacitor via Flash Reduction. *ETRI Journal*, *40*(2), 275-282.

Kepić, D., Sandoval, S., Pino, Á. P. d., György, E., Cabana, L., Ballesteros, B., & Tobias, G. (2017). Nanosecond Laser‐Assisted Nitrogen Doping of Graphene Oxide Dispersions. *ChemPhysChem*, *18*(8), 935-941.

Khan, F. I., & Ghoshal, A. K. (2000). Removal of volatile organic compounds from polluted air. *Journal of Loss Prevention in the Process Industries*, *13*(6), 527-545.

Khlyustova, A., Sirotkin, N., Kusova, T., Kraev, A., Titov, V., & Agafonov, A. (2020). Doped TiO_2: the effect of doping elements on photocatalytic activity. *Materials Advances*, *1*(5), 1193-1201.

Kim, J., Zhou, R., Murakoshi, K., & Yasuda, S. (2018). Advantage of semi-ionic bonding in fluorine-doped carbon materials for the oxygen evolution reaction in alkaline media. *RSC Advances*, *8*(26), 14152-14156.

Kim, S. B., & Hong, S. C. (2002). Kinetic study for photocatalytic degradation of volatile organic compounds in air using thin film TiO_2 photocatalyst. *Applied Catalysis B: Environmental*, *35*(4), 305-315.

Kim, S. C. (2002). The catalytic oxidation of aromatic hydrocarbons over supported metal oxide. *Journal of Hazardous Materials*, *91*(1-3), 285-299.

Kim, S. C., Nahm, S. W., Shim, W. G., Lee, J. W., & Moon, H. (2007). Influence of physicochemical treatments on spent palladium based catalyst for catalytic oxidation of VOCs. *Journal of Hazardous Materials*, *141*(1), 305-314.

Kim, S. R., Parvez, M. K., & Chhowalla, M. (2009). UV-reduction of graphene oxide and its application as an interfacial layer to reduce the back-transport reactions in dye-sensitized solar cells. *Chemical Physics Letters*, *483*(1-3), 124-127.

Kong, L., Li, X., Song, P., & Ma, F. (2021). Porous graphitic carbon nitride nanosheets for photocatalytic degradation of formaldehyde gas. *Chemical Physics Letters*, *762*, 138132.

Kovalevskiy, N., Lyulyukin, M., Selishchev, D., & Kozlov, D. (2018). Analysis of air photocatalytic purification using a total hazard index: Effect of the composite TiO_2/zeolite photocatalyst. *Journal of Hazardous Materials*, *358*, 302-309.

Krishnamoorthy, K., Mohan, R., & Kim, S.-J. (2011). Graphene oxide as a photocatalytic material. *Applied Physics Letters*, *98*(24), 244101.

Kuang, Y., Shang, J., & Zhu, T. (2019). Photo-Activated Graphene Oxide to Enhance Photocatalytic Reduction of CO_2. *ACS Applied Materials & Interfaces*.

Kulathunga, K., Gannoruwa, A., & Bandara, J. (2016). Infrared light active photocatalyst for the purification of airborne indoor pollutants. *Catalysis Communications*, *86*, 9-13.

Kulathunga, K., Yan, C.-F., & Bandara, J. (2020). Photocatalytic removal of airborne indoor pollutants by IR illuminated silver coated TiO_2 catalyst: Advantage of one-dimensional TiO_2 nanostructures in IR active photocatalysis. *Colloids and Surfaces A: Physicochemical and Engineering Aspects*, *590*, 124509.

Kumar, V., Kumar, A., Lee, D.-J., & Park, S.-S. (2021). Estimation of number of graphene layers using different methods: a focused review. *Materials*, *14*(16), 4590.

Labour, J. M. o. H., & Welfare. (2001). Committee on sick house syndrome: indoor air pollution, progress report no. 3. In: Office of Chemical Safety, Pharmaceutical and Food Safety Bureau.

Latorre‐Sánchez, M., Primo, A., & García, H. (2013). P‐doped graphene obtained by pyrolysis of modified alginate as a photocatalyst for hydrogen generation from water‐methanol mixtures. *Angewandte Chemie International Edition*, *52*(45), 11813-11816.

Lavorato, C., Primo, A., Molinari, R., & Garcia, H. (2014). N‐Doped Graphene Derived from Biomass as a Visible‐Light Photocatalyst for Hydrogen Generation from Water/Methanol Mixtures. *Chemistry‐A European Journal*, *20*(1), 187-194.

Lee, S. J., Theerthagiri, J., Nithyadharseni, P., Arunachalam, P., Balaji, D., Kumar, A. M., Madhavan, J., Mittal, V., & Choi, M. Y. (2021). Heteroatom-doped graphene-based materials for sustainable energy applications: A review. *Renewable and Sustainable Energy Reviews*, *143*, 110849.

Lee, T., Kim, S., & Jang, H. (2016). Black phosphorus: Critical review and potential for water splitting photocatalyst. *Nanomaterials*, *6*(11), 194.

Lee, W. H., Suk, J. W., Chou, H., Lee, J., Hao, Y., Wu, Y., Piner, R., Akinwande, D., Kim, K. S., & Ruoff, R. S. (2012). Selective-area fluorination of graphene with fluoropolymer and laser irradiation. *Nano Letters*, *12*(5), 2374-2378.

Li, C., Xu, Y., Tu, W., Chen, G., & Xu, R. (2017). Metal-free photocatalysts for various applications in energy conversion and environmental purification. *Green Chemistry*, *19*(4), 882-899.

Li, H., & Bubeck, C. (2013). Photoreduction processes of graphene oxide and related applications. *Macromolecular Research*, *21*(3), 290-297.

Li, P., Kim, S., Jin, J., Do, H. C., & Park, J. H. (2020). Efficient photodegradation of volatile organic compounds by iron-based metal-organic frameworks with high adsorption capacity. *Applied Catalysis B: Environmental*, *263*, 118284.

Li, R., He, C., Cheng, L., Lin, G., Wang, G., Shi, D., Li, R. K.-Y., & Yang, Y. (2017). Polyoxometalate-enabled photoreduction of graphene oxide to bioinspired nacre-like composite films for supercapacitor electrodes. *Composites Part B: Engineering*, *121*, 75-82.

Li, X., Tang, T., Li, M., & He, X. (2015a). Nitrogen-doped graphene films from simple photochemical doping for n-type field-effect transistors. *Applied Physics Letters*, *106*(1), 013110.

Li, X., Tang, T., Li, M., & He, X. (2015b). Photochemical doping of graphene oxide thin films with nitrogen for electrical conductivity improvement. *Journal of Materials Science: Materials in Electronics*, *26*(3), 1770-1775.

Li, X., Xu, Y., Hu, G., Luo, Z., Xu, D., Tang, T., Wen, J., Li, M., Zhou, T., & Cheng, Y. (2018). Self-assembled formation of conjugated 3D reduced graphene oxide-wrapped helical CNTs nanostructure and nitrogen-doped using photochemical doping for high-performance supercapacitor electrodes. *Electrochimica Acta*, *280*, 33-40.

Li, X., Zhang, L., Yang, Z., Wang, P., Yan, Y., & Ran, J. (2020). Adsorption materials for volatile organic compounds (VOCs) and the key factors for VOCs adsorption process: A review. *Separation and Purification Technology*, *235*, 116213.

Li, Z., Del Cul, G. D., Yan, W., Liang, C., & Dai, S. (2004). Fluorinated carbon with ordered mesoporous structure. *Journal of the American Chemical Society*, *126*(40), 12782-12783.

Li, Z., Xu, S. C., Zhang, C., Liu, X. Y., Gao, S. S., Hu, L. T., Guo, J., Ma, Y., Jiang, S. Z., & Si, H. P. (2016). High-performance SERS substrate based on hybrid structure of graphene oxide/AgNPs/Cu film@ pyramid Si. *Scientific Reports*, *6*, 38539.

Liao, Y., Xie, C., Liu, Y., & Huang, Q. (2013). Enhancement of photocatalytic property of ZnO for gaseous formaldehyde degradation by modifying morphology and crystal defect. *Journal of Alloys and Compounds*, *550*, 190-197.

Lin, T., Huang, F., Liang, J., & Wang, Y. (2011). A facile preparation route for boron-doped graphene, and its CdTe solar cell application. *Energy & Environmental Science*, *4*(3), 862-865.

Linquip Team. (2020). *Natural Ventilation: Types, Advantages and Disadvantages*. Retrieved May 1, 2022 from https://www.linquip.com/blog/natural-ventilation/

Liscio, A., Veronese, G. P., Treossi, E., Suriano, F., Rossella, F., Bellani, V., Rizzoli, R., Samorì, P., & Palermo, V. (2011). Charge transport in graphene–polythiophene blends as studied by Kelvin Probe Force Microscopy and transistor characterization. *Journal of Materials Chemistry*, *21*(9), 2924-2931.

Liu, F., Tang, N., Tang, T., Liu, Y., Feng, Q., Zhong, W., & Du, Y. (2013). Photochemical doping of graphene oxide with nitrogen for photoluminescence enhancement. *Applied Physics Letters*, *103*(12), 123108.

Liu, G., Niu, P., Yin, L., & Cheng, H.-M. (2012). α-Sulfur crystals as a visible-light-active photocatalyst. *Journal of the American Chemical Society*, *134*(22), 9070-9073.

Liu, G., Yin, L. C., Niu, P., Jiao, W., & Cheng, H. M. (2013). Visible‐light‐responsive β‐rhombohedral boron photocatalysts. *Angewandte Chemie International Edition*, *52*(24), 6242-6245.

Liu, H., Liu, Y., & Zhu, D. (2011). Chemical doping of graphene. *Journal of Materials Chemistry*, *21*(10), 3335-3345.

Liu, J., Bai, H., Wang, Y., Liu, Z., Zhang, X., & Sun, D. D. (2010). Self‐assembling TiO2 nanorods on large graphene oxide sheets at a two‐phase interface and their anti‐recombination in photocatalytic applications. *Advanced Functional Materials*, *20*(23), 4175-4181.

Liu, Y.-Q., Ma, J.-N., Liu, Y., Han, D.-D., Jiang, H.-B., Mao, J.-W., Han, C.-H., Jiao, Z.-Z., & Zhang, Y.-L. (2017). Facile fabrication of moisture responsive graphene

actuators by moderate flash reduction of graphene oxides films. *Optical Materials Express*, *7*(7), 2617-2625.

Liu, Y., Li, J., Li, W., Li, Y., Zhan, F., Tang, H., & Chen, Q. (2016). Exploring the nitrogen species of nitrogen doped graphene as electrocatalysts for oxygen reduction reaction in Al–air batteries. *International Journal of Hydrogen Energy*, *41*(24), 10354-10365.

Loh, K. P., Bao, Q., Eda, G., & Chhowalla, M. (2010). Graphene oxide as a chemically tunable platform for optical applications. *Nature Chemistry*, *2*(12), 1015.

Low, F. W., Lai, C. W., & Hamid, S. B. A. (2015). Easy preparation of ultrathin reduced graphene oxide sheets at a high stirring speed. *Ceramics International*, *41*(4), 5798-5806.

Lu, N., Wang, P., Su, Y., Yu, H., Liu, N., & Quan, X. (2019). Construction of Z-Scheme g-C_3N_4/RGO/WO_3 with in situ photoreduced graphene oxide as electron mediator for efficient photocatalytic degradation of ciprofloxacin. *Chemosphere*, *215*, 444-453.

Lu, Y.-F., Lo, S.-T., Lin, J.-C., Zhang, W., Lu, J.-Y., Liu, F.-H., Tseng, C.-M., Lee, Y.-H., Liang, C.-T., & Li, L.-J. (2013). Nitrogen-doped graphene sheets grown by chemical vapor deposition: Synthesis and influence of nitrogen impurities on carrier transport. *ACS Nano*, *7*(8), 6522-6532.

Luo, J., Dong, G., Zhu, Y., Yang, Z., & Wang, C. (2017). Switching of semiconducting behavior from n-type to p-type induced high photocatalytic NO removal activity in g-C_3N_4. *Applied Catalysis B: Environmental*, *214*, 46-56.

Luo, Y., Chen, J., Liu, J., Shao, Y., Li, X., & Li, D. (2016). Hydroxide $SrSn(OH)_6$: a new photocatalyst for degradation of benzene and rhodamine B. *Applied Catalysis B: Environmental*, *182*, 533-540.

Luo, Z., Vora, P. M., Mele, E. J., Johnson, A. C., & Kikkawa, J. M. (2009). Photoluminescence and band gap modulation in graphene oxide. *Applied Physics Letters*, *94*(11), 111909.

Lv, T., Wu, M., Guo, M., Liu, Q., & Jia, L. (2019). Self-assembly photocatalytic reduction synthesis of graphene-encapusulated $LaNiO_3$ nanoreactor with high efficiency and stability for photocatalytic water splitting to hydrogen. *Chemical Engineering Journal*, *356*, 580-591.

Lyons, J. L., Janotti, A., & Van de Walle, C. G. (2013). Impact of group-ii acceptors on the electrical and optical properties of GaN. *Japanese Journal of Applied Physics*, *52*(8S), 08JJ04.

Ma, Z., Ren, F., Deng, Y., & Volinsky, A. A. (2020). Structural, electrochemical and optical properties of Ni doped ZnO: Experimental and theoretical investigation. *Optik*, *219*, 165204.

Main, D. M., & Hogan, T. J. (1983). Health effects of low-level exposure to formaldehyde. *Journal of Occupational Medicine.: Official Publication of the Industrial Medical Association 25*(12), 896-900.

Malaka, T., & Kodama, A. M. (1990). Respiratory health of plywood workers occupationally exposed to formaldehyde. *Archives of Environmental Health: An International Journal*, *45*(5), 288-294.

Malecha, K. T., & Nizkorodov, S. A. (2016). Photodegradation of secondary organic aerosol particles as a source of small, oxygenated volatile organic compounds. *Environmental Science & Technology*, *50*(18), 9990-9997.

Mamaghani, A. H., Haghighat, F., & Lee, C.-S. (2017). Photocatalytic oxidation technology for indoor environment air purification: the state-of-the-art. *Applied Catalysis B: Environmental*, *203*, 247-269.

Mamaghani, A. H., Haghighat, F., & Lee, C.-S. (2018a). Gas phase adsorption of volatile organic compounds onto titanium dioxide photocatalysts. *Chemical Engineering Journal*, *337*, 60-73.

Mamaghani, A. H., Haghighat, F., & Lee, C.-S. (2018b). Photocatalytic degradation of VOCs on various commercial titanium dioxides: Impact of operating parameters on removal efficiency and by-products generation. *Building and Environment*, *138*, 275-282.

Mangadlao, J. D., Cao, P., Choi, D., & Advincula, R. C. (2017). Photoreduction of Graphene Oxide and Photochemical Synthesis of Graphene–Metal Nanoparticle Hybrids by Ketyl Radicals. *ACS Applied Materials & Interfaces*, *9*(29), 24887-24898.

Manikandan, V. S., Sidhureddy, B., Thiruppathi, A. R., & Chen, A. (2019). Sensitive electrochemical detection of caffeic acid in wine based on fluorine-doped graphene oxide. *Sensors*, *19*(7), 1604.

Mannan, M., & Al-Ghamdi, S. G. (2021). Active Botanical Biofiltration in Built Environment to Maintain Indoor Air Quality. *Frontiers in Built Environment*, 99.

Mannan, M., Hirano, Y., Quitain, A., Koinuma, M., & Kida, T. (2018). Boron doped graphene oxide: synthesis and application to glucose responsive reactivity. *Journal of Material Sciences & Engineering*, *7*, 1-6.

Marcano, D. C., Kosynkin, D. V., Berlin, J. M., Sinitskii, A., Sun, Z., Slesarev, A., Alemany, L. B., Lu, W., & Tour, J. M. (2010). Improved synthesis of graphene oxide. *ACS Nano*, *4*(8), 4806-4814.

Mathkar, A., Tozier, D., Cox, P., Ong, P., Galande, C., Balakrishnan, K., Leela Mohana Reddy, A., & Ajayan, P. M. (2012). Controlled, stepwise reduction and band gap manipulation of graphene oxide. *The Journal of Physical Chemistry Letters*, *3*(8), 986-991.

Matsoso, B. J., Ranganathan, K., Mutuma, B. K., Lerotholi, T., Jones, G., & Coville, N. J. (2016). Time-dependent evolution of the nitrogen configurations in N-doped graphene films. *RSC Advances*, *6*(108), 106914-106920.

Matsumoto, Y., Koinuma, M., Ida, S., Hayami, S., Taniguchi, T., Hatakeyama, K., Tateishi, H., Watanabe, Y., & Amano, S. (2011). Photoreaction of graphene oxide nanosheets in water. *The Journal of Physical Chemistry C*, *115*(39), 19280-19286.

McDonald, M. P., Morozov, Y., Hodak, J. H., & Kuno, M. (2015). Spectroscopy and microscopy of graphene oxide and reduced graphene oxide. In *Graphene Oxide* (pp. 29-60). Springer.

Md Noor, J., Hawari, R., Mokhtar, M., Yussof, S., Chew, N., Norzan, N., Rahimi, R., Ismail, Z., Singh, S., & Baladas, J. (2020). Methanol outbreak: a Malaysian tertiary hospital experience. *International Journal of Emergency Medicine*, *13*(1), 1-7.

Medina, E., Wellon, G. C., & Evegren, F. (2017). *Methanol safe handling manual*. Retrieved May 5, 2022 from https://www.methanol.org/wp-content/uploads/2017/03/Safe-Handling-Manual.pdf

Meng, S., Li, D., Sun, M., Li, W., Wang, J., Chen, J., Fu, X., & Xiao, G. (2011). Sonochemical synthesis, characterization and photocatalytic properties of a novel cube-shaped $CaSn(OH)_6$. *Catalysis Communications*, *12*(11), 972-975.

MG HKIAQ. (2003). A guide on indoor air quality certification scheme for office and public places. Government of Hong Kong Special Administrative Region. *Indoor Air Quality Management Group*.

Mirzaei, A., Leonardi, S., & Neri, G. (2016). Detection of hazardous volatile organic compounds (VOCs) by metal oxide nanostructures-based gas sensors: A review. *Ceramics International*, *42*(14), 15119-15141.

Miyauchi, M., Irie, H., Liu, M., Qiu, X., Yu, H., Sunada, K., & Hashimoto, K. (2016). Visible-light-sensitive photocatalysts: nanocluster-grafted titanium dioxide for indoor environmental remediation. *The Journal of Physical Chemistry Letters*, *7*(1), 75-84.

Mo, J., Zhang, Y., & Xu, Q. (2013). Effect of water vapor on the by-products and decomposition rate of ppb-level toluene by photocatalytic oxidation. *Applied Catalysis B: Environmental*, *132*, 212-218.

Mohandoss, M., Gupta, S. S., Nelleri, A., Pradeep, T., & Maliyekkal, S. M. (2017). Solar mediated reduction of graphene oxide. *RSC Advances*, *7*(2), 957-963.

Mokhtar Mohamed, M., Mousa, M. A., Khairy, M., & Amer, A. A. (2018). Nitrogen graphene: A new and exciting generation of visible light driven photocatalyst and energy storage application. *ACS Omega*, *3*(2), 1801-1814.

Mølhave, L. (1991). Volatile organic compounds, indoor air quality and health. *Indoor Air*, *1*(4), 357-376.

Monteiro, R. A., Miranda, S. M., Rodrigues-Silva, C., Faria, J. L., Silva, A. M., Boaventura, R. A., & Vilar, V. J. (2015). Gas phase oxidation of n-decane and PCE by photocatalysis using an annular photoreactor packed with a monolithic catalytic bed coated with P25 and PC500. *Applied Catalysis B: Environmental*, *165*, 306-315.

Moreira, V. R., Lebron, Y. A. R., da Silva, M. M., de Souza Santos, L. V., Jacob, R. S., de Vasconcelos, C. K. B., & Viana, M. M. (2020). Graphene oxide in the remediation of norfloxacin from aqueous matrix: simultaneous adsorption and degradation process. *Environmental Science and Pollution Research*, *27*(27), 34513-34528.

Mortazavi, S., Mollabashi, M., Barri, R., Jones, K., Xiao, J. Q., Opila, R. L., & Shah, S. I. (2018). Modification of graphene oxide film properties using KrF laser irradiation. *RSC Advances*, *8*(23), 12808-12814.

Mull, B., Möhlmann, L., & Wilke, O. (2017). Photocatalytic degradation of toluene, butyl acetate and limonene under UV and visible light with titanium dioxide-graphene oxide as photocatalyst. *Environments*, *4*(1), 9.

Murashkina, A. A., Rudakova, A. V., Ryabchuk, V. K., Nikitin, K. V., Mikhailov, R. V., Emeline, A. V., & Bahnemann, D. W. (2018). Influence of the dopant concentration on the photoelectrochemical behavior of Al-doped TiO_2. *The Journal of Physical Chemistry C*, *122*(14), 7975-7981.

Murzin, P. D., Murashkina, A., Emeline, A., & Bahnemann, D. (2020). Effect of Sc 3+/V 5+ Co-doping on photocatalytic activity of TiO_2. *Topics in Catalysis*, 1-7.

Musico, Y. L. F., Kakati, N., Labata, M. F. M., Ocon, J. D., & Chuang, P.-Y. A. (2019). One-pot hydrothermal synthesis of heteroatom co-doped with fluorine on reduced graphene oxide for enhanced ORR activity and stability in alkaline media. *Materials Chemistry and Physics*, *236*, 121804.

Muthoosamy, K., Bai, R. G., Abubakar, I. B., Sudheer, S. M., Lim, H. N., Loh, H.-S., Huang, N. M., Chia, C. H., & Manickam, S. (2015). Exceedingly biocompatible and thin-layered reduced graphene oxide nanosheets using an eco-friendly mushroom extract strategy. *International Journal of Nanomedicine*, *10*, 1505.

Nadzir, M. S. M., Ooi, M. C. G., Alhasa, K. M., Bakar, M. A. A., Mohtar, A. A. A., Nor, M. F. F. M., Latif, M. T., Abd Hamid, H. H., Ali, S. H. M., & Ariff, N. M. (2020). The impact of movement control order (MCO) during pandemic COVID-19 on local air quality in an urban area of Klang valley, Malaysia. *Aerosol and Air Quality Research*, *20*(6), 1237-1248.

Nah, Y. C., Paramasivam, I., & Schmuki, P. (2010). Doped TiO_2 and TiO_2 nanotubes: synthesis and applications. *ChemPhysChem*, *11*(13), 2698-2713.

Nakajima, T., Koh, M., Gupta, V., Žemva, B., & Lutar, K. (2000). Electrochemical behavior of graphite highly fluorinated by high oxidation state complex fluorides and elemental fluorine. *Electrochimica Acta*, *45*(10), 1655-1661.

Nam, S., Jeong, Y. J., Park, C. E., & Jang, J. (2017). Enhanced gas barrier properties of graphene-TiO_2 nanocomposites on plastic substrates assisted by UV photoreduction of graphene oxide. *Organic Electronics*, *48*, 323-329.

Nanakoudis, A. (2019). *What is SEM? Scanning Electron Microscopy Explained*. Retrieved May 2, 2022 from https://www.thermofisher.com/blog/microscopy/what-is-sem-scanning-electron-microscopy-explained/

Newport. (2020). *Introduction to Solar Radiation*. Retrieved May 5, 2022 from https://www.newport.com/t/introduction-to-solar-radiation

Ngidi, N. P., Ollengo, M. A., & Nyamori, V. O. (2020). Tuning the properties of boron-doped reduced graphene oxide by altering the boron content. *New Journal of Chemistry*, *44*(39), 16864-16876.

Nguyen, B.-S., Xiao, Y.-K., Shih, C.-Y., Nguyen, V.-C., Chou, W.-Y., & Teng, H. (2018). Electronic structure manipulation of graphene dots for effective hydrogen evolution from photocatalytic water decomposition. *Nanoscale*, *10*(22), 10721-10730.

Nguyen, D. K., Tran, N. T. T., Nguyen, T. T., Chiu, Y.-H., & Lin, M.-F. (2019). Essential Properties of Fluorinated Graphene and Graphene Nanoribbons. In *2D and 3D Graphene Nanocomposites* (pp. 47-77). Jenny Stanford Publishing.

Ni, M., Leung, M. K., Leung, D. Y., & Sumathy, K. (2007). A review and recent developments in photocatalytic water-splitting using TiO_2 for hydrogen production. *Renewable and Sustainable Energy Reviews*, *11*(3), 401-425.

Nia, Z. K., Chen, J.-Y., Tang, B., Yuan, B., Wang, X.-G., & Li, J.-L. (2017). Optimizing the free radical content of graphene oxide by controlling its reduction. *Carbon*, *116*, 703-712.

Nicola, M., Alsafi, Z., Sohrabi, C., Kerwan, A., Al-Jabir, A., Iosifidis, C., Agha, M., & Agha, R. (2020). The socio-economic implications of the coronavirus pandemic (COVID-19): A review. *International Journal of Surgery*, *78*, 185-193.

Nishikawa, M., Shiroishi, W., Honghao, H., Suizu, H., Nagai, H., & Saito, N. (2017). Probability of Two-Step Photoexcitation of Electron from Valence Band to Conduction Band through Doping Level in TiO_2. *The Journal of Physical Chemistry A*, *121*(32), 5991-5997.

Noguchi, T., Fujishima, A., Sawunyama, P., & Hashimoto, K. (1998). Photocatalytic degradation of gaseous formaldehyde using TiO_2 film. *Environmental Science & Technology*, *32*(23), 3831-3833.

Novoselov, K. S., Geim, A. K., Morozov, S. V., Jiang, D.-e., Zhang, Y., Dubonos, S. V., Grigorieva, I. V., & Firsov, A. A. (2004). Electric field effect in atomically thin carbon films. *Science*, *306*(5696), 666-669.

Oh, J., Chang, Y. H., Kim, Y.-H., & Park, S. (2016). Thickness-dependent photocatalytic performance of graphite oxide for degrading organic pollutants under visible light. *Physical Chemistry Chemical Physics*, *18*(16), 10882-10886.

Oh, K.-J., Park, D.-W., Kim, S.-S., & Park, S.-W. (2010). Breakthrough data analysis of adsorption of volatile organic compounds on granular activated carbon. *Korean Journal of Chemical Engineering*, *27*(2), 632-638.

Okazaki, N., Takahashi, M., Murai, H., & Tada, A. (1999). XPS studies of a boron phosphate sample: unreacted H_3BO_3 or its derivative on the surface. *Phosphorus Research Bulletin*, *9*, 63-68.

Olumurewa, K., Olofinjana, B., Fasakin, O., Akhigbe, G., Eleruja, M., & Ajayi, E. (2020). Effect of hydrothermal and chemical treatment on the optical and electrical properties of reduced graphene oxide deposited on ITO glass. *Materials Research Express*, *7*(10), 105606.

Ott, W. R. (1982). Concepts of human exposure to air pollution. *Environment International*, *7*(3), 179-196.

Park, M.-S., Kim, K. H., Kim, M.-J., & Lee, Y.-S. (2016). NH_3 gas sensing properties of a gas sensor based on fluorinated graphene oxide. *Colloids and Surfaces A: Physicochemical and Engineering Aspects*, *490*, 104-109.

Park, M.-S., & Lee, Y.-S. (2016). Functionalization of graphene oxide by fluorination and its characteristics. *Journal of Fluorine Chemistry*, *182*, 91-97.

Parthiban, V., Bhuvaneshwari, B., Karthikeyan, J., Murugan, P., & Sahu, A. (2019). Fluorine-enriched mesoporous carbon as efficient oxygen reduction catalyst: understanding the defects in porous matrix and fuel cell applications. *Nanoscale Advances*, *1*(12), 4926-4937.

Pedrosa, M., Da Silva, E. S., Pastrana-Martínez, L. M., Drazic, G., Falaras, P., Faria, J. L., Figueiredo, J. L., & Silva, A. M. (2020). Hummers' and Brodie's graphene oxides as photocatalysts for phenol degradation. *Journal of Colloid and Interface Science*, *567*, 243-255.

Peera, S. G., Sahu, A., Arunchander, A., Bhat, S., Karthikeyan, J., & Murugan, P. (2015). Nitrogen and fluorine co-doped graphite nanofibers as high durable oxygen reduction catalyst in acidic media for polymer electrolyte fuel cells. *Carbon*, *93*, 130-142.

Physical Electronics. (2022). *XPS / ESCA*. Physical Electronics, Inc. (PHI). Retrieved May 3, 2022 from https://www.phi.com/surface-analysis-techniques/xps-esca.html

Pichat, P. (2019). A brief survey of the practicality of using photocatalysis to purify the ambient air (indoors or outdoors) or air effluents. *Applied Catalysis B: Environmental*, *245*, 770-776.

Plotnikov, V., Smirnov, V., Alfimov, M., & Shul'ga, Y. M. (2011). The graphite oxide photoreduction mechanism. *High Energy Chemistry*, *45*(5), 411-415.

Purssell, R. (2018). *Methanol Ingestion*. Retrieved April 28, 2022 from https://www.bcemergencynetwork.ca/clinical_resource/methanol-ingestion/

Putri, L. K., Ng, B.-J., Er, C.-C., Ong, W.-J., Chang, W. S., Mohamed, A. R., & Chai, S.-P. (2020). Insights on the impact of doping levels in oxygen-doped gC_3N_4 and its effects on photocatalytic activity. *Applied Surface Science*, *504*, 144427.

Putri, L. K., Ng, B.-J., Ong, W.-J., Lee, H. W., Chang, W. S., & Chai, S.-P. (2017). Heteroatom nitrogen-and boron-doping as a facile strategy to improve photocatalytic activity of standalone reduced graphene oxide in hydrogen evolution. *ACS Applied Materials & Interfaces*, *9*(5), 4558-4569.

Putri, L. K., Ong, W.-J., Chang, W. S., & Chai, S.-P. (2015). Heteroatom doped graphene in photocatalysis: a review. *Applied Surface Science*, *358*, 2-14.

Putri, L. K., Tan, L.-L., Ong, W.-J., Chang, W. S., & Chai, S.-P. (2016). Graphene oxide: exploiting its unique properties toward visible-light-driven photocatalysis. *Applied Materials Today*, *4*, 9-16.

PVEducation. (2015). *Energy of Photon*. Retrieved May 5, 2022 from https://www.pveducation.org/pvcdrom/properties-of-sunlight/energy-of-photon

Qiao, X., Liao, S., Wang, G., Zheng, R., Song, H., & Li, X. (2016). Simultaneous doping of nitrogen and fluorine into reduced graphene oxide: a highly active metal-free electrocatalyst for oxygen reduction. *Carbon*, *99*, 272-279.

Qu, X.-G., Liu, W.-X., Ma, J., & Cao, W. (2009). Research on photodegradation of formaldehyde by nanocrystalline N-TiO_2 powders under visible light irradiation. *Research on Chemical Intermediates*, *35*(3), 313-320.

Rabchinskii, M. K., Shnitov, V. V., Dideikin, A. T., Aleksenskii, A. E., Vul', S. P., Baidakova, M. V., Pronin, I. I., Kirilenko, D. A., Brunkov, P. N., & Weise, J. (2016). Nanoscale perforation of graphene oxide during photoreduction process in the argon atmosphere. *The Journal of Physical Chemistry C*, *120*(49), 28261-28269.

Rahman, M. Z., Kibria, M. G., & Mullins, C. B. (2020). Metal-free photocatalysts for hydrogen evolution. *Chemical Society Reviews*, *49*(6), 1887-1931.

Raillard, C., Hequet, V., Le Cloirec, P., & Legrand, J. (2006). Photocatalytic oxidation of methyl ethyl ketone over sol-gel and commercial TiO_2 for the improvement of indoor air. *Water Science and Technology*, *53*(11), 107-115.

Rani, P., & Jindal, V. (2013). Designing band gap of graphene by B and N dopant atoms. *RSC Advances*, *3*(3), 802-812.

Rao, Z., Lu, G., Chen, L., Mahmood, A., Shi, G., Tang, Z., Xie, X., & Sun, J. (2022). Photocatalytic oxidation mechanism of Gas-Phase VOCs: Unveiling the role of holes, •OH and $•O_2-$. *Chemical Engineering Journal*, *430*, 132766.

Reddy, K. R., Hassan, M., & Gomes, V. G. (2015). Hybrid nanostructures based on titanium dioxide for enhanced photocatalysis. *Applied Catalysis A: General*, *489*, 1-16.

Rezaee, A., Rangkooy, H., Khavanin, A., & Jafari, A. J. (2014). High photocatalytic decomposition of the air pollutant formaldehyde using nano-ZnO on bone char. *Environmental Chemistry Letters*, *12*(2), 353-357.

Riley, M., Wu, V., Liu, S., Gill, W., Lu, T.-M., & Plawsky, J. (2014). Surface area and porosity in obliquely grown photocatalytic titanium dioxide for air purification. *Journal of Applied Physics*, *115*(17), 174907.

Ritchie, H., & Roser, M. (2013). Indoor Air Pollution. *Our World in Data*.

Robertson, J., & Davis, C. (1995). Nitrogen doping of tetrahedral amorphous carbon. *Diamond and Related Materials*, *4*(4), 441-444.

Rocha, F. S., Gomes, A. J., Lunardi, C. N., Kaliaguine, S., & Patience, G. S. (2018). Experimental methods in chemical engineering: Ultraviolet visible spectroscopy—UV‐Vis. *The Canadian Journal of Chemical Engineering*, *96*(12), 2512-2517.

Romanos, J., Beckner, M., Stalla, D., Tekeei, A., Suppes, G., Jalisatgi, S., Lee, M., Hawthorne, F., Robertson, J., & Firlej, L. (2013). Infrared study of boron–carbon chemical bonds in boron-doped activated carbon. *Carbon*, *54*, 208-214.

Rosso, C., Filippini, G., Criado, A., Melchionna, M., Fornasiero, P., & Prato, M. (2021). Metal-Free Photocatalysis: Two-Dimensional Nanomaterial Connection toward Advanced Organic Synthesis. *ACS Nano*, *15*(3), 3621-3630.

Russell, J. A., Hu, Y., Chau, L., Pauliushchyk, M., Anastopoulos, I., Anandan, S., & Waring, M. S. (2014). Indoor-biofilter growth and exposure to airborne chemicals drive similar changes in plant root bacterial communities. *Applied and environmental microbiology*, *80*(16), 4805-4813.

Saha, J., & Chouhan, P. (2020). Indoor air pollution (IAP) and pre-existing morbidities among under-5 children in India: are risk factors of coronavirus disease (COVID-19)? *Environmental Pollution*, *266*, 115250.

Saha, S., Samanta, P., Murmu, N. C., Banerjee, A., Ganesh, R. S., Inokawa, H., & Kuila, T. (2018). Modified electrochemical charge storage properties of h-BN/rGO superlattice through the transition from n to p type semiconductor by fluorine doping. *Chemical Engineering Journal*, *339*, 334-345.

Saison, T., Gras, P., Chemin, N., Chanéac, C., Durupthy, O., Brezova, V., Colbeau-Justin, C., & Jolivet, J.-P. (2013). New insights into Bi_2WO_6 properties as a visible-light photocatalyst. *The Journal of Physical Chemistry C*, *117*(44), 22656-22666.

Salthammer, T. (2016). Very volatile organic compounds: an understudied class of indoor air pollutants. *Indoor Air*, *26*(1), 25-38.

Sanalife. (2021). *What You Can Do To Improve Indoor Air Quality In Your Office*. Retrieved May 5, 2022 from https://www.sanalifewellness.com/blog/what-you-can-do-to-improve-indoor-air-quality-in-your-office

Sandoval, S., Kumar, N., Oro-Solé, J., Sundaresan, A., Rao, C. N., Fuertes, A., & Tobias, G. (2016). Tuning the nature of nitrogen atoms in N-containing reduced graphene oxide. *Carbon*, *96*, 594-602.

Sarkar, S., Roy, R., Das, B. K., & Chattopadhyay, K. K. (2021). Temperature-dependent site selection of boron doping in chemically derived graphene. *Carbon*, *184*, 253-265.

Savva, K., Lin, Y.-H., Petridis, C., Kymakis, E., Anthopoulos, T., & Stratakis, E. (2014). In situ photo-induced chemical doping of solution-processed graphene oxide for electronic applications. *Journal of Materials Chemistry C*, *2*(29), 5931-5937.

Scardamaglia, M., Struzzi, C., Osella, S., Reckinger, N., Colomer, J.-F., Petaccia, L., Snyders, R., Beljonne, D., & Bittencourt, C. (2016). Tuning nitrogen species to control the charge carrier concentration in highly doped graphene. *2D Materials*, *3*(1), 011001.

Schiros, T., Nordlund, D., Pálová, L., Prezzi, D., Zhao, L., Kim, K. S., Wurstbauer, U., Gutiérrez, C., Delongchamp, D., & Jaye, C. (2012). Connecting dopant bond type with electronic structure in N-doped graphene. *Nano Letters*, *12*(8), 4025-4031.

Schreck, M., & Niederberger, M. (2019). Photocatalytic gas phase reactions. *Chemistry of Materials*, *31*(3), 597-618.

Serpone, N. (1997). Relative photonic efficiencies and quantum yields in heterogeneous photocatalysis. *Journal of Photochemistry and Photobiology A: Chemistry*, *104*(1-3), 1-12.

Shahzad, F., Zaidi, S. A., & Koo, C. M. (2017). Synthesis of multifunctional electrically tunable fluorine-doped reduced graphene oxide at low temperatures. *ACS Applied Materials & Interfaces*, *9*(28), 24179-24189.

She, X., Wu, J., Xu, H., Mo, Z., Lian, J., Song, Y., Liu, L., Du, D., & Li, H. (2017). Enhancing charge density and steering charge unidirectional flow in 2D non-metallic semiconductor-CNTs-metal coupled photocatalyst for solar energy conversion. *Applied Catalysis B: Environmental*, *202*, 112-117.

Shen, Y., Wang, L., Wu, Y., Li, X., Zhao, Q., Hou, Y., & Teng, W. (2015). Facile solvothermal synthesis of $MnFe_2O_4$ hollow nanospheres and their photocatalytic degradation of benzene investigated by in situ FTIR. *Catalysis Communications*, *68*, 11-14.

Shi, L., Li, P., Zhou, W., Wang, T., Chang, K., Zhang, H., Kako, T., Liu, G., & Ye, J. (2016). n-Type boron phosphide as a highly stable, metal-free, visible-light-active photocatalyst for hydrogen evolution. *Nano Energy*, *28*, 158-163.

Shulga, Y. M., Martynenko, V., Muradyan, V., Baskakov, S., Smirnov, V., & Gutsev, G. (2010). Gaseous products of thermo-and photo-reduction of graphite oxide. *Chemical Physics Letters*, *498*(4-6), 287-291.

Sim, Y., Surendran, S., Cha, H., Choi, H., Je, M., Yoo, S., Seok, D. C., Jung, Y. H., Jeon, C., & Kim, D. J. (2022). Fluorine-doped graphene oxide prepared by direct plasma treatment for supercapacitor application. *Chemical Engineering Journal*, *428*, 132086.

Simon, J., Protasenko, V., Lian, C., Xing, H., & Jena, D. (2010). Polarization-induced hole doping in wide–band-gap uniaxial semiconductor heterostructures. *Science*, *327*(5961), 60-64.

Singh, A. P., Kumari, S., Shrivastav, R., Dass, S., & Satsangi, V. R. (2008). Iron doped nanostructured TiO_2 for photoelectrochemical generation of hydrogen. *International Journal of Hydrogen Energy*, *33*(20), 5363-5368.

Singh, M., Kaushal, S., Singh, P., & Sharma, J. (2018). Boron doped graphene oxide with enhanced photocatalytic activity for organic pollutants. *Journal of Photochemistry and Photobiology A: Chemistry*, *364*, 130-139.

Siong, V. L. E., Lee, K. M., Juan, J. C., Lai, C. W., Tai, X. H., & Khe, C. S. (2019). Removal of methylene blue dye by solvothermally reduced graphene oxide: a metal-free adsorption and photodegradation method. *RSC Advances*, *9*(64), 37686-37695.

Siong, V. L. E., Tai, X. H., Lee, K. M., Juan, J. C., & Lai, C. W. (2020). Unveiling the enhanced photoelectrochemical and photocatalytic properties of reduced graphene oxide for photodegradation of methylene blue dye. *RSC Advances*, *10*(62), 37905-37915.

Sittig, M. (1981). Handbook of toxic and hazardous chemicals.

Sleiman, M., Conchon, P., Ferronato, C., & Chovelon, J.-M. (2009). Photocatalytic oxidation of toluene at indoor air levels (ppbv): Towards a better assessment of conversion, reaction intermediates and mineralization. *Applied Catalysis B: Environmental*, *86*(3-4), 159-165.

SM, S. N., & Maiya, M. (2019). Photocatalytic degradation of gaseous toluene using self-assembled air filter based on chitosan/activated carbon/TiO_2. *Journal of Environmental Chemical Engineering*, *7*(6), 103455.

Sokolov, D. A., Shepperd, K. R., & Orlando, T. M. (2010). Formation of graphene features from direct laser-induced reduction of graphite oxide. *The Journal of Physical Chemistry Letters*, *1*(18), 2633-2636.

Spinelle, L., Gerboles, M., Kok, G., Persijn, S., & Sauerwald, T. (2017). Review of portable and low-cost sensors for the ambient air monitoring of benzene and other volatile organic compounds. *Sensors*, *17*(7), 1520.

Spinelle, L., Gerboles, M., Kok, G., & Sauerwald, T. (2015). Sensitivity of VOC sensors for air quality monitoring within the EURAMET key-VOC project. Proceedings of the Fourth Eunetair Scientific Meeting, Linköping, Sweden,

Srikanth, V. V., Sampath Kumar, P., & Kumar, V. B. (2012). A brief review on the in situ synthesis of boron-doped diamond thin films. *International Journal of Electrochemistry*, *2012*.

Stankovich, S., Dikin, D. A., Piner, R. D., Kohlhaas, K. A., Kleinhammes, A., Jia, Y., Wu, Y., Nguyen, S. T., & Ruoff, R. S. (2007). Synthesis of graphene-based nanosheets via chemical reduction of exfoliated graphite oxide. *Carbon*, *45*(7), 1558-1565.

Štengl, V., Bakardjieva, S., Grygar, T. M., Bludská, J., & Kormunda, M. (2013). TiO_2-graphene oxide nanocomposite as advanced photocatalytic materials. *Chemistry Central Journal*, *7*(1), 41.

Stobinski, L., Lesiak, B., Malolepszy, A., Mazurkiewicz, M., Mierzwa, B., Zemek, J., Jiricek, P., & Bieloshapka, I. (2014). Graphene oxide and reduced graphene oxide studied by the XRD, TEM and electron spectroscopy methods. *Journal of Electron Spectroscopy and Related Phenomena*, *195*, 145-154.

Sun, C., & Corbett, B. (2018). Trifluoroacetic acid: Three times the fluoride, three times the toxicity? *The American Journal of Emergency Medicine*, *36*(3), 529. e521-529. e522.

Sun, X., Zhang, Y., Song, P., Pan, J., Zhuang, L., Xu, W., & Xing, W. (2013). Fluorine-doped carbon blacks: highly efficient metal-free electrocatalysts for oxygen reduction reaction. *Acs Catalysis*, *3*(8), 1726-1729.

Superior Health Council. (2017). *Indoor air quality in Belgium* F. C. S. a. E. Federal Public Service Health.

Suszanowicz, D. (2018). Optimisation of heat loss through ventilation for residential buildings. *Atmosphere*, *9*(3), 95.

Tai, X. H., Lai, C. W., Yang, T. C. K., Johan, M. R., Lee, K. M., Chen, C.-Y., & Juan, J. C. (2022). Highly Effective Removal of Volatile Organic Pollutants with pn Heterojunction Photoreduced Graphene Oxide-TiO2 Photocatalyst. *Journal of Environmental Chemical Engineering*, *10*(2), 107304.

Takehira, H., Islam, M. S., Karim, M. R., Shudo, Y., Ohtani, R., Lindoy, L. F., Taniguchi, T., Osada, M., & Hayami, S. (2017). Photoreduction Dependent p‐and n‐Type Semiconducting Field‐Effect Transistor Properties in Undoped Reduced Graphene Oxide. *ChemistrySelect*, *2*(24), 6941-6944.

Talukder, N., Wang, Y., Nunna, B. B., & Lee, E. S. (2021). Nitrogen-doped graphene nanomaterials for electrochemical catalysis/reactions: A review on chemical structures and stability. *Carbon*, *185*, 198-214.

Tan, L.-L., Ong, W.-J., Chai, S.-P., & Mohamed, A. R. (2014). Band gap engineered, oxygen-rich TiO_2 for visible light induced photocatalytic reduction of CO_2. *Chemical Communications*, *50*(52), 6923-6926.

Tang, F., & Yang, X. (2012). A "deactivation" kinetic model for predicting the performance of photocatalytic degradation of indoor toluene, o-xylene, and benzene. *Building and Environment*, *56*, 329-334.

Tang, Z.-R., Zhang, Y., Zhang, N., & Xu, Y.-J. (2015). New insight into the enhanced visible light photocatalytic activity over boron-doped reduced graphene oxide. *Nanoscale*, *7*(16), 7030-7034.

Tayebi, M., Tayyebi, A., & Lee, B.-K. (2019). Improved photoelectrochemical performance of molybdenum (Mo)-doped monoclinic bismuth vanadate with increasing donor concentration. *Catalysis Today*, *328*, 35-42.

Taylor, J., Mavrogianni, A., Davies, M., Das, P., Shrubsole, C., Biddulph, P., & Oikonomou, E. (2015). Understanding and mitigating overheating and indoor PM2. 5 risks using coupled temperature and indoor air quality models. *Building Services Engineering Research and Technology*, *36*(2), 275-289.

Temerov, F., Haapanen, J., Mäkelä, J. M., & Saarinen, J. J. (2021). Photocatalytic Activity of Multicompound TiO2/SiO2 Nanoparticles. *Inorganics*, *9*(4), 21.

The National Institute for Occupational Safety and Health (NIOSH). (2011). *Methanol : Systemic Agent*. Retrieved May 5, 2022 from https://www.cdc.gov/niosh/ershdb/emergencyresponsecard_29750029.html

Thevenet, F., Guillard, C., & Rousseau, A. (2014). Acetylene photocatalytic oxidation using continuous flow reactor: Gas phase and adsorbed phase investigation, assessment of the photocatalyst deactivation. *Chemical Engineering Journal*, *244*, 50-58.

Thirumalainambi, R., Bardina, J. E., & Miyazawa, O. (2005). Nonintrusive techniques of inspections during the pre-launch phase of space vehicle. Modeling, Simulation, and Verification of Space-Based Systems II,

Thiruppathi, A. R., Sidhureddy, B., Keeler, W., & Chen, A. (2017). Facile one-pot synthesis of fluorinated graphene oxide for electrochemical sensing of heavy metal ions. *Electrochemistry Communications*, *76*, 42-46.

Tian, J., Tan, J., Hu, N., Liu, T., Wang, Y., Zhong, H., Cheng, J., & Zhang, X. (2018). Characteristics analysis for total volatile organic compounds emissions of methanol-diesel fuel. *Journal of the Energy Institute*, *91*(4), 527-533.

Tian, K., Wang, J., Cao, L., Yang, W., Guo, W., Liu, S., Li, W., Wang, F., Li, X., & Xu, Z. (2020). Single-site pyrrolic-nitrogen-doped sp2-hybridized carbon materials and their pseudocapacitance. *Nature Communications*, *11*(1), 1-10.

Titus, D., Samuel, E. J. J., & Roopan, S. M. (2019). Nanoparticle characterization techniques. In *Green Synthesis, Characterization and Applications of Nanoparticles* (pp. 303-319). Elsevier.

Tobaldi, D., Dvoranová, D., Lajaunie, L., Rozman, N., Figueiredo, B., Seabra, M., Škapin, A. S., Calvino, J., Brezová, V., & Labrincha, J. (2021). Graphene-TiO_2 hybrids for photocatalytic aided removal of VOCs and nitrogen oxides from outdoor environment. *Chemical Engineering Journal*, *405*, 126651.

Todorova, N., Giannakopoulou, T., Boukos, N., Vermisoglou, E., Lekakou, C., & Trapalis, C. (2017). Self-propagating solar light reduction of graphite oxide in water. *Applied Surface Science*, *391*, 601-608.

Tokode, O., Prabhu, R., Lawton, L. A., & Robertson, P. K. (2017). A photocatalytic impeller reactor for gas phase heterogeneous photocatalysis. *Journal of Environmental Chemical Engineering*, *5*(4), 3942-3948.

Tsai, K.-A., Hsieh, P.-Y., Lai, T.-H., Tsao, C.-W., Pan, H., Lin, Y.-G., & Hsu, Y.-J. (2020). Nitrogen-doped graphene quantum dots for remarkable solar hydrogen production. *ACS Applied Energy Materials*, *3*(6), 5322-5332.

Tsai, W.-T. (2017). Overview of green building material (GBM) policies and guidelines with relevance to indoor air quality management in Taiwan. *Environments*, *5*(1), 4.

Tu, N. D. K., Choi, J., Park, C. R., & Kim, H. (2015). Remarkable conversion between n-and p-type reduced graphene oxide on varying the thermal annealing temperature. *Chemistry of Materials*, *27*(21), 7362-7369.

Tu, Y., Nakamoto, H., Ichii, T., Utsunomiya, T., Khatri, O. P., & Sugimura, H. (2017). Fabrication of reduced graphene oxide micro patterns by vacuum-ultraviolet irradiation: From chemical and structural evolution to improving patterning precision by light collimation. *Carbon*, *119*, 82-90.

Tu, Y., Utsunomiya, T., Ichii, T., & Sugimura, H. (2017). Enhancing the electrical conductivity of vacuum-ultraviolet-reduced graphene oxide by multilayered stacking. *Journal of Vacuum Science & Technology B, Nanotechnology and Microelectronics: Materials, Processing, Measurement, and Phenomena*, *35*(3), 03D110.

Tu, Y., Utsunomiya, T., Kokufu, S., Soga, M., Ichii, T., & Sugimura, H. (2017). Immobilization of Reduced Graphene Oxide on Hydrogen-Terminated Silicon Substrate as a Transparent Conductive Protector. *Langmuir*, *33*(41), 10765-10771.

Ţucureanu, V., Matei, A., & Avram, A. M. (2016). FTIR spectroscopy for carbon family study. *Critical Reviews in Analytical Chemistry*, *46*(6), 502-520.

Türk, S., Altınsoy, I., Efe, G. Ç., Ipek, M., Özacar, M., & Bindal, C. (2018). The effect of reduction of graphene oxide on the formation of hydroxyapatite and tricalcium phosphate. *Vacuum*, *148*, 1-10.

Umweltbundesamt. (2007). Evaluation of indoor air contaminants by means of reference and guideline values: Handreichung der Ad-hoc-Arbeitsgruppe der Innenraumlufthygiene-Kommission des Umweltbundesamtes und der Obersten Landesgesundheitsbehörden. *Bundesgesundheitsblatt-Gesundheitsforschung-Gesundheitsschutz*, *50*, 990-1005.

United States Environmental Protection Agency. (2017). Volatile Organic Compounds' Impact on Indoor Air Quality.

United States Environmental Protection Agency. (2022). *Technical Overview of Volatile Organic Compounds*. Retrieved April 26, 2022 from https://www.epa.gov/indoor-air-quality-iaq/technical-overview-volatile-organic-compounds

University of Cambridge. (2020). *Direct and Indirect Band Gap Semiconductors*. Retrieved December 3, 2020 from https://www.doitpoms.ac.uk/tlplib/semiconductors/direct.php

UVResources. (2020). *UV-C Lamps: Playing it Safe*. Retrieved May 5, 2022 from http://www.uvresources.com/blog/uv-c-lamps-staying-safe/#:~:text=UV%2DC's%20effects%20on%20the,known%20carcinogen%20for%20human%20skin.

Van Khai, T., Na, H. G., Kwak, D. S., Kwon, Y. J., Ham, H., Shim, K. B., & Kim, H. W. (2012). Comparison study of structural and optical properties of boron-doped and undoped graphene oxide films. *Chemical Engineering Journal*, *211*, 369-377.

Wang, F., Aravind, S. J., Wu, H., Forys, J., Venkataraman, V., Ramanujachary, K., & Hu, X. (2017). Tunable green graphene-silk biomaterials: Mechanism of protein-based nanocomposites. *Materials Science and Engineering: C*, *79*, 728-739.

Wang, F., Ng, W. K. H., Jimmy, C. Y., Zhu, H., Li, C., Zhang, L., Liu, Z., & Li, Q. (2012). Red phosphorus: an elemental photocatalyst for hydrogen formation from water. *Applied Catalysis B: Environmental*, *111*, 409-414.

Wang, H. I., Braatz, M.-L., Richter, N., Tielrooij, K.-J., Mics, Z., Lu, H., Weber, N.-E., Müllen, K., Turchinovich, D., & Kläui, M. (2017). Reversible photochemical control of doping levels in supported graphene. *The Journal of Physical Chemistry C*, *121*(7), 4083-4091.

Wang, K.-h., Tsai, H.-h., & Hsieh, Y.-h. (1998). A study of photocatalytic degradation of trichloroethylene in vapor phase on TiO_2 photocatalyst. *Chemosphere*, *36*(13), 2763-2773.

Wang, L., Sofer, Z., Luxa, J., & Pumera, M. (2014). Nitrogen doped graphene: influence of precursors and conditions of the synthesis. *Journal of Materials Chemistry C*, *2*(16), 2887-2893.

Wang, P., Zhan, S., Xia, Y., Ma, S., Zhou, Q., & Li, Y. (2017). The fundamental role and mechanism of reduced graphene oxide in {rGO}/Pt-{TiO}2 nanocomposite for high-performance photocatalytic water splitting. *Applied Catalysis B: Environmental*, *207*, 335-346. https://doi.org/10.1016/j.apcatb.2017.02.031

Wang, S., Ang, H., & Tade, M. O. (2007). Volatile organic compounds in indoor environment and photocatalytic oxidation: state of the art. *Environment International*, *33*(5), 694-705.

Wang, S., Ding, Z., Chang, X., Xu, J., & Wang, D.-H. (2020). Modified nano-TiO_2 based composites for environmental photocatalytic applications. *Catalysts*, *10*(7), 759.

Wang, T., Ni, C., & Janotti, A. (2017). Band alignment and p-type doping of $ZnSnN_2$. *Physical Review B*, *95*(20), 205205.

Wang, W., & Ku, Y. (2003). Photocatalytic degradation of gaseous benzene in air streams by using an optical fiber photoreactor. *Journal of Photochemistry and Photobiology A: Chemistry*, *159*(1), 47-59.

Wang, X., Li, X., Zhang, L., Yoon, Y., Weber, P. K., Wang, H., Guo, J., & Dai, H. (2009). N-Doping of Graphene Through Electrothermal Reactions with Ammonia. *Science*, *324*, 768-771.

Wang, X., Sun, G., Routh, P., Kim, D.-H., Huang, W., & Chen, P. (2014). Heteroatom-doped graphene materials: syntheses, properties and applications. *Chemical Society Reviews*, *43*(20), 7067-7098.

Wang, Y., Chen, Y., Lacey, S. D., Xu, L., Xie, H., Li, T., Danner, V. A., & Hu, L. (2018). Reduced graphene oxide film with record-high conductivity and mobility. *Materials Today*, *21*(2), 186-192.

Wang, Z., Dong, Y., Li, H., Zhao, Z., Bin Wu, H., Hao, C., Liu, S., Qiu, J., & Lou, X. W. D. (2014). Enhancing lithium–sulphur battery performance by strongly binding the discharge products on amino-functionalized reduced graphene oxide. *Nature Communications*, *5*(1), 1-8.

Wang, Z., Li, P., Chen, Y., He, J., Liu, J., Zhang, W., & Li, Y. (2014). Phosphorus-doped reduced graphene oxide as an electrocatalyst counter electrode in dye-sensitized solar cells. *Journal of Power Sources*, *263*, 246-251.

Wei, Z., Sun, J., Xie, Z., Liang, M., & Chen, S. (2010). Removal of gaseous toluene by the combination of photocatalytic oxidation under complex light irradiation of UV and visible light and biological process. *Journal of Hazardous Materials*, *177*(1-3), 814-821.

Weon, S., Choi, E., Kim, H., Kim, J. Y., Park, H.-J., Kim, S.-m., Kim, W., & Choi, W. (2018). Active {001} facet exposed TiO_2 nanotubes photocatalyst filter for volatile organic compounds removal: from material development to commercial indoor air cleaner application. *Environmental Science & Technology*, *52*(16), 9330-9340.

Weon, S., He, F., & Choi, W. (2019). Status and challenges in photocatalytic nanotechnology for cleaning air polluted with volatile organic compounds: visible light utilization and catalyst deactivation. *Environmental Science: Nano*, *6*(11), 3185-3214.

Wilson, N., Pandey, P., Beanland, R., Rourke, J., Lupo, U., Rowlands, G., & Römer, R. (2010). On the structure and topography of free-standing chemically modified graphene. *New Journal of Physics*, *12*(12), 125010.

Withgott, J. H., Laposata, M., & Murck, B. (2007). Environment: The Science Behind the Stories, 3e.

Witjaksono, G., Junaid, M., Khir, M. H., Ullah, Z., Tansu, N., Saheed, M. S. B. M., Siddiqui, M. A., Ba-Hashwan, S. S., Algamili, A. S., & Magsi, S. A. (2021). Effect of Nitrogen Doping on the Optical Bandgap and Electrical Conductivity of Nitrogen-Doped Reduced Graphene Oxide. *Molecules*, *26*(21), 6424.

Wolkoff, P. (2018). Indoor air humidity, air quality, and health–An overview. *International Journal of Hygiene and Environmental Health*, *221*(3), 376-390.

Wong, C. P. P., Lai, C. W., Lee, K. M., & Hamid, S. B. A. (2015). Advanced chemical reduction of reduced graphene oxide and its photocatalytic activity in degrading reactive black 5. *Materials*, *8*(10), 7118-7128.

World Health Organization. (1990). *Indoor air quality: biological contaminants: report on a WHO meeting, Rautavaara, 29 August-2 September 1988*. World Health Organization. Regional Office for Europe.

World Health Organization. (1997). Methanol: health and safety guide.

World Health Organization. (2010). WHO guidelines for indoor air quality: selected pollutants.

World Health Organization. (2021). *Household air pollution and health*. World Health Organization. Retrieved May 5, 2022 from https://www.who.int/news-room/fact-sheets/detail/household-air-pollution-and-health

Worsley, M. A., Pham, T. T., Yan, A., Shin, S. J., Lee, J. R., Bagge-Hansen, M., Mickelson, W., & Zettl, A. (2014). Synthesis and characterization of highly crystalline graphene aerogels. *ACS Nano*, *8*(10), 11013-11022.

Wu, J., Xie, L., Li, Y., Wang, H., Ouyang, Y., Guo, J., & Dai, H. (2011). Controlled chlorine plasma reaction for noninvasive graphene doping. *Journal of the American Chemical Society*, *133*(49), 19668-19671.

Wu, M., Cao, C., & Jiang, J. (2010). Light non-metallic atom (B, N, O and F)-doped graphene: a first-principles study. *Nanotechnology*, *21*(50), 505202.

Wu, M. S., Xu, X. Y., Xu, X., Wang, X. T., Zhao, X. T., Pei, M., Ma, X. H., Wang, M. Z., Wang, F., & Li, J. X. (2015). Comparison of Removal Efficiency of Formaldehyde by Chlorine Dioxide, Photocatalyst and Active Carbon. Applied Mechanics and Materials,

Wu, S.-S., Hou, W.-C., & Wang, D. K. (2020). Photocatalytic reduction of Cr (vi) by graphene oxide materials under sunlight or visible light: the effects of low-molecular-weight chemicals. *Environmental Science: Nano*, *7*(8), 2399-2409.

Wu, Y., Wang, P., Zhu, X., Zhang, Q., Wang, Z., Liu, Y., Zou, G., Dai, Y., Whangbo, M. H., & Huang, B. (2018). Composite of $CH_3NH_3PbI_3$ with Reduced Graphene Oxide as a Highly Efficient and Stable Visible‐Light Photocatalyst for Hydrogen Evolution in Aqueous HI Solution. *Advanced Materials*, *30*(7), 1704342.

Xia, C., Peng, Y., Zhang, H., Wang, T., Wei, S., & Jia, Y. (2014). The characteristics of n-and p-type dopants in SnS_2 monolayer nanosheets. *Physical Chemistry Chemical Physics*, *16*(36), 19674-19680.

Xiang, Q., Yu, J., & Jaroniec, M. (2012). Graphene-based semiconductor photocatalysts. *Chemical Society Reviews*, *41*(2), 782-796.

Xie, H., Liu, B., & Zhao, X. (2016). Facile process to greatly improve the photocatalytic activity of the TiO_2 thin film on window glass for the photodegradation of acetone and benzene. *Chemical Engineering Journal*, *284*, 1156-1164.

Xing, M., Fang, W., Yang, X., Tian, B., & Zhang, J. (2014). Highly-dispersed boron-doped graphene nanoribbons with enhanced conductibility and photocatalysis. *Chemical Communications*, *50*(50), 6637-6640.

Xing, T., Zheng, Y., Li, L. H., Cowie, B. C., Gunzelmann, D., Qiao, S. Z., Huang, S., & Chen, Y. (2014). Observation of active sites for oxygen reduction reaction on nitrogen-doped multilayer graphene. *ACS Nano*, *8*(7), 6856-6862.

Xu, Y.-J., Zhuang, Y., & Fu, X. (2010). New insight for enhanced photocatalytic activity of TiO_2 by doping carbon nanotubes: a case study on degradation of benzene and methyl orange. *The Journal of Physical Chemistry C*, *114*(6), 2669-2676.

Xue, B., & Zou, Y. (2018). High photocatalytic activity of ZnO–graphene composite. *Journal of Colloid and Interface Science*, *529*, 306-313.

Xue, B., Zou, Y., & Yang, Y. (2017). A UV-light induced photochemical method for graphene oxide reduction. *Journal of Materials Science*, *52*(21), 12742-12750.

Xue, Y., Liu, J., Chen, H., Wang, R., Li, D., Qu, J., & Dai, L. (2012). Nitrogen‐doped graphene foams as metal‐free counter electrodes in high‐performance dye‐sensitized solar cells. *Angewandte Chemie International Edition*, *51*(48), 12124-12127.

Yadav, A., Yadav, M., Gupta, S., Popat, Y., Gangan, A., Chakraborty, B., Ramaniah, L., Fernandes, R., Miotello, A., & Press, M. (2019). Effect of graphene oxide loading on TiO_2: Morphological, optical, interfacial charge dynamics-A combined experimental and theoretical study. *Carbon*, *143*, 51-62.

Yang, M.-L., Zhang, N., Lu, K.-Q., & Xu, Y.-J. (2017). Insight into the role of size modulation on tuning the band gap and photocatalytic performance of semiconducting nitrogen-doped graphene. *Langmuir*, *33*(13), 3161-3169.

Yang, M., Wang, L., Li, M., Hou, T., & Li, Y. (2015). Structural stability and O_2 dissociation on nitrogen-doped graphene with transition metal atoms embedded: A first-principles study. *Aip Advances*, *5*(6), 067136.

Yao, C., Yuan, A., Zhang, H., Li, B., Liu, J., Xi, F., & Dong, X. (2019). Facile surface modification of textiles with photocatalytic carbon nitride nanosheets and the excellent performance for self-cleaning and degradation of gaseous formaldehyde. *Journal of Colloid and Interface Science*, *533*, 144-153.

Yeh, T.-F., Chan, F.-F., Hsieh, C.-T., & Teng, H. (2011). Graphite oxide with different oxygenated levels for hydrogen and oxygen production from water under illumination: the band positions of graphite oxide. *The Journal of Physical Chemistry C*, *115*(45), 22587-22597.

Yeh, T.-F., Chen, S.-J., Yeh, C.-S., & Teng, H. (2013). Tuning the electronic structure of graphite oxide through ammonia treatment for photocatalytic generation of H_2 and O_2 from water splitting. *The Journal of Physical Chemistry C*, *117*(13), 6516-6524.

Yeh, T. F., Syu, J. M., Cheng, C., Chang, T. H., & Teng, H. (2010). Graphite oxide as a photocatalyst for hydrogen production from water. *Advanced Functional Materials*, *20*(14), 2255-2262.

Yeh, T. F., Teng, C. Y., Chen, S. J., & Teng, H. (2014). Nitrogen‐doped graphene oxide quantum dots as photocatalysts for overall water‐splitting under visible light Illumination. *Advanced Materials*, *26*(20), 3297-3303.

Yeom, D.-Y., Jeon, W., Tu, N. D. K., Yeo, S. Y., Lee, S.-S., Sung, B. J., Chang, H., Lim, J. A., & Kim, H. (2015). High-concentration boron doping of graphene nanoplatelets by simple thermal annealing and their supercapacitive properties. *Scientific Reports*, *5*(1), 1-10.

Yin, W., Bai, L., Zhu, Y., Zhong, S., Zhao, L., Li, Z., & Bai, S. (2016). Embedding metal in the interface of a p-n heterojunction with a stack design for superior Z-scheme photocatalytic hydrogen evolution. *ACS Applied Materials & Interfaces*, *8*(35), 23133-23142.

Yu, C., & Crump, D. (1998). A review of the emission of VOCs from polymeric materials used in buildings. *Building and Environment*, *33*(6), 357-374.

Yu, J. C., Lin, J., & Kwok, R. W. (1998). Ti1-x Zr x O_2 Solid Solutions for the Photocatalytic Degradation of Acetone in Air. *The Journal of Physical Chemistry B*, *102*(26), 5094-5098.

Yu, M., Shang, J., & Kuang, Y. (2021). Efficient photocatalytic reduction of chromium (VI) using photoreduced graphene oxide as photocatalyst under visible light irradiation. *Journal of Materials Science & Technology*, *91*, 17-27.

Yu, S. S., Zheng, W. T., & Jiang, Q. (2009). Electronic properties of nitrogen-/boron-doped graphene nanoribbons with armchair edges. *IEEE Transactions on Nanotechnology*, *9*(1), 78-81.

Yu, W., Sisi, L., Haiyan, Y., & Jie, L. (2020). Progress in the functional modification of graphene/graphene oxide: A review. *RSC Advances*, *10*(26), 15328-15345.

Yu, X., Han, P., Wei, Z., Huang, L., Gu, Z., Peng, S., Ma, J., & Zheng, G. (2018). Boron-doped graphene for electrocatalytic N2 reduction. *Joule*, *2*(8), 1610-1622.

Zbořil, R., Karlický, F., Bourlinos, A. B., Steriotis, T. A., Stubos, A. K., Georgakilas, V., Šafářová, K., Jančík, D., Trapalis, C., & Otyepka, M. (2010). Graphene fluoride: a stable stoichiometric graphene derivative and its chemical conversion to graphene. *Small*, *6*(24), 2885-2891.

Zhang, C., Fu, L., Liu, N., Liu, M., Wang, Y., & Liu, Z. (2011). Synthesis of nitrogen‐doped graphene using embedded carbon and nitrogen sources. *Advanced Materials*, *23*(8), 1020-1024.

Zhang, F., Li, X., Zhao, Q., Zhang, Q., Tadé, M., & Liu, S. (2015). Fabrication of α-Fe2O3/In2O3 composite hollow microspheres: A novel hybrid photocatalyst for toluene degradation under visible light. *Journal of Colloid and Interface Science*, *457*, 18-26.

Zhang, H., Fan, L., Dong, H., Zhang, P., Nie, K., Zhong, J., Li, Y., Guo, J., & Sun, X. (2016). Spectroscopic investigation of plasma-fluorinated monolayer graphene and application for gas sensing. *ACS Applied Materials & Interfaces*, *8*(13), 8652-8661.

Zhang, J., Hu, Y., Qin, J., Yang, Z., & Fu, M. (2020). TiO_2-UiO-66-NH_2 nanocomposites as efficient photocatalysts for the oxidation of VOCs. *Chemical Engineering Journal*, *385*, 123814.

Zhang, J., Zhao, C., Liu, N., Zhang, H., Liu, J., Fu, Y. Q., Guo, B., Wang, Z., Lei, S., & Hu, P. (2016). Tunable electronic properties of graphene through controlling bonding configurations of doped nitrogen atoms. *Scientific Reports*, *6*(1), 1-10.

Zhang, Q., Wang, B. X., Zhou, Y. L., Hong, J.-m., & Yu, Y. B. (2022). Electrocatalytic degradation of acetaminophen by fluorine-doped graphene oxide: Efficiency and mechanism under constant current and pulse current supply. *Journal of Physics and Chemistry of Solids*, *161*, 110443.

Zhang, Q., Zhou, Y.-l., Yu, Y.-b., Chen, B.-Y., & Hong, J.-m. (2020). Exploring catalytic performance of boron-doped graphene electrode for electrochemical degradation of acetaminophen. *Applied Surface Science*, *508*, 145111.

Zhang, X., Gao, B., Creamer, A. E., Cao, C., & Li, Y. (2017). Adsorption of VOCs onto engineered carbon materials: a review. *Journal of Hazardous Materials*, *338*, 102-123.

Zhang, X., Huang, J., Ding, K., Hou, Y., Wang, X., & Fu, X. (2009). Photocatalytic decomposition of benzene by porous nanocrystalline $ZnGa_2O_4$ with a high surface area. *Environmental Science & Technology*, *43*(15), 5947-5951.

Zhang, X., Qin, C., Gong, Y., Song, Y., Zhang, G., Chen, R., Gao, Y., Xiao, L., & Jia, S. (2019). Co-adsorption of an anionic dye in the presence of a cationic dye and a heavy metal ion by graphene oxide and photoreduced graphene oxide. *RSC Advances*, *9*(10), 5313-5324.

Zhang, X., Yang, Y., Li, H., Zou, X., & Wang, Y. (2016). Non-TiO_2 photocatalysts used for degradation of gaseous VOCs. *Progress in Chemistry*, *28*(10), 1550.

Zhang, Y., Liu, W., & Niu, H. (2008). Native defect properties and p-type doping efficiency in group-IIA doped wurtzite AlN. *Physical Review B*, *77*(3), 035201.

Zhang, Y., Tang, Z.-R., Fu, X., & Xu, Y.-J. (2010). TiO_2− graphene nanocomposites for gas-phase photocatalytic degradation of volatile aromatic pollutant: is TiO_2− graphene truly different from other TiO_2− carbon composite materials? *ACS Nano*, *4*(12), 7303-7314.

Zhang, Y. L., Guo, L., Xia, H., Chen, Q. D., Feng, J., & Sun, H. B. (2014). Photoreduction of graphene oxides: methods, properties, and applications. *Advanced Optical Materials*, *2*(1), 10-28.

Zhang, Z., Jiang, Z., & Shangguan, W. (2016). Low-temperature catalysis for VOCs removal in technology and application: a state-of-the-art review. *Catalysis Today*, *264*, 270-278.

Zhao, J., & Yang, X. (2003). Photocatalytic oxidation for indoor air purification: a literature review. *Building and Environment*, *38*(5), 645-654.

Zhao, L., Levendorf, M., Goncher, S., Schiros, T., Palova, L., Zabet-Khosousi, A., Rim, K. T., Gutierrez, C., Nordlund, D., & Jaye, C. (2013). Local atomic and electronic structure of boron chemical doping in monolayer graphene. *Nano Letters*, *13*(10), 4659-4665.

Zhao, X., Wang, Z., Xie, Y., Xu, H., Zhu, J., Zhang, X., Liu, W., Yang, G., Ma, J., & Liu, Y. (2018). Photocatalytic Reduction of Graphene Oxide – TiO_2 Nanocomposites for Improving Resistive - Switching Memory Behaviors. *Small*, *14*(29), 1801325.

Zhou, Z., Gao, J., Zhang, G., Dong, Y., Wang, Z., Li, J., & Lyu, J. (2020). Optimizing graphene-TiO_2 interface properties via Fermi level modulation for photocatalytic degradation of volatile organic compounds. *Ceramics International*, *46*(5), 5887-5893.

Zhu, Z., Liu, F., & Zhang, W. (2015). Fabricate and characterization of $Ag/BaAl_2O_4$ and its photocatalytic performance towards oxidation of gaseous toluene studied by FTIR spectroscopy. *Materials Research Bulletin*, *64*, 68-75.

Zhu, Z., & Wu, R.-J. (2015). The degradation of formaldehyde using a Pt@ TiO_2 nanoparticles in presence of visible light irradiation at room temperature. *Journal of the Taiwan Institute of Chemical Engineers*, *50*, 276-281.

Zou, W., Gao, B., Ok, Y. S., & Dong, L. (2019). Integrated adsorption and photocatalytic degradation of volatile organic compounds (VOCs) using carbon-based nanocomposites: A critical review. *Chemosphere*, *218*, 845-859.

Zou, X., Dong, Y., Ke, J., Ge, H., Chen, D., Sun, H., & Cui, Y. (2020). Cobalt monoxide/tungsten trioxide pn heterojunction boosting charge separation for efficient visible-light-driven gaseous toluene degradation. *Chemical Engineering Journal*, *400*, 125919.